MICROCOPY RESOLUTION TEST CHART
NATIONAL BUREAU OF STANDARDS-1963-A

(12)

AFGL-TR-87-0148

MULTI-TECHNIQUE STUDY OF IONOSPHERIC STRUCTURES CAUSING DEGRADATION IN
TRANS-IONOSPHERIC COMMUNICATIONS SYSTEMS

Sunanda Basu
Patricia Doherty
Eileen MacKenzie
M. Patricia Hagan

DTIC
ELECTE
AUG 05 1987
S
D

AD-A183 542

The Trustees of Emmanuel College
400 The Fenway
Boston, Massachusetts 02115

Final Report
3 December 1983 – 31 January 1987

20 April 1987

87   8   4   022

"This technical report has been reviewed and is approved for publication"

WILLIAM K. VICKERY
Contract Manager
Ionospheric Effects Branch

HERBERT C. CARLSON, Chief
Ionospheric Effects Branch
Ionospheric Physics Division

FOR THE COMMANDER

ROBERT A. SKRIVANEK
Director
Ionospheric Physics Division

A183542

REPORT DOCUMENTATION PAGE

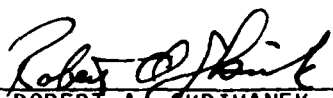| 1a. REPORT SECURITY CLASSIFICATION Unclassified	1b. RESTRICTIVE MARKINGS None		
2a. SECURITY CLASSIFICATION AUTHORITY N/A	3. DISTRIBUTION/AVAILABILITY OF REPORT Approved for publication; distribution unlimited		
2b. DECLASSIFICATION/DOWNGRADING SCHEDULE N/A			
4. PERFORMING ORGANIZATION REPORT NUMBER(S) Technical Report - Final	5. MONITORING ORGANIZATION REPORT NUMBER(S) AFGL-TR-87-0148		

6a. NAME OF PERFORMING ORGANIZATION Emmanuel College	6b. OFFICE SYMBOL (If applicable) PRD	7a. NAME OF MONITORING ORGANIZATION Air Force Geophysics Laboratory
6c. ADDRESS (City, State and ZIP Code) 400 The Fenway Boston MA 02115		7b. ADDRESS (City, State and ZIP Code) Hanscom AFB MA 01731 ATTN: Mr. William K. Vickery
8a. NAME OF FUNDING/SPONSORING ORGANIZATION USAF AFSC ESD PKR	8b. OFFICE SYMBOL (If applicable)	9. PROCUREMENT INSTRUMENT IDENTIFICATION NUMBER F19628-84-K-0003

8c. ADDRESS (City, State and ZIP Code) Hanscom AFB MA 01731	10. SOURCE OF FUNDING NOS.			
	PROGRAM ELEMENT NO.	PROJECT NO.	TASK NO.	WORK UNIT NO.
11. TITLE (Include Security Classification) see 16.	62101F	4643	AA	AC

12. PERSONAL AUTHOR(S)
Sunanda Basu; Patricia Doherty; Eileen MacKenzie; M. Patricia Hagan

13a. TYPE OF REPORT Final	13b. TIME COVERED FROM 12/3/83 TO 1/31/87	14. DATE OF REPORT (Yr., Mo., Day) 87 April 20	15. PAGE COUNT 116

16. SUPPLEMENTARY NOTATION
Multi Technique Study of Ionospheric Structures Causing Degradation in Trans-Ionospheric Communications Systems

17. COSATI CODES			18. SUBJECT TERMS (Continue on reverse if necessary and identify by block number)
FIELD	GROUP	SUB. GR.	VHF/UHF & GHz amplitude scintillation, phase scintillation, F-region irregularities, equatorial irregularities, (continued on reverse)

19. ABSTRACT (Continue on reverse if necessary and identify by block number)

Multiple diagnostics have been used at different latitude regimes of the globe to probe large and small scale ionospheric structures which cause degradation in trans-ionospheric communication systems. It was determined that the equatorial anomaly crest had the most disturbed F-region irregularity environment giving rise to saturated GHz scintillation and phase scintillations as large as 16 radians at 244 MHz. At the magnetic equator a host of techniques during the Project Condor rocket campaign in Peru established that the largest GHz scintillations maximize in association with extended 3m backscatter plane structures and that spaced-receiver scintillation measurements yield irregularity drift velocities in fairly good agreement with the 50 MHz radar interferometer drifts. By combining in-situ data of irregularities with scintillations, a new class of extended VHF scintillation producing irregularities was isolated known as bottomside sinusoidal.

(Continued on reverse)

20. DISTRIBUTION/AVAILABILITY OF ABSTRACT UNCLASSIFIED/UNLIMITED ☒ SAME AS RPT. ☐ DTIC USERS ☐	21. ABSTRACT SECURITY CLASSIFICATION Unclassified	
22a. NAME OF RESPONSIBLE INDIVIDUAL William Vickery	22b. TELEPHONE NUMBER (Include Area Code) (617) 377-3220	22c. OFFICE SYMBOL AFGL/LIS

19. cont.

In the polar cap, the overwhelming control of the sunspot cycle in dictating magnitude and occurrence of scintillations was established. Large total electron content (TEC) increases were observed in the polar cap using GPS satellites and phase scintillation events as large as 12 radians at 250 MHz were observed. It was found that multipath effects from the local environment of the receiving antenna can cause severe contamination of ionospheric group delay measurements made with the GPS pseudorandom noise receivers.

In the auroral oval a new class of irregularities was identified which was associated with shears in the background convective plasma flow. AE-D and DMSP satellites were used to obtain evidence for shallow spectral slopes of density irregularities in conjunction with velocity shears and steep spectral slopes in regions of energetic electron precipitation where E-layer conductivity was high.

Measurements of midlatitude TEC showed the importance of downward fluxes of electrons from the equatorial regions.

18. cont.

high-latitude irregularities, satellite in-situ, rocket in-situ, radar backscatter, generation mechanisms, velocity shears, energetic electron precipitation, E-region conductivity, power spectra, Fresnel oscillations, Total Electron Content (TEC), Multipath effects, electron content enhancements, plasma convection

TABLE OF CONTENTS

iii

MULTI-TECHNIQUE STUDY OF IONOSPHERIC STRUCTURES CAUSING DEGRADATION IN TRANS-IONOSPHERIC COMMUNICATIONS SYSTEMS

Summary

A variety of diagnostic techniques has been used at equatorial, middle, auroral and polar latitudes to probe large and small scale ionospheric structures which cause degradation in trans-ionospheric communications systems.

By conducting ionospheric scintillation measurements at various stations in different latitude regimes of the globe, we were able to establish that the equatorial anomaly crest region is the most disturbed irregularity environment with 30 dB fluctuations observed at 1.5 GHz and 7 dB fluctuations observed even at 4 GHz (Attachment 1). We were also able to provide the first long-term measurements of phase scintillation at such a location – the rms phase deviations being as large as 16 radians at 244 MHz (for 100-sec detrend period) in the pre-midnight hours of high sunspot years (Attachment 2).

The polar cap was also found to be a seat of large phase fluctuations at 250 MHz with values as large as 12 radians being observed (with 82-sec detrend period) at Thule, Greenland (Attachments 2 and 3). It is quite possible that these large phase scintillations occur in conjunction with large increases in total electron content (TEC) observed with Global Positioning System (GPS) satellites at Thule, with factors of 2 increases in TEC above the background not uncommon (Attachment 4). By

conducting continuous intensity scintillation measurements at Thule over half a solar cycle, the very significant effect of sunspot number in controlling the magnitude and occurrence of scintillations was established (Attachment 2).

In the auroral oval a new class of irregularities was identified which was associated with shears in the background convective plasma flow (Scientific Report 2 - Basu et al., Geophysical Research Letters, 13, 101-104, 1986). Multiple diagnostic instruments such as the incoherent scatter EISCAT radar, the coherent backscatter STARE radar and the HiLat satellite in-situ measurements of ion drift were utilized to determine the presence of velocity shears. The small scale irregularities (< 1 km) were found to have relatively shallow spectral slopes and large power spectral densities at hundreds of m scalelength as evidenced by the substantial scintillation even at 413 MHz. An earlier study done jointly with the Atmosphere Explorer-D and DMSP satellites also provided evidence for shallow spectral slopes of density irregularities in conjunction with velocity shear regions and steep spectral slopes in regions of energetic electron precipitation where E-layer conductivity was high (Attachment 5). The large temporal and spatial variability of the background plasma flow gives rise to large variations in decorrelation times and in phase and intensity scintillation rates which adversely affect communications systems at 250 MHz operating in the high latitude environment (Attachments 2 and 3).

Measurements of TEC made at mid-latitude stations such as Haifa (L = 1.24) and Athens (L = 1.37) showed the importance of

2

downward fluxes of electrons from the equatorial regions in causing post-sunset increases of TEC at the lower latitude station of Haifa (Attachment 6). The problems involved in the determination of absolute ionospheric time delay from GPS signals were studied. It was found that multipath effects from the local environment of the receiving antenna can cause severe contamination of ionospheric group delay measurements made with the GPS pseudorandom noise receivers (Attachment 7).

At the magnetic equator, scintillations caused by a new class of irregularities known as bottomside sinusoidal (bss) were isolated (Attachment 8). The unique feature of this class of irregularities is that Fresnel oscillations are observed in their spectra indicating that these irregularities occur in relatively thin layers (probably < 50 km in altitude extent). The patches containing these bss irregularities, however, are quite extended in the E-W direction sometimes covering more than 1000 km.

A host of diagnostics was used to study the other well-known class of equatorial irregularities known as "bubbles" during an extensive rocket campaign conducted in Peru called "Project Condor". Using scintillation, radar backscatter, and digital ionosonde data, it could be shown that two factors, other than the classical Rayleigh-Taylor plasma instability process, must operate to yield the longest-scale horizontal organization of spread-F structures. These two factors are probably shears in the background plasma flow and gravity wave induced vertical motions as discussed in Attachment 9. A careful analysis of the GHz scintillation data obtained during Project Condor established

3

that the height integrated rms electron density deviation of
∿200 m scale irregularities causing 1.7 GHz scintillations
maximizes in extended 3-m backscatter plume structures. Further,
the spaced-receiver scintillation measurements yielded
irregularity drift velocities in fairly good agreement with the
50 MHz radar interferometer results (Attachment 10). All the
above equatorial irregularity results, as well as, the importance
of nighttime F-region dynamics in controlling the magnitude of
scintillations were summarized in a recent review of equatorial
scintillations (Scientific Report 1 - Basu and Basu, J. Atmos.
Terr. Phys., 47, 753-768, 1985).

ATTACHMENT 1

UHF/GHz scintillation observed at Ascension Island from 1980 through 1982

J. P. Mullen, E. MacKenzie, and Santimay Basu

Emmanuel College, Boston, Massachusetts

H. Whitney

Air Force Geophysics Laboratory, Hanscom Air Force Base, Massachusetts

Three years' scintillation measurements taken at Ascension Island have been reduced and are presented here. The 1.5-GHz and 257-MHz signals of Marisat were supplemented by 3.9-GHz observations during January–May 1981. While their temporal patterns are similar to those found earlier in the Afro-American zone, they exhibited unusually frequent occurrence of heavy scintillation at gigahertz frequencies often exceeding 30 dB at 1.5 GHz and 7 dB at 4 GHz. These patterns are attributed in part to the position of the station near the southern peak of the Appleton anomaly. Comparisons are made between these and similar observations taken at Hong Kong, near the northern peak of the anomaly.

INTRODUCTION

Scintillation measurements from the geostationary satellite Marisat at UHF (257 MHz) and L band frequencies (1541 MHz) were initiated at Ascension Island (7.95°S, 14.38°W) in December 1979. Three years' data (1980–1982) have been analyzed to provide statistical information on the intense scintillation observed here, which is more severe than that observed at other equatorial stations [*Aarons et al.*, 1981]. During early 1981 (January–May), measurements were also available on C band (3.9 GHz) from this satellite. The scintillation magnitudes of L band and C band measurements were obtained following the standard reduction procedure of *Whitney* [1974]. The UHF scintillation data were scaled only to the extent that times of scintillation occurrence ≥ 10 dB were noted.

THE DATA

Figure 1 shows a sample of scintillation on all 3 frequencies obtained on February 3, 1981. Saturated scintillation was seen at UHF, with up to 31 dB at L band and 7.3 dB at C band. This could be considered a common occurrence at this time.

Figures 2 and 3 are contour plots of the percent occurrence of scintillation greater than 6 dB (Figure 2) and 15 dB (Figure 3) at the L band frequency as a function of local time (LT = UT − 1 hour) during 1980–1982. These generally follow the equatorial patterns described earlier [*Mullen et al.*, 1977, 1983; *Paulson*, 1981] in which heavy scintillation commonly occurs during September–April with little in May–August. The sunrise and sunset times at an altitude of 110 km corresponding to the E region height are indicated by the dotted lines in both diagrams. It may be noted that the contours of scintillation occurrence are confined in the time interval between sunset and about 4 hours prior to sunrise. Occasional intrusion of the dotted line inside the occurrence contours is caused by the 15-min time resolution of the computed SI index. An examination of the raw data, however, reveals that the sunset always precedes the onset of scintillation. A detailed examination of the occurrence pattern will be made in a later section. Based on this pattern, in 1981 and 1982, data was not taken during the light occurrence months.

In order to show the time history of the onset and decay of UHF and L band scintillations in the course of a single night, we illustrate in Figure 4 the daily occurrence of UHF scintillation SI ≥ 10 dB and L band scintillation SI ≥ 1 dB as a function of local time (LT = UT − 1 hour) for the month of March 1980. We have chosen this particular month as it shows the maximum occurrence of scintillation. The striking features of simultaneous onset of scintillations at both frequencies at about 2000 LT, the

IONOSPHERIC AMPLITUDE SCINTILLATION
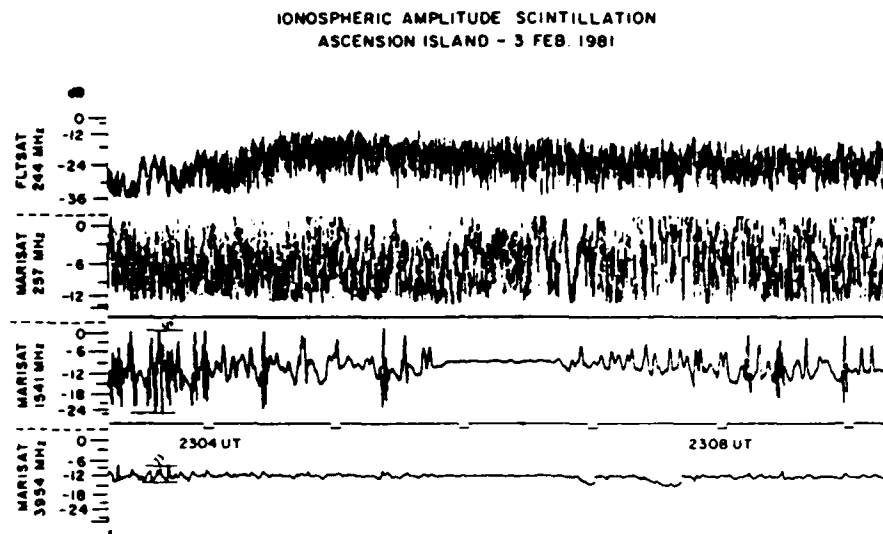ASCENSION ISLAND - 3 FEB. 1981

Fig. 1.   Sample of scintillation observed at Ascension Island on February 3, 1981.

decay of L band scintillations seen after local midnight, and the persistence of UHF scintillations as long as 0400 LT are seen.

Cases of L band scintillations without any accompanying UHF scintillations (e.g., March 5 and 6 between 0000 and 0100 LT) are a result of the data analysis procedures. The UHF data were scaled to exact on/off times of scintillation index ≥ 10 dB while the L band data were scaled in the standard 15-min reduction scheme which assigns a decibel value to 15-min data blocks. In Figure 5, a similar daily occurrence pattern for February 1981 is shown when the C band (3.94 GHz) scintillation data were available in addition to the UHF (257 MHz) and L band (1.54 GHz) frequencies. The diagram indicates that the onset of scintillations in the wide frequency interval of 257 MHz to 3.94 GHz is near simultaneous but the decay of scintillations is progressive from the highest to the lowest frequency. This implies that the irregularities in the scale-length range of about 700 m and 175 m, corresponding to Fresnel dimensions of 257 MHz and 3.94 GHz, respectively, attain their maximum strength simultaneously, but the lifetime of the 700-m irregularities is several hours longer than the 175-m irregularities.

In view of the localization of scintillations mentioned above, further analysis was done in two 4-hour time blocks, namely, the premidnight time block between 2000-2400 LT and the postmidnight block between 0000-0400 LT. Figures 6 and 7 show the L band monthly occurrence levels of various

fading depths during these two most active 4-hour time blocks. The fading depths correspond to scintillation indices as shown in Table 1.

For premidnight scintillation, the peak month of the 3 years is March 1980. In view of the very low occurrence of postmidnight scintillations, it is difficult to assign any statistical significance to the observed seasonal pattern. The premidnight occurrence peak is approximately 4 times as great as the postmidnight.

Within the premidnight time period (Figure 6), it appears that two patterns of fade levels occur. At the lowest level of fade occurrence (>5 dB), one broad maximum runs from September-March. At the highest level of fade occurrence (>20 dB) two distinct maxima emerge from the broad background, the first in September-October and the second in February-March. An asymmetry between the two equinoxes may be noted, which seems to vary over the years. In the 1980-1981 period, scintillations are accentuated in March, whereas in 1981-1982, the occurrence is higher in September.

The pattern of magnetic activity on a monthly basis suggests a possible explanation for these exceptions. The statistics presented in this paper have been compiled regardless of magnetic activity index, Kp. As noted in Aarons et al. [1981], increased magnetic index inhibited scintillation (during January-February 1980). Aarons et al. [1980] noted this at Huancayo, Peru at which time it was seen that this decrease was of differing severity in different seasons.
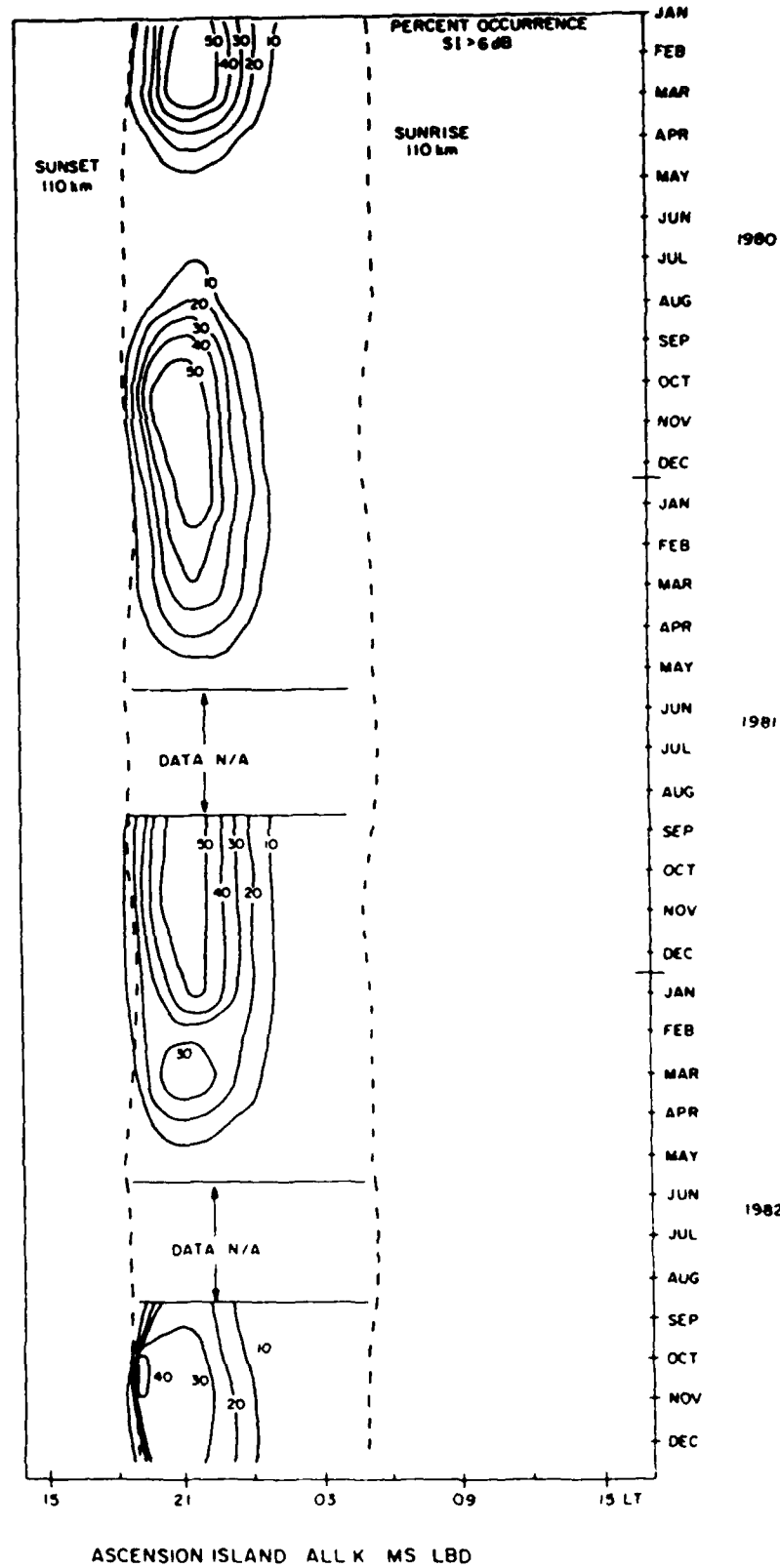
Fig 2. Percent occurrence of L band scintillation (> 6 dB) at Ascension Island during 1980–1982
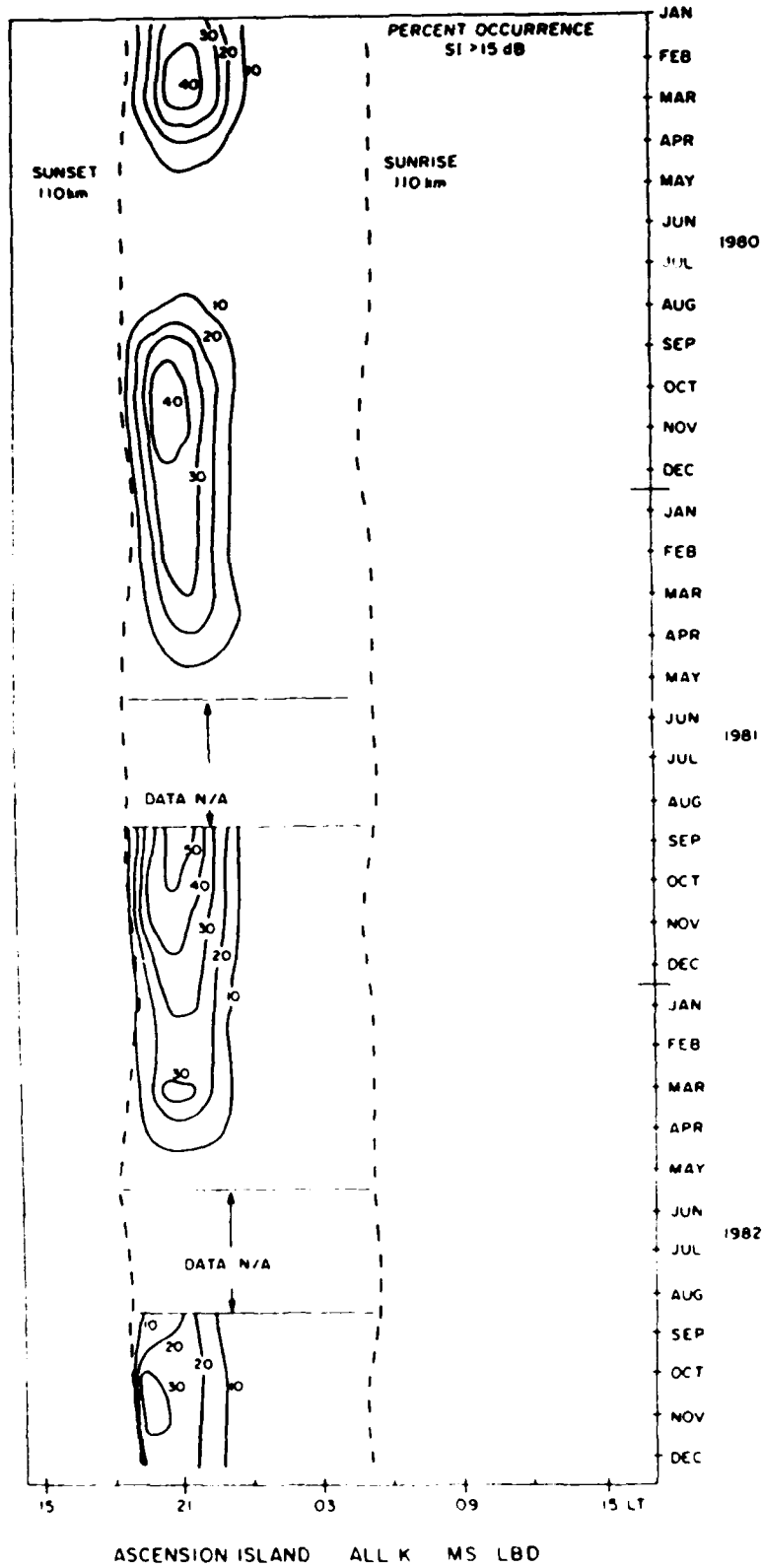
Fig. 3. Percent occurrence of L band scintillation (> 15 dB) at Ascension Island during 1980–1982

OCCURRENCE OF SCINTILLATION AT ASCENSION ISLAND
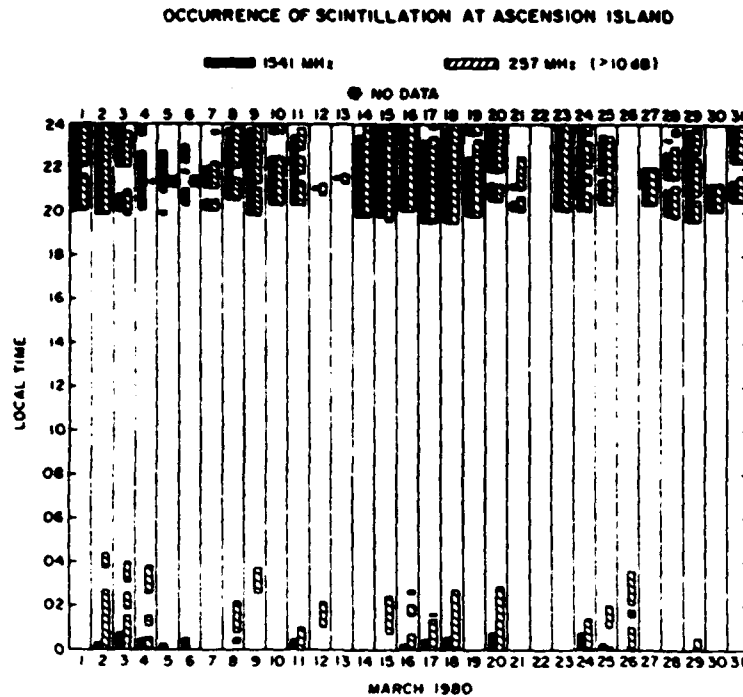
Fig. 4   Daily occurrence of UHF $(SI \geq 10$ dB) and L band $(SI \geq 1$ dB) scintillation during March 1980 as a function of local time.

and in May–July actually reversed to an increase. In March 1980, when the percentage occurrence of scintillation was higher than anticipated, the percentage of time that the magnetic activity index Kp was dis-

Fig 5   Daily occurrence of UHF $(SI \geq 10$ dB), L band $(SI \geq 1$ dB), and C band $(SI \geq 1$ dB) scintillation during February 1981 as a function of local time

turbed (>3) was less than in other months, and in March 1981, when the percentage occurrence of scintillation was lower than anticipated, the percentage of time that the magnetic activity index was disturbed (>3) was greater than in the other months. In September–October 1982, reduced sunspot number and increased magnetic index seemed to link together to reduce SI (decibels).

Various percentiles of scintillation occurrence at 1541 MHz were computed during 1900 LT to 2300 LT, the period of maximum scintillation activity. Figure 8 shows for the year 1980 the median, the 90th and 99th percentiles of occurrence: that is, the percentage of time where scintillation is equal to or less than the ordinate. It may be noted that in March 1980, scintillation index as high as 18 dB was attained at 1541 MHz for 50% of the time. It is also significant to note that scintillation index exceeding 29 dB was observed 10% of the time over the broad period of September 1980 to March 1981. Figures 9 and 10 show similar statistics for 1981 and 1982. These diagrams depict the vulnerability of 1541 MHz communication links in the extremely disturbed ionospheric environment at Ascension Island. An outage as large as 10% for systems with fade margins of 24 dB is a common occurrence for about 6 months between September and March
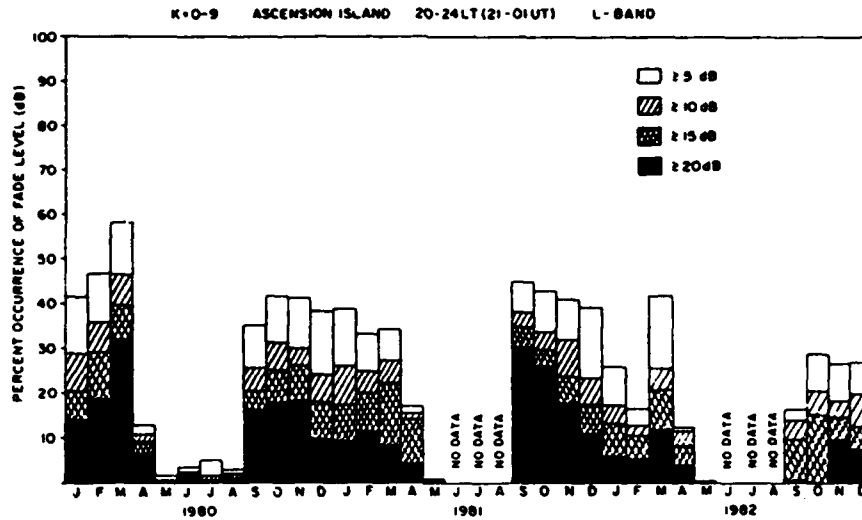
Fig. 6.   L band monthly occurrence levels of fading depths ≥5, 10, 15, 20 dB in the premidnight time period (2000–2400 LT).

DISCUSSION

The high intensity and occurrence of gigahertz scintillation observed at Ascension Island have been described by *Christiansen* [1971], *Aarons et al.* [1983], *Basu et al.* [1980a], and *Basu and Basu* [1981]. Among others, *Aarons et al.* [1981] hypothesize that the dominant underlying factor is penetration by the raypath of the equatorial anomaly crest. They c ipare the Ascension observations with those taken ⎣t Huancayo (2.5°N dip) and attribute the

greater anomaly region scintillation to higher nocturnal electron densities (and therefore higher value of electron density deviation, ΔN) than at the magnetic equator. Electron density levels in the evening at Ascension greater than 4 times that found at the dip equator have been suggested by *Gerard et al.* [1977].

In the postsunset period, the near simultaneous onset of scintillations in the broad frequency interval of 257 MHz to 3945 MHz is significant. Since the Fresnel dimensions of 257 MHz and 3945 MHz ob-

Fig. 7   L band monthly occurrence levels of fading depths ≥5, 10, 15, 20 dB in the postmidnight time period (0000–0400 LT).

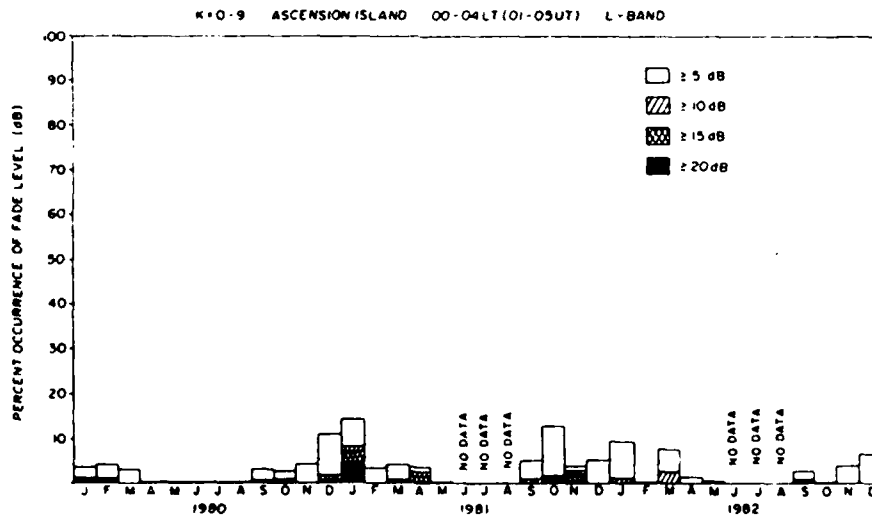TABLE I. Conversion of Fade Level to Scintillation Index

Fade Level, dB	Scintillation Index, dB
≥ 5	≥ 8.6
≥ 10	≥ 15.7
≥ 15	≥ 22.6
≥ 20	≥ 28.2

servations are about 700 m and 175 m, respectively, it is concluded that the irregularities in this broad scale range attain maximum spectral intensity simultaneously. The lifetime of short-scale irregularities is, however, several hours shorter than the larger scales as indicated by the earlier decay of scintillations at higher frequencies. This extends the initial observation of simultaneous generation of large- and small-scale irregularities found by *Basu et al.* [1980b] in Peru using scintillation recordings, the Jicamarca radar backscatter, and in situ data from AE-E.

Fang and Liu [1983], observing at Hong Kong (dip = 30°N), have reported generally similar results to those found at Ascension. Observing at 4 GHz, they find scintillation occurrence equinoctial in character as we do at Ascension; during peak hours in September 1979 scintillation of 2–6 dB occurs up to 45% of the time, and up to 65% in March 1980. Our extensive observations at 1.5 GHz confirm the above result.

Fig. 9. Monthly median, 90th and 99th percentiles of scintillation occurrence in 1981 (2000–2400 UT).

Width of the anomaly crest

Assuming that the results at Ascension and Hong Kong are due to their respective positions under the southern and northern crests of the anomaly, the question rises as to why the reported scintillation observed at Taipei, Taiwan (dip = 35°N) is so much less intense and less frequent. This has been studied by *Wernik et al.* [1983] whose findings indicate that the region is characterized by extremely sharp latitudinal gradient of total electron content. They invoke the suggestion of *DasGupta et al.* [1981] and state that the extreme latitudinal gradients at the anomaly region may result from the sharp altitude distribution of the plumes in the equatorial region.

Sensitivity to magnetic index (Kp)

An attempt was made to study this problem from a data set obtained during May, June and August 1980 when scintillation occurrence is minimum. During May, there were no L band scintillation. UHF scintillations were seen on five occasions. The magnetic indices (Kp) for these times were 5, 4, 1, 4, 3, and 5. During June, UHF scintillation again occurred on 5 nights. On 2 nights, the UHF activity was accompanied by L band scintillations when the Kp values were 5- and 5+, respectively. This is in agreement with earlier work [*Mullen*, 1973] which indicated that during periods of minimum scintil-

Fig. 8. Monthly median, 90th and 99th percentiles of scintillation occurrence in 1980 (2000–2400 UT)

ASCENSION ISLAND   1541 MHz   20 - 24 UT
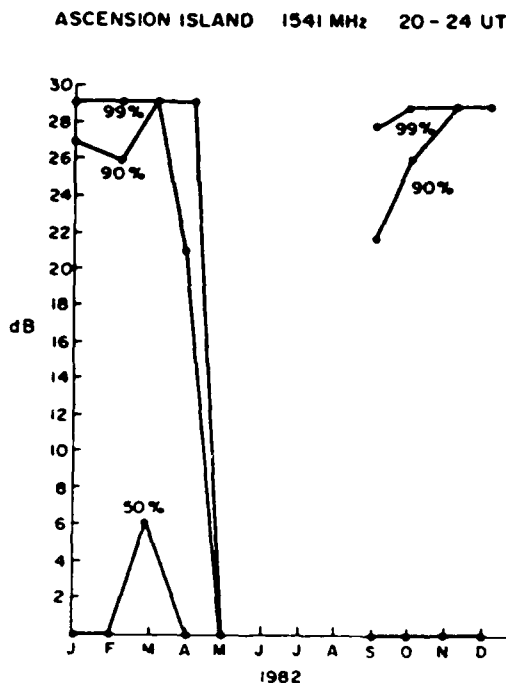

Fig. 10 Monthly median, 90th and 99th percentiles of scintillation occurrence in 1982 (2000-2400 UT).

lation activity, scintillation occurrence is enhanced by magnetic activity. However, on several nights when the Kp values reached 5 or higher, no scintillation was seen. The data during July and August indicated that 75% of cases with strong scintillation activity were magnetically disturbed. Obviously, an elevated Kp cannot be the sole triggering mechanism during this period. During other months, elevated Kp has been shown to inhibit scintillation [Koster, 1972].

CONCLUSIONS

Three years' observations of 1.5-GHz scintillations at Ascension Island, supplemented by 257 MHz most of the time and 3.9 GHz part of the time, are reduced and presented here.

Unusually heavy scintillation observed on gigahertz signals at Ascension Island is attributed to ray penetration of the F region irregularities in an environment of high background ionization density that develops in the region of the Appleton Anomaly shortly after sunset. The postsunset enhancement of background ionization density is most marked near Ascension Island where the transport of ionization in the magnetic meridian through the agency of the zonal neutral wind is facilitated due to the high mag-

netic declination in this longitude sector. The results measured at Ascension are compared to those measured at Hong Kong which is also under the anomaly crest and are found generally similar. Scintillation commenced simultaneously at UHF and GHz frequencies. Scintillation diminished and stopped first at the higher frequencies leading to the conclusion that the irregularities achieve maximum intensity together, and the larger scale sizes decay more slowly.

Magnetic dependence of "off season" scintillation has been examined as a trigger mechanism and found inadequate to explain the day-to-day variability of scintillations.

Gigahertz scintillation occurrence peaks during the premidnight hours (2000-2400 LT) when 10% outage of L band links with 25-dB fade margins are observed.

In general, scintillation magnitude falls off as sunspot number decreases, mainly as a result of the decrease of F region ionization density in the postsunset hours. The decrease of scintillation occurrence is possibly a result of the limited altitude extent of the irregularities at the magnetic equator.

REFERENCES

Aarons, J., J. P. Mullen, J. R. Koster, R. F. daSilva, J. R. Medeiros, R. T. Medeiros, A. Bushby, J. Pantoja, J. Lanat, and M. R. Paulson, Seasonal and geomagnetic control of equatorial scintillations in the two longitude sectors, J. Atmos. Terr. Phys., 42, 861, 1980

Aarons, J., H. E. Whitney, E. MacKenzie, and S. Basu, Microwave equatorial scintillation intensity during solar maximum, Radio Sci., 16, 939, 1981

Aarons, J., J. A. Klobuchar, H. E. Whitney, J. Austen, and C. L. Rino, Gigahertz scintillations associated with equatorial patches, Radio Sci., 18, 421, 1983

Basu, S., and S. Basu, Equatorial scintillations A review, J. Atmos. Terr. Phys., 43, 473, 1981

Basu, S., S. Basu, J. P. Mullen, and A. Bushby, Long-term 1.5-GHz amplitude scintillation measurements at the magnetic equator, Geophys. Res. Lett., 7, 259, 1980a

Basu, S., J. P. McClure, S. Basu, W. B. Hanson, and J. Aarons, Coordinated study of equatorial scintillation and in situ and radar observations of nighttime F region irregularities, J. Geophys. Res., 85, 5119, 1980b

Christiansen, R. M., Preliminary report of S-band propagation disturbance during ALSEP mission support, Rep. X-861-71-239, Goddard Space Flight Center, Greenbelt, Md., 1971

DasGupta, A., A. Maitra, and S. Basu, Occurrence of nighttime VHF scintillation near the equatorial anomaly crest in the Indian sector, Radio Sci., 16, 1455, 1981

Fang, D. J., and C. H. Liu, A morphological study of gigahertz equatorial scintillations in the Asian region, *Radio Sci.*, *18*, 241, 1983

Gerard, J. C., D. N. Anderson, and S. Matsushita, Magnetic storm effects on the tropical ultraviolet airglow, *J. Geophys. Res.*, *82*, 1126, 1977.

Koster, J. R., Equatorial scintillation, *Planet Space Sci.*, *20*, 1999, 1972.

Mullen, J. P., Sensitivity of equatorial scintillation to magnetic activity, *J. Atmos. Terr. Phys.*, *35*, 1187, 1973.

Mullen, J. P., S. Basu, H. E. Whitney, A. Bushby, J. Lanat, and J. Pantoja, Statistics of VHF and L-band scintillation at Huancayo, Peru, *J. Atmos. Terr. Phys.*, *39*, 1243, 1977.

Mullen, J. P., S. Basu, H. E. Whitney, Y. N. Huang, V. Badillo, and A. Bushby, Longitude and solar control of equatorial scintillations, paper presented at International Symposium on Beacon Studies of the Earth's Environment, Natl Phys Lab, New Delhi, India, Feb. 7 11, 1983

Paulson, M. R., Scintillation of VHF/UHF and *L* band satellite signals at Guam, *Radio Sci.*, *16*, 877, 1981

Wernik, A. W., S. Franke, C. H. Liu, and D. J. Fang, Nighttime VHF and GHz scintillations in the East Asian sector of the equatorial anomaly, *Geophys. Res. Lett.*, *10*, 155, 1983

Whitney, H. E., Notes on the relationship of scintillation index to probability distributions and their uses for system design. *Rep AFCRL-TR-74-0004*, Air Force Cambridge Res Lab, Bedford Mass., 1974

AD778092

S. Basu, E. MacKenzie, and J. P. Mullen Emmanuel College, Boston, MA 02115

H. Whitney, Air Force Geophysics Laboratory, Hanscom Air Force Base, MA 01731

250 MHz/GHz Scintillation Parameters in the Equatorial, Polar, and Auroral Environments

SANTIMAY BASU, EILEEN MARTIN MacKENZIE, SUNANDA BASU, EMANOEL COSTA, PAUL F. FOUGERE, SENIOR MEMBER, IEEE, HERBERT C. CARLSON, JR., AND HERBERT E. WHITNEY

Abstract—Ionospheric scintillation effects encountered in the equatorial anomaly crest, polar cap, and auroral regions have been contrasted to provide information for the design and evaluation of the performance of multifrequency satellite communication links in these regions. The equatorial anomaly region is identified as the most disturbed irregularity environment where the amplitude and phase structures of 250 MHz and L-band scintillations are primarily dictated by the strength of scattering rather than ionospheric motion. In the anomaly region, the spectra of intense amplitude scintillations at these frequencies are characterized by uniform power spectral density from the lowest frequency (10 MHz) to 4 Hz at 257 MHz and to 1 Hz at L-band (1541 MHz) and steep rolloff at higher fluctuation frequencies with power law indexes of −5 to −7. Such structures are compatible with intensity decorrelation times of 0.1 and 0.3 s at 257 and 1541 MHz, respectively. The phase spectra at 244 MHz are described by power law variation of psd with frequency with typical spectral indexes of −2.4. The strong scattering at VHF induces extreme phase rates of 200° in 0.1 s. The 90th percentile values of rms phase deviation at 244 MHz with 100 s detrend are found to be 16 rad in the early evening hours, whereas amplitude scintillation can cover the entire dynamic range of 30 dB not only in the 250 MHz band but at L-band as well. In the polar cap, the 50th and 90th percentile values of rms phase deviation at 250 MHz for 82 s detrend are 3 and 12 rad, respectively, with comparable values being obtained in the auroral oval. The corresponding values for the S_4 index of scintillation are 0.5 and 0.8 in the polar cap, which are slightly higher than those recorded in the auroral oval. The power law index of phase scintillation at high latitudes is in the vicinity of −2.3, which is not a result of very strong turbulence as in the equatorial region but is considered to be a consequence of shallow irregularity spectral indexes. The phase rates at auroral locations are an order of magnitude smaller than in the equatorial region and attain values of 100° in 0.5 s. The extreme variability of ionospheric motion in the auroral oval sensitively controls the structure of scintillations.

The long-term morphology (period 1979–1984) of intensity scintillations at 250 MHz in the polar cap shows that, in addition to the absence of diurnal variation of scintillations, and the presence of an annual variation with a pronounced minimum during local summer, there exists a marked solar control of scintillation activity such that it abruptly decreases when the solar activity falls below a threshold level.

I. INTRODUCTION

SATELLITE communication links in the 250 MHz/GHz range can be subjected to the effects of ionospheric scintillations which are caused by the irregularities of electron density in the F-region of the ionosphere. These irregularities impose random phase perturbations on the wavefront of a satellite signal during its passage through the ionosphere. As the wavefront with perturbed phase travels toward the ground, intensity and phase fluctuations develop across the wavefront due to phase mixing. In the case of an orbiting satellite, these intensity and phase fluctuations sweep past a receiver because of the satellite motion and the receiver output registers time variations of intensity and phase known as intensity or phase scintillations. On the other hand, in the case of a geostationary satellite, the motion of the ionospheric irregularities carries the intensity and phase variations across a fixed ray path and causes scintillations on a communication link. It should be remembered that the ray path from a satellite orbiting, at an altitude of 1000 km, sweeps past the ionospheric irregularities assumed to be at 350 km at a speed of ~3 km s⁻¹. On the other hand, the speed of F-region irregularities relative to a receiver on the ground is typically on the order of 100 m s⁻¹. As a result, the scintillation rate of orbiting satellite signals is generally an order of magnitude faster than in the case of geostationary satellites.

Scintillations cause both enhancements and fadings about the median level of the signal as the radio signals sweep across the irregular ionosphere. When these fadings exceed the specified fade margin of a link, its performance is degraded. The degree of degradation will depend on the magnitude of fadings relative to the margin, the duration of the fade, the rate of fading, the type of modulation, and the criteria of acceptability. On a global scale, the degradations are most serious for propagation paths which transit the low latitude irregularity belt around the magnetic equator and the high latitude environment encompassing the auroral oval and polar cap regions (cf. Fig. 1 given in [1]).

The morphology of scintillations has been studied for several years and documented for the equatorial, midlatitude, auroral, and polar cap regions. Intensity scintilla-

tion measurements with orbiting and geostationary satellites provided the major database for such long-term studies [1]. The morphology of phase scintillations was developed by the use of multifrequency phase coherent DNA wide-band satellite transmissions in the equatorial [2] and auroral regions [3], [4]. More recently, near-stationary polar beacon satellites, which can be viewed at high elevation angles from high latitude stations, have been used to develop the morphology of phase and intensity scintillations in the auroral oval and polar cap regions [5]. In addition, case studies of ionospheric scintillations have been made in conjunction with rocket, radar, satellite in situ, and optical measurements [6]–[8]. These investigations have provided much insight into the mechanisms of irregularity formation and are expected to be helpful in developing predictive systems of scintillations based on geophysics [9].

In this paper, we first isolate very disturbed irregularity environments at both high and low latitudes, provide quantitative measures for the level of disturbance encountered by communication links in these regions, and analyze further the results in a form that can be used to evaluate communication system performance. We shall emphasize the difference between the structures of scintillation at high and low latitudes and isolate the appropriate parameters of concern to communication links operating in these two distinct disturbed regions of the globe.

II. DATA AND METHOD OF ANALYSIS

We have used both intensity and phase scintillation data from Thule, Greenland (76.5°N, 68.7°W), a polar cap station; Goose Bay, Labrador (53.3°N, 60.3°W), located in the nighttime auroral oval; and Ascension Island (7.9°S, 14.4°W), an equatorial anomaly station where the critical frequency of the $F2$ layer attains high values in the postsunset period when the ionospheric irregularities become most pronounced.

At Ascension Island, 244 MHz signals from the geostationary satellite, Fleetsatcom, were recorded digitally by a computer-controlled phase-lock receiver. The processing of the phase and intensity scintillation data using the phase-lock system has been described earlier [10], [11]. This system was operated over a limited period of time, namely, Jan.–Feb. 1981 and Jan.–Feb. 1982, corresponding to periods of strong scintillation activity at this location. In addition to the above, total power receiving systems are employed to make routine recordings of signal intensity from Fleetsatcom at 244 MHz and from the geostationary satellite, Marisat, at a variety of frequencies, namely, 257, 1541, and 3954 MHz. Round-the-clock observations by this total power system are recorded on chart recorders and manually analyzed to determine intensity scintillation magnitude over 15-min intervals [12]. During special campaign periods, however, the signals were recorded on magnetic tapes to perform spectral analysis and to evaluate both the first- and second-order parameters related to scintillation statistics.

ASCENSION ISLAND
FEB. 3, 1981
2142 UT
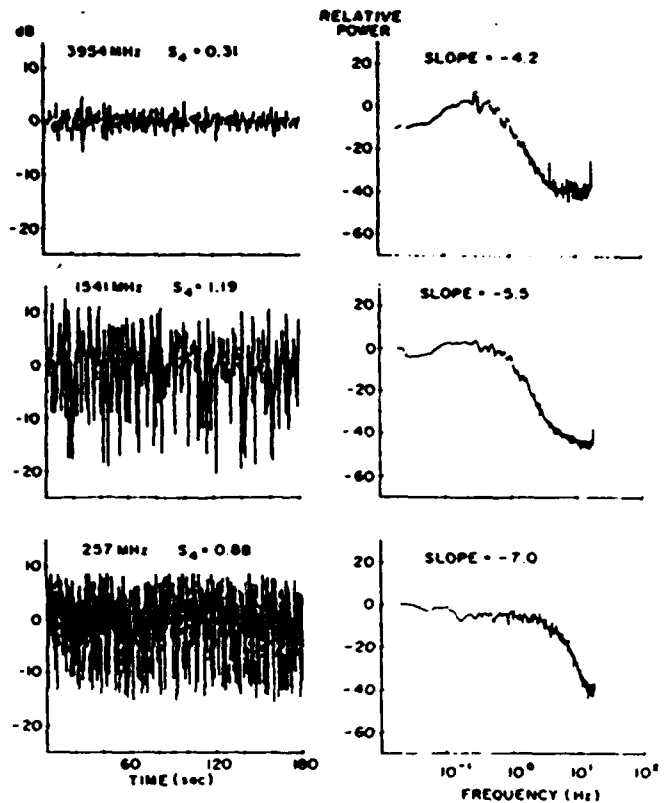
Fig. 1. A 3-min data segment of scintillations observed at 3954, 1541, and 257 MHz at Ascension Island and their respective spectra.

At the high latitude stations, Thule and Goose Bay, 250 MHz signals from near-stationary polar beacon satellites were received at high elevation angles by both the computer-controlled phase-locked receiver and the total power system. In view of the periodic frequency updating of this satellite at 168-s intervals, the phase and intensity scintillation data could be processed over 82-s intervals spaced 168 s apart [5]. The total power system acquired intensity scintillation data on chart recorders on a round-the-clock mode which were analyzed manually as mentioned earlier.

III. RESULTS

A. Ascension Island

During the last sunspot maximum period, the most severe scintillation activity was encountered at this equatorial station [13], [14]. Fig. 1 shows a sample of such an extreme case of scintillation activity which was recorded on multifrequency transmissions from Marisat. The left-hand panel shows, from the top, intensity scintillations at 3954, 1541, and 257 MHz over a 3-min period in the early evening hours. The right-hand panel shows the corresponding power spectra for the samples with the power law index (slope) of the best fit straight line to the linear rolloff portions indicated on the diagram. On the left-hand panel, the second central moment of signal intensity,

namely, the S_4 index of intensity scintillations defined in [15], is labeled to provide a quantitative measure of intensity fluctuations. At the lowest frequency, 257 MHz shown in the bottom panel, the S_4 index of scintillations attains a value of 0.88 approaching the saturation condition of $S_4 \sim 1$. The rate of fading is extremely fast and approaches the receiver response time of 0.1 s. A receiver with larger dynamic range and faster response time would have recorded fading depths much larger than the 15 dB level registered in the figure. At higher frequencies, the phase perturbations are reduced so that scintillation magnitudes are expected to be less. In general, when scintillations are not very intense ($S_4 < 0.6$), intensity scintillation magnitudes (S_4) follow a frequency (f) dependence of $f^{-1.5}$ shown in [16]. The middle panel, however, shows that at 1541 MHz in the L-band, the S_4 index remains at the saturated level somewhat exceeding unity. This signifies that the irregularity environment is so intense that saturated scintillations are obtained at 1541 MHz, and 257 MHz scintillations are driven far into saturation. The level of activity can be gauged from the top panel which shows that even in the C-band (3954 MHz), scintillation with $S_4 = 0.31$ is obtained. From an engineering standpoint, this corresponds to a fluctuation of 6 dB [17].

The power spectra of scintillations obtained by the use of the fast Fourier transform (FFT) algorithnm are shown in the right-hand panel of Fig. 1 [18]. The spectrum of weak scintillations at 3954 MHz is shown in the top panel. It is characterized by maximum power spectral density (psd) at a frequency (f_m) of about 0.4 Hz. This frequency can be expressed as $f_m = u/\sqrt{2}\lambda z$ where u is the drift speed of irregularities orthogonal to the propagation path, λ is the radio wavelength, and z is the slant range from the observing site to the irregularities [19]. For these observations, $\lambda = 0.076$ m, $z = 450$ km, and $f_m = 0.4$ Hz, so that the value of u is derived as 104 m s^{-1}. This is in agreement with the observed values in the equatorial region where, during the early evening hours, the drift speed of F-layer irregularities with respect to the ground generally varies between 100-200 m s^{-1} [20]. In contrast to only a factor of 2 variation of drift speed in the equatorial region the speed in the auroral oval can vary by a factor of 10 or more. This causes a considerable shift of f_m even for a given geometry and a specified frequency as will be shown later in the paper. The other features to be noted are the slopes of the spectra on either side of the maximum psd. Since both psd and frequency are plotted on a logarithmic scale, a linear slope indicates a power law variation of psd with frequency. The spectrum of 3954 MHz scintillations indicates that at the low-frequency end, the variation can be approximated by f^{+1} and the variation of psd at the high-frequency end can be expressed by $f^{-4.2}$. These spectral slopes are typically observed and have been related to the spectra of ionospheric irregularities [18] based on which the scintillation spectra have been successfully modeled [19].

The middle right hand panel shows the spectrum of 1541 MHz signals which represents the case of saturated scintillations. In contrast to the 3954 MHz spectrum discussed above, the spectral maximum in this case is broad and covers a frequency range of 0.1 Hz-1 Hz. The high-frequency slope is also steeper indicating a power law index of -5.5. The broad spectral width and steep spectral slopes are characteristics of strong intensity scintillations [21], [22], [19]. In fact, on the basis of the expression for f_m given in the previous paragraph, which is valid for weak scintillations, one expects that at 1541 MHz, a lower value of f_m will be obtained. Instead, f_m extends to much higher values due to strong scattering [23]. Since the autocorrelation function and power spectra are Fourier transform pairs, the increased spectral width signifies a shorter autocorrelation interval. Henceforth, the time interval for 50 percent decorrelation will be referred to as the decorrelation time (τ). For practical purposes, it is found that the inverse of the frequency $f = 2$ Hz, namely, 0.5 s, where the psd falls to a level of 20 dB below the maximum, corresponds quite well to the decorrelation time.

The lowest panel in Fig. 1 shows the scintillation spectrum of 257 MHz transmissions which is driven far into saturation. The spectral broadening is extreme in this case and extends to 4 Hz. The spectral slope is steepest and corresponds to a power law index of -7. The decorrelation time is found to be 0.13 s signifying an extreme fading rate. It should be noted that although the S_4 indexes for both 1541 and 257 MHz are approximately unity indicating saturation, the decorrelation interval still varies, becoming shorter at the lower frequency which suffers stronger scattering.

Fig. 2(a) and (b) shows the cumulative distribution function (cdf) of signal amplitude for the C- and L-band frequencies illustrated in Fig. 1. The cdf is a first-order statistic and is useful for defining the minimum margin requirements for communication links in nondiversity systems. The diagrams indicate the cdf for the observations (solid line) as well as the theoretical Nakagami m-distribution discussed in [24] which is indicated by dotted lines at the m value ($m = 1/S_4^2$) appropriate for the data sample. It can be seen that the theoretical distributions represent the observations quite well over a wide range of activity levels, being weak at 3954 MHz and strong at 1541 MHz. For intense scintillations such as seen on 1541 MHz, the cdf approaches a Rayleigh distribution ($m = 1$). The Nakagami m-distribution has been earlier shown to be useful for describing the effects of scintillations on satellite communication links [25].

In addition to the cdf which describes the probability distribution of the depth of fading, a statistical description of the fading rate is necessary to fully characterize the effects of scintillations on communication links. The information on the fading rate is contained in the power spectra of scintillations which we have described earlier. Another way of obtaining this information is to employ a level crossing technique. This gives the distribution of fade duration across a set of specified fading levels. Often, this representation is simpler and easier to interpret in re-
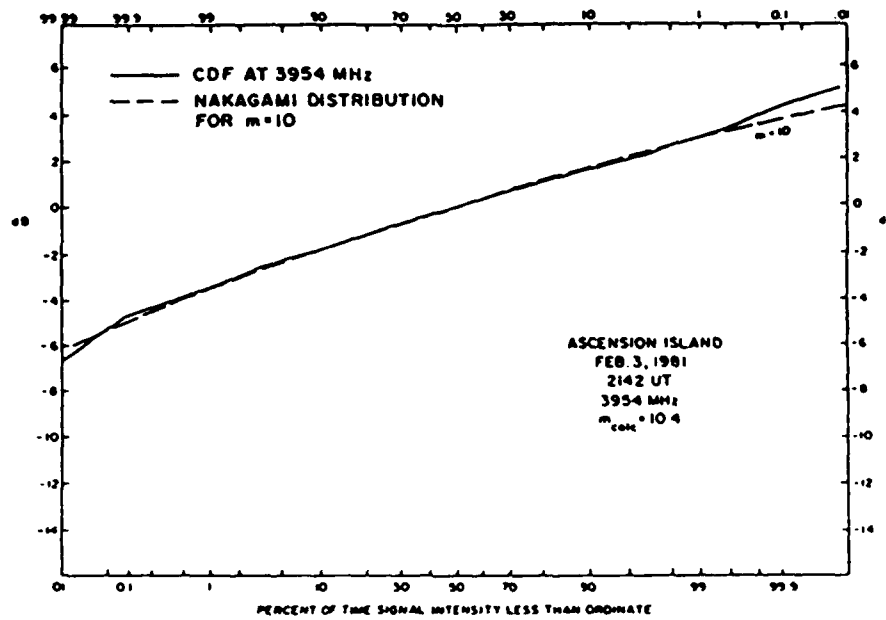
(a)
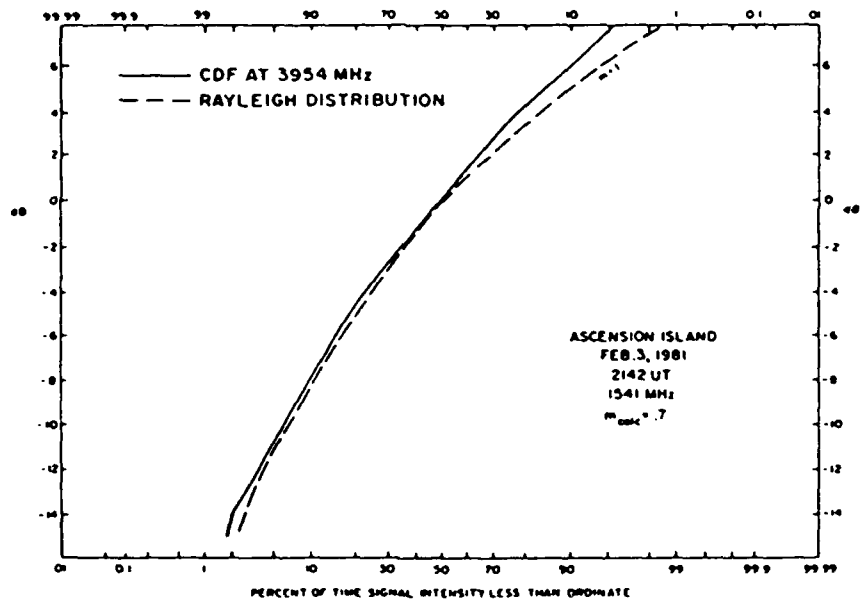
(b)

Fig. 2. (a) The cumulative amplitude distribution of scintillations at 3954
MHz shown in Fig. 1. (b) Same as in Fig. 2(a) for scintillations at
1541 MHz.

lation to systems applications. The left- and right-hand panels in Fig. 3 show the distribution of fades obtained at 3954 and 1541 MHz, respectively, over the first 1.5 min of the 3-min signal segments illustrated in Fig. 1. The shortest fade duration that could be measured in conformity with the data digitization rate was 0.04 s. The left-hand panel shows the distribution of fade duration for the 3954 MHz scintillation sample. Four separate fade depth levels at 1 dB intervals are found to be appropriate for this sample of weak scintillation. At the − 1 dB fade level, the flat top portion of the curve commences to slope

downwards at a fade duration of 0.2 s, which represents the longest fade duration at this fade level. The maximum number of fades encountered at the − 1 dB level is 54. This number reduces with decrease in fade duration and attains a count of 27, i.e., 50 percent of the maximum count at a fade duration of 0.08 s. At the next lower fade level of − 2 dB, the maximum number of fades reduces to 22. The − 4 dB fade level lies on the abscissa indicating that fades do not reach this level. The right-hand panel shows the corresponding distribution for 1541 MHz scintillation which is much more intense and is, in fact, sat-
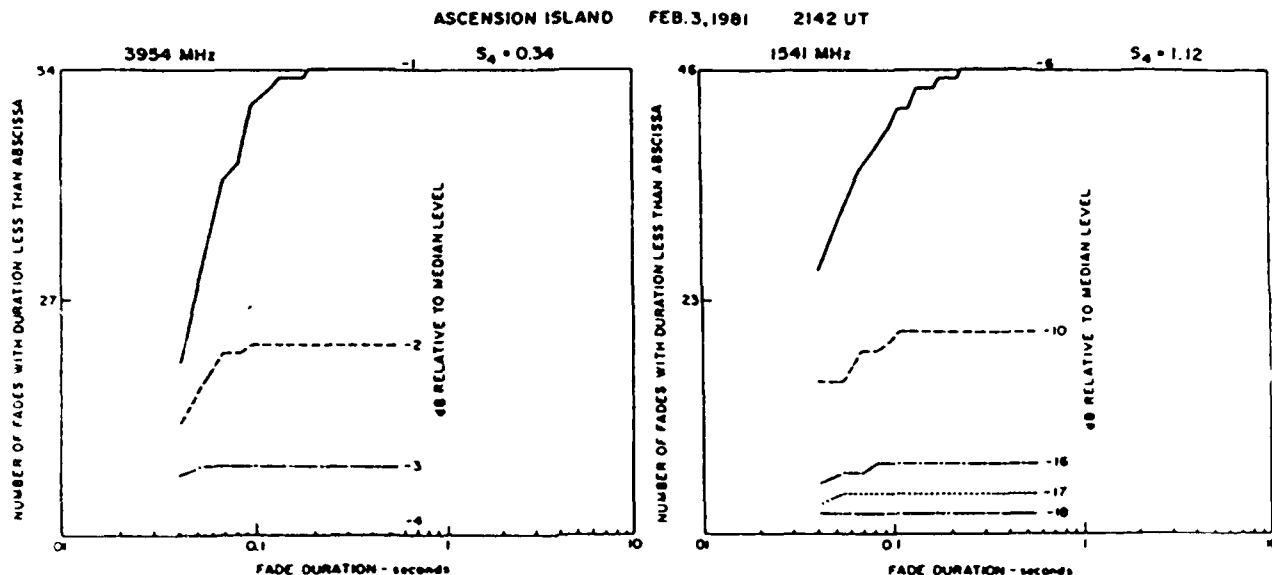
ASCENSION ISLAND   FEB.3,1981   2142 UT

Fig. 3. Distribution of the fade durations for the period of weak scintillations at 3954 MHz and strong scintillations at 1541 MHz illustrated in Fig. 1.

urated at $S_4 = 1.12$. In this case, the fade levels are chosen at wider intervals. The distribution is interesting in the sense that the number of fades is drastically reduced at higher fade levels exceeding -16 dB. Thus, although the fade depth of strong 1541 MHz scintillations exceeds 20 dB, the number of fades at -16 dB level in one 1.5-min interval is only 7 and the maximum fade duration does not exceed 0.1 s.

We shall next concentrate on the results of both intensity and phase measurements at Ascension Island performed with the computer-controlled receiver discussed in Section II. These measurements were performed by the use of 244 MHz transmissions from Fleetsatcom. The intensity and phase scintillation data were analyzed over successive 150 s periods. Since the 257 MHz intensity scintillation data acquired from the Marisat satellite have been discussed in earlier publications [14], [19], we shall comment primarily on the phase scintillation data which are quite unique and are being reported here for the first time.

Fig. 4 shows the 50th and 90th percentiles of the S_4 index of intensity scintillation (defined earlier) and rms phase deviation (σ_ϕ) over 150-s periods (detrended with a 0.01 Hz filter) as a function of local time. The time interval corresponds to the postsunset to postmidnight period (20–04 LT) (local time) when equatorial F-region irregularities are most intense and abundant. The period Jan.-Feb. 1981 corresponds to a period of high scintillation occurrence as previously mentioned. The number of data points in each 2-h block is indicated along the abscissa. It may be noted that in the early evening hours between 20-22 LT, both the median and 90th percentile values of S_4 and σ_ϕ are highly elevated. The intensity scintillation data saturated at a level of approximately $S_4 = 0.8$ because of receiver constraints. With the Marisat sat-

ASCENSION ISLAND   JAN-FEB 1981   ALL K
FLT (244 MHz)
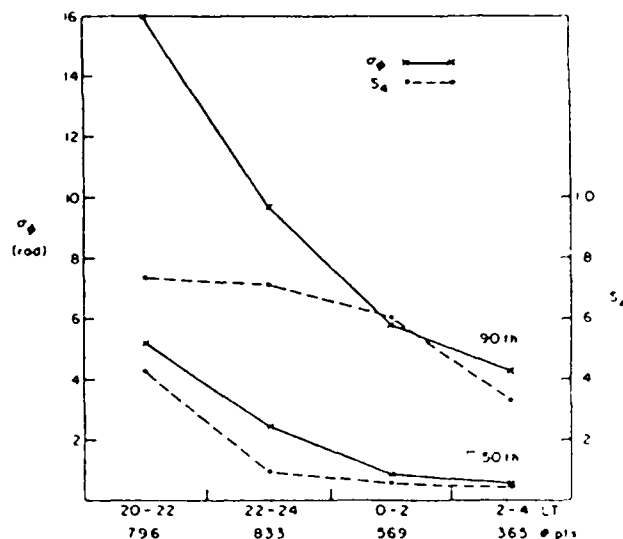
Fig. 4. The median (50th percentile) and 90th percentile values of phase and intensity scintillations at 244 MHz in terms of four 2-h blocks of local time (LT) during Jan.-Feb. 1981 at Ascension Island.

ellite, we have shown that both the 257 MHz and L-band intensity scintillations at this station become saturated with $S_4 \approx 1.0$. The saturation of intensity scintillation data at about 0.8 did not, however, affect phase measurements. It may be noted that the 90th percentile of rms phase deviation in the 20–22-h block is as large as 16 rad with 100 s detrend. In a similar propagation geometry, the values of rms phase deviation may be scaled to shorter detrend intervals (T_d) by multiplying the given values by $[T_d/100]^{(p-1)/2}$, where $p(\sim 2.5)$ is the phase spectral index [26]. From Fig. 4, it may also be noted that the

ASCENSION ISLAND   FEB.3,1981   222430 UT
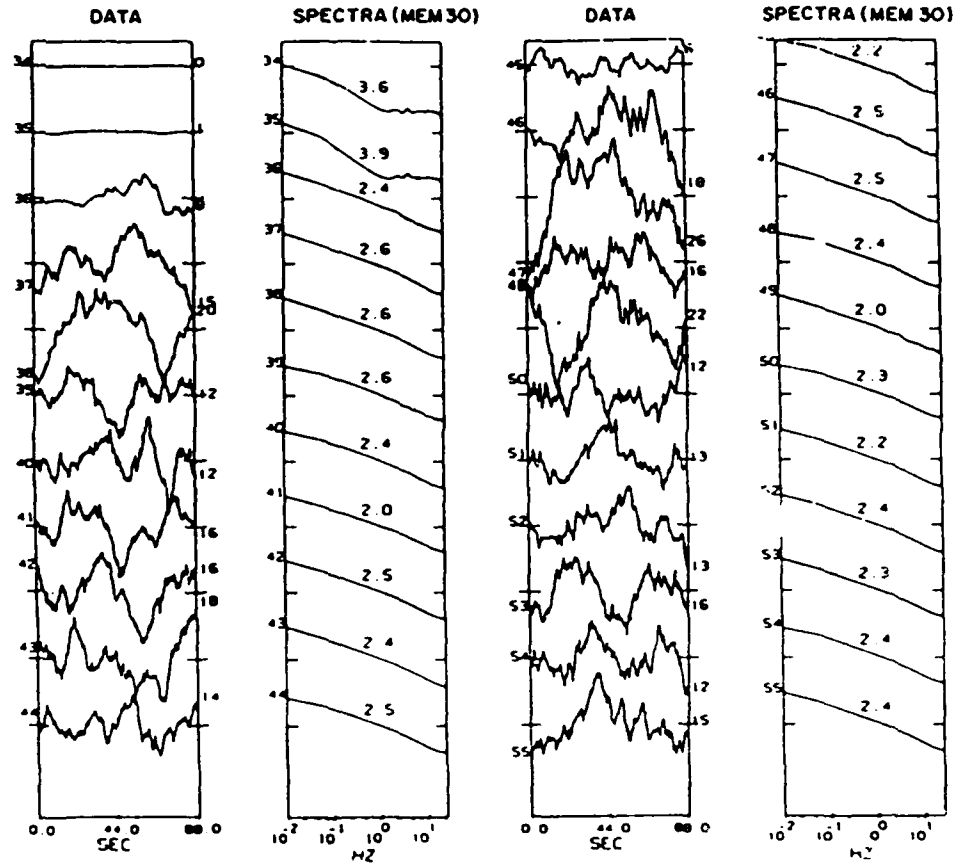
Fig. 5. Phase scintillation data segments at 244 MHz over 88-s intervals and their spectra in alternate panels acquired at Ascension Island on Feb. 3, 1981.

50th and 90th percentile values of these scintillation parameters decrease sharply with increasing local time owing to the decay of irregularity strength.

We shall now discuss the 244 MHz phase scintillation data that were acquired from the Fleetsat satellite at Ascension Island on Feb. 3, 1981. Multifrequency intensity scintillation data from the Marisat satellite for this day have already been presented earlier. Fig. 5 shows a sequence of phase scintillation data over successive 88-s intervals and their spectra obtained by the maximum entropy method [27] in the adjacent panels. The signal segments and their spectra are numbered on the left-hand side of each panel for ease of comparison. The rms phase deviation in radians for each 88-s interval is indicated on the right-hand side of the data segments. The intervals between the tic marks on the data panel represent 50 rad and on the spectral panels psd of 80 dB. The initial data segments with no activity are not shown and the panels start from the 34th data segment, which commences at 222430 universal time (UT). The first two data segments (34 and 35) show very little phase variation. The corresponding phase spectra show that the noise floor extends from the Nyquist frequency of 25 Hz to about 0.2 Hz. Phase power spectral densities (psd) are noticeable only

at lower frequencies. A sudden onset of scintillations may be noted in the third panel. The corresponding spectra indicates an abrupt increase of psd at all frequencies up to 25 Hz. The numbers alongside the spectra indicate the magnitude of maximum instantaneous spectral slopes. The spectral slopes attain values ranging between -2 to -2.5 during the period of scintillations, but remain much higher before the onset of scintillations as may be noted from the first two spectra. It is worthwhile to recall that the spectral slope of intensity scintillations at a similar frequency (cf. Fig. 1) and a similar period of intense activity is very steep. This is caused by the refractive effects of large scale irregularities of electron density on the structure of intensity scintillations [21], [22]. Until recently, one expected that the spectra of weak intensity scintillations and phase scintillations of any magnitude would reflect the slope of irregularity spectra in the ionosphere. In fact, the slope of -4.2 in the weak scintillation spectrum at 3954 MHz as shown in Fig. 1 reflects very well the average one-dimensional irregularity spectral slope of -3.5 at small scales [18]. The spectral slopes of strong phase scintillations at 244 MHz, however, indicate shallow spectral slopes in the vicinity of -2.5 The apparent discrepancy has been resolved by Rino and Owen [28]. They simulated an

ASCENSION ISLAND   JAN-FEB 1981 $S_4 > .6$ ASCENSION ISLAND   JAN-FEB 1981 $S_4 > .6$
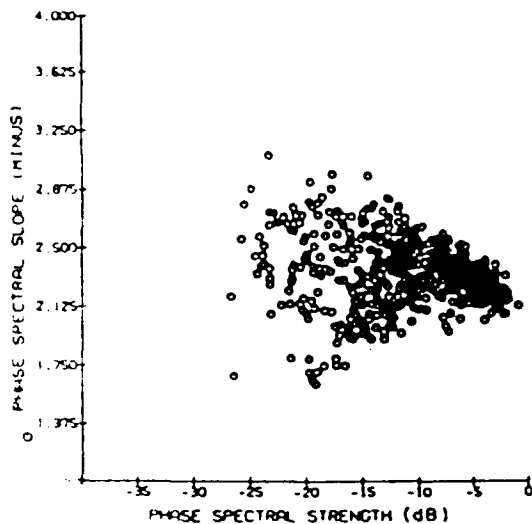

Fig. 6. A scatter plot of the phase spectral slope against phase spectral strength (dB) at Ascension Island at 244 MHz. The slope approaches a value of −2 at high phase spectral strengths.

Fig. 7. A scatter plot of intensity decorrelation time against the phase spectral strength of 244 MHz scintillations recorded at Ascension Island. The theoretical dependence of the two parameters in the strong scatter regime for a phase spectral index $p_\phi = -2.4$ is indicated by the straight line.

ionospheric phase screen, allowed a radio wave to propagate through it, and computed numerically the phase structure and phase spectra at various distances from the screen. They showed that due to the diffractive effects of phase in a strong scattering medium, the phase structure develops large, near-discontinuous phase changes (termed "cycle slips") and yields phase spectra with slopes approaching −2.

Fig. 6 shows a scatter plot of phase spectral slope versus phase spectral strength in decibels which is defined as the phase psd at 1 Hz when the S_4 index exceeds 0.6, i.e., for strong scintillations. The data were acquired at Ascension Island during Jan.-Feb. 1981. At low values of phase spectral strengths or high decibel numbers, phase spectral slopes show a wide scatter between −2 and −2.9 in Fig. 6, but at high values of phase psd, the slopes approach a value of −2. This provides observational support to the "cycle slip" argument presented in the previous paragraph.

In Fig. 7, we show an interesting plot of intensity decorrelation time at 244 MHz on a logarithmic scale against phase spectral strength (decibels) for strong scintillations ($S_4 > 0.6$). It may be noted that with increased phase spectral strengths in this regime, the intensity scintillations systematically develop finer structures on the ground so that the decorrelation time decreases from about 1 to 0.05 s. By using the method outlined in [26], it is possible to derive the average spectral slope from the slope of the best fit straight line to the scatter plot of Fig. 7. The scatter diagram indicates a spectral slope of −2.4. This is in very good agreement with the phase spectral slopes of the data segments illustrated in Fig. 5.

The results shown in Figs. 6 and 7 imply that in the disturbed equatorial ionosphere, the structures . . . ten-

sity and phase scintillations are controlled by the strength of scattering. The decorrelation time is a function of the spatial structure of intensity variation on the ground as well as the ionospheric drift which controls the motion of the spatial structure past a receiving antenna. The fact that the decorrelation time is so well ordered in terms of the phase spectral strength indicates that the drift velocity does not vary much between the postsunset and the midnight period, and it is the strength of the irregularities which control primarily the fading pattern of scintillations. This is, however, not true at high latitudes where the phase spectral strength of the integrated strength of irregularities is not as intense as in the equatorial region, but the drift velocity can vary by an order of magnitude within a short interval of time. At high latitudes, therefore, the fading pattern is primarily controlled by the irregularity drift.
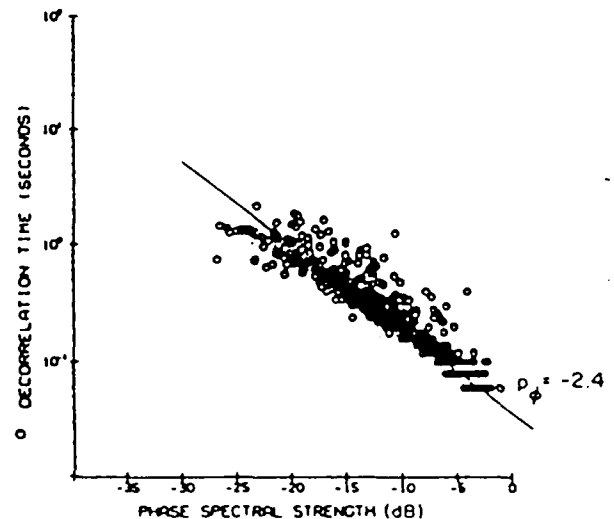
From Fig. 5 it was evident that in intense equatorial phase scintillation events, considerable power resides in the regime of high fluctuation frequencies. This is equivalent to stating that the probability of having a high rate of change of phase is considerable. The phase rate, on the other hand, is a measure of the Doppler spread the signal undergoes in traversing the irregularities of the ionosphere. In Fig. 8, the probability distribution of the phase rate in phase scintillations has been computed over 0.1-s intervals during a 30-min period of intense scintillations at Ascension Island. Since the Nyquist frequency is 25 Hz, the phase rate could have been computed over a much shorter time interval. However, at small sampling intervals, the noise becomes comparable to the signal and the derived phase rates would have been contaminated by the phase rate of noise signals. In Fig. 8(a), the occurrence

ASCENSION ISLAND   PHASE RATE   FEB.3,1981
$\Delta t = 0.1$ sec   222717-230237 UT

(a)

Fig. 8. (a) The distribution of phase rate of 244 MHz scintillations at Ascension Island. The high values at the two ends indicate percent occurrence of values $> 500°$ s^{-1}.

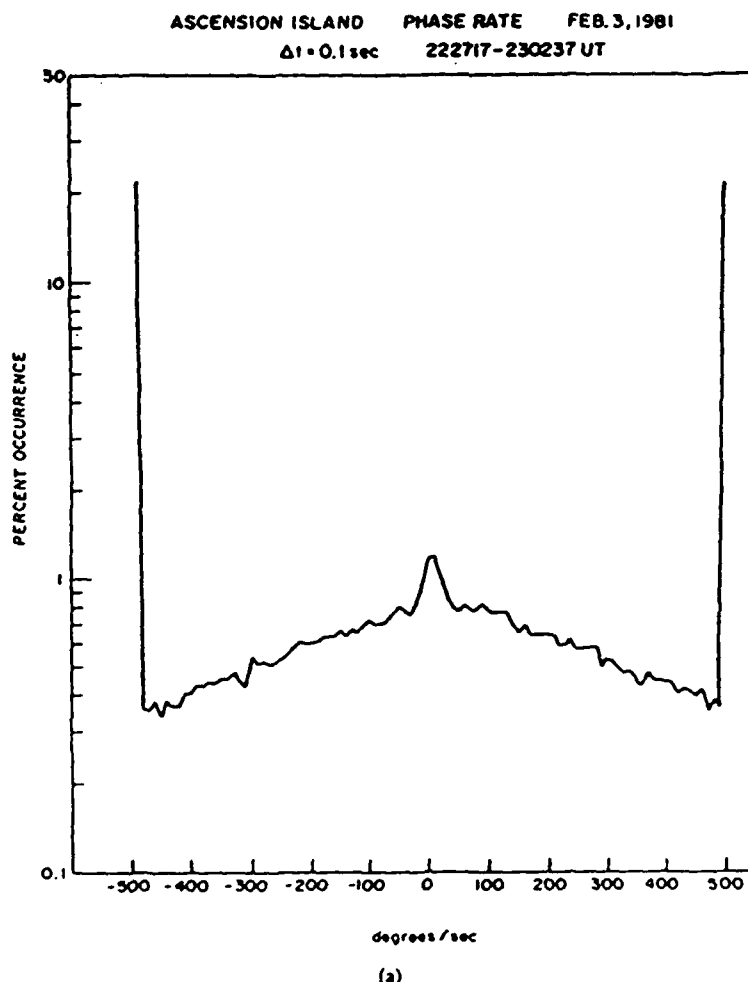of phase rate between $\pm 500°$ s^{-1} has been plotted. It is found that nearly 20 percent of the total population (10^5 points) contains phase rates in excess of $\pm 500°$ s^{-1}. The distribution of population with extreme phase rates has been plotted in Fig. 8(b) over a wider range extending from ± 500 to $\pm 2300°$ s^{-1}. It may be noted that phase rates as high as $2000°$ s^{-1} or $2°$ ms^{-1} occur in 0.1 percent of the population with extreme phase rates which, in turn, represents 20 percent of the total number of observations during approximately a half-hour period. Such extreme phase rates have considerable deleterious effects on radar systems. Since the phase scintillation magnitude varies inversely as frequency [29], the above phase rate may be scaled from the 244 MHz observations to 2.4 GHz as $0.2°$ ms^{-1}.

B. Thule, Greenland

At Thule, a polar cap station, the phase and intensity scintillation data were acquired by receiving 250 MHz transmissions from the near-stationary Air Force satellites at high elevation angles. The ionospheric intersection of

the ray path covered a corrected geomagnetic latitude range of 85-89°N. Since scintillations are better ordered in terms of corrected geomagnetic latitude (CGLAT) and magnetic local time (MLT) at high latitudes, we shall use this system of coordinates as described in [30]. The phase and intensity measurements were made with the computer-controlled phase-lock receiver during specified intervals as mentioned in Section II.

The morphology of intensity scintillations [31] and that of both phase and intensity scintillations [5] from Thule have been discussed earlier. In this paper, we shall present phase and intensity scintillation data during Jan.-Feb. 1982 not previously published, and use it to contrast its behavior against the Ascension Island observations. We have also extended the intensity scintillation morphology further through the years of low sunspot number to illustrate the control of solar activity on polar cap scintillations.

Fig. 9 shows the variation of 250 MHz intensity scintillation index (S_4) and rms phase deviation (σ_ϕ) over 82-s intervals with magnetic local time as observed at Thule

ASCENSION ISLAND   PHASE RATE   Δt = 0.1 sec   FEB. 3, 1981
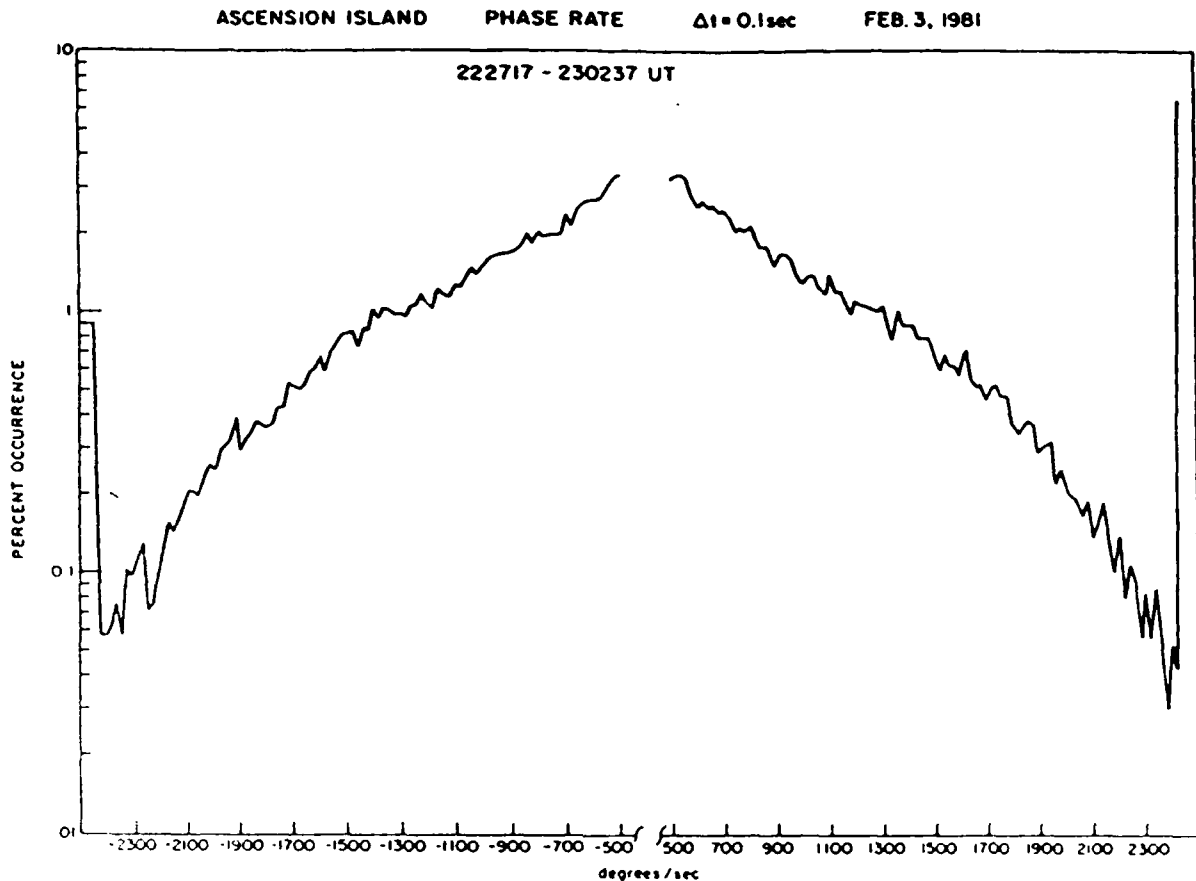
(b)

Fig. 8. (Continued) (b) The distribution of the population with extreme
phase rates which corresponded to the two ends of the diagram in Fig. 8(a)
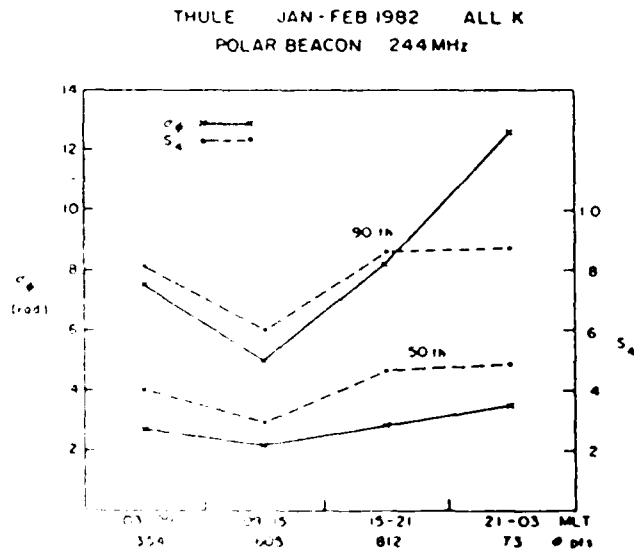
Fig. 9. The median (50th percentile) and the 90th percentile values of phase
and intensity scintillation at 250 MHz in terms of four 6-h MLT blocks
observed at Thule

during Jan.-Feb. 1982. It may be noted that at Thule, the
scintillation activity during years of high sunspot numbers
persists at all hours, the median value of phase ranging
between 3 and 5 rad over the entire diurnal period. This

behavior is in sharp contrast to that at Ascension Island,
an equatorial station, where strong scintillations are, in
general, confined between the postsunset to midnight
hours. In view of this, the scintillation statistics in Fig. 4
were derived between 20-04 LT. At auroral locations,
such as Goose Bay, scintillations on magnetically quiet
days are again confined to nighttime periods as discussed
in [5]. Thus, an absence of diurnal variation of scintilla-
tions during periods of high solar activity is a feature con-
fined only to the polar cap. The level of 250 MHz scin-
tillations is also high, the 90th percentiles of rms phase
attaining values as high as 12 rad and intensity scintilla-
tions remaining near saturation with $S_4 \sim 0.9$.

The long-term statistics of 250 MHz intensity scintil-
lations derived with total power receiving systems are
shown in Fig. 10. The figure shows the variation of scin-
tillation occurrence at various fade depths for 1979-1984.
The highest fade level of ≥ 20 dB represents a peak-to-
peak fluctuation level of ≥ 28 dB. The scintillations min-
imize during the summer months so that the annual vari-
ation becomes most conspicuous. During the sunlit pe-
riod, the high conductivity at E-region heights (~ 100 km)
is not favorable for the maintenance of irregularities in the
overlying F-region of the ionosphere [32]. In other pe-
riods, particularly during the autumnal equinox, fade
depths as large as 20 dB with 20 percent occurrence could
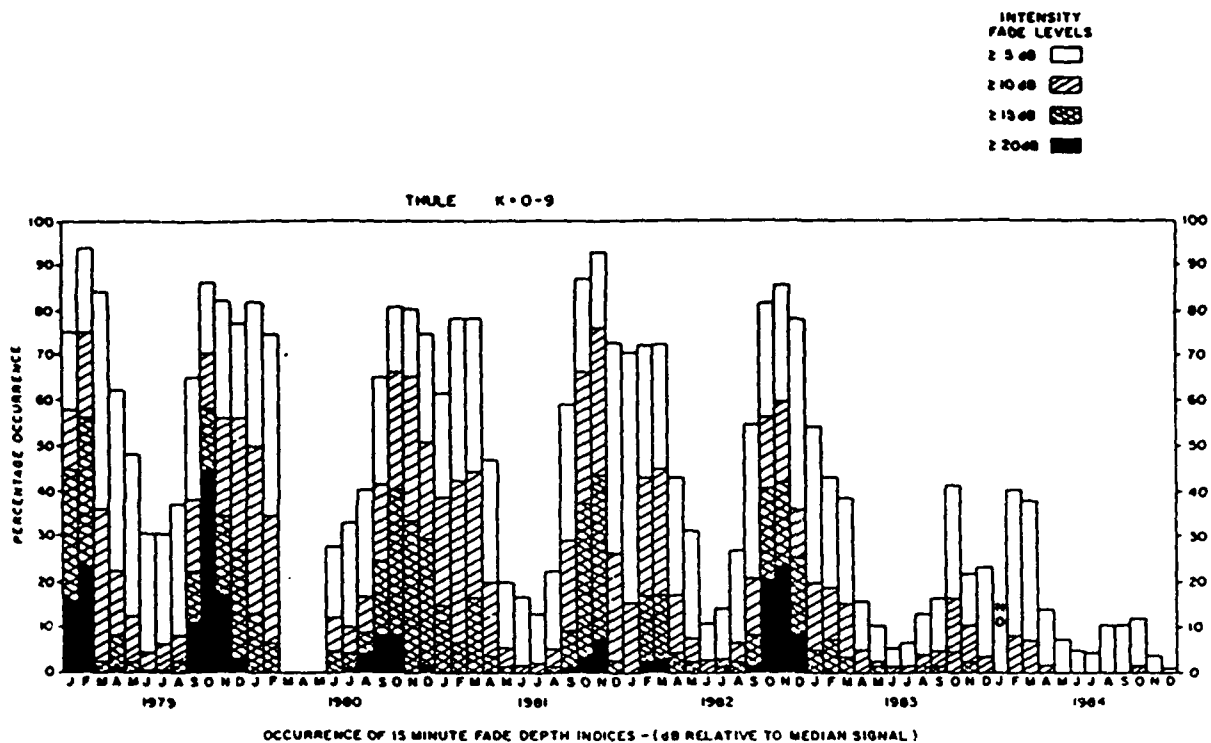
Fig. 10. Thule intensity scintillation statistics at 250 MHz during 1979-1984.

be obtained up to 1982. The scintillation activity did not vary much during the period 1979-1982 when sunspot numbers varied between 200 and 100. With further reduction of sunspot numbers, scintillations showed an abrupt decline during 1983 and 1984. Thus, there seems to be a lower threshold of solar activity below which irregularities of sufficient integrated strength are not encountered.

Fig. 11 shows the occurrence contours of fade levels at 250 MHz that exceed 10 dB on both a monthly and diurnal basis. As pointed out in the previous paragraphs, the annual variation of scintillations is the more prominent feature and the diurnal variation is virtually absent at Thule. However, there emerges a diurnal pattern in the Oct.-Nov. period which becomes most conspicuous during the low sunspot years of 1983 and 1984. The maximum activity during these months seems to be confined to the afternoon period around 15 MLT.

The strong scintillation events with S_4 exceeding 0.6, that could be recorded by the phase-lock receiving system at 250 MHz, were sorted. The intensity decorrelation time and phase spectral strengths were determined and their mutual dependence is plotted in Fig. 12. The best fit straight line through the scatter plots corresponded to the theoretical dependence [26] expected for the case of strong scattering with phase spectral slope of -2.2. It signifies that during strong scintillations at Thule, the intensity scintillation structure is largely governed by the phase spectal strength. Increased scatter around the best fit line signifies that the drift speed may vary by a factor of 3-4.

On the other hand, the scatter in Fig. 7 is much less, indicating that the variation of drift speed is small in the equatorial region. At the auroral station of Goose Bay, a similar plot (not shown here) indicates considerable scatter as well due to the high variability of drift speeds.

C. Goose Bay, Labrador

We shall not discuss in great detail the features of scintillations at Goose Bay, an auroral station, but refer to [5] which compared the characteristics of polar cap and auroral scintillations. In short, the auroral station shows a well-ordered diurnal variation of scintillations with a nighttime maximum and daytime minimum, whereas we have shown the absence of such ordering in the polar cap region, such as Thule. The auroral scintillation magnitudes are, on the average, similar to that in the polar cap although, on occasions, more active conditions prevail in the polar cap. The polar cap scintillation pattern exhibits the presence of discrete structures, whereas in the auroral oval, intense scintillation events continue for hours without showing much variation in magnitude. The major feature of an auroral station is the extreme variability of drift speed. It is not uncommon to observe a change in speed from 100 m s^{-1} to 1000 m s^{-1} within a 30-min period. This variability in speed affects greatly the temporal structure parameters of scintillations such as the decorrelation time or the rate of change of phase and intensity. Fig. 13 shows the rate of change of intensity at 250 MHz encountered on two successive nights, Mar. 7 and 8, 1982. The scheme of the plot is similar to the phase rate plot in Fig.

PERCENT OCCURRENCE OF INTENSITY FADE
THULE   LEVELS > 10 dB
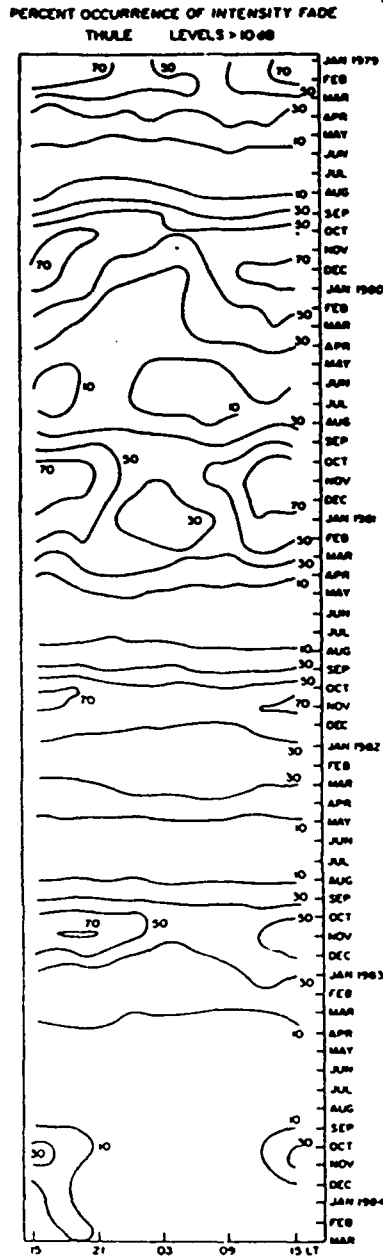
Fig. 11. Intensity scintillations at Thule at 250 MHz on a seasonal and local time basis. The contour levels represent percent occurrence.

THULE   JAN-FEB 1982 $S_4 > .6$

Fig. 12. A scatter plot of the intensity decorrelation time against phase spectral strength observed at Thule at 250 MHz. The theoretical dependence of the two parameters for a phase spectral index of −2.2 is indicated by the straight line.

GOOSE BAY   INTENSITY RATE $\Delta t = 0.5$ sec   1982
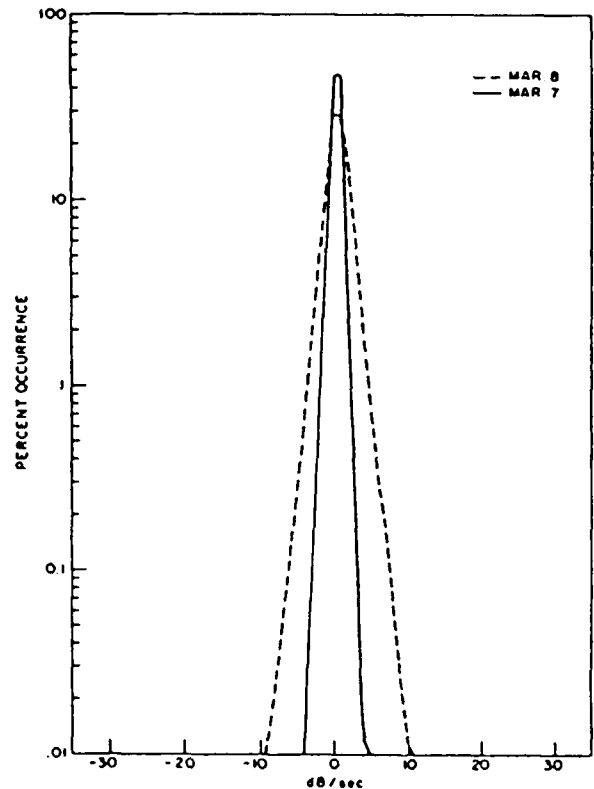
Fig. 13. The distribution of intensity rate of scintillations at 250 MHz Goose Bay on two successive nights with different ionospheric drift. The drift was lower on Mar. 7 by a factor of 6 as compared to Mar.

8(a) for Ascension Island, except for the longer data interval (0.5 s) used to compute the rates at the auroral location. Shorter time intervals could not be used here because of possible noise contamination. At the equatorial station, intervals as short as 0.1 s could be used to compute phase rates as high levels of ionospheric turbulence developed high-frequency structures much above the noise floor. Fig. 13 shows that at Goose Bay, on Mar. 7, 1982, the intensity rate of 3 dB s^{-1} occurs in 0.1 percent of the total population, whereas it increases to about 7 dB s^{-1} at the same 0.1 percent level on Mar. 8, 1982. Intensity spectral studies revealed that the irregularity drift speed was 65 m s^{-1} on Mar. 7, 1982, and increased to 390 m s^{-1} on Mar. 8, 1982 [5]. The sixfold increase in drift

speed is reflected in increased intensity rates. Fig. shows the phase rate plots at the same frequency for t two days. It may be noted that at 0.1 percent level, t phase rate may attain values as high as 250° s^{-1} at
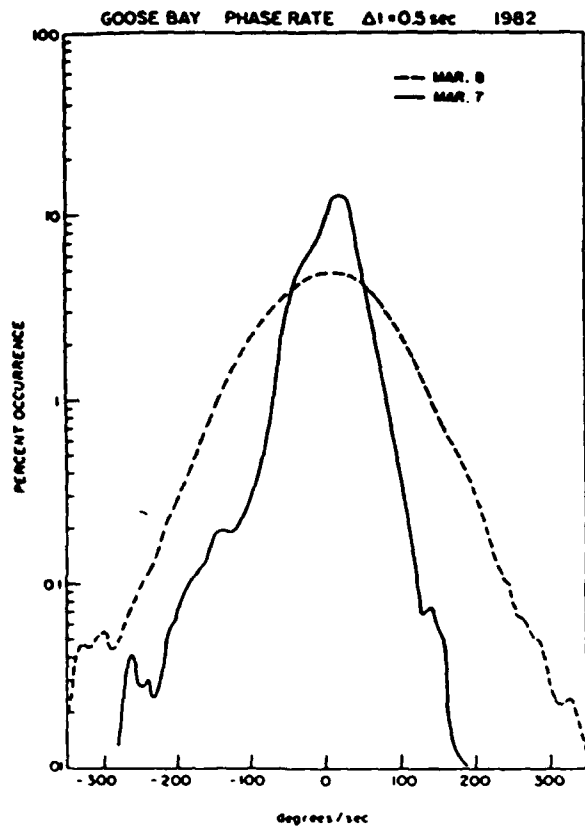
Fig. 14. Same as for Fig. 13, except here the distribution of phase rate of scintillations at 250 MHz is shown.

auroral location when drift speed is high. If the change can be linearly extrapolated to smaller time intervals, the above value translates to $0.25°$ ms^{-1}. This is an order of magnitude smaller than the phase rate encountered at Ascension Island and illustrated in Fig. 8(b).

IV. SUMMARY

The results on the structure of multifrequency amplitude scintillations covering the 250 MHz–4 GHz band of frequencies at the crest of the equatorial anomaly and the structure of approximately 250 MHz phase and amplitude scintillations in the equatorial anomaly, auroral, and polar cap regions can be summarized as follows.

At Ascension Island, located at the crest of the equatorial anomaly, the most disturbed irregularity environment on a global basis was encountered during the last sunspot maximum period. At this location, the disturbance level was so intense that not only the 250 MHz but also the 1541 MHz transmissions from geostationary satellites exhibited saturated intensity scintillations which covered the 30 dB dynamic range of receivers that were used to record the satellite transmissions. Even the transmissions at 4 GHz registered fluctuations as large as 6 dB. The median and the 90th percentile values of rms phase deviation at 244 MHz with 100 s detrend are 6 and 16 rad, respectively, during the early evening hours. The

phase spectral strengths (phase psd at 1 Hz) which indicate the strength of turbulence are found to attain values as high as −2 dB. This is at least 10 dB above the most intense levels that are obtained at the polar cap or auroral stations. The extreme levels of turbulence at Ascension Island induce strong scattering of 257 and 1541 MHz signals and thereby dictate the structures of amplitude and phase scintillations at both frequencies. The amplitude scintillation spectra at these frequencies under such situations show uniform psd up to fluctuation frequencies as high as a few hertz, and give rise to steep power law spectral indexes of −5 to −7. The intensity decorrelation times are consequently reduced to values as low as 0.06 s at 257 MHz. The phase spectral slopes at 244 MHz approach a value of −2.5 which is much shallower than is expected from either the *in situ* irregularity spectra or weak amplitude scintillations spectra at 4 GHz. This probably arises from sharp discontinuous phase changes or "cycle slips" [28] that develop due to phase diffraction effects under strong scatter conditions. In view of these discontinuous phase changes, extreme phase rates of 2–3° ms^{-1} were observed. This is rather significant for UHF radar applications.

In the polar cap (Thule), the median and 90th percentile values of rms phase deviation at 250 MHz for 82-s detrend are observed to be 3 and 12 rad, respectively. The corresponding values for the S_4 index of scintillations are 0.5 and 0.8. These values are in reasonable agreement with those published in [5] for another period of observations. The point of interest is the absence of any diurnal variation of polar cap scintillations, its annual variation with a pronounced minimum during local summer, and rather abrupt decrease of scintillations when the solar activity decreases below a threshold level. The irregularity spectral strengths in the polar cap or auroral stations are shown to be not as intense as in the equatorial region. At high latitudes, the phase spectral indexes of about −2.2 cannot be attributed to strong scattering effects, but are probably a result of shallow irregularity spectral indexes in the ionosphere. At auroral locations, the variability of ionospheric motion greatly controls the temporal structure of scintillations. The phase rates at 250 MHz are typically of the order of 0.2–0.3° ms^{-1}, but may show considerable changes due to the variability of ionospheric motion.

ACKNOWLEDGMENT

REFERENCES

[1] J. Aarons, "Global morphology of ionospheric scintillation," *Proc. IEEE*, vol. 70, pp. 360–378, 1982.

[2] R. C. Livingston, "Comparison of multifrequency equatorial scintillation: American and Pacific sectors," *Radio Sci.*, vol. 15, p. 801, 1980.

[3] C. L. Rino and S. J. Matthews, "On the morphology of auroral zone radio wave scintillation," *J. Geophys. Res.*, vol. 85, p. 4139, 1980.

[4] S. Basu, S. Basu, R. C. Livingston, H. E. Whitney, and E. MacKenzie, "Comparison of ionospheric scintillation statistics from the North Atlantic and Alaskan sectors of the auroral oval using the WIDEBAND satellite," Air Force Geophys. Lab., Hanscom AFB, MA, Rep. AFGL-TR-81-0266, AD A111871, Sept. 1981.

[5] S. Basu, S. Basu, E. MacKenzie, and H. E. Whitney, "Morphology of phase and intensity scintillations in the auroral oval and polar cap," *Radio Sci.*, vol. 20, pp. 347–356, 1985.

[6] C. L. Rino, R. C. Livingston, R. T. Tsunoda, R. M. Robinson, J. F. Vickrey, C. Senior, M. D. Cousins, J. Owen, and J. A. Klobuchar, "Recent studies of the structure and morphology of auroral zone F-region irregularities," *Radio Sci.*, vol. 18, pp. 1167–1180, 1983.

[7] S. Basu and S. Basu, "Equatorial scintillations: Advances since ISEA-6," *J. Atmos. Terr. Phys.*, vol. 47, pp. 753–768, 1985.

[8] S. Basu, S. Basu, C. Senior, D. Weimer, E. Nielsen, and P. F. Fougere, "Velocity shears and sub-km scale irregularities in the nighttime auroral F-region," *Geophys. Res. Lett.*, vol. 13, p. 101, 1986.

[9] E. J. Fremouw and J. A. Secan, "Modeling and scientific application of scintillation results," *Radio Sci.*, vol. 19, pp. 687–694, 1984.

[10] S. Basu, S. Basu, R. C. Livingston, E. MacKenzie, and H. E. Whitney, "Phase and amplitude scintillation statistics at 244 MHz from Goose Bay using a geostationary satellite," Air Force Geophys. Lab., Hanscom AFB, MA, Rep. AFGL-TR-82-0222, AD A124291, Aug. 1982.

[11] S. Basu, E. MacKenzie, S. Basu, H. C. Carlson, D. A. Hardy, F. J. Rich, and R. C. Livingston, "Coordinated measurements of low-energy electron precipitation and scintillations/TEC in the auroral oval," *Radio Sci.*, vol. 18, p. 1151, 1983.

[12] H. E. Whitney and S. Basu, "The effect of ionospheric scintillation on VHF/UHF satellite communications," *Radio Sci.*, vol. 12, p. 123, 1977.

[13] J. Aarons, H. E. Whitney, E. MacKenzie, and S. Basu, "Microwave equatorial scintillation intensity during solar maximum," *Radio Sci.*, vol. 16, pp. 939–945, 1981.

[14] J. P. Mullen, E. MacKenzie, S. Basu, and H. E. Whitney, "UHF/GHz scintillation observed at Ascension Island from 1980 through 1982," *Radio Sci.*, vol. 20, pp. 357–365, 1985.

[15] B. H. Briggs and I. A. Parkin, "On the variation of radio star and satellite scintillation with zenith angle," *J. Atmos. Terr. Phys.*, vol. 25, pp. 339–365, 1963.

[16] C. L. Rufenach, "Wavelength dependence of radio scintillation: Ionosphere and interplanetary irregularities," *J. Geophys. Res.*, vol. 79, pp. 1562–1566, 1974.

[17] H. E. Whitney, "Notes on the relationship of scintillation index to probability distributions and their uses for system design," Air Force Cambridge Res. Lab., Rep. AFCRL-TR-74-0004, AD778092, Bedford, MA, 1974.

[18] S. Basu, S. Basu, J. P. McClure, W. B. Hanson, and H. E. Whitney, "High-resolution topside in-situ data of electron densities and VHF/GHz scintillations in the equatorial region," *J. Geophys. Res.*, vol. 88, p. 403, 1983.

[19] S. J. Franke and C. H. Liu, "Observations and modeling of multifrequency VHF and GHz scintillations in the equatorial region," *J. Geophys. Res.*, vol. 88, p. 7075, 1983.

[20] S. Basu and H. E. Whitney, "The temporal structure of intensity scintillations near the magnetic equator," *Radio Sci.*, vol. 18, p. 263, 1983.

[21] C. L. Rino, "Numerical computations for a one-dimensional power law phase screen," *Radio Sci.*, vol. 15, p. 41, 1980.

[22] H. G. Booker and G. MajidiAhi, "Theory of refractive scattering in scintillation phenomena," *J. Atmos. Terr. Phys.*, vol. 43, p. 1199, 1981.

[23] R. Umeki, C. H. Liu, and K. C. Yeh, "Multifrequency studies of ionospheric scintillations," *Radio Sci.*, vol. 12, p. 311, 1977.

[24] M. Nakagami, "The m-distribution—A general formula of intensity distribution of rapid fading," in *Statistical Methods of Radio Wave Propagation*, W. C. Hoffman, Ed. Elmsford, NY: Pergamon, Symposium Publications Div., 1980.

[25] H. E. Whitney, J. Aarons, R. S. Allen, and D. R. Seeman, "Estimation of the cumulative amplitude probability distribution function of ionospheric scintillations," *Radio Sci.*, vol. 7, pp. 1095–1104, 1972.

[26] C. L. Rino and J. Owen, "The time structure of transionospheric radio wave scintillation," *Radio Sci.*, vol. 15, p. 479, 1980.

[27] P. F. Fougere, "On the accuracy of spectrum analysis of red noise processes using maximum entropy and periodogram methods: Simulation studies and application to geophysical data," *J. Geophys. Res.*, vol. 90, pp. 4355–4366, 1985.

[28] C. L. Rino and J. Owen, "Numerical simulations of intensity scintillation using the power law phase screen model," *Radio Sci.*, vol. 19, p. 891, 1984.

[29] E. J. Fremouw, R. L. Leadabrand, R. C. Livingston, M. D. Cousins, C. L. Rino, B. C. Fair, and R. A. Long, "Early results from the DNA Wideband satellite experiment—Complex-signal scintillation," *Radio Sci.*, vol. 13, p. 167, 1978.

[30] J. A. Whalen, "Auroral oval plotter and nomograph for determining corrected geomagnetic local time, latitude and longitude for high latitudes in the northern hemisphere," Air Force Cambridge Research Laboratory, Bedford, MA, Rep. AFCRL-TR-70-0422, AD 713170, 1970.

[31] J. Aarons, J. P. Mullen, H. E. Whitney, A. Johnson, and E. Weber, "VHF scintillation activity over polar latitudes," *Geophys. Res. Lett.*, vol. 8, p. 277, 1981.

[32] J. F. Vickrey and M. C. Kelley, "The effects of a conducting E layer on classical F-region cross-field plasma diffusion," *J. Geophys. Res.*, vol. 87, p. 4461, 1982.

Santimay Basu received the Ph.D. degree in radio physics and electronics in 1964 from Calcutta University, India.

He was a Reader at the Institute of Radio Physics and Electronics from 1965 to 1975 with a sabbatical break in 1971 and 1972 when he was a Senior National Academy of Sciences Resident Research Associate at the Air Force Geophysics Laboratory, Hanscom AFB, MA. His teaching responsibilities at Calcutta included microwave transmission systems, antennas, and ionospheric radio propagation. He built up an active research group at Calcutta University specializing in low latitude radio propagation problems. In 1976 he joined Emmanuel College, Boston, MA, as a Physicist where he was instrumental in organizing intensive studies of ionospheric irregularities and their impact on communications systems. He joined the Ionospheric Effects Branch of AFGL in 1985 where he is responsible for organizing and conducting research on ionospheric structuring, their effects on radio wave propagation, and on ionospheric instability processes induced by high power radio waves. He has published more than 50 journal articles in the areas of natural and artificial irregularities and communication problems at high and low latitudes.

Eileen Martin MacKenzie was born in Boston, MA, in 1951. She received the M.S. degree in physics from Northeastern University, Boston, in 1978.

She is a Physicist in the Physics Research Division of Emmanuel College, Boston. Since 1972 she has been involved in developing large scintillation databases, statistical analyses, and modeling efforts. Additional work has included coordination of scintillation parameters with in situ data, such as auroral imagery and particle precipitation patterns.

Sunanda Basu received the Ph.D. degree in 1972 in radio physics from Calcutta University, India.

She continued as a Research Associate at Calcutta University until 1975. In 1975 she accepted a National Academy of Sciences Resident Research Associateship at the Air Force Geophysics Laboratory, Hanscom AFB, MA, and since 1978 has been at Emmanuel College, Boston, MA, as a Physicist. Her major interest is in multitechnique studies of natural and artificial ionospheric irregularities, and she has organized many intensive campaigns for their study at the magnetic equator and at high latitudes with support from AFGL, NSF, and NASA.

Dr. Basu was a member of the Guest Investigator Team on the NASA Atmosphere Explorer Program and is currently a member of the Dynamics Explorer Guest Investigator Team. She was an Associate Editor of the *Journal of Geophysical Research (Space Physics)* during 1983-1985 and has recently been elected President of the Hanscom Chapter of Sigma Xi.

Emanoel Costa received the B.S. and M.S. degrees in electrical engineering from the Military Institute of Engineering (IME), Rio de Janeiro, Brazil, in 1972 and 1974, respectively. He received the Ph.D. degree from Cornell University, Ithaca, NY, in 1977.

Since 1978 he has been with the Pontifical Catholic University of Rio de Janeiro (PUC/RJ), Brazil, where he is an Associate Professor at the Center for Telecommunication Studies (CETUC). On a sabbatical leave from this position, he spent the period between November 1984 and June 1986 at the Physics Research Division, Emmanuel College, Boston, MA, working on space-receiver analysis of ionospheric irregularity anisotropies and drifts. His research interests are in the areas of tropospheric and ionospheric effects on radiowave propagation and telecommunication systems.

Paul F. Fougere (M'83-SM'85) received the B.S. and M.S. degrees from Boston College, Boston, MA. In a part time effort he obtained the Ph.D. degree from Boston University with a dissertation on the electronic structure of diatomic molecules.

He spent a year at the Naval Research Laboratory in Washington, DC, working on ultrasonics, and another year at the General Electric Company in Lynn, MA. At this point he joined the Geomagnetism Branch at the Air Force Cambridge Research Center (now known as the Air

Force Geophysics Laboratory, AFGL). At AFGL he has worked on magnetic field analysis, especially spherical harmonic analysis; one of his models became part of the first International Geomagnetic Reference Field. Later work centered on theory and application of maximum entropy power spectral analysis, which he is currently applying, within the Ionospheric Effects Branch, to a large number of problems of interest to AFGL, such as ionospheric scintillation, ionospheric densities and velocities, neutral air densities, electric field data, Fourier transform spectroscopy, and Fourier transform mass spectrometry.

Herbert C. Carlson, Jr. was born in Brooklyn, NY, in 1937. He received the Ph.D. degree in radio propagation from Cornell University, Ithaca, NY, in 1965.

In 1973, leaving the position of Head of the Ionospheric Physics Department at Arecibo, he went to the University of Texas at Dallas to participate in the beginning of the Atmospheric Explorer Satellite Program. He served at the National Science Foundation from 1977 to 1979 as Aeronomy Program Director, while also developing a major new National Science Foundation initiative in atmospheric sciences. From 1979 to 1981 he served as its first Program Manager for upper atmospheric facilities. He is Chief of the Ionospheric Effects Branch at the Air Force Geophysics Laboratory, Hanscom AFB, MA. His publications are primarily in the areas of ionospheric and plasma physics, ionospheric modification with high-power HF "heating," radar techniques applied to sensing ionospheric properties, and mesosphere-stratosphere-troposphere winds, optical sensing of thermospheric properties, and high-latitude ionospheric irregularity processes as they affect RF systems

Herbert E. Whitney, photograph and biography not available at the time of publication.

ATTACHMENT 3

Morphology of phase and intensity scintillations in the auroral oval and polar cap

Sunanda Basu, Santimay Basu, and E. MacKenzie

Emmanuel College, Boston, Massachusetts

H. E. Whitney

Air Force Geophysics Laboratory, Hanscom Air Force Base, Massachusetts

The first long-term measurements of phase scintillations at high latitudes from a quasi-stationary Air Force satellite at 250 MHz are reported. The measurements were made from Goose Bay, Labrador covering the corrected geomagnetic latitude range of 64° 72 N and Thule, Greenland covering the corrected geomagnetic latitude range of 85' -89' N. Data from December 1979, March-April 1980 and March-April 1982 are presented from both stations. The sunspot numbers during these specific time periods were approximately the same. The scintillation magnitudes were higher during the vernal equinox at both stations than during the winter solstice. The Goose Bay data showed a well ordered diurnal variation with a nighttime maximum and daytime minimum, whereas the Thule data showed no such ordering The limited phase scintillation data set from Thule is augmented by intensity scintillation measurements made during 1979-1982 using the same quasi-stationary satellites The long-term Thule data shows that the major variation in scintillation activity is annual with minimum scintillations observed in the local summer, as was determined earlier by Aarons et al (1981) In contrast to the pronounced annual variation, the dependence of overall scintillation activity on sunspot cycle is not greatly evident during 1979 1982 when the sunspot number varied approximately between 100 and 200. It was found that both Goose Bay and Thule could show phase scintillations of the order of 10 rad (with 82-s detrend period) even during magnetically quiet times One such case study, conducted during March 1982, is presented and second-order parameters such as phase and intensity spectral strengths and slopes and intensity decorrelation times are discussed for this event at both stations The use of geostationary satellite data shows the importance of enhanced magnetospheric convection velocities on the observation of large phase scintillation values at both sites This underscores the need for incorporating irregularity dynamics in the currently developed static models of ionospheric scintillation

INTRODUCTION

Ground-based measurements over 2 decades have established the broad morphological features of three major scintillation regions, two covering the auroral ovals and polar caps and the third one approximately centered on the magnetic equator [*Aarons,* 1982] Most of the morphological information, however, has come from intensity scintillation measurements [*Basu and Basu,* 1981; *Basu and Aarons,* 1980; *Aarons et al.,* 1981]. It has been well known for a long time that amplitude scintillations can degrade the performance of satellite communication systems (cf reviews by *Aarons* [1982] and *Yeh and Liu* [1982] and references therein). More recently, it has

become clear that naturally occurring phase scintillations can impair the performance of satellite systems that use synthetic aperture processing to achieve high angular resolution [*Fremouw et al.,* 1978].

The only long-term study of phase scintillations was made by using the DNA Wideband satellite, there being two observing stations at the equator [*Livingston,* 1980] and one within the auroral oval in the Alaskan sector [*Rino and Matthews,* 1980] This was supplemented later by Wideband phase scintillation measurements made from Goose Bay [*Basu et al.,* 1981]. This satellite orbit, however, was sun-synchronous and thus observations were only available near local midnight and during prenoon hours To extend the coverage over a 24-hour period, a novel system of measuring phase scintillations using transmissions from the geostationary satellite Fleetsat parked at 100°W was put into operation at
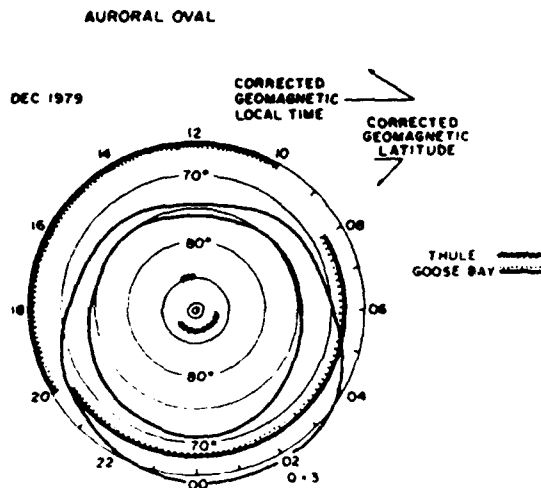
AURORAL OVAL

Fig. 1. Polar plot of available data from Thule and Goose Bay for December 1979 as a function of corrected geomagnetic latitude (CGL) and corrected geomagnetic time (MLT). The $Q = 3$ auroral oval [Feldstein and Starkov, 1967] is shown for reference.

Goose Bay, the details of which are given in Basu et al. [1982]. Unfortunately, the ionospheric intersection of the ray path from the satellite to Goose Bay was at 60° invariant so that in general, under magnetically quiet conditions, the auroral oval was considerably poleward of this point and the median phase and amplitude fluctuations were quite small. However, during severe magnetic storms when the auroral oval moves substantially equatorwards, a case study was presented in which large phase fluctuations exceeding 10 rad (with 150-s detrend period) were observed at 60° invariant [Basu et al., 1983a].

It is the object of this paper to present preliminary results of phase and amplitude scintillation morphology using high-inclination quasi-geostationary polar beacons from Goose Bay and Thule transmitting at approximately 250 MHz. The corrected geomagnetic latitude (CGL) coverage was 64°–72°N and 85°–89°N, respectively. Thus this data set is expected to provide the first phase scintillation measurements from deep within the polar cap as well as to supplement the Wideband auroral oval phase morphology with similar data using a quasi-stationary satellite as a source. The important point to note is that the scale-length coverage of phase scintillations for a fixed detrend interval with a geostationary (or quasi-stationary) satellite as a source is dependent on the ionospheric drift velocity as discussed by Basu et al. [1983a]. This is contrary to the situation when an orbiting satellite such as Wideband is the source of transmissions. In such cases, particularly at high lati-

tudes where the magnetic field is nearly vertical, the scale-length coverage is dictated by the effective velocity of the satellite [Fremouw et al., 1978] and is generally independent of the ionospheric drift. Thus in the phase scintillation data to be presented in this paper, an additional source of variability, namely ionospheric drift, has to be considered in addition to the strength of turbulence [Rino, 1979] of the medium itself.

RECEIVING SYSTEM AND DATA PROCESSING

The measurements described in the following sections were made using an extended dynamic range receiver with an extremely stable local oscillator. The receiver operates under computer control and once tuned to within a few hertz of a signal detected in a 10-Hz bandwidth, self-tunes to within ± 1 millihertz of the mean frequency as determined by the zero crossings averaged over a 20-s period. Subsequent changes in frequency, either due to changes in ionospheric or geometrical Doppler, are sensed by the system which then retunes. At each retune, the local oscillator frequency information is recorded to allow reconstruction of the long-term phase in subsequent processing. In particular, for the polar beacons which are in highly eccentric orbits, every 168 s the transmitted frequency is shifted approximately 14 Hz to assist in minimizing the range of departures of the received frequency from the local reference caused by time variation of the Doppler shift. In addition, the changing center frequency of the received signal causes it to drift toward the edge of the receiver passband. To avoid loss of signal, appropriate local oscillator frequency shifts at the receiver (while maintaining phase continuity) are performed to restore centering of the signal within the passband.

Once a signal is properly acquired by the receiver, its quadrature components are sampled at 50 Hz and are digitally recorded along with time and pertinent system information. During initial off-line processing, these data are converted to signal intensity and continuous phase. Because of the satellite frequency updates every 168 s and the problem of acquiring lock immediately after each such update, it was found most suitable to consider data blocks of 82-s length (i.e., 4096 points) for computation of the phase and intensity statistics. The phase is first detrended by fitting to a second degree polynomial before the rms phase deviation is computed. Phase and intensity spectra are also computed using a fast Fourier transform technique in order to determine the phase and
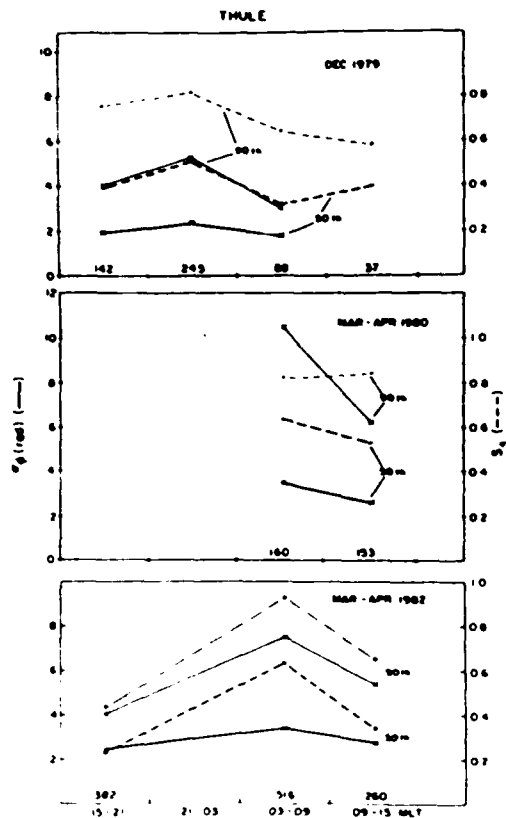
Fig. 2a

Fig 2 The median (50th percentile) and 90th percentile phase
and intensity scintillation values are shown in terms of four 6-hour
MLT blocks during December 1979, March-April 1980, and
March-April 1982 for Thule (Figure 2a) and Goose Bay (Figure
2b) Number of points in each bin is also indicated

intensity spectral indices (p_ϕ, p_i) and spectral
strengths at 1 HZ (T_ϕ, T_i) as was done earlier by
Fremouw et al. [1978].

RESULTS AND DISCUSSION

In principle, the polar beacons are sufficient in
number to provide a 24-hour coverage at high north-
ern latitudes. Indeed, such continuous measurements
were used by Aarons et al. [1981] to determine a
polar cap intensity scintillation morphology using
data recorded on paper charts. The same is true for
the 4-year continuous intensity scintillation data pre-
sented in this paper. Unfortunately, the situation is
not quite so simple for phase measurements. The in-
strument is highly sophisticated and hence needs
more expert and frequent supervision, a requirement
that is particularly difficult to meet at Thule. All the

beacons are not equally good sources for the phase
measurements so that certain times of day are very
inadequately covered. However, the most important
constraint of all is the digital processing of the tapes,
which is so time consuming that only a part of the
recorded data can be analyzed. The phase measuring
system became operational at both stations in De-
cember 1979 and has been running semicontinuously
(other than some long periods of system outage) until
the middle of 1983. In this preliminary report we will
present phase and intensity scintillation data from
December 1979, March-April 1980 and March-April
1982, when good quality data were available from
both stations simultaneously. Figure 1 gives the
coverage in corrected geomagnetic latitude (CGL)
and corrected geomagnetic time (MLT) provided by
the measurements at the two stations during the De-
cember 1979 period with the $Q = 3$ statistical auroral
oval [Feldstein and Starkov, 1967] provided for refer-
ence. In general, the subionospheric (350 km) cover-
age is between 84°-89°CGL for Thule (station coor-
dinates: 76.5°N, 68.7°W) and 64°-72° for Goose Bay
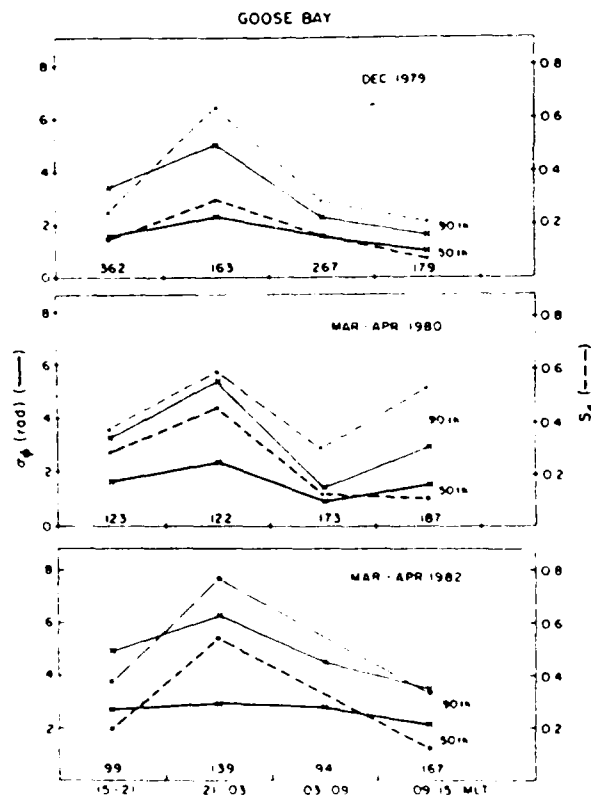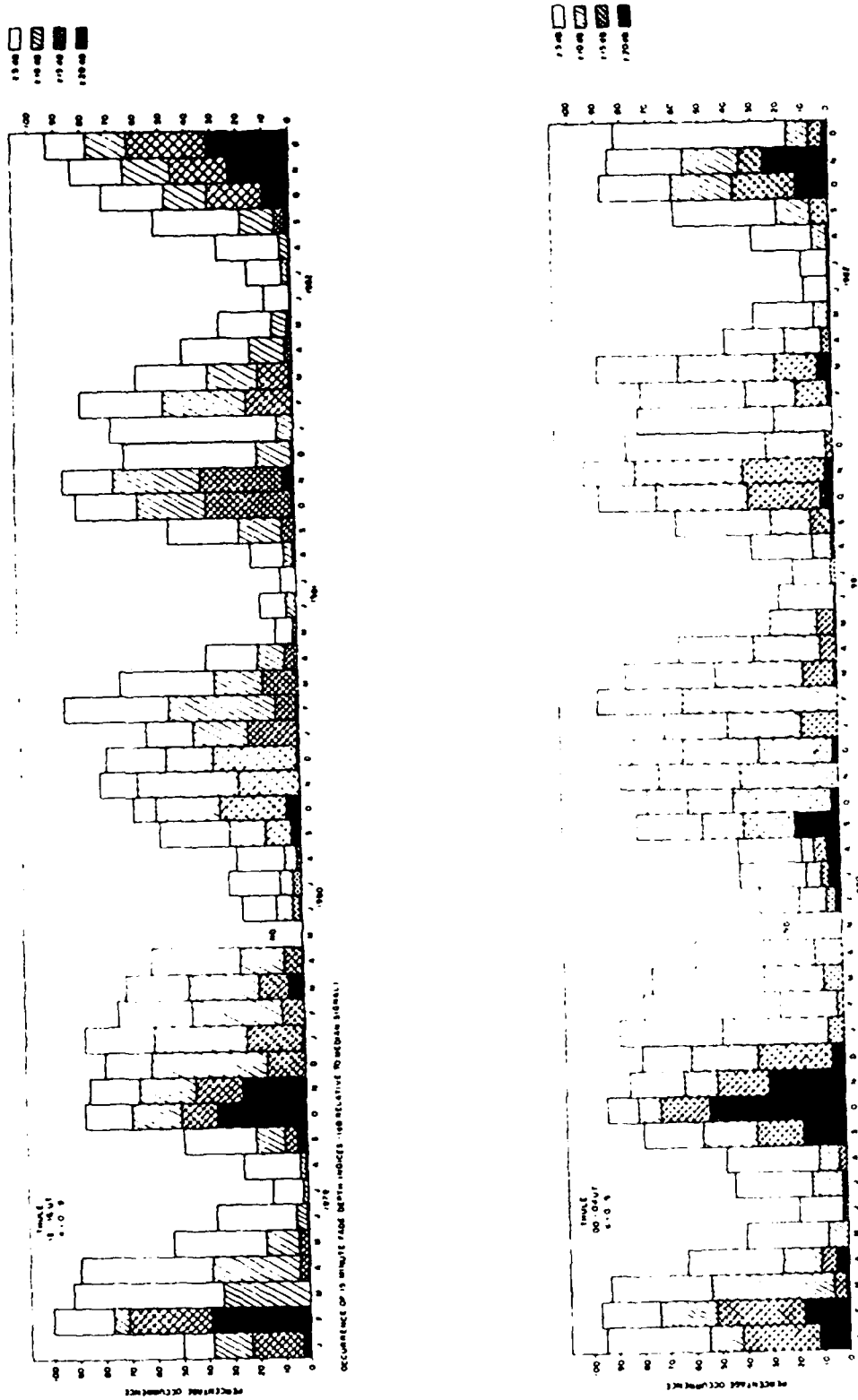(station coordinates: 53.3°N, 60.3°W) with the iono-

Fig 2b

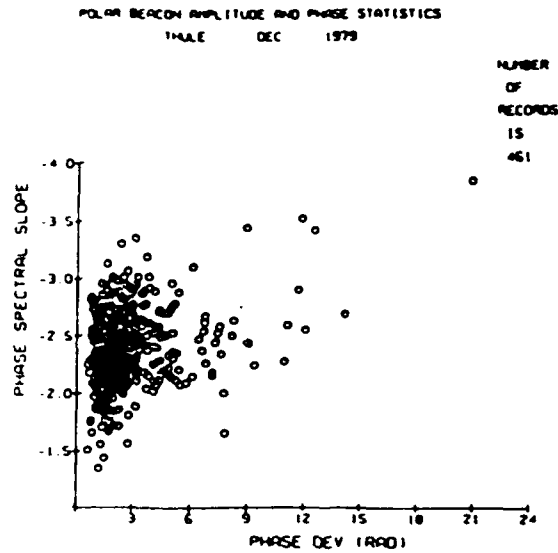Fig. 3. Thule intensity statistics for (top) noontime and (bottom) midnight periods during 1979-1982.

POLAR BEACON AMPLITUDE AND PHASE STATISTICS

THULE   DEC   1979

NUMBER
OF
RECORDS
IS
461

Fig. 4   Scatter plot of phase spectral index p_ϕ against rms phase deviation σ_ϕ for December 1979 at Thule.

spheric zenith angle at Thule always being less than 40° while at Goose Bay it is less than 60°. The average intersection locations and times of coverage for each of the other two seasonal periods while varying in detail are generally similar to that shown in Figure 1. Thus, in general, the Thule intersection explores the ionosphere deep within the polar cap, whereas the Goose Bay intersection explores the auroral oval in the evening to postmidnight period and the subauroral region at other times of the day.

The median (i.e., 50th percentile) phase and intensity scintillation values during December 1979, when, as mentioned earlier, data taking began at the two stations, are shown in the top panels of Figures 2a and 2b. The parameters plotted are the standard deviation of phase, σ_ϕ, obtained by using a detrend interval of 82 s, and the S_4 index or the second central moment of intensity as defined by Briggs and Parkin [1963]. The day is broken up into four 6-hour intervals centered around 1800, 2400, 0600 and 1200 MLT. The number of 82-s data samples per each 6-hour block is shown at the bottom of the respective diagrams. The choice of such large time blocks was necessitated by the uneven diurnal coverage at Thule, in particular. All the data are for $Kp < 3.5$. The Goose Bay data show the expected midnight maximum and midday minimum of scintillations at an auroral oval station. The highest median phase value is 2 rad increasing to 5 rad at the 90th percentile level. The corresponding intensity scintillations were

0.2 and 0.6, respectively. Thule showed approximately the same phase levels. However, the intensity scintillations were much higher, the median value of S_4 at midnight being 0.5 and the corresponding 90th percentile being 0.8. The diurnal variation of S_4 at Thule is also not as noticeable as at Goose Bay. Unfortunately, the Thule phase data for the midday hours were of poor quality and are not plotted.

The scintillation magnitudes for the vernal equinox seasons of March–April 1980 and March–April 1982 for Thule and Goose Bay are shown in the second and third panels of Figures 2a and 2b, again for $Kp < 3.5$ conditions. Although the general diurnal pattern is similar at Goose Bay, the Thule data (which show incomplete coverage) exhibit somewhat higher levels in the 0300–1500 MLT periods than the corresponding ones in December 1979. Since the Thule phase scintillation coverage is still inadequate, we show in Figure 3 (top and bottom) the intensity scintillation statistics obtained from the same satellites, but using the system described by Aarons et al. [1981], over a 4-year period beginning January 1979. Figure 3 (top) shows the statistics during the period around local noon (1200–1600 UT), while Figure 3 (bottom) shows the statistics for the midnight period (0000–0400 UT). The different hatchings show fade depth indices ranging from ≥ 5 dB to ≥ 20 dB. On a month-by-month comparison between the daytime and nighttime periods, one finds only minor differences in occurrence characteristics. The other 4-hourly time periods also show similar behavior indicating the lack of diurnal control as pointed out first

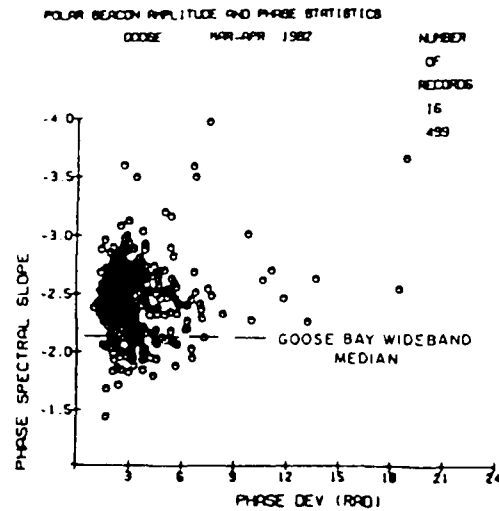POLAR BEACON AMPLITUDE AND PHASE STATISTICS

GOOSE   MAR–APR   1982

NUMBER
OF
RECORDS
16
499

GOOSE BAY WIDEBAND
MEDIAN

Fig. 5   Scatter plot of phase spectral index p_ϕ against rms phase deviation σ_ϕ for March–April 1982 at Goose Bay.
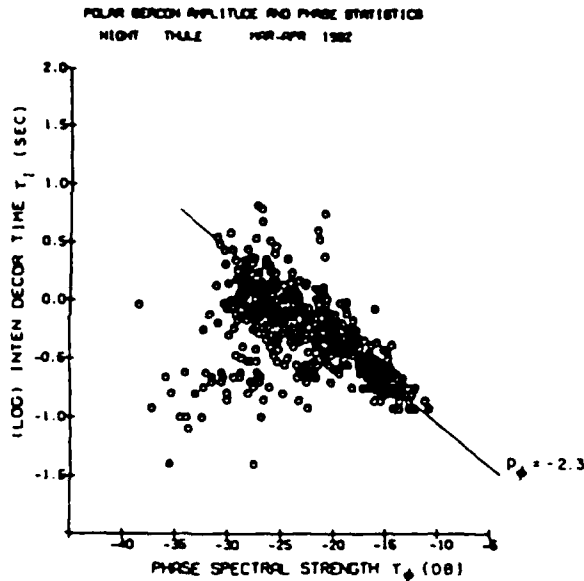
Fig. 6. A scatter plot of the intensity decorrelation time τ_I against the phase spectral strength T_ϕ. The theoretical dependence of τ_I on T_ϕ in the strong scatter regime for a phase spectral index $p_\phi = -2.3$ is indicated by the straight line.

by *Aarons et al.* [1981]. Further, magnetic activity has little or no effect, so that all data are included in the intensity statistics shown in Figure 3. The seasonal control is strong with maximum activity during

Fig. 7 Root mean square (rms) phase deviation σ_ϕ and intensity scintillation index S_4 at Goose Bay on March 7, 1982. Decorrelation time is also shown. Intensity spectra at time indicated by arrow (0418 : 43 UT) are shown in Figure 9a.

Fig. 8. Root mean square (rms) phase deviation σ_ϕ and intensity scintillation index S_4 at Goose Bay on March 8, 1982. Decorrelation time is also shown. Intensity spectra at time indicated by arrow (0417 : 02 UT) are shown in Figure 9b

the equinoxes and local winter, and minimum occurrence during local summer. The minimum activity during summer is probably due to the enhanced E region conductivity which reduces the lifetime of F region irregularities as they convect through the sunlit polar cap [*Vickrey and Kelley*, 1982]. In contrast to the consistent and pronounced annual variation of scintillations observed over the 4-year period, the dependence of scintillation activity on sunspot number remains less clear. In general, similar levels of seasonal activity were observed even though the sunspot number varied approximately between 200 and 100 during this 4-year period. It remains to be seen whether a further reduction in sunspot number will be accompanied by a reduction in scintillation activity as was determined by *Aarons et al.* [1981]. Indeed, *Buchau et al.* [this issue], based on a limited data set, find that scintillations at Thule were much reduced during December 1983 when the sunspot number was 33.

A parameter of interest both for modelling considerations [*Fremouw and Secan*, 1984a], as well as, underestanding F region irregularity structure [*Basu et al.*, 1984] is the spectral index of phase scintillations. We show scatter plots of this index, p_ϕ,

GOOSE BAY   MARCH 7, 1982
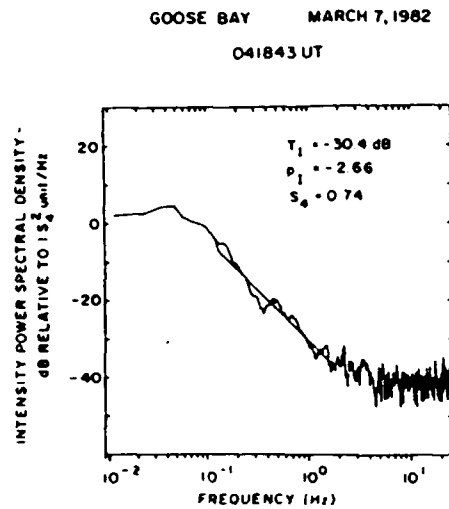
041843 UT

Fig. 9a. Spectra of intensity scintillation index S_4 from Goose Bay on March 7, 1982, at 0418:43 UT. The intensity spectral index $p_I = -2.66$; the corresponding intensity spectral strength $T_I = -30.4$ dB.

against the phase deviation σ_ϕ for December 1979 at Thule in Figure 4 and for March–April 1982 at Goose Bay in Figure 5. Both diagrams, while not showing a strong positive correlation between p_ϕ and σ_ϕ, at least indicate the absence of any decreasing trend of p_ϕ with σ_ϕ. This finding is thus contrary to the behavior of p_ϕ against σ_ϕ at the equatorial region found from Wideband [Fremouw and Secan, 1984b]. The median p_ϕ value observed from Goose Bay in the present case is -2.4. This is higher than the median value of $p_\phi = -2.1$ observed at Goose Bay with Wideband as a source [Basu et al., 1981]. The Wideband median p_ϕ is indicated in Figure 5. The p_ϕ values obtained with the quasi-stationary satellite in the present case are, however, quite comparable to those obtained from the Fleetsat data [Basu et al., 1982]. It was pointed out in the Introduction that the major difference between phase scintillation measurements using orbiting beacons and that made by using geostationary satellites is that in the former case the scale-length coverage is obtained by using the effective velocity of the satellite while in the latter case it is the ionospheric drift that dictates the largest scale-length coverage. Further, while there is great variability in the ionospheric drift, it is, in general, much smaller than the approximately 3 km s^{-1} effective velocity of orbiting beacons at high latitudes. As such, the scale-length coverage in the phase spectrum for the determination of p_ϕ is generally confined to longer scale-lengths in the orbiting case than is

obtained by stationary satellites. Thus if longer scale-lengths at auroral latitudes have shallower spectral slopes as observed at the equator [Livingston et al., 1981; Basu et al., 1983b], then the varying spectral slope observations referred to above can be explained on this basis. In situ data of high-latitude electron densities is currently being studied to resolve this question.

Another parameter of interest to systems engineers is the intensity decorrelation time [Umeki et al., 1977; Rino and Owen, 1980; Basu and Whitney, 1983]. We show in Figure 6 a scatter plot of the logarithm of the intensity decorrelation interval τ_I versus phase spectral strength T_ϕ dB. The systematic reduction of τ_I with increasing T_ϕ in the strong scatter regime ($T_\phi > -15$ dB) is noticeable. It is possible to obtain an estimate of the phase spectral slope, p_ϕ, from the nature of dependence of log τ_I on T_ϕ dB by using the work of Rino and Owen [1980]. For the nighttime Thule data obtained during March–April 1982, the scatter diagram yielded a value of -2.3 for the phase spectral slope, p_ϕ. This value is in remarkably good agreement with the median value of -2.3 for the phase spectral slope, p_ϕ, determined for the nighttime Thule data during this period.

Since this data base is fairly unique, it was felt that communications systems users may benefit from the discussion and illustration of examples of severe phase and amplitude scintillation events at both stations in order to get an order of magnitude estimate

GOOSE BAY   MARCH 8, 1982

041702 UT

Fig. 9b. Spectra of intensity scintillation index S_4 from Goose Bay on March 8, 1982, at 0417:02 UT. The intensity spectral index $p_I = -2.44$, the corresponding intensity spectral strength $T_I = -20.3$ dB.
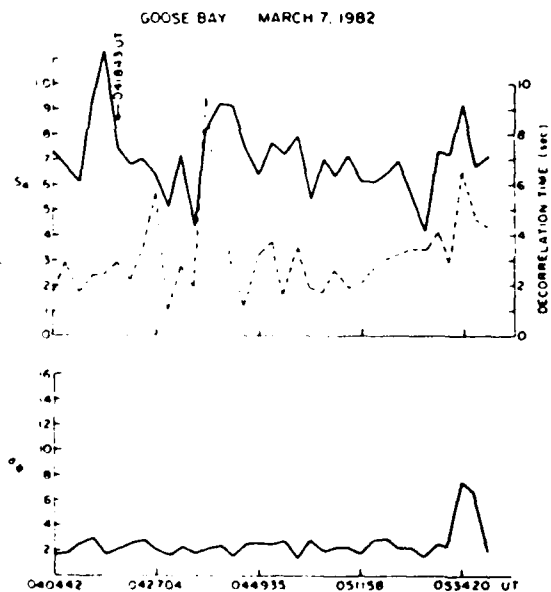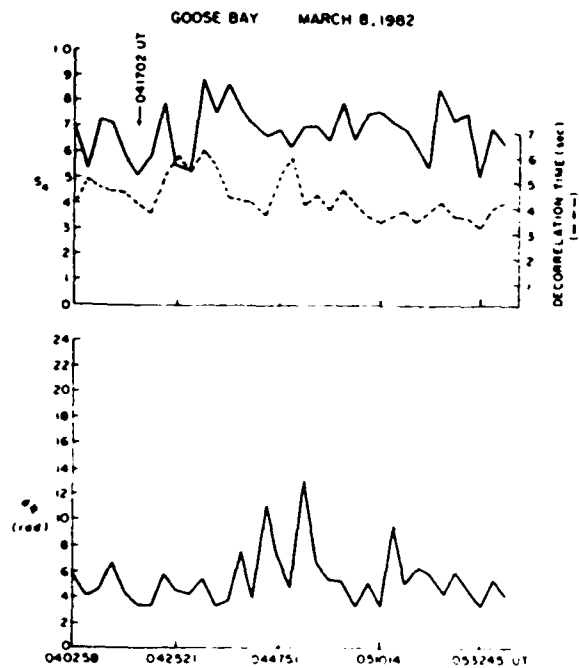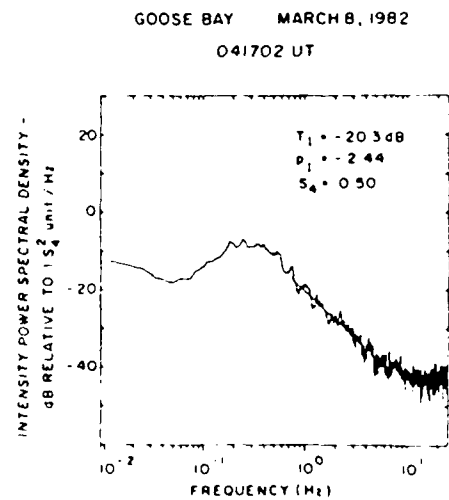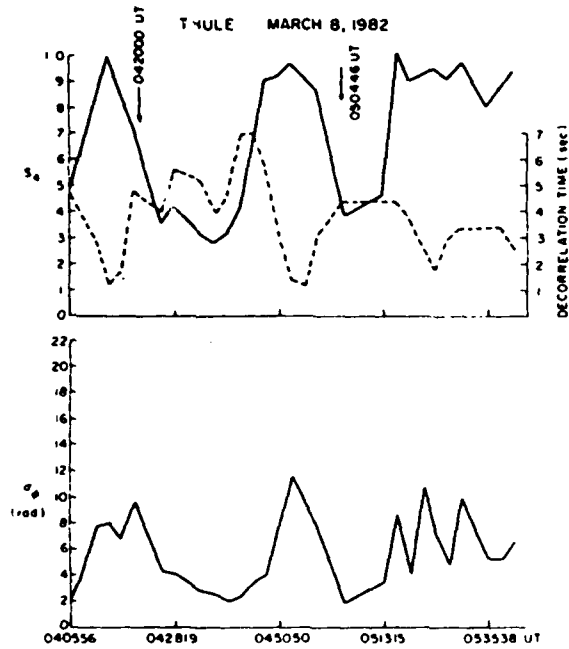
Fig. 10. Root mean square (rms) phase deviation σ_ϕ and intensity scintillation index S_4 at Thule on March 8, 1982. Decorrelation time is also shown. Phase and intensity spectra at times indicated by arrows (0504 : 46 UT and 0420 : 00 UT) are shown in Figures 11 and 12, respectively.

of such second-order parameters as the phase and amplitude spectral strengths at 1 Hz, namely, T_ϕ and T_I, the corresponding phase and intensity spectral slopes, p_ϕ and p_I, as well as the 50% decorrelation time of signal intensity under relatively strong scatter

conditions but under varying irregularity drift conditions. In order to do so, we present in Figures 7 and 8 the time history of scintillations on March 7 and 8, 1982, near magnetic midnight at Goose Bay. The two consecutive Goose Bay days are shown to emphasize the great impact that irregularity drift variation (driven by magnetospheric convection) has on the intensity decorrelation time and the magnitude of phase scintillation. It should be noted that the decorrelation times are plotted in seconds for March 7 and in tenths of seconds for March 8, even though the S_4 magnitudes are virtually the same on both days. The corresponding σ_ϕ curves also show a great contrast although this contrast is somewhat reduced by the fact that there is always a residual of approximately 1 rad in these single frequency phase measurements using quasi-stationary sources. In Figures 9a and 9b we show the spectra obtained at 0418 : 43 UT on March 7 and at 0417 : 02 UT on March 8. These specific times are identified by arrows in Figures 7 and 8, respectively. Since the universal times of the two samples are so close, the positions of the satellite on the 2 days were identical with respect to Goose Bay. However, we find the Fresnel maximum frequency (f_F) to be 0.05 Hz in Figure 9a and 0.3 Hz in Figure 9b. Using the relationship $f_t = u/(2\lambda z)^{1/2}$, where u is the drift velocity, λ is the radio wavelength and z is the slant range, we obtain the drift in a direction perpendicular to the propagation path to be 65 ms^{-1} on March 7 and 390 ms^{-1} on March 8.

The Thule S_4 and σ_ϕ data for March 8, 1982, are

Fig. 11. Spectra of (a) rms phase deviation σ_ϕ and (b) intensity scintillation index S_4 from Thule on March 8, 1982, at 0504 : 46 UT, a time of low σ_ϕ. The phase spectral index $p_\phi = -2.26$, the corresponding phase spectral strength $T_\phi = -25.4$ dB. The intensity spectral index $p_I = -2.46$, the corresponding intensity spectral strength $T_I = -24.4$ dB.
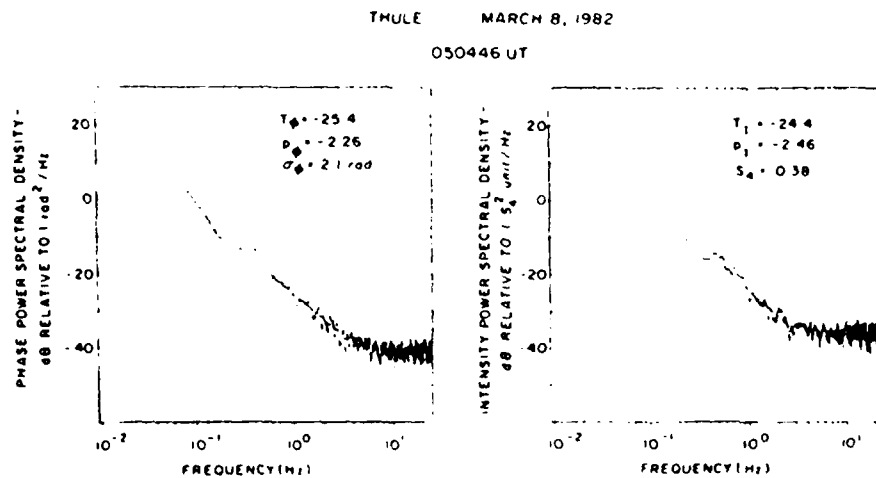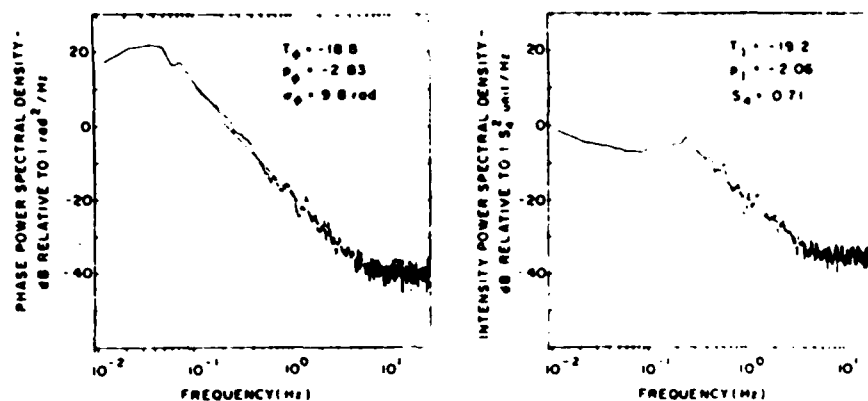
THULE   MARCH 8, 1982

042000 UT

Fig. 12   Spectra of (a) rms phase deviation σ_ϕ and (b) intensity scintillation index S_4 from Thule on March 8, 1982, at 0420 UT, a time of high σ_ϕ. The phase spectral index $p_\phi = -2.83$, the corresponding phase spectral strength $T_\phi = -18.8$ dB. The intensity spectral index $p_I = -2.06$; the corresponding intensity spectral strength $T_I = -19.2$ dB.

shown in Figure 10. They correspond to the same time period as the Goose Bay data shown in Figure 8. The difference in the scintillation character which seems to be typical of the respective domains is the presence of more discrete irregularity structures in the polar cap and more uniform turbulence in the auroral oval. Such discrete scintillation structures were also observed by *Weber and Buchau* [1981] in the polar cap when sun-aligned arcs were observed near Thule. The strength of turbulence seems somewhat higher at Thule as in this case S_4 actually achieves a value of unity. The decorrelation time is also correspondingly lower achieving a value as small as 0.1 s. Such decorrelation times are observed near the equator at a similar frequency using the Marisat satellite but the S_4 indices in that case were driven far into saturation with the S_4 index being continuously greater than or equal to unity for a period of 90 min [cf. *Basu et al.*, 1983b, Figure 8].

The phase and intensity scintillation spectra from Thule under conditions of low σ_ϕ and high σ_ϕ are shown in Figures 11a, b and 12a, 12b, respectively. These times are identified by two arrows in Figure 10. The phase strength parameter T_ϕ at 1 Hz, is given by -25.4 dB in the weak scintillation case and is -18.8 dB in the strong scintillation case. We note that the low σ_ϕ value is associated with a shallow slope ($p_\phi = -2.3$) compared to the high σ_ϕ value which is associated with a steeper slope ($p_\phi = -2.8$). This is in keeping with the trend observed in the scatter diagram shown in Figure 4. The two corresponding intensity spectra are shown in Figures 11b

and 12b. From a consideration of the Fresnel maximum in these cases which is $f_F = 0.24$ Hz (particularly discernible in Figure 12b) we obtain a velocity perpendicular to the propagation path of 260 ms^{-1}, which is somewhat smaller than the velocity obtained at Goose Bay at the same time. We have been able to obtain (through the courtesy of W. B. Hanson) Dynamics Explorer 2 data, in particular, a DE-2 orbit that passes fairly close to both the Goose Bay and Thule intersections on March 8, 1982, at approximately the same universal time. It is our object to investigate drift variations and in situ density structure variations in the DE-2 data and to study the extent to which they are mapped in phase and intensity scintillation data.

SUMMARY

The results on the statistics of 250 MHz phase and amplitude scintillations obtained during the period 1979–1982 at an auroral (Goose Bay, Labrador) and a polar cap (Thule, Greenland) station from high elevation angle observations of quasi-stationary satellites can be summarized as follows

The median and the 90th percentile values of rms phase deviation at 250 MHz for 82-s detrend interval are 2 and 6 rad, respectively, at both the auroral and polar cap locations. The corresponding values for the S_4 index of intensity scintillations are 0.3 and 0.6 for the auroral and 0.5 and 0.8 for the polar cap station

The auroral station exhibits the well-documented diurnal variation of scintillation with maximum nighttime occurrence of scintillation. In the polar

cap, on the other hand, this diurnal variation is not evident.

In the polar cap, a strong annual variation of scintillation arising from a deep minimum in the activity during local summer months was observed. The summer minimum is probably related to the enhanced E region conductivity which reduces the lifetime of F region irregularities convected across the sunlit polar cap. During the period of observations when sunspot numbers ranged between 100 and 200, the dependence of scintillations on sunspot activity was not very evident.

The median values of phase spectral index at the auroral and polar cap locations were found to be similar, being -2.4 at Goose Bay and -2.3 at Thule. At auroral locations, the intensity decorrelation time was observed to range between 0.1 s to a few seconds for similar scintillation magnitudes. This presumably arises from the extreme variability of convection velocities in the auroral oval. In the polar cap, a systematic decrease of intensity decorrelation time with increasing phase spectral strength for strong scintillations was observed. This dependence was utilized to derive a phase spectral slope which was in good agreement with the median value stated above.

REFERENCES

Aarons. J., Global morphology of ionospheric scintillations, *Proc. IEEE*, 70, 360, 1982.

Aarons. J., J. P. Mullen, H. Whitney, A. Johnson, and E. Weber, VHF scintillation activity over polar latitudes, *Geophys. Res. Lett.*, 8, 277, 1981.

Basu, S., and Su Basu, Equatorial scintillation—A review, *J. Atmos. Terr. Phys.*, 43, 473, 1981.

Basu, S., and H. E. Whitney, The temporal structure of intensity scintillations near the magnetic equator, *Radio Sci.*, 18, 263, 1983.

Basu, Su., and J. Aarons, The morphology of high-latitude VHF scintillation near 70°W, *Radio Sci.*, 15, 59, 1980.

Basu, Su, S. Basu, R. C. Livingston, H. E. Whitney, and E. MacKenzie, Comparison of ionospheric scintillation statistics from the North Atlantic and Alaskan sectors of the auroral oval using the Wideband satellite, *Rep. AFGL-TR-81-0266*, Air Force Geophys. Lab., Hanscom Air Force Base, Mass., 1981, ADA111871.

Basu, Su., S. Basu, R. C. Livingston, E. MacKenzie, and H. E. Whitney, Phase and amplitude scintillation statistics at 244 MHz from Goose Bay using a geostationary satellite, *Rep. AFGL-TR-82-0222*, Air Force Geophys. Lab., Hanscom Air Force Base, Mass., Aug. 6, 1982, ADA124291.

Basu, Su., E. MacKenzie, S. Basu, H. C. Carlson, D. A. Hardy, F. J. Rich, and R. C. Livingston, Coordinated measurements of low-energy electron precipitation and scintillations/TEC in the auroral oval, *Radio Sci.*, 18, 1151, 1983a.

Basu, Su., S. Basu, J. P. McClure, W. B. Hanson, and H. E. Whitney, High-resolution topside in situ data of electron densities and VHF/GHz scintillations in the equatorial region, *J. Geophys. Res.*, 88, 403, 1983b.

Basu, Su., S. Basu, E. MacKenzie, W. P. Coley, W. B. Hanson, and C. S. Lin, F region electron density irregularity spectra near auroral acceleration and shear regions, *J. Geophys. Res.*, 89, 5554, 1984.

Briggs, B. H., and I. A. Parkin, On the variation of radio star and satellite scintillation with zenith angle, *J. Atmos. Terr. Phys.*, 25, 339, 1963.

Buchau, J., E. J. Weber, H. C. Carlson, Jr., J. G. Moore, B. W. Reinisch, and R. C. Livingston, Ionospheric structures in the polar cap and their relation to satellite scintillation, *Radio Sci.*, 20, this issue.

Feldstein, Y. I., and G. V. Starkov, Dynamics of auroral belt and polar geomagnetic disturbances, *Planet. Space Sci.*, 15, 209, 1967.

Fremouw, E. J., and J. A. Secan, Modeling and scientific application of scintillation results, *Radio Sci.*, 19, 687, 1984c.

Fremouw, E. J., and J. A. Secan, Improvements in operational codes describing the ambient ionosphere, *Progr. Rep. 6*, Physical Dynamics Inc., Bellevue, Wash., February 1984b.

Fremouw, E. J., R. L. Leadabrand, R. C. Livingston, M. D. Cousins, C. L. Rino, B. C. Fair, and R. A. Long, Early results from the DNA Wideband satellite experiment: Complex-signal scintillation, *Radio Sci.*, 13, 167, 1978.

Livingston, R. C., Comparison of multifrequency equatorial scintillation: American and Pacific sectors, *Radio Sci.*, 15, 801, 1980.

Livingston, R. C., C. L. Rino, J. P. McClure, and W. B. Hanson, Spectral characteristics of medium-scale equatorial F region irregularities, *J. Geophys. Res.*, 86, 2421, 1981.

Rino, C. L., A power-law phase screen model for ionospheric scintillation, 1, Weak scatter, *Radio Sci.*, 14, 1135, 1979.

Rino, C. L., and S. J. Matthews, On the morphology of auroral zone radio wave scintillation, *J. Geophys. Res.*, 85, 4139, 1980.

Rino, C. L., and J. Owen, The time structure of transionospheric radio wave scintillation, *Radio Sci.*, 15, 479, 1980.

Umeki, R., C. H. Liu, and K. C. Yeh, Multifrequency studies of ionospheric scintillation, *Radio Sci.*, 12, 311, 1977.

Vickrey, J. F., and M. C. Kelley, The effects of a conducting E layer on classical F region cross-field plasma diffusion, *J. Geophys. Res.*, 87, 4461, 1982.

Weber, E. J., and J. Buchau, Polar cap F layer auroras, *Geophys. Res. Lett.*, 8, 125, 1981.

Yeh, K. C., and C. H. Liu, Radiowave scintillations in the ionosphere, *Proc. IEEE*, 70, 324, 1982.

S. Basu, Su. Basu, and E. MacKenzie, Emmanuel College, Boston, MA 02115.

H. E. Whitney, Air Force Geophysics Laboratory, Hanscom Air Force Base, MA 01731.
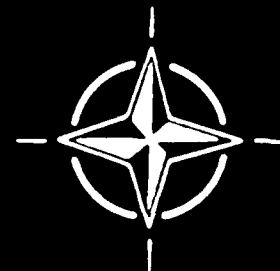
JUNE 1985

AGARD

ADVISORY GROUP FOR AEROSPACE RESEARCH & DEVELOPMENT

7 RUE ANCELLE 92200 NEUILLY SUR SEINE FRANCE

Paper Reprinted from
Conference Proceedings No.382

**PROPAGATION EFFECTS ON MILITARY
SYSTEMS IN THE HIGH LATITUDE REGION**

NORTH ATLANTIC TREATY ORGANIZATION

38

TOTAL ELECTRON CONTENT AND L-BAND AMPLITUDE
AND PHASE SCINTILLATION MEASUREMENTS IN THE POLAR CAP IONOSPHERE

J.A. Klobuchar and G.J. Bishop
Ionospheric Physics Division
Air Force Geophysics Laboratory
Hanscom AFB, MA 01731

P. H. Doherty
Physics Research Division
Emmanuel College
400 The Fenway
Boston, MA. 02115

SUMMARY

The first measurements of absolute Total Electron Content (TEC) and L-band amplitude and phase scintillation were made from Thule, Greenland, a polar cap station, in early 1984. These measurements were made using signals transmitted from the Global Positioning System (GPS) satellites. The variability of the TEC, especially during the afternoon to pre-midnight hours, is large, with increases in TEC above the background values of greater than 100 percent not uncommon. During one disturbed time quasi-periodic TEC enhancements having periods as short as ten minutes and amplitudes equal to the background TEC were observed for over two hours. The TEC during some of the disturbed periods in the dark Thule ionosphere exceeded mid-latitude daytime values. Amplitude scintillations were small, not exceeding 3 dB peak to peak during the entire observing period, but they were associated with the times of TEC enhancements, with some evidence for stronger scintillation occurring during the negative gradients of the TEC enhancements. Phase scintillations were highest during some of the times of enhanced TEC, and depend critically upon the phase detrend interval used.

INTRODUCTION

Measurements of total electron content (TEC) obtained from high elevation angle satellites have been obtained for the first time from the polar cap station located at Thule, Greenland, 76.5° geographic latitude, 86° invariant latitude. The only previous TEC measurements reported from Thule, ([1]Mendillo and Klobuchar, 1973) were recordings of Faraday rotation obtained from a geostationary satellite viewed at an approximate 5° elevation angle where the ionospheric intersection of the ray path to the satellite was over the auroral zone rather than the polar cap.

It is particularly important to study the behavior of the F region in the polar cap during the winter when solar EUV is minimal, and much of the F region is dominated by transport, rather than by local production. TEC measurements are also important because of ionospheric time delay effects on satellite positioning systems.

In addition to making the first high elevation absolute TEC measurements from Thule, both L-band amplitude and phase scintillation data were also obtained. During an eight day period in January-February, 1984 approximately 120 hours of recordings were obtained during both relatively magnetically quiet and magnetically disturbed conditions. Amplitude scintillation can limit satellite communications ([2]Aarons, et. al.,1982) while phase scintillation, a measure of irregularities of scale size greater than a few hundred meters can seriously affect the imaging from satellite-borne Synthetic Aperature Radars (SARs), ([3]Szuszczewicz, et. al., 1983).

THE MEASUREMENT TECHNIQUE

Dual frequency, L-band, psuedo-random-code modulated signals transmitted from the US Defense Department Global Positioning System (GPS) satellites were used for determining absolute TEC and for the measurements of amplitude and phase scintillation. GPS is an advanced satellite system, ([4]Parkinson and Gilbert, 1983), in which the user determines his range and range-rate from signals transmitted from 4 satellites by comparing his own clock time against those received from the 4 satellites. In this manner the three dimensional user position and velocity are determined. A fourth satellite is required to correct any user clock error. In order to provide simultaneous visibility of at least 4 satellites to a user anywhere on, or near, the earth's surface, a total of 18 satellites will eventually be required.

For our measurements in early 1984 only 5 satellites were available for navigation, affording only a few hours of simultaneous 4 satellite visibility per day. However, due to both the high geographic latitude of Thule, and the high inclination of the GPS satellites, there was at least one of the total of 5 satellites above 20° elevation for over 18 hours per day during our test period, thereby allowing us to make TEC and scintillation observations for over 3/4 of each day during our test period.

The importance of the GPS satellites for ionospheric research lies in the dual, coherently transmitted frequencies designed for the navigation user to correct for the group delay and carrier phase advance effects of the earth's ionosphere which otherwise would degrade both the range and range rate accuracy of the measurements. The signals

from the GPS satellites can be reduced, by the use of an appropriate receiving system, to equivalent coherent carriers at 1.228 and 1.575 GHz with coherent modulation at 10.23 MHz from which both the carrier phase advance and the modulation group delay can be directly measured, ([5]Rino, et. al.,1981). Carrier phase advance can be related to relative TEC , ([6]deMendonca, 1963), as:

$$\delta\phi_c = \frac{1.34 \times 10^{-7}}{f} \quad TEC \quad\quad (cycles)$$

where: TEC is in el/m^2 column and f is the carrier frequency in Hertz.

Since ionospheric changes imposed on the phase of a radio frequency wave transmitted from a satellite are more easily measured by comparison against a reference phase at a higher frequency we can write the difference in the ionospheric phase advance at two frequencies, referenced to the lower frequency as:

$$\Delta(\delta\phi) = \frac{40.31}{cf_2} \times \frac{(m^2 - 1)}{m^2} \quad TEC$$

where $m = 154/120$ for GPS satellites, $c = 2.998 \times 10^8$ m/sec, $f_2 = 1.228$ GHz. For the GPS frequencies: $TEC = 2.32 \times 10^{16} \Delta(\delta\phi_c)$ el/m^2 where $\Delta(\delta\phi_c)$ is in cycles.

Because of the relatively close spacing of the two coherent GPS carriers the measured ionospheric phase at the lower frequency, f_2, minus that at the higher frequency, f_1, is only 39% of the total phase advance at f_2. Nevertheless, this technique has excellent sensitivity of better than 0.1 radians r.m.s. in a 16 Hertz bandwidth using a nearly omnidirectional antenna and automaticallly removes all the contributions to phase changes due to geometric Doppler changes.

The measured differential carrier phase advance from the GPS satellites, $\Delta(\delta\phi_c)$, can be related to the equivalent ionospheric phase advance, $\delta\phi_c(f)$, at any single frequency, f, by:

$$\delta\phi_c(f) = \frac{1.228 \times 10^9}{f} \times 2.546\ \Delta(\delta\phi_c)_{GPS}, \quad \text{where f is in Hertz.}$$

For ease of comparing our phase scintillation results against those of others we have referenced them to an equivalent single frequency carrier phase advance at a standard frequency of 1 GHz.

The differential carrier phase advance measurement can be used to measure the relative changes in TEC with great accuracy. The background values of TEC, however, generally produce much more than one complete cycle of diff rential carrier phase advance; thus, some other technique must be used to determine the absolute TEC values.

The GPS satellites also transmit coherently derived modulated signals on each of the two carriers, providing a means for measuring absolute TEC values. The group delay measured between the two, 10.23 MHz equivalent modulation envelopes at the carrier frequencies is related to the equivalent TEC by:

$$TEC = 2.852 \times 10^{16} \delta(\Delta t_m)$$

where $\delta(\Delta t_m)$ is the differential group delay measured at the two modulation frequencies in nanoseconds.

In order to obtain an absolute value of TEC, while at the same time retaining the excellent relative accuracy of the phase measurements, it is only necessary to utilize the group delay data to obtain one value of TEC to fix the relative phase advance scale throughout each satellite pass to an absolute one. In practice, several independent values of group delay are fitted on an r.m.s. basis to the continuous relative scale of carrier phase advance.

The carrier phase advance, amplitude scintillation at the two frequencies, and the group delay were all sampled at a 20Hz rate. Group delay was averaged over a one minute interval to obtain smooth absolute values of TEC, and the differential carrier phase data was high pass filtered with various detrend times to illustrate the relative size of the observed phase scintillations remaining after detrending.

THE MEASUREMENTS-IONOSPHERIC REGION PENETRATED

Figure 1 illustrates the geometry of the GPS satellites as a function of elevation and azimuth as viewed from Thule during the middle of our eight day observing period. The satellites are in 12 hour, sidereal synchronous orbits which cross over essentially the same position in the sky approximately 4 minutes earlier each day. The receiving system was capable of receiving only one satellite at a time, thus we generally observed the satellite with the highest elevation angle. Note that in figure 1 only the heavier portion of each satellite's track was received.
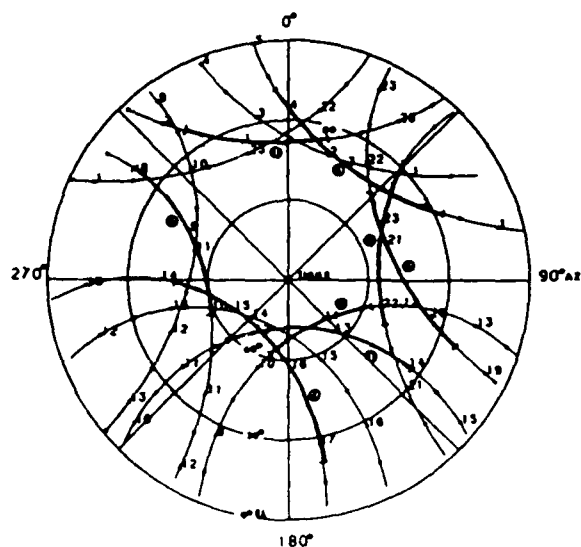
THULE
DAY 32 YEAR 84

Fig. 1. Elevation & azimuth of GPS satellites as viewed from Thule, Greenland on February 1, 1984. The heavy portions of each satellite track indicate the times & locations of actual GPS data recording.

Fig. 2. Locus of 400 km height intersection of ray path to indicated GPS satellites. Invariant latitudes are also shown.

In figure 2 the equivalent ionospheric location of the propagation path to each satellite at an average height of 400 km is shown, along with both the geogra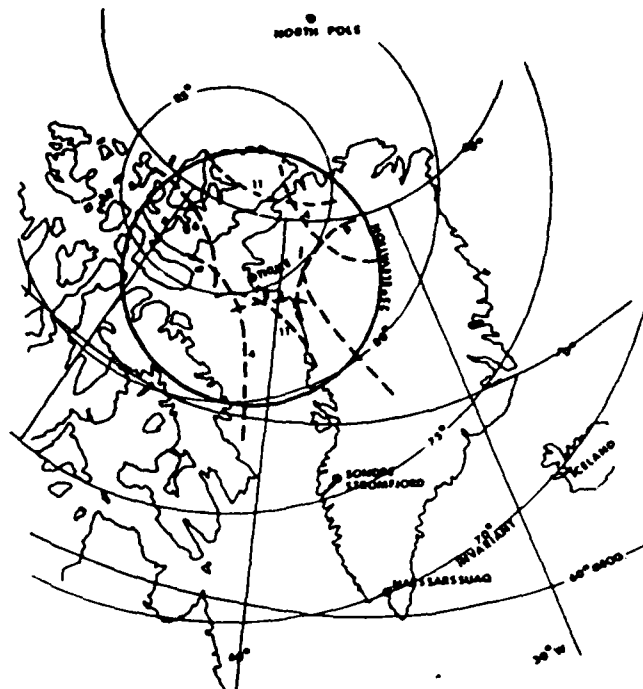phic and corrected geomagnetic latitudes. Note that most of the data taken from Thule refer to corrected geomagnetic latitudes above 80°, the only exceptions being when satellites were not visible at higher elevation angles. At those times we followed a satellite down to below 25° elevation. The corrected geomagnetic latitudes through which we measured ionospheric effects from the GPS satellite signals were always above the poleward side of the statistical position of the auroral oval as determined by [7]Feldstein and Starkov, (1967); thus, direct auroral precipitation effects on the TEC should not occur often at the invariant latitudes of our observations. However, Weber (private communication) has frequently observed sub-visual auroras above 80° corrected geomagnetic latitude using an all-sky image intensified optical system. During our eight day observing period several such auroral forms were recorded by Weber above 80° corrected geomatic latitude. The comparison of those results with TEC changes will reported elsewhere.

THE MEASUREMENTS-TEC RESULTS

The diurnal behavior of equivalent vertical TEC for our eight day observation period is shown on the daily overplot curves in figure 3. A clear diurnal variation of TEC can be seen in these daily overplot curves with a maximum in the local afternoon sector and a minimum in the predawn period. Thule at 76.5° N. geographic latitude has a maximum solar elevation angle above the horizon at a height of 150 km, assumed to be near the height of maximum production, of only 9.5° during our observing period. This maximum occurs at 1650 hours U.T. , nearly coincident with the time of our observed diurnal TEC maximum. Thus, even though the sun is indeed very low, there is still some apparent solar production of F region electron density. It is possible that the observed diurnal variation shown in figure 3 is actually a U.T. effect having the same phase as the solar controlled TEC would have. With observations from only one station it is not possible to separate U.T. and local time effects.

Of greater importance than the apparent solar controlled diurnal changes in the polar cap F region is the large day-to-day variability in TEC we observed, mainly during the afternoon (U.T.) and extending until the midnight hours (U.T.). The variability of the TEC during this period, also seen in figure 3, is extremely high on a percentage basis, especially during the period 20-24 hours U.T.
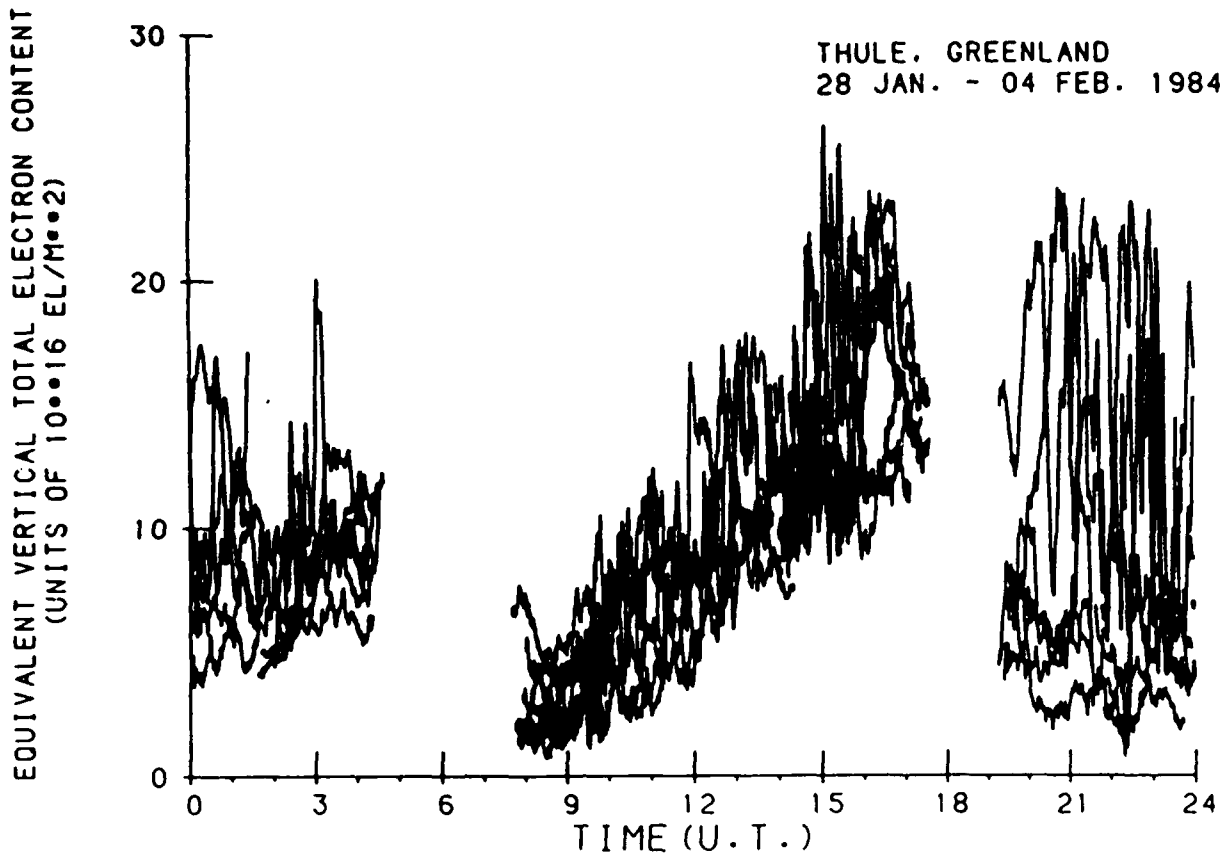
Fig. 3. Diurnal behavior of equivalent vertical TEC vs UT for the period 28 Jan-4 Feb 84.
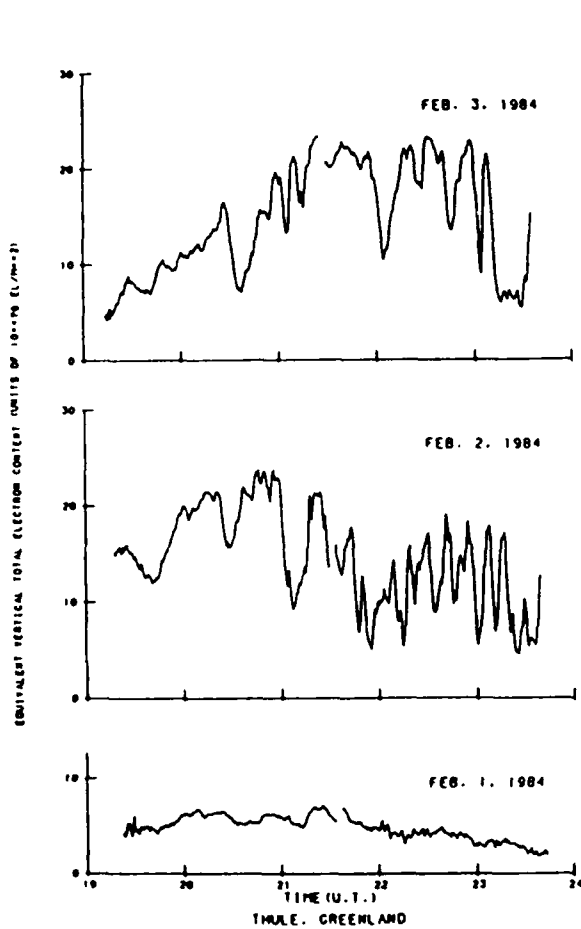
Fig. 4. TEC for the pre-midnight hours of 1-3 February 1984.
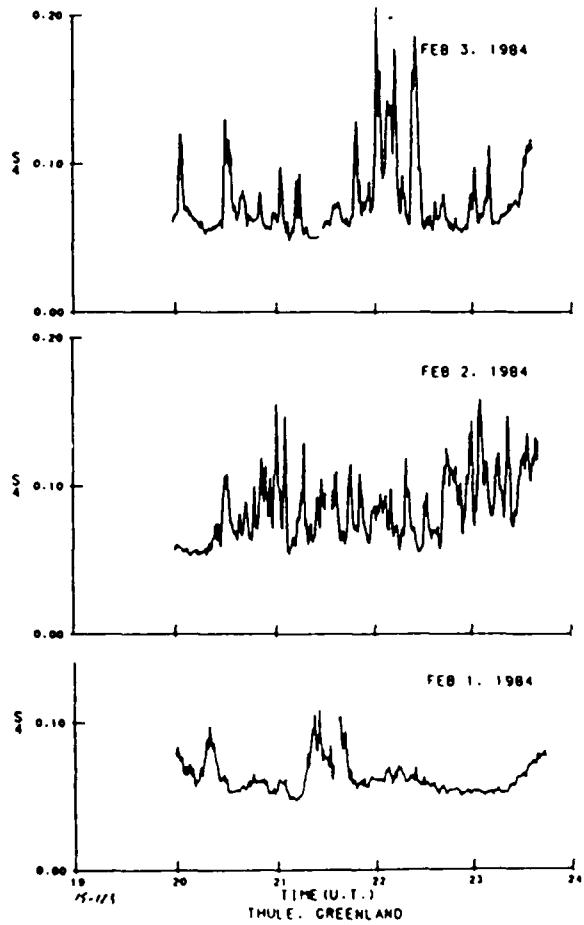
Fig. 5. Example of amplitude scintillation on 1.2 GHz for the prenight hours of 1-3 Feb 84.

42

Figure 4 shows a particularly dynamic period during the late hours of February 2 and 3 when the equivalent vertical TEC values varied in a quasi-periodic manner for several hours, having periodic components as short as ten minutes, particularly on February 2, and amplitudes of approximately 50% of the mean TEC during the time. For comparison, figure 4 also shows the variation of TEC during the same period of the day on February 1 when the background TEC was very low and quiet. If we assume that the diurnal TEC behavior seen on February 1 is the contribution remaining from direct solar production earlier in the day, and is representative of quiet ionospheric conditions during our eight day observing period, then the large enhancements seen on the evenings of February 2 and 3 represent much greater than a 100% enhancement above the solar controlled TEC.

THE MEASUREMENTS-AMPLITUDE AND PHASE SCINTILLATION

Amplitude scintillation measurements at L-band and higher frequencies have not previously been made in the polar cap. In our 8 days of observations we observed numerous short periods of several minutes duration having significant amplitude scintillation. Figure 5 shows the S_4 amplitude scintillation index on 1.228 GHz for the premidnight U.T. periods of 1-3 February, the same days for which the equivalent vertical TEC was shown in figure 4. The S_4 values for February 1, with the exception of two minor peaks near 2015 and 2120 U.T., represent the contribution of receiver noise in the absence of scintillation. The numerous short term peaks of S_4 seen in figure 5 on 2 and 3 February occurred during the same time of day when large TEC enhancements were seen. In a detailed comparison between the occurrence of amplitude scintillation and the TEC enhancements we found that many of the peaks in S_4 occurred on the negative gradients of the TEC enhancements.

Figure 6. Example of phase scintillation seen on 3 February 1984, for detrend intervals of 150, 100 and 10 seconds.

Phase scintillation effects are shown in the recorded differential carrier phase records shown in figure 6. Three different linear phase detrend intervals were used to construct the phase scintillation residuals illustrated in figure 6. These high pass detrend cutoff times were 10 seconds, 100 seconds an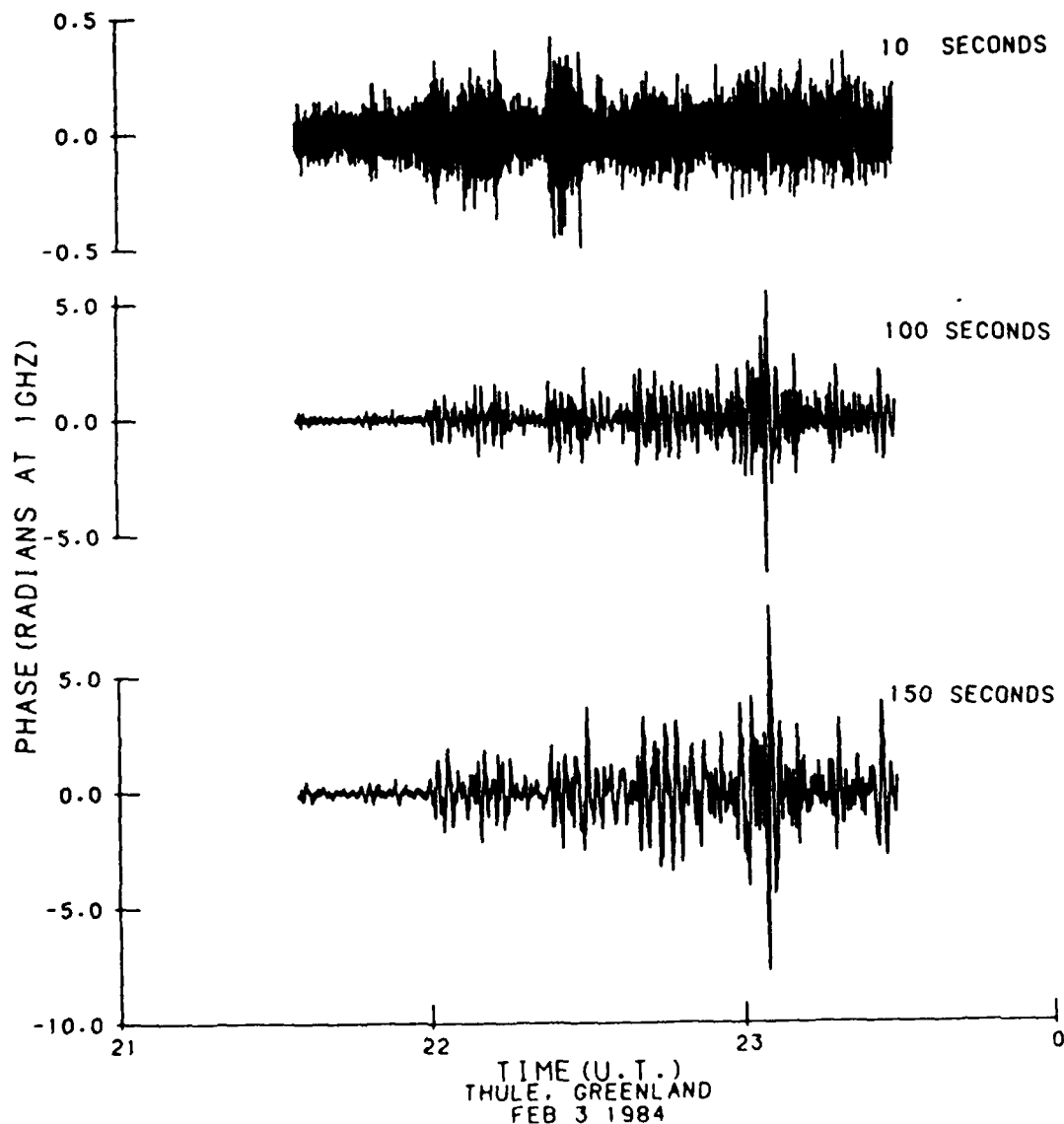d 150 seconds. Note that one of the largest phase deviations seen at the longer two detrend intervals completely disappears when the shortest detrend interval of 10 seconds is used.

With the relatively slow velocity of the GPS satellites through the ionosphere most of the phase excursions from a linear detrend are produced by the movement of irrregular ionization structure through the viewing direction to the satellite. When the shortest detrend interval of ten seconds is used the size of the ionospheric structure responsible for the residual phase observed is similiar to the less than one kilometer size irregularities responsible for amplitude scintillations. The longer detrend intervals, on the other hand, depict the larger scale changes in background TEC which occur with time scales fast enough for them to be called "phase scintillation" by most workers. The use of the dual frequencies on the GPS satellites allows us to record ionospheric phase changes for periods as long as the total satellite viewing time over our station, which is a few hours for most satellites, so that any reasonable length of phase detrending interval can be used depending upon the scale size of the ionospheric structure which one desires to investigate.

DISCUSSION

The diurnal variation of TEC shows a clear minimum during the predawn period and a maximum near local noon. However, the day to day variability in TEC is very large. Because of the rapid time changes seen in the enhancements of TEC which occur throughout the day, but are particularly large in the evening and pre-midnight hours, it is tempting to say that those enhancements are due either to direct auroral precipitation or to motion of plasma into the ray path of the GPS satellite being received at the time. If we assume that the enhancements in TEC add directly to the direct solar produced TEC, which should be small in the winter polar cap ionosphere, we can then consider that the direct solar produced TEC is represented approximately by the minima of the curves shown in figure 3. The enhancements above our assumed level of solar produced ionization then are truly large. For instance, the enhancements in TEC which occur near 21 hours U.T., which range up to 24×10^{16} el/m^2 represent at least a several hundred percent increase, or approximately 21×10^{16} el/m^2, above the minimum value of TEC for 21 hours. For comparison purposes the dirunal maximum values of equivalent vertical TEC measured at Hamilton, MA (42.6°N.) did not exceed 22×10^{16} el/m^2 at any time during this same 8 day period.

[8]Basu, et. al., (1983) using a reasonable value for the flux into the auroral region estimated an order of magnitude time of 700 seconds necessary to increase TEC by 10^{17} el/m^2. We therefore cannot immediately rule out direct production from particle precipitation in all cases, as many of our observed increases in TEC occur over that approximate time interval. However, all-sky images of 6300Å emission made by [9]Weber, et. al. (1984) and by [10]Buchau, et. al. (1983) have shown that large scale patches of plasma drift in the anti-sunward direction across the polar cap during magnetically disturbed periods.

If we assume that the ten minute periodic TEC enhancements are not locally produced, but drift through our ray path with a velocity of from 250 to 700 m/sec, typical of the velocities seen by [10]Buchau, et. al., (1983) in the polar cap during disturbed periods, then we obtain scale sizes for these TEC enhancements between 150 to over 400 km. These enhancements are certainly large enough to be seen as individual patches with the resolution of all-sky optical imaging systems. [9]Weber, et. al., (1984) reported on large scale plasma patches of size 800-1000 km in horizontal extent drifting in the anti-sunward direction in the polar cap during a moderately disturbed period.

The phase scintillation illustrated in figure 6, is referenced to a standard frequency of 1 GHz, which we propose should be a standard frequency for researchers to reference their phase scintillation results. When we compare our phase scintillation results obtained in the polar cap with those of [8]Basu, et. al., (1983), taken looking through the southern edge of the auroral region from Goose Bay, Labrador using similiar detrend intervals, we find good agreement. They showed phase fluctuations of a few radians, referenced to 1 GHz, in general agreement with our results.

The periods of enhanced phase scintillation we observed with the longer detrend times did not generally agree with observations of weak amplitude scintillation in individual cases, or with the times of individual TEC enhancements. There was general overall agreement, however, between the overall occurrence of enhanced phase scintillation and observable amplitude scintillation during the periods when the TEC was showing large variability.

CONCLUSIONS

Signals from the GPS satellites have been used to make the first absolute TEC and L-band amplitude and phase scintillation measurements of the polar cap ionosphere. TEC enhancements from the assumed solar controlled TEC background were very large and were likely due to ionization produced elsewhere and convected over the polar cap. Amplitude scintillation generally occurs during periods of TEC enhancements with a preference for scintillation to occur on the negative gradients of the large TEC enhancements. Ionospheric measurements using the dual frequency carrier and modulation transmissions of the GPS satellites can be used to greatly improve our understanding of the physical processes which govern transionospheric propagation in the polar cap ionosphere.

REFERENCES

1. Mendillo, M. and J.A. Klobuchar, "Low elevation angle measurements of total electron content taken from Thule, Greenland", AFCRL-TR-73-0098, No. 257, 1973, AD762481, available from National Technical Information Service (NTIS), 5285 Port Royal Road, Springfield, VA 22151.

2. Aarons, Jules, "Global morphology of ionospheric scintillations", Proceedings of the IEEE, 70, No. 4, 360-378, 1982.

3. Szuszczewicz, E.P., P. Rodriguez, M. Singh and S. Mango, "Ionospheric irregularities and their potential impact on synthetic aperture radars", Radio Sci., 18, No. 5, 765-774, 1983.

4. Parkinson, Bradford W. and Stephen W. Gilbert, "NAVSTAR: Global positioning system - Ten years later", Proceedings of the IEEE, 71, No. 10, 1177-1186, 1983.

5. Rino, C.L., M.D. Cousins and J.A. Klobuchar, "Amplitude and phase scintillation measurements using the Global Positioning system", in Effect of the Ionosphere on Radiowave Systems, J.M. Goodman, editor, U.S. Government Printing Office, Wash. D.C., 1981.

6. de Mendonca, Fernando, "Ionospheric studies with the differential Doppler technique", in Radio Astronomical and Satellite Studies of the Atmosphere, J. Aarons, editor, North Holland Publishing Co. - Amsterdam, 1963.

7. Feldstein, Y.I. and G.V. Starkov, "Dynamics of auroral belt and polar geomagnetic disturbances", Planet. Space Sci., 15, 209-229, 1967.

8. Basu, Sunanda, Eileen MacKenzie, Santimay Basu, H.C. Carlson, D.A. Hardy, F.J. Rich, and R.C. Livingston, "Coordinated measurements of low-energy electron precipitation and scintillations/TEC in the auroral oval", Radio Sci., 18, No. 6, 1151-1165, 1983.

9. Weber, E.J., J. Buchau, J.G. Moore, J.R. Sharber, R.C. Livingston, J.D. Winningham and B.W. Reinisch, "F layer ionization patches in the polar cap", J. Geophys. Res., 89, No. A3, 1683-1694, 1984.

10. Buchau, J., B.W. Reinisch, E.J. Weber, and J.G. Moore, "Structure and dynamics of the winter polar cap F region", Radio Sci., 18, No. 6, 995-1010, 1983.

DISCUSSION

R.A.Greenwald, US

What is the short wavelength resolution of the TEC measurements (small scale size)? Why aren't these measurements of the same structures as the longer wavelength structures measured with the scintillation technique?

Author's Reply

With the combination of both amplitude and phase scintillation we can measure irregularity scale sizes from a few hundred metres to several hundreds of kilometres.

E.J.Fremouw, US

The fact that you observe intensity scintillation predominantly on the trailing edge of the TEC features is just what one would expect from the ExB instability. The fact that it is better correlated with the TEC structure than is phase scintillation is interesting in view of recent NRL suggestions of an outerscale cutoff for ExB in the presence of finite layer thickness. I think this is a point worth pursuing.

Author's Reply

Our initial result is preliminary as it is based upon a very limited data set. We, of course, intend to pursue this work further.

C.L.Rino, US

Dr Fremouw made a comment regarding a long wavelength cutoff of the ExB instability that would restrict growth above 1 km based on NRL theory. The cutoff is well known, but it remains very uncertain what its precise nature or impact is.

Author's Reply

One of the major advantages of using signals from the GPS satellites is that we can make simultaneous measurements of amplitude and phase scintillations using relatively slowly moving satellites, thereby observing irregularities covering a wide range of wavelengths.

A.Rodger, UK

There is obviously a strong diurnal variation in the occurrence of the 300 km scale size irregularities. Is this consistent with a source mechanism in the cusp when Thule is effectively downstream from the cusp?

Author's Reply

We believe the source of the large TEC enhancements is the mid-day midlatitude ionosphere with resulting convection reaching the polar cap in the pre-midnight time sector.

F Region Electron Density Irregularity Spectra Near Auroral Acceleration and Shear Regions

SUNANDA BASU, SANTIMAY BASU, AND E. MACKENZIE

Emmanuel College

W. R. COLEY AND W. B. HANSON

University of Texas at Dallas

C. S. LIN

Southwest Research Institute

Spectral characteristics of auroral F region irregularities were studied by the use of high-resolution (~35 m) density measurements made by the retarding potential analyzer (RPA) on board the Atmosphere Explorer D (AE-D) satellite during two orbits when the satellite was traversing the high-latitude ionosphere in the evening sector. Coordinated DMSP passes provided synoptic coverage of auroral activity. The auroral energy input was estimated by intergrating the low-energy electron (LEE) data on AE-D. It was found that the one-dimensional in situ spectral index (p_1) of the irregularities at scale lengths of < 1 km showed considerable steepening in regions of large auroral acceleration events with p_1 values of ~ -3. This is interpreted as resulting from the effects of E region conductivity on the F region irregularity structure. The regions in between the precipitation structures, where presumably the E region conductivity was small, were generally associated with large shears in the horizontal E-W drifts and large velocities, as measured by the ion drift meter on board AE-D. The maximum drifts measured were ~2 km s^{-1}, corresponding to an electric field of 100 mV m^{-1}. The large-velocity regions were also associated with substantial ion heating and electron density depletions. The largest shear magnitudes observed were ~ 80 m s^{-1} km^{-1}, and the shear gradient scale lengths were ~ 10 km, which was approximately the resolution of the ion drift meter data set used. The spectral characteristics of irregularities in the large, variable flow regions were very different, with p_1 being ~ -1. Since these regions were also associated with the largest irregularity amplitudes, it seemed probable that either the velocity shears or, alternatively, the large velocities provided a source of irregularities in the auroral F region ionosphere. Current work on plasma instabilities related to velocity shears and two-dimensional fluid turbulence is briefly summarized and critically compared to the findings of the present study.

1. INTRODUCTION

The existence of plasma density irregularities throughout the high-latitude environment has been well established by means of a variety of techniques [*Basu et al.*, 1983a; *Fejer and Kelley*, 1980, and references therein]. However, very few measurements are available regarding the spectral characteristics of these irregularities since the pioneering study of *Dyson et al.* [1974] established their power law nature. *Phelps and Sagalyn* [1976] used high-latitude topside ionospheric data from ISIS 1 to show that most spectra analyzed by them could be fit by a simple power law with a one-dimensional spectral index ranging between -1.5 and -2.5.

At equatorial latitudes, high-resolution in situ data obtained both from rockets and from satellites (mostly Atmosphere Explorer E) showed a two-component irregularity spectrum which was found to be associated with intense scintillation events [*Rino et al.*, 1981; *Basu et al.*, 1983b]. Indeed, *Kelley et al.* [1982] found a multicomponent spectrum with the spectral index steepening considerably for scale lengths of ~ 10 m. On the other hand, *Valladares et al.* [1983] have identified a band-limited spectrum associated with bottomside irregularities at low latitudes. It is the object of this paper to make a similar intensive study of high-resolution (~ 35 m) electron density irregularity spectra from Atmosphere Explorer D (AE-D) data in the auroral environment to determine whether the type of particle precipitation or the nature of the electric field variation leaves any specific signatures on the irregularity spectra. This should help to isolate the types of instabilities operating in localized regions of the auroral environment. The fact that high-latitude irregularities are omnipresent over vast regions of space certainly argues against a unique instability mechanism operating everywhere [*Fejer and Kelley*, 1980]. In addition, it has been shown recently that a conducting E layer at high latitudes significantly reduces the lifetime of small-scale F region irregularities [*Vickrey and Kelley*, 1982]. This indicates that F region irregularities which are either generated in or convected into regions where the E layer is conducting could have a spectrum very different from that obtained in regions where no precipitation is present.

In the following section we present a brief description of the instrumentation used to obtain the data sets discussed in the paper. In the next two sections we present a host of different types of data from two AE-D passes over the auroral zone, which allows us to study the irregularity spectra and define the sources of energy input into the regions from which such spectra are obtained. We were also fortunate enough to have DMSP conjunctions which allowed us to determine the type of auroral luminosity associated with the particle precipitation. In the last section we present some discussion regarding specific plasma instability and velocity turbulence mechanisms that have been postulated in the literature for irregu-
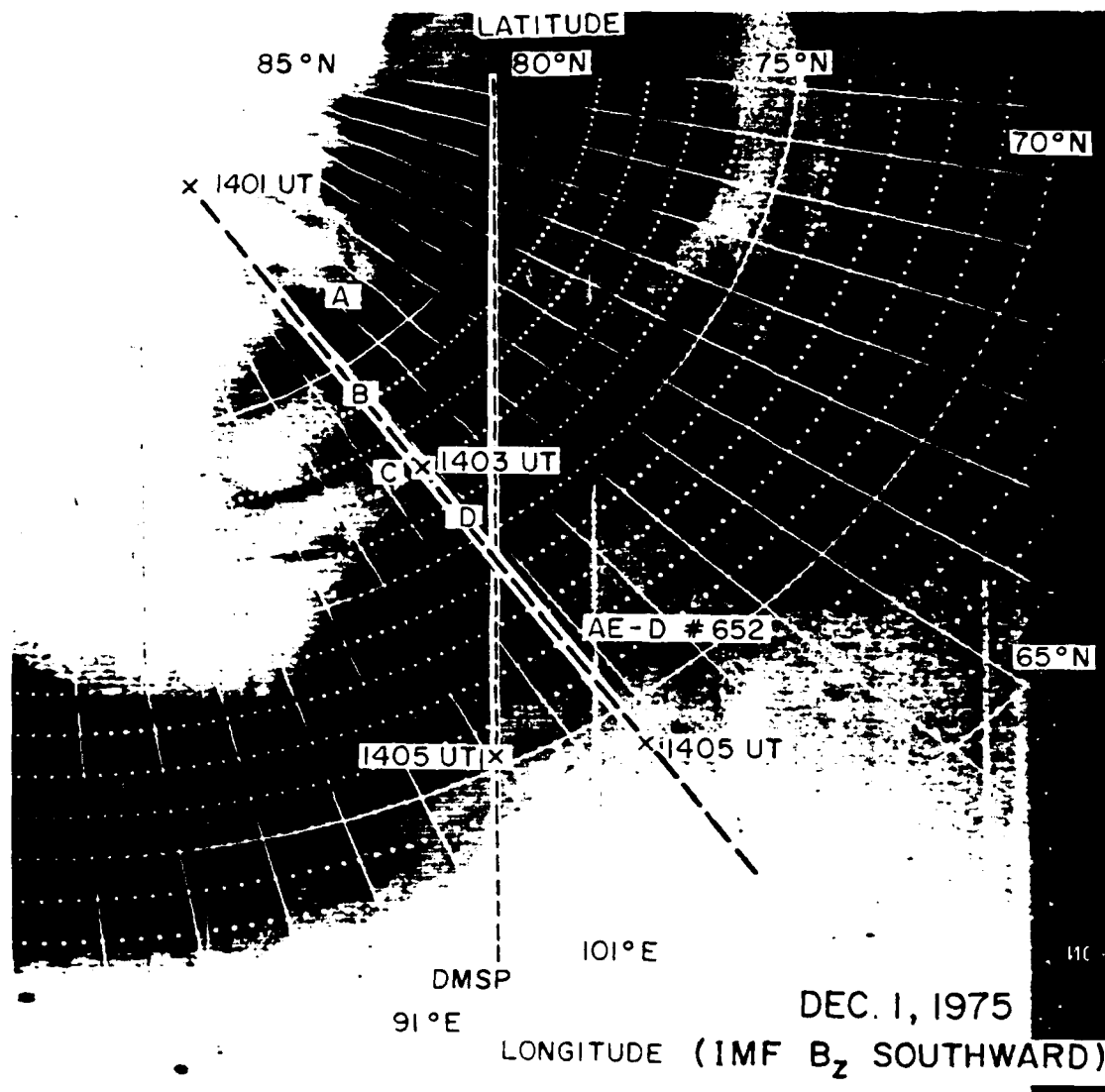
47

Fig. 1. AE-D orbit 652 superimposed on DMSP photograph taken on December 1, 1975, showing an active auroral display during IMF B_z southward conditions. The DMSP photograph is a negative, so that the bright arcs are represented by the dark features. Letters A, B, C, and D identify the gaps in the particle precipitation region on orbit 652 and are also shown in Figure 2.

larity generation but which either do or do not fit the AE-D observations.

2. INSTRUMENTATION ON AE-D AND DMSP

The AE-D spacecraft was launched in October 1975 into a 90° inclination orbit with initial perigee and apogee of 150 and 4000 km, respectively. The AE-D data presented here are for two orbits, one obtained on December 1, 1975, and the other on November 5, 1975, when the satellite was traversing the F region through the evening sector of the auroral oval in the northern hemisphere. The data sets on those orbits that have been used for the purposes of this paper were obtained from the retarding potential analyzer (RPA), the ion drift meter (IDM), the low-energy electron experiment (LEE), and the photoelectron spectrometer (PES).

The major focus of this paper is on the high-resolution ion density measurements made by the RPA [Hanson et al., 1973] at intervals of 4.45 ms (i.e., with a spatial resolution of ~35 m). These data are then used to determine the root mean square irregularity amplitude, $\Delta N/N$, over 3 s of data and also to compute the power spectrum of the 3 s sample. The RPA also provided estimates of the ion temperature T_i and the component of the drift along the orbital track (i.e., N-S) at approximately 6-s intervals. The IDM provided simultaneous measurements of the E-W component of ion drift perpendicular to the satellite velocity vector with a resolution of approximately 1.3 s or about 10 km along the spacecraft orbit, with a sensitivity of ~20 m s^{-1} [Hanson and Heelis, 1975]. The integration of the LEE data [Hoffman et al., 1973] provided a measure of the energy deposited into the ionosphere with 1-s resolution.

The energy deposition rate R was computed in a manner similar to that done by Lin and Hoffman [1982a] as the total electron energy flux contained within the local loss cone z_0,

$$R = 2\pi S \int dE \int_0^{z_0} dz \sin z J(E, z) E \qquad (1)$$

where $S = 1.6 \times 10^{-9}$ erg (keV)$^{-1}$ is the conversion factor,
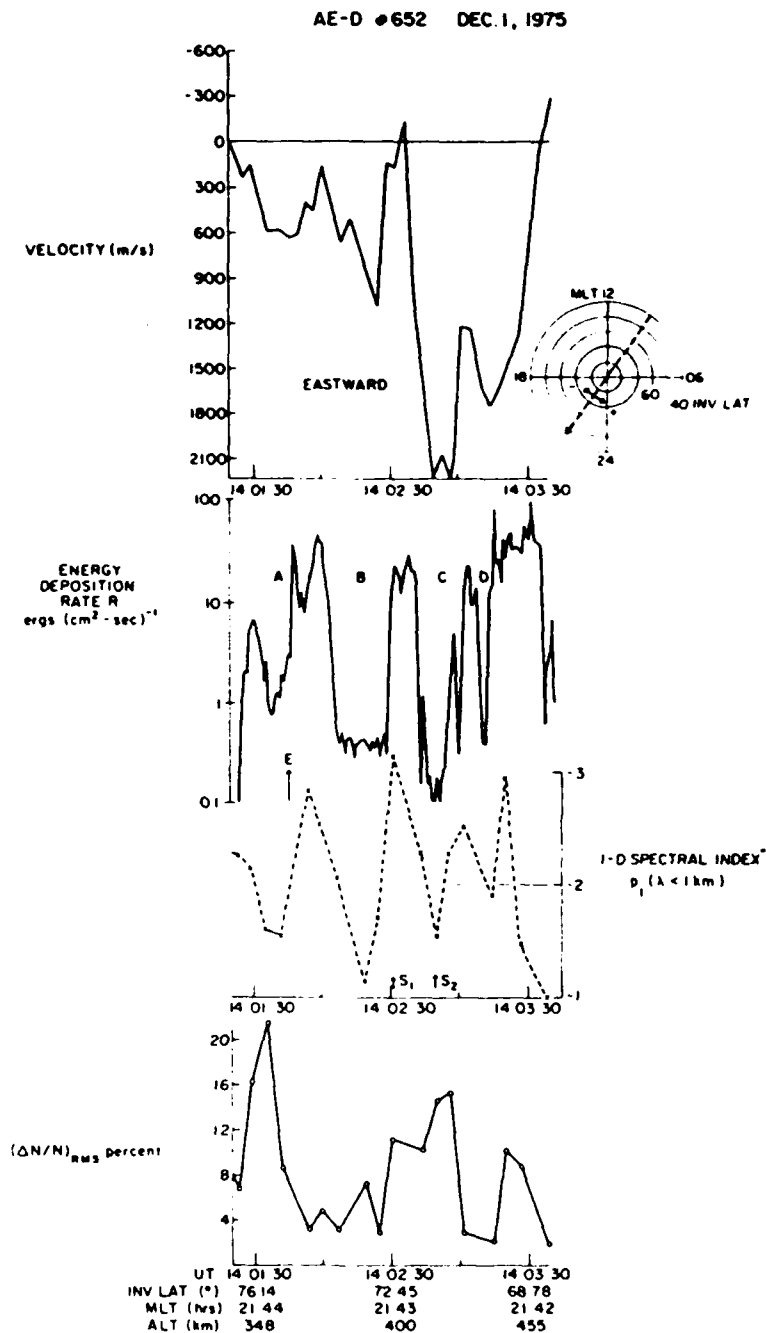
48

Fig. 2. AE-D orbit 652 data between 1401:30 and 1403:30 UT on December 1, 1975, showing the E-W velocity from the IDM, the energy deposition rate R obtained from the LEE experiemnt, the one-dimensional spectral index for scale lengths less than 1 km, and the irregularity amplitude $(\Delta N/N)_{RMS}$ percent, the latter two obtained from the RPA. Note steep spectral index in precipitation regions and shallow spectral index together with large irregularity amplitude in large structured flow regions. The orbit has been plotted on a magnetic local time-invariant latitude coordinate system to help in the interpretation of the drift measurements. The arrow marked E indicates the mean time of two LEE spectra shown in Figure 5 and the two arrows marked S_1 and S_2 indicate the times for which density spectra have been shown in Figures 4a and 4b.

and R is in units of ergs $(cm^2 s)^{-1}$. The integration is computed from 0 to α_0 for the pitch angle and from 200 eV to 25 keV for the energy of the LEE detectors. At the AE-D altitude, α_0 is approximately 67 in the auroral zone. The particle flux $J(E, \alpha)$ was measured simultaneously at two pitch angles

by two energy-stepped detectors, and the flux was linearly interpolated for all the pitch angles within α_0.

The PES experiment consisted of two spectrometers in the energy range between 2 and 500 eV that measured electrons at angles of ~20 and 160 [Doering et al., 1973]. The instru-

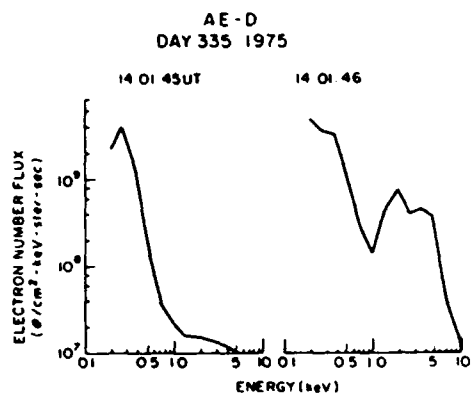AE-D
DAY 335 1975

14 01 45UT   14 01 46

Fig. 3. LEE spectrum obtained at 1401.45 UT showing no acceleration and that obtained at 1401.46 UT showing particle acceleration

ment mode was such that for one AE-D pass (652) the detector was looking up continuously (i.e., pitch angle 20) while making one 16-point spectrum per 0.25 s. For the other orbit (344) the detector was looking continuously downward (i.e., pitch angle 160).

The AE-D orbits fortunately occurred at times when coordinated observations of the visual aurora were possible with the U.S. Air Force DMSP (Defense Meteorological Satellite Program) satellites, thus providing a synoptic view of the auroral behavior in the vicinity of the AE-D orbits. These particular DMSP satellites were in dawn-dusk sun-synchronous polar orbits with nominal characteristics of 830-km altitude, 98.75 inclination, and 101.5-min period. Images of the aurora are produced by a line-scanning radiometer which builds up pictures by repetitive scanning (~1.8 Hz) across the earth along the orbital track. *Eather* [1979] has shown that the block 5B/5C DMSP satellites, from which these two orbits were obtained, can detect auroral forms of intensities of ~170 R of 5577 O I.

3. OBSERVATIONS

3.1 AE-D Orbit 652

In Figure 1 we show the track of AE-D across the auroral forms observed by the DMSP satellite. The DMSP picture shown is a negative, so that the dark areas represent visual aurora. The B_z component of the interplanetary magnetic field (IMF) was large and southward (~ -3 γ) during the pass and during the previous hour, and a rather dramatic auroral display is seen as a result. It may be noted that the temporal and spatial overlap of the DMSP satellite coverage and the AE-D orbit are excellent, both satellites approaching the center of the diagram at 1403 UT. A grid of geographic latitude and longtiude appropriate for a 100-km altitude level is superimposed on the DMSP photograph.

The data obtained from some of the different instruments on AE-D between 1401:30 and 1403:30 UT when it was traversing the auroral forms are shown in Figure 2. The top panel shows the variation of the E-W component of the ion drift obtained from the IDM. The direction of the drifts can be best understood on the basis of the polar plot of invariant latitude and magnetic local time (MLT) which shows orbit 652 coming into the evening auroral oval from the dayside polar

cap. The satellite altitude and magnetic coordinates are given at the bottom of Figure 2. Positive drifts on the nightside refer to eastward, or toward dawn, drifts, whereas the negative drifts signify the opposite directions. While corotation velocities of the order of +200 m s⁻¹ have not been subtracted from the data, it is quite clear that large variations of eastward drift giving rise to large shears in the drift velocity are occurring within the auroral oval. The largest drift structure just prior to 1403 UT corresponds to a southward electric field of ~100 mV m⁻¹.

The second panel shows the variation of the energy deposition rate R (defined in section 2) of the 0.2- to 25-keV electrons as a function of position along the satellite track. At least five distinct precipitation regions with energy of >5 ergs (cm² s)⁻¹ are observed. The gaps in between the precipitation regions marked A, B, C and D are also identified on the DMSP photograph of the auroral arc system. It is important to note that the large shears in the horizontal drift and large convective flows occur in between particle precipitation regions, as was noted earlier by *Burch et al* [1976a]. The major particle precipitation regions are all associated with visual auroras and may be identified with inverted V-type particle precipitation and auroral electron acceleration [*Burch et al*, 1976a; *Lin and Hoffman*, 1982b]. To prove that auroral acceleration was indeed occurring, we exhibit two consecutive spectra of electron energy at 1401.45 and 1401.46 UT in Figure 3, which shows an unaccelerated spectrum at 1401.45 UT with acceleration over the range 2.5 keV appearing in the next second. The mean time of these two spectra is identified on the second panel of Figure 2 by an arrow marked E. The accelerated spectrum of 1401.46 UT is typical of a 5-s interval which, using the computations of *Lin and Hoffman* [1982a], gave rise to 10 kR of 5577-Å emission and can thus be identified with a visual arc. A narrow but very bright arc is clearly visible in the DMSP photograph at that location.

The most important aspect of our study is embodied in the last two panels of Figure 2, in which we show the rms irregularity amplitude (fourth panel) computed over 3 s of high-resolution RPA density data and the one-dimensional spectral index of the (ΔN/N) spectrum (third panel). The spectral index shows a marked steepening (~ -3) within auroral precipitation/acceleration regions, thereby indicating most probably the effect of a conducting E region on the structure of F region irregularities through an enhancement of the cross-field diffusion, as discussed by *Vickrey and Kelley* [1982]. Even more remarkable are the rather shallow spectra with spectral index values of ~ -1 in regions which are in between precipitation regions. These regions are associated with large structured horizontal drifts in the E-W direction. An examination of the irregularity amplitude shows that these large structured velocity regions are also usually associated with large irregularity amplitudes of >10%. The strong precipitation regions, on the other hand, while invariably identified by steep stpectra, are not always associated with large irregularity amplitudes. Further discussion of these features will be given in section 4.

In order to study closely the differences in spectral characteristics we show in Figures 4a and 4b the high-resolution irregularity waveforms and their spectra obtained in the precipitation (1402:31 UT) and large-velocity (1402:50 UT) regions, respectively. These times are identified by two arrows marked S_1 and S_2 on the third panel of Figure 2. The waveform in the precipitation region, which is also associated with auroral acceleration, shown in a 3-s sample of the high-resolution density data on the lower panel of Figure 4a exhib-
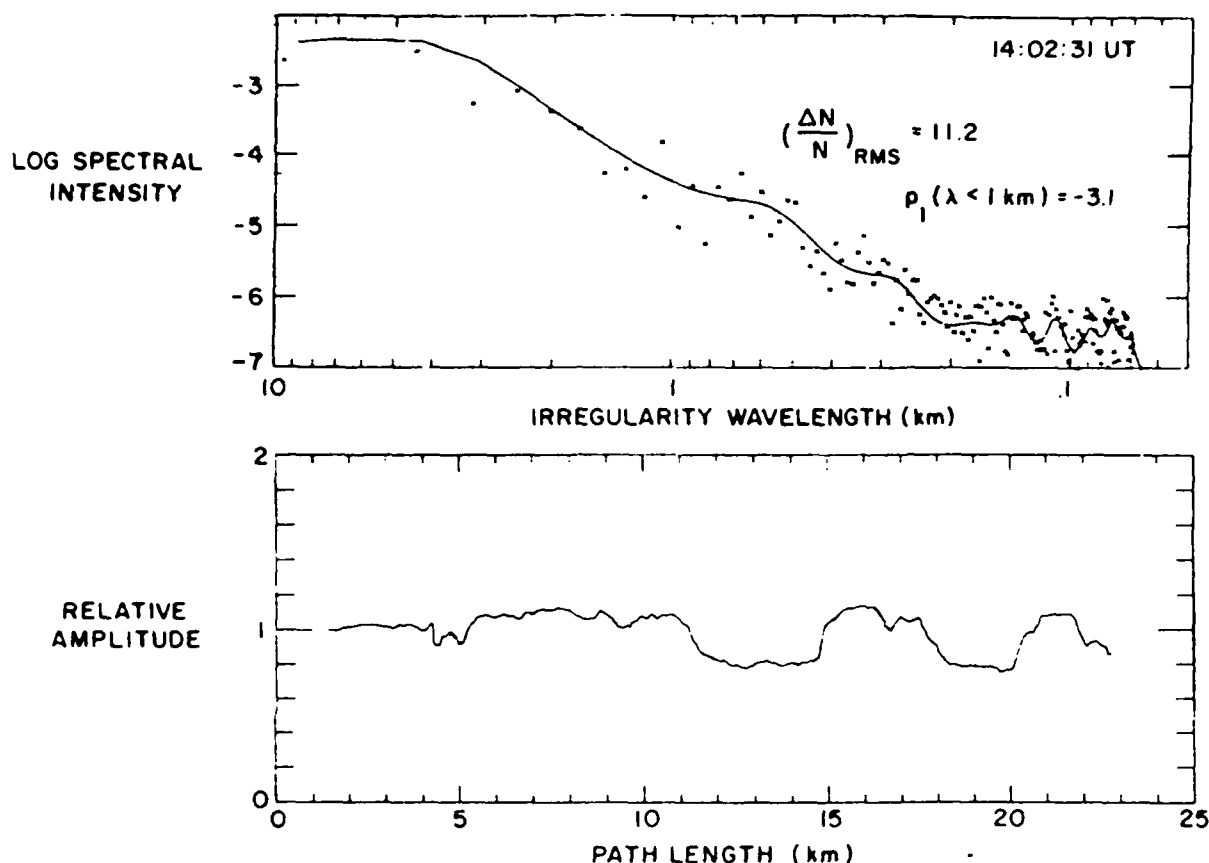
50

Fig 4*a* The lower panel shows 3-s sample of high-resolution RPA data of relative amplitudes attained on AE-D orbit 652 near the point marked S, on Figure 2. The irregularity amplitude $(\Delta N/N)_{RMS} = 11.2\%$. The upper panel shows a power spectrum of the linearly detrended data corresponding to the 3-s sample shown below obtained by the FFT (crosses) and maximum entropy (solid lines) techniques. Note that this sample, obtained within an auroral acceleration region, has little high-frequency structure in the density, leading to a steep spectrum with one-dimensional spectral index $p_1 = -3.1$ for scale lengths of < 1 km

its much less high-frequency structure than that observed in the corresponding panel of Figure 4*b*, even though both are plotted on the same relative amplitude scale and have similar irregularity amplitudes. This difference in irregularity structure is reflected in the respective spectra which are shown in the top panels of each diagram. To obtain these spectra, the respective samples were linearly detrended, and the zero mean time series of positive and negative fluctuations, ΔN, from the trend line were obtained. The percentage fluctuations of $\Delta N/N$, N being derived from the trend line, were subjected to spectral analysis by both the fast Fourier transform (FFT) and the maximum entropy (MEM) methods. The FFT program was the same as the one used earlier by Dyson et al. [1974]. The spectra were normalized such that the integral of the fluctuation power $\int S(f) \, df$ over the observed frequency range equals the variance of the original time series of $\Delta N/N$. The frequency (f) scale was converted to irregularity scale length (λ) by using the relation $\lambda = v/f$, where v is the satellite velocity. In view of its geophysical importance we shall illustrate the power spectra in terms of irregularity wavelength. The crosses indicate the spectral estimates obtained by the FFT technique, and the solid line represents the MEM spectrum. It should be kept in mind that these spectra, obtained from in situ data, are one-dimensional power spectra of $\Delta N/N$.

The spectrum obtained in the auroral acceleration region is reminiscent of the spectrum observed by AE-E within a topside equatorial bubble [Basu et al., 1983*b*] with a flat spectral index at long scale lengths, > 5 km, and a steep spectral index of −3.5 at scale lengths of < 1 km. The large-velocity region spectrum, on the other hand, has a very shallow slope, with the linear least squares fit to scale lengths of < 1 km showing a slope of − 1.5. To focus on the differences of the two spectral classes, we superimpose the MEM spectrum from Figure 4*a* on that from Figure 4*b* in Figure 4*c*. It shows that even though the spectral intensity is the same at 500 m in both cases, the spectral intensities at shorter scale lengths are almost 1 order of magnitude greater in the large-velocity region all the way down to 70 m. It may be noted that the irregularity amplitudes of the samples are approximately the same. This signifies that the power spectral densities at the largest scale lengths (∼10 km) of both samples are almost equal. These differences in spectral behavior should have important ramifications for VHF/UHF scintillations and their frequency dependence, as will be discussed in the last section

To obtain further information on the structured convective flow regions, we studied the ambient density N, from the IDM and the ram component of the velocity and T, from the RPA for orbit 652 as well as the very low energy electron data from
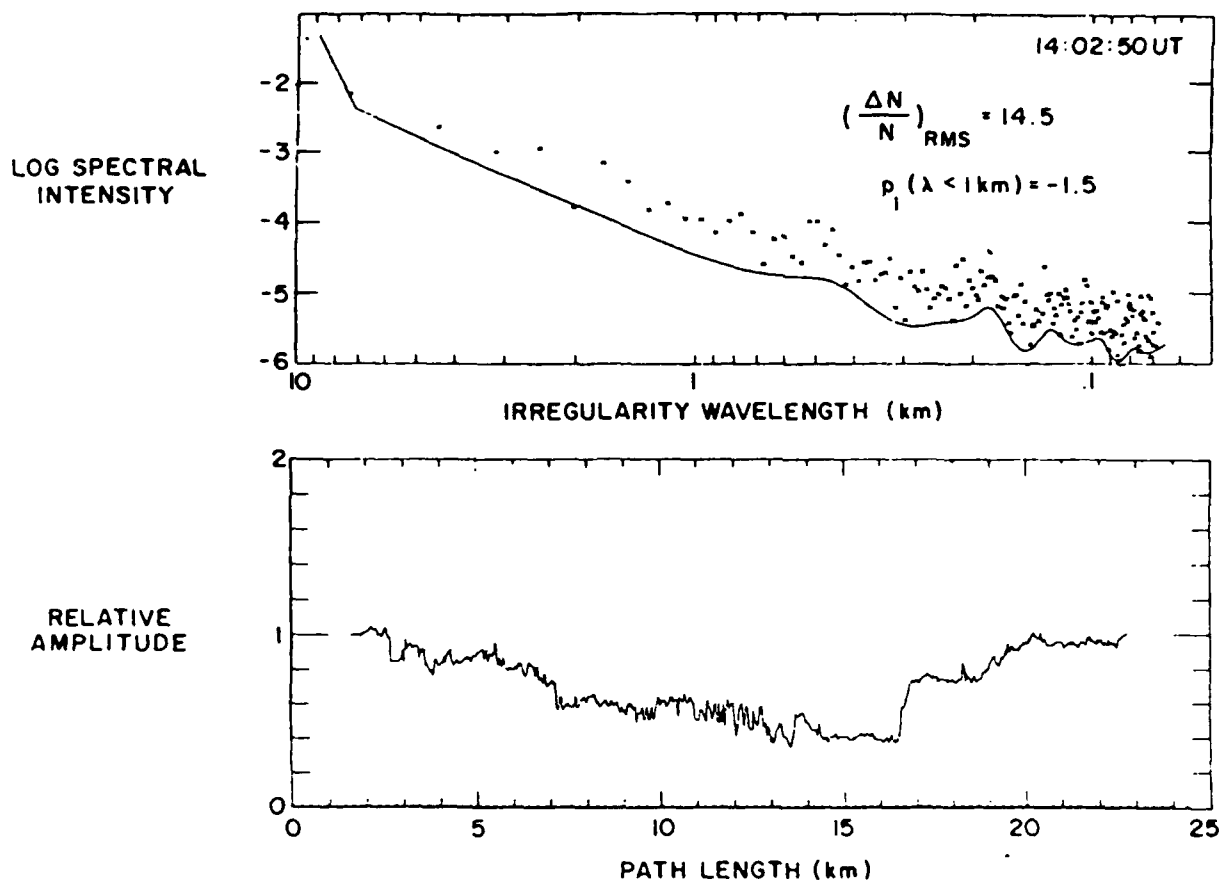
Fig. 4b Same as Figure 4a except that the data are obtained near point S₂ in Figure 2. The irregularity amplitude (ΔN/N)ʀᴍꜱ = 14.5%. Note that this sample, obtained within a large structured flow region, has considerable high-frequency structure in the density, leading to a shallow spectrum with one-dimensional spectral index p_1 = −1.5 for scale lengths of <1 km.

the PES In order to facilitate comparisons with Figure 2 we have repeated in Figure 5 the top panel of ion drifts from Figure 2 and have added the drift velocity data obtained by the RPA along the satellite orbit. Positive drift indicates motion toward the spacecraft, and negative drift away from the spacecraft. The corresponding N_i data are shown in the second panel, T_i data in the third panel, and the energy-time spectrogram from the PES instrument in the fourth panel. The drift velocity measured by the RPA is obtained along the same direction as the N_i measurements. It is interesting to note that the component of the drift along the satellite orbit (which is mostly N-S) is quite small in regions where large E-W velocities are observed. The only region where both the N-S and the E-W components of drift are approximately equal in magnitude is that near 1401:45 UT, probably a region of rotational discontinuity [Heelis et al., 1980] between the general antisunward flow over the polar cap and the sunward and large eastward flows seen in the auroral oval.

The N_i data are plotted only once per half second, even though much higher resolution is available from the IDM. There is a reduction of N_i associated with each high-velocity region. This is probably due to the increased ion temperature, as seen in the third panel, associated with the large electric fields and a consequent increase of the charge exchange reaction rate of

$$O^+ + N_2 \rightarrow NO^+ + N$$

The NO⁺ recombines rapidly, and thus the total ion (electron) density decreases [Schunk et al., 1976]. The ion temperature has a spectacular increase in excess of 4000 K in association with ion drifts of ~2 km s⁻¹. However, as discussed by St. Maurice and Torr [1978], when ion convection velocities are so large, an "effective" temperature (which can be considerably smaller than the measured ion temperature) has to be used in computing the above reaction rate.

The PES spectrum shown in the fourth panel of Figure 5 was obtained with the spectrometer pointing upward (pitch angle 20), so that upgoing particles are not sensed. What is
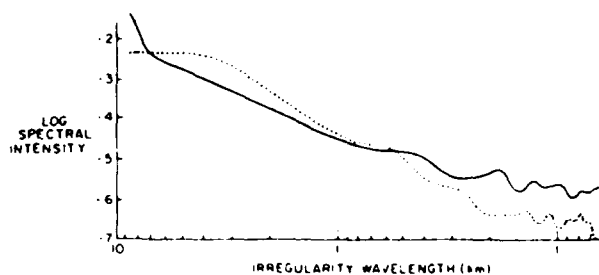

Fig 4c Superposition of the MEM spectra from Figure 4a (solid line) and Figure 4b (dashed line) showing much larger power spectral densities at scale lengths of < 500 m in the spectrum obtained within a large structured flow region

observed consistently is an almost total lack of precipitating particles even at these low energies in the regions of shear flow. The four gaps in the LEE precipitation marked A, B, C, and D on Figure 2 can be clearly identified in the PES spectrum, with A becoming a very narrow region between two very intense precipitation events and B, C, and D being more comparable to the gap widths in the LEE data. It is indeed interesting to note that all particles with energies as low as 2 eV, the threshold of the PES instrument, are generally absent in the regions which we have identified earlier to be associated with large southward electric fields and rapid variations in their magnitude. Thus it is probably realistic to assume that the gap regions are threaded by magnetic field lines which terminate in relatively nonconducting E regions.

3.2. Orbit 344

We present a second set of data from AE-D, obtained during IMF B_z northward conditions, when a similar relationship between particle precipitation, large structured convective flow, and electron density spectral behavior was observed, even though the satellite was at much lower altitudes. Figure 6 shows the track of AE-D orbit 344 on November 5, 1975, plotted on the corresponding DMSP photograph. Unfortunately, in this case the DMSP satellite photograph refers to a time that is 5 min after the AE-D pass over the same geographic region. However, in keeping with the northward B_z condition we find a rather quiet auroral display as compared to that shown in Figure 1. The IDM drifts, integrated LEE energy flux, and irregularity amplitude and spectral index plots from the RPA are shown in Figure 7. Again one observes the anticorrelation of the large electric field region with the particle precipitation region and the association of each region with a particular type of spectral index. In particular, there is a rather spectacular westward shear flow region centered at 0811:15 UT which occurs on the equatorward side of the visual aurora. This region is associated with a large irregularity amplitude of 20% and a shallow spectral index of ~ − 1. Within the precipitation region centered at 0811 UT, however, the irregularity amplitude is quite small and the spectral index is − 3.

The LEE spectra obtained at 0811:00 UT and 0811:07 UT, shown in Figure 8, clearly depict the signature of an auroral acceleration region with a secondary peak around 5 keV, although the number fluxes are an order of magnitude lower than the fluxes observed during orbit 652. The total energy deposition is in excess of 10 ergs $(cm^2 \ s)^{-1}$. Thus again we have evidence of steepening of F region irregularity spectra caused by the enhanced cross-field diffusion due to the presence of underlying E region conductivity. On the other hand, the immediately equatorward region has a < 0.1 erg $(cm^2 \ s)^{-1}$ energy deposition rate but a very large irregularity amplitude with shallow spectra, which tends to indicate that the large structured flow region is a strong source of ~ 100-m irregularity scale lengths.

Another interesting oppositely directed spikelike shear flow event is centered around 0810:30 UT, with the precipitation event occurring in the region between the spikes. Such events were studied earlier by Burch et al. [1976b] and were found to occur near the large-scale reversal from sunward to antisunward convection on the nightside. In this case, too, it is probably located at such a boundary, as we shall show in Figure 9, where the ram component of the drift is also plotted. The irregularity amplitude is not as large as one generally
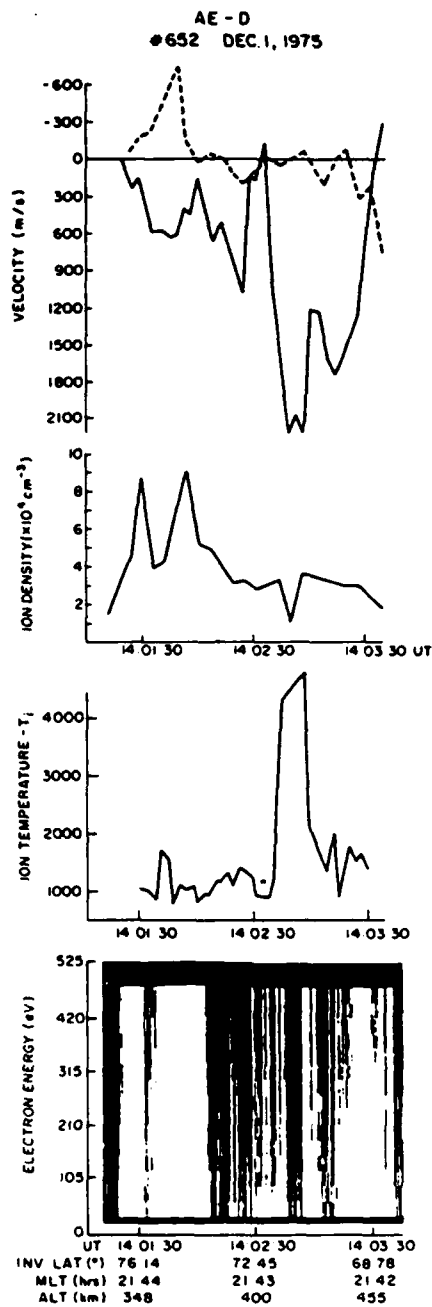

Fig. 5. AE-D orbit 652 data between 1401:30 and 1403:30 UT showing both the E-W drift from the IDM (solid line) and the drift parallel to the satellite velocity from the RPA (dashed line) on the first panel, the ion concentration N_i from the IDM on the second panel, the ion temperature T_i from the RPA on the third panel, and the energy-time spectrogram from the PES on the fourth panel. The PES was looking upward at 20° pitch angle, so that it could sense only the precipitating flux. A large enhancement in T_i is noted in conjunction with a large convective flow region and consequent reduction in N_i.

observes in association with shear flows, and only the eastward directed shear is associated with the characteristic shallow spectrum. It is somewhat relevant to note that no visual feature that coincides with the precipitation region near 0810:30 UT could be identified on the DMSP photo taken 5 min later, so that it must have been a relatively short-lived event.

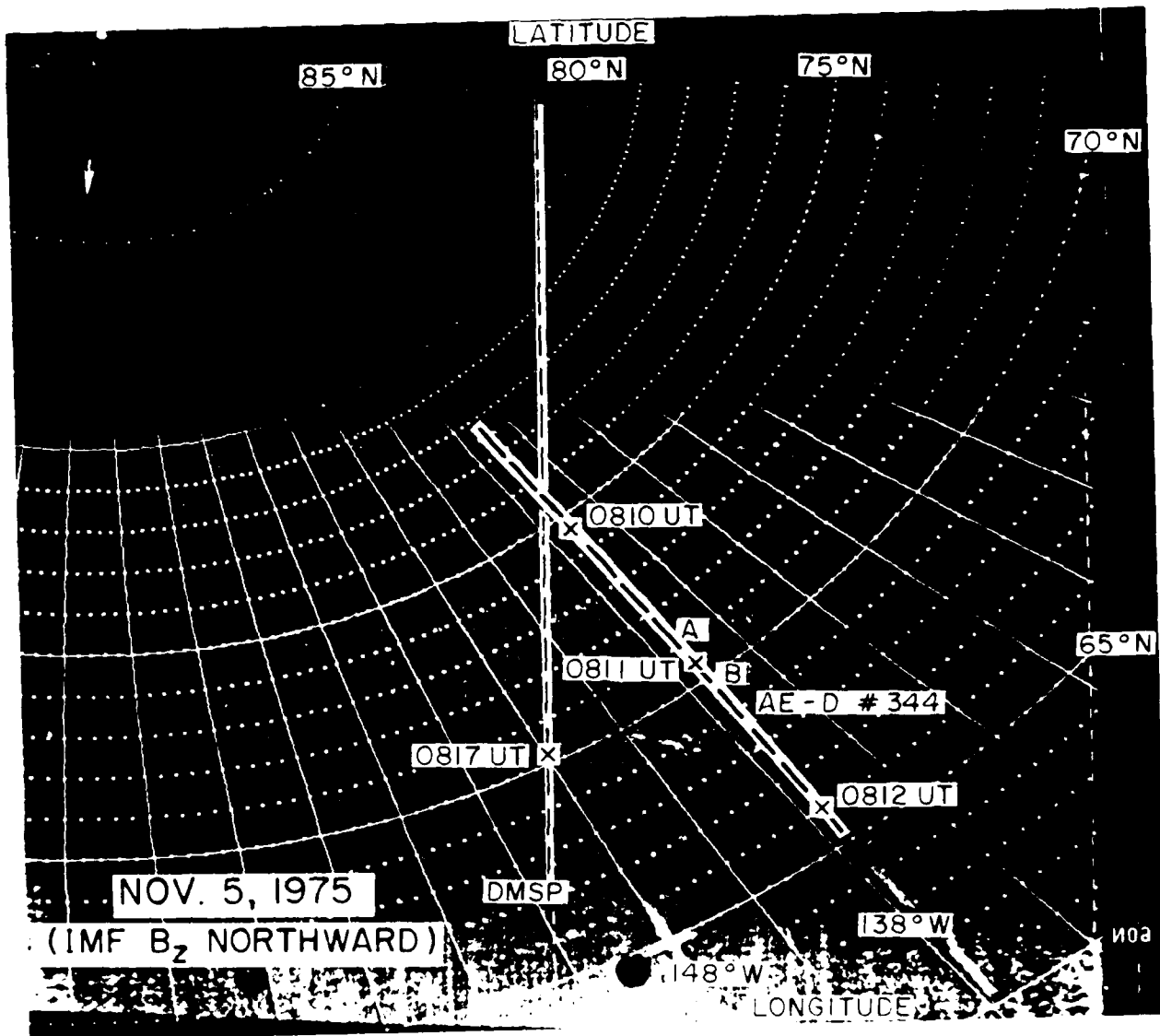In Figure 9 we have plotted the component of the drift

Fig. 6. Same as Figure 1 except for orbit 344 on November 5, 1975, showing quiet auroral behavior during IMF B_z northward conditions. Letters A and B identify the gaps in the particle precipitation region on orbit 344 and are also shown in Figure 7.

along the satellite velocity direction (as well as replotted the E-W velocity measurements). N_e, T_e and energy-time spectrogram from PES for orbit 344 in the same format that was used for orbit 652. Again we find the N-S component of the drift to be less structured than the westward drift. The oppositely directed spikelike E-W flows seem to indicate the boundary between the generally antisunward flows over the polar cap and the generally sunward and westward flow over the auroral oval. The N_e in this low-altitude case provides clear evidence of ionization created by particle precipitation with the energy deposition panel of Figure 7 appearing very similar to the N_e behavior in Figure 9. Thus the depletion in density in high-velocity regions for orbit 344 is probably caused by the absence of a particle source. The absence of a particle source even at the lowest energies can be confirmed from the PES data, where dark bands are seen in association with large structured velocity regions. The important point to note in this case is that the PES was looking downward, so it was measuring only the upgoing fluxes. However, no intensi-

fication of upgoing electron fluxes was observed in conjunction with the spikes in flow velocities, in contrast to the findings obtained by de la Beaujardiere and Heelis [1984]. As on orbit 652, the large flow velocity regions are associated with large enhancements in T_e, even though in this case values of ~ 2000 K are seen rather than values in excess of 4000 K as in the former case.

4. DISCUSSION

The new information obtained from a discussion of the two AE-D orbits has been the association of distinctly different irregularity spectral characteristics of the thermal plasma with auroral acceleration and large structured flow regions. While the auroral acceleration regions were found to produce steep spectra with one-dimensional spectral index values (for $\lambda < 1$ km) of ~ -3, the large flow regions were characterized by very shallow spectra with spectral index values of ~ -1. The steep spectra in acceleration regions are consistent with the work of Vickrey and Kelley [1982], who showed that the rate

5-4

of cross-field plasma diffusion in the F region ionosphere is significantly increased when the magnetic field lines thread a highly conducting E region below. The lifetime of small-scale F region irregularities is thereby reduced, and a steep spectrum is expected within bright auroral arc regions where the E region Pedersen conductivity is quite high. The irregularities observed in such regions may be the result of local processes or may have been convected into such regions. In other words, we do not claim that auroral arcs are always sources of large-
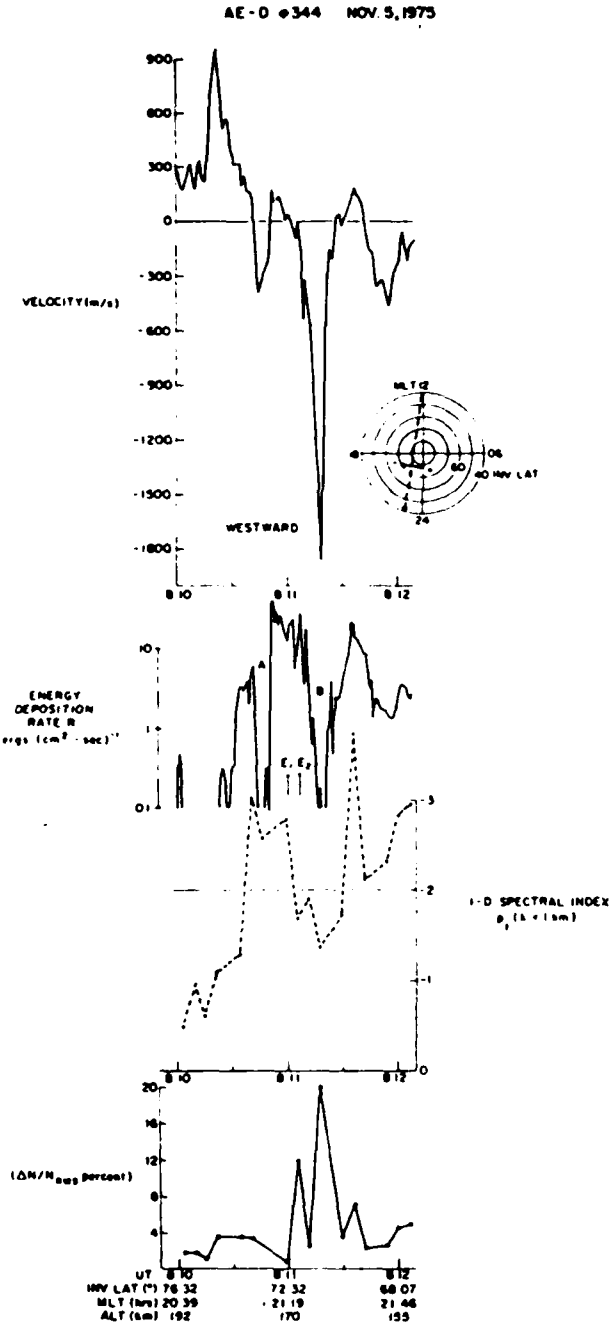
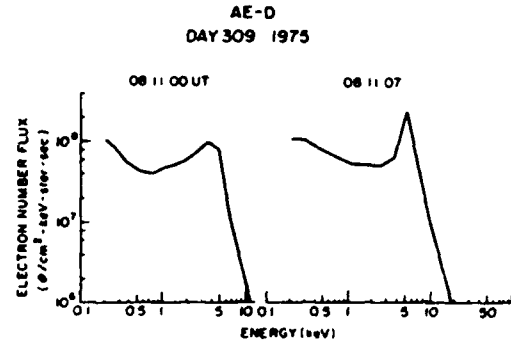

Fig. 8. LEE spectra obtained at 0811:00 and 0811:07 UT, both showing evidence of particle acceleration.

amplitude F region irregularities, since their efficacy as source regions depends on the spectra of the incoming particles and the time history of such precipitation events [Basu et al., 1983a; Muldrew and Vickrey, 1982].

The large structured flow regions, on the other hand, are generally associated with large-amplitude irregularities. In trying to determine a generation mechanism for these irregularities, it is instructive to note that Keskinen and Ossakow [1983a] have studied the nonlinear evolution of equatorward convecting auroral plasma enhancements that initially contain only a N-S density gradient. These plasma enhancements were shown to be unstable and to break up into primary north-south aligned fingerlike structures that themselves contain sharp E-W and N-S density gradients. If these long-wavelength primary irregularities have a component of convection in the E-W direction, then secondary smaller-scale approximately L shell aligned structures could grow on the E-W density gradients of the primary irregularities. Keskinen and Ossakow [1983a] further state that the E-W convection must be of sufficient magnitude in comparison with the N-S convection to prevent velocity shear stabilization [Huba et al., 1983]. In the present situation, the E-W convection is, indeed, much larger than the N-S convection. However, the shallow spectral characteristics of these irregularities do not conform to those obtained by the numerical simulations of Keskinen and Ossakow [1983a].

Our finding of large-amplitude irregularities together with a shallow spectrum implies the existence of large power spectral densities at short scale lengths of ~ 100 m. The fact that in the adjacent precipitation regions there is an order of magnitude reduction of power spectral densities at such scale lengths strongly suggests that either the large velocities themselves or the shears in these velocities provide a source for plasma density irregularities in the F region in this scale length regime. This finding seems to contradict most current analytical work on plasma instabilities, which shows that velocity shears tend to stabilize small-scale irregularity growth in the F region, as briefly mentioned earlier. For instance, Huba et al. [1983], who studied the E × B instability with an inhomogeneous E field, and Guzdar et al. [1982] and Satyanarayana and Ossakow [1984], who considered, respectively, the Rayleigh-Taylor instability and the current convective instability with velocity shears, all come to this same conclusion. However, all the authors above considered a linear theory of the specific instability, while the observations reported here are almost certainly in the nonlinear regime. In a recent review, Keskinen and Ossakow [1983b] stressed the importance of being able to

Fig. 7. Same as Figure 2 except for AE-D orbit 344 between 0810 and 0812 UT on November 5, 1975. The arrows marked E$_1$ and E$_2$ indicate the times of two LEE spectra shown in Figure 8.
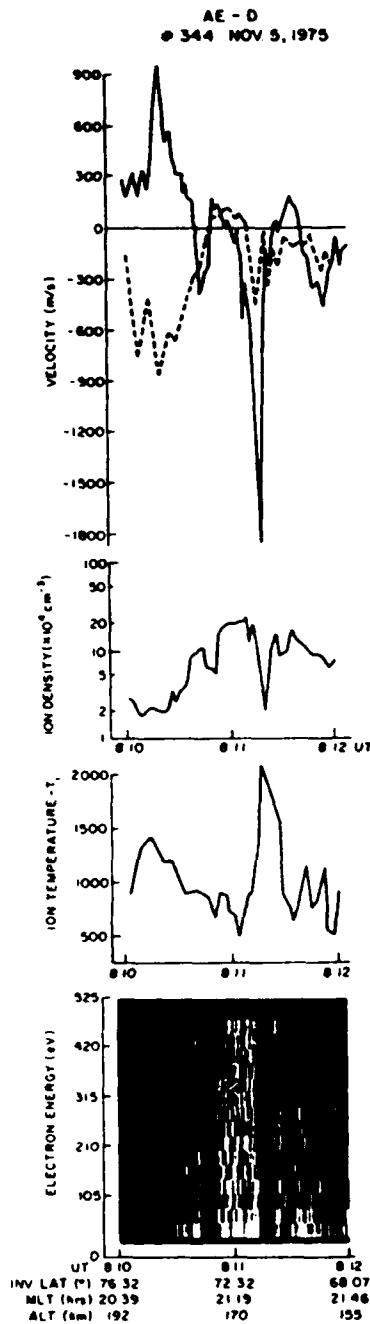
AE - D
344 NOV 5, 1975

Fig. 9. Same as Figure 5 except for AE-D orbit 344 between 0810 and 0812 UT. The PES was looking downward at 160° pitch angle, so that it could sense only the upgoing fluxes.

model these shears in nonlinear numerical simulation studies which would shed some light on the saturated amplitudes and spectra of these irregularities. We hope these observations will provide a fresh incentive to the theorists and simulation groups for further studies on the effect of large structured flows on plasma instabilities.

To help in their endeavor, we would like to provide some further characteristics of the structured flow regions. The largest magnitude of the velocity shear observed was 80 m s^{-1} km^{-1} (equivalent to 4 mV m^{-1} km^{-1}), while the smallest gradient scale length of the shear was determined to be 12 km. The latter figure is almost exactly equal to the resolution of

the data set used. Thus it seems quite probable that the shear gradient scale length could be considerably smaller and the velocity shear magnitude somewhat larger than those quoted above. The largest electric field found in the shear region was ~ 100 mV m^{-1}. In addition, we have seen that the large velocities cause substantial ion heating which, in turn, can create marked depletions in the upper F region ambient density by changing the ion chemistry, as observed on orbit 652. We also found that the large structured flows were generally confined to regions where the E layer was relatively nonconducting. The presence of these large velocities seems to be relatively independent of the state of the magnetosphere, being observed in conjunction with a rather active auroral display during IMF B_z southward conditions and during a northward B_z quiet arc configuration. The large velocities also seem to be a persistent feature of the magnetosphere-ionosphere interaction in that they were observed on consecutive AE-D orbits, e.g., on both orbit 651 and orbit 652. Given the wide variety of conditions under which they were observed and found to be associated with large-amplitude irregularities (~ 20%) in both highly collisional and weakly collisional regimes, they may provide a significant source of F region irregularities in the auroral environment.

Earlier studies by Kelley and Carlson [1977] and Kintner [1976] of velocity shears detected by rockets and satellites do not address the question of the spectral characteristics of density irregularities associated with velocity shears. To our knowledge the only mention of a k^{-1} density spectrum appears in the work of Kelley and Ott [1978], who used the theory of turbulence in two-dimensional fluids to make such a prediction for the density spectrum appropriate for the wake of a rising bubble in the equatorial ionosphere. The associated velocity turbulence would take the form of a k^{-3} spectrum. Kintner [1976] and Kelley and Kintner [1978] used similar fluid turbulence arguments to explain their high-latitude electrostatic turbulence data. Later, Fejer and Kelley [1980], in their comprehensive review, pointed out that such velocity (i.e., electrostatic) turbulence in the presence of horizontal gradients (possibly due to particle precipitation) at high latitudes will create density variations in the same scale length regime. Fejer and Kelley [1980] also pointed out that, semantically at least, it is important to note that this turbulence generation process is not a plasma instability but a nonlinear wave-wave coupling effect. Furthermore, this method of describing turbulent plasmas circumvents the linear instability theory completely and addresses directly the fully developed state. Recent ongoing studies indicate that two-dimensional turbulence driven by large velocities could give rise to a k^{-1} density fluctuation spectrum (C. E. Seyler, private communication, 1983).

As far as scintillation measurements are concerned, the wide variation of spectral indices in the auroral acceleration and large structured flow regions should give rise to similar variations in the scintillation spectra. Indeed, in one such case study involving rocket probe, scintillation, and incoherent scatter radar observations of irregularities in the auroral ionosphere, phase spectral slopes varying from −1 to −4 were obtained [Kelley et al., 1980]. The HILAT satellite, which combines various in situ measurements and a multifrequency beacon [Fremouw et al., 1983], should provide a unique opportunity of studying scintillation spectra and determining the auroral conditions associated with such spectra. In particular, the multifrequency beacon should provide an opportunity of determining the variation of scintillation magnitude with frequency, a variation which is expected to be small in large flow regions with shallow spectral slopes. Further, in view of the 56

density depletion associated with these regions, scintillations may maximize on the walls of such regions, as was observed for the case of equatorial bubbles [*Basu et al.*, 1983*b*].

One parameter of great importance that was not measured by AE-D was field-aligned currents. It is expected that the upward field-aligned currents that flow within auroral arcs [*Burke et al.*, 1980] would be associated with downward return currents that may or may not flow in the contiguous shear regions [*Burke et al.*, 1983]. It is necessary to determine whether strong field-aligned currents do indeed flow through the regions of structured velocity, as they may independently provide a source of irregularities. *Chaturvedi* [1976], by invoking the collisional ion cyclotron instability, has shown that strong field-aligned currents in the auroral *F* region ionosphere can lead to irregularities with scale sizes of hundreds of meters perpendicular to the magnetic field. In particular, the observed reduction of density in the large flow regions makes the ion cyclotron instability a viable alternative for the generation of irregularities in such regions.

REFERENCES

Basu, Su., E. MacKenzie, S Basu, H C Carlson, D A Hardy, F. J Rich, and R. C. Livingston, Coordinated measurements of low-energy electron precipitation and scintillation/TEC in the auroral oval, *Radio Sci.*, *18*, 1151, 1983*a*

Basu, Su., S. Basu, J. P. McClure, W B Hanson, and H E Whitney, High-resolution topside in situ data of electron densities and VHF/GHz scintillations in the equatorial region, *J. Geophys. Res.*, *88*, 403, 1983*b*

Burch, J L, S A. Fields, W B Hanson, R A Heelis, R A Hoffman, and R W Janetzke, Characteristics of auroral electron acceleration regions observed by Atmosphere Explorer C, *J Geophys. Res., 81*, 2223, 1976*a*

Burch, J. L., W. Lennartsson, W B Hanson, R A. Heelis, J H Hoffman, and R A Hoffman, Properties of spikelike shear flow reversals observed in the auroral plasma by Atmosphere Explorer C, *J Geophys. Res., 81*, 3886, 1976*b*

Burke, W J., D A. Hardy, F. J. Rich, M. C. Kelley, M. Smiddy, B. Shuman, R C Sagalyn, R P Vancour, P. J. L Wildman, and S T Lai, Electrodynamic structure of the late evening sector of the auroral zone, *J. Geophys. Res., 85*, 1179, 1980

Burke, W J, M. Silevitch, and D. A. Hardy, Observations of small-scale auroral vortices by the S3-2 satellite, *J. Geophys. Res., 88*, 3127, 1983

Chaturvedi, P. K., Collisional ion cyclotron waves in the auroral ionosphere, *J. Geophys. Res., 81*, 6169, 1976.

de la Beaujardiere, O., and R A Heelis, Velocity spike at the poleward edge of the auroral zone, *J. Geophys. Res., 89*, 1627, 1984.

Doering, J P., C O Bostrom, and J. C. Armstrong, The photoelectron-spectrometer experiment on Atmosphere Explorer, *Radio Sci., 8*, 387, 1973

Dyson, P L, J P. McClure, and W. B Hanson, In situ measurements of the spectral characteristics of *F* region ionospheric irregularities, *J Geophys Res, 79*, 1497, 1974

Eather, R H, DMSP calibration, *J Geophys Res., 84*, 4134, 1979

Fejer, B G. and M C. Kelley, Ionospheric irregularities, *Rev Geophys Space Phys., 18*, 401, 1980

Fremouw, E. J., C. L. Rino, J F. Vickrey, D A. Hardy, R E. Huffman, F J Rich, C-I Meng, K A Potocki, T A. Potemra, W. B. Hanson, R A Heelis, and L A Wittwer, The HILAT program, *Eos Trans AGU, 64*, 163, 1983

Guzdar, P N, P Satyanarayana, J D Huba, and S L Ossakow,

Influence of velocity shear on the Rayleigh-Taylor instability, *Geophys. Res. Lett., 9*, 547, 1982.

Hanson, W. B., and R. A. Heelis, Techniques for measuring bulk gas motions from satellites, *Space Sci. Instrum., 1*, 493, 1975.

Hanson, W. B., D. R Zuccaro, C. R. Lippincott, and S. Sanatani, The retarding-potential analyzer on Atmosphere Explorer, *Radio Sci., 8*, 333, 1973.

Heelis, R. A., J. D. Winningham, W. B. Hanson, and J. L. Burch, The relationships between high-latitude convection reversals and the energetic particle morphology observed by Atmosphere Explorer, *J. Geophys. Res., 85*, 3315, 1980.

Hoffman, R. A., J. L. Burch, R. W. Janetzke, J. F. McChesney, S. H. Way, and D. S. Evans, Low-energy electron experiment for Atmosphere Explorer-C and -D, *Radio Sci., 8*, 393, 1973.

Huba, J. D., S. L. Ossakow, P. Satyanarayana, and P. N. Guzdar, Linear theory of the $E \times B$ instability with an inhomogeneous electric field, *J. Geophys. Res., 88*, 425, 1983.

Kelley, M C., and C. W. Carlson, Observations of intense velocity shear and associated electrostatic waves near an auroral arc, *J Geophys. Res., 82*, 2343, 1977.

Kelley, M C., and P. M. Kintner, Evidence for two-dimensional inertial turbulence in a cosmic-scale low-β plasma, *Astrophys. J., 220*, 339, 1978

Kelley, M C., and E Ott, Two-dimensional turbulence in the equatorial spread F, *J. Geophys. Res., 83*, 4369, 1978.

Kelley, M. C., K D. Baker, J. C Ulwick, C. L. Rino, and M J Baron, Simultaneous rocket probe, scintillation, and incoherent scatter radar observations of irregularities in the auroral zone ionosphere, *Radio Sci., 15*, 491, 1980.

Kelley, M C., R C. Livingston, C. L. Rino, and R T Tsunoda, The vertical wave number spectrum of topside equatorial spread F Estimates of backscatter levels and implications for a unified theory, *J Geophys Res, 87*, 5217, 1982.

Keskinen, M J., and S L Ossakow, Nonlinear evolution of plasma enhancements in the auroral ionosphere. 2, Small-scale irregularities, *J Geophys Res., 88*, 474, 1983*a*

Keskinen, M J, and S L Ossakow, Theories of high-latitude ionospheric irregularities: A review, *Radio Sci., 18*, 1077, 1983*b*.

Kintner, P. M., Observations of velocity shear driven plasma turbulence, *J. Geophys. Res., 81*, 5114, 1976.

Lin, C. S., and R. A Hoffman, Narrow bursts of intense electron precipitation fluxes within inverted-V events, *Geophys Res Lett., 9*, 211, 1982*a*

Lin, C S., and R. A. Hoffman, Observations of inverted-V electron precipitation, *Space Sci. Rev., 33*, 415, 1982*b*.

Muldrew, D B, and J. F. Vickrey, High-latitude F region irregularities observed simultaneously with ISIS 1 and the Chatanika radar, *J Geophys. Res., 87*, 8263, 1982.

Phelps, A D R., and R. C. Sagalyn, Plasma density irregularities in the high-latitude topside ionosphere, *J. Geophys Res., 81*, 515, 1976.

Rino, C. L., R T. Tsunoda, J. Petriceks, R C. Livingston, M C Kelley, and K. D. Baker, Simultaneous rocket-borne beacon and in situ measurements of equatorial spread F intermediate wavelength results, *J. Geophys. Res., 86*, 2411, 1981.

Satyanarayana, P., and S. L. Ossakow, Velocity shear stabilization of the current convective instability, *J. Geophys. Res., 89*, 3019, 1984

Schunk, R. W., P. M. Banks, and W. J. Raitt, Effects of electric fields and other processes upon the nighttime high-latitude F layer, *J Geophys. Res., 81*, 3271, 1976.

St.-Maurice, J.-P., and D. G. Torr, Nonthermal rate coefficients in the ionosphere: The reactions of O^+ with N_2, O_2, and NO, *J Geophys. Res., 83*, 969, 1978.

Valladares, C E., W B Hanson, J P. McClure, and B. L. Cragin, Bottomside sinusoidal irregularities in the equatorial F region, *J Geophys Res., 88*, 8025, 1983.

Vickrey, J. F., and M C. Kelley, The effects of a conducting E layer on classical F region cross-field plasma diffusion, *J Geophys Res, 87*, 4461, 1982

Su. Basu, S Basu, and E. MacKenzie, Emmanuel College, 400 The Fenway, Boston, MA 02115

W R Coley and W B Hanson, University of Texas at Dallas, Richardson TX 75080

C S Lin, Southwest Research Institute, San Antonio, TX 78284

ATTACHMENT 6

Spatial variability of total electron content in the eastern Mediterranean region

Haim Soicher

Center for Communications Systems, U.S. Army Communications-Electronics Command

John A. Klobuchar

Ionospheric Physics Branch, Air Force Geophysics Laboratory

Patricia H. Doherty

Emmanuel College

Faraday rotation observations were conducted at Haifa, Israel (32.87°N, 35.09°E), and Athens, Greece (37.97°N, 23.72°E), during the maximum phase of the current solar cycle using the VHF beacon of the SIRIO satellite. The subionospheric points (at 420 km) are (29.9°N, 27.9°E) and (34.5°N, 18.4°E), and the subionospheric *L* shell values are 1.24 and 1.37, respectively. Expected latitudinal and local time differences in total electron content (TEC) for the two locales are observed. However, the Haifa data are characterized by generally occurring, seasonally independent, large postsunset electron content maxima which are absent for the Athens data. Furthermore, the postsunset increases would appear to be a solar maximum phenomenon, as they are not observed during the minimum phase of the solar cycle. The postsunset increases are attributed to electron fluxes arriving from the equatorial regions along the magnetic lines of force. The correlation coefficients of hourly TEC at the Haifa/Athens locales exhibit a seasonally independent diurnal variation with minimum values at night and maximum values generally at the end of the buildup phase of TEC variation. The daytime ratios of the standard deviation of TEC to the average TEC are generally seasonally independent and behave quite similarly at the two locales, with daytime values below ~25%.

INTRODUCTION

Total electron content (TEC) measurements were made at Haifa, Israel [*Soicher et al.*, 1982] (32.87°N, 35.09°E), and Athens, Greece (37.97°N, 23.72°E), by monitoring the polarization rotation of VHF transmission from the geostationary SIRIO satellite, which is located at 15°W. The subionospheric points (i.e., the coordinates of the point at which the path from the satellite to the observation station intersects a mean ionospheric altitude of 420 km) for the Haifa and Athens locales are (29.9°N, 27.9°E) and (34.5°N, 18.4°E), respectively; the invariant latitudes are 26.2° and 31.4°, respectively; the magnetic dip angles are 41.8° and 48.4°, respectively; and the *L* shell values are 1.24 and 1.37, respectively. The ionospheric characteristics observed are considered to be those which are prevalent at the subionospheric points

rather than at the locations of the receiving apparatus. The beacon frequency of SIRIO used in the observations was 136.14 MHz.

The transmission from the satellite was continuous except for an occasional deliberate shutdown of the satellite beacon for power conservation requirements. Occasional interference and loss of power at the receiver site have also caused some data gaps.

At any one location, TEC is a quantity that is observed to vary diurnally, from day to day, seasonally, with the phase of the 11-year solar cycle, and in response to ionospheric disturbances. The data here were taken during the maximum phase of the current solar cycle (cycle 21, which is a relatively high one in comparison to other cycles), and thus the TEC values represent maximum expected values in this region of the world.

DATA

The superimposed diurnal variation of 15-min TEC values, normalized to the vertical direction and
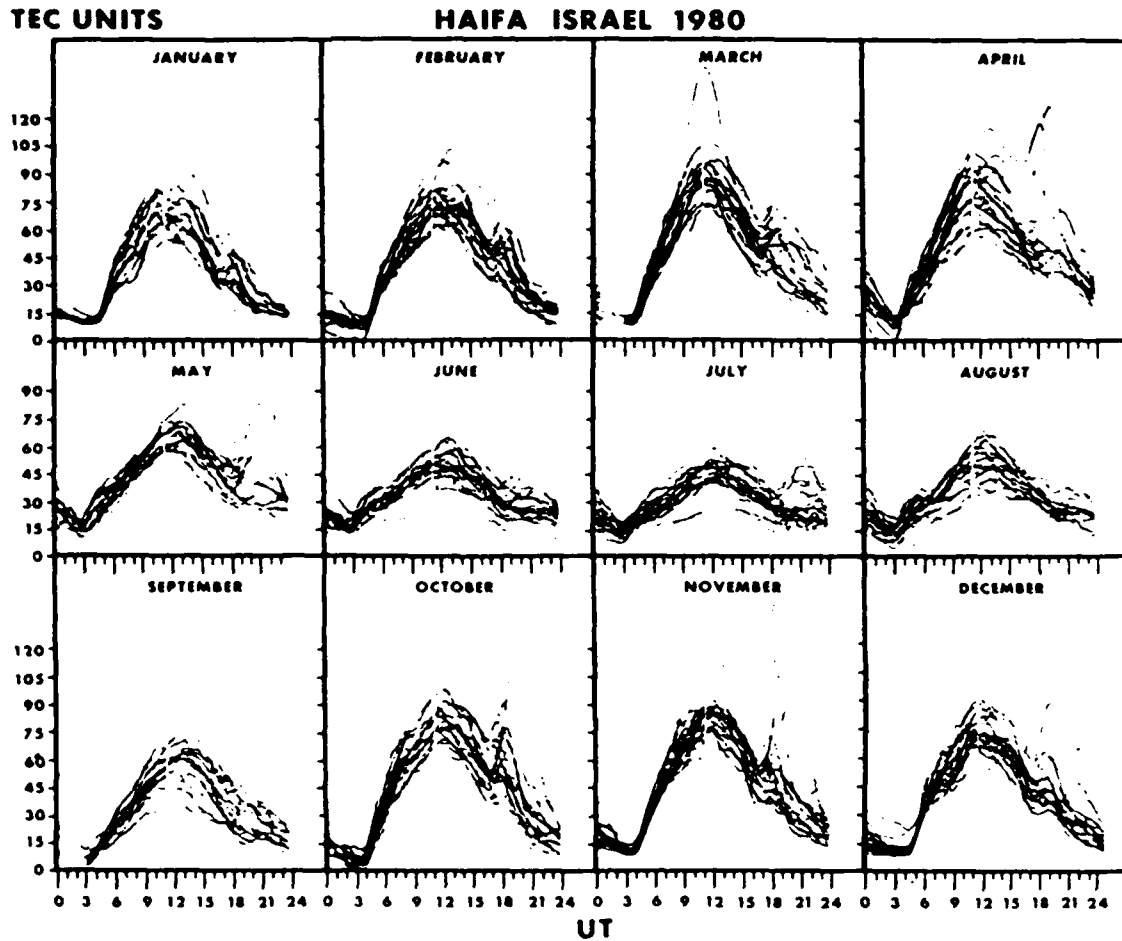
TEC UNITS   HAIFA ISRAEL 1980

Fig. 1   Superimposed diurnal variations of total electron content (TEC) for Haifa, Israel, for January through December 1980 versus time in UT (1 TEC unit = 10^{16} el m^{-2})

grouped in monthly intervals for the calendar year 1980, are shown in Figures 1 and 2 for the Haifa and Athens locations, respectively. The monthly averages of the TEC data for the same months are displayed in Figures 3 and 4, respectively.

At both locations the daytime TEC maximizes at the equinoxes (the spring (vernal) equinox has larger absolute TEC values then the autumnal equinox) and minimizes at the summer periods.

At both locations the electron content increases rapidly after local sunrise. The rate of increase is quite steep for the equinoctial and winter periods and significantly slower in the summer period. After reaching a diurnal maximum the TEC begins to decrease fairly rapidly. However, the Haifa TEC data are characterized by generally occurring, seasonally

independent, large postsunset increases which last for 2–3 hours. These increases are generally absent for the Athens data. For Haifa, the TEC, after reaching a diurnal maximum, begins to decrease fairly rapidly. Following the maximum, TEC may gradually decay to reach a minimum just prior to the next sunrise. On many days, however, TEC may reach a secondary maximum quite dramatically. The peak of the secondary enhancement occurs at about 1800 UT, i.e., about an hour or so after local sunset. The postsunset TEC increase is observed at most seasons but is most pronounced in the late equinoctial and winter periods. For Athens the TEC secondary increase is rarely observed, and after the diurnal maximum is reached, the TEC gradually decays to its minimum value.
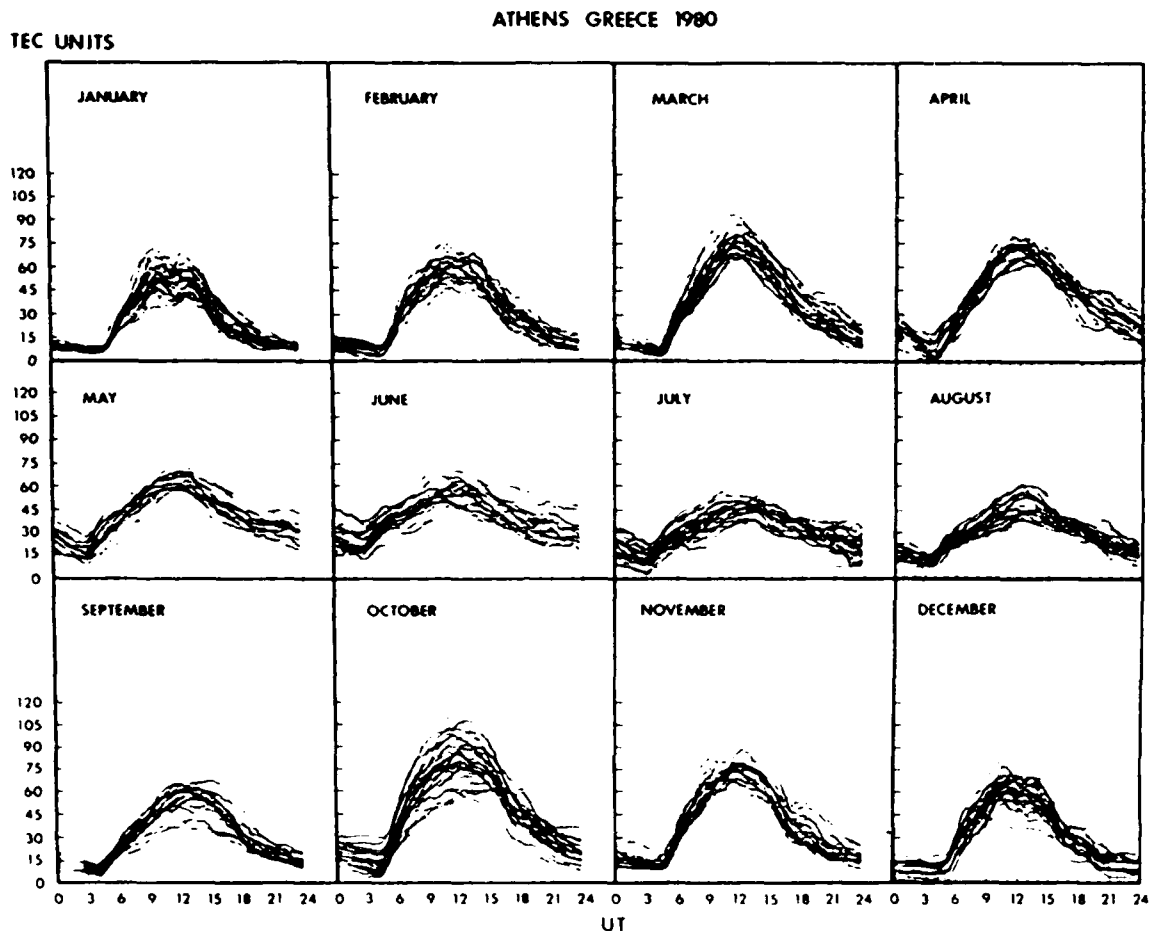
ATHENS GREECE 1980

TEC UNITS

Fig 2   Same as Figure 1 but for Athens, Greece

Some of the gross characteristics of TEC are similar at both locations. For example, the sharply lower daytime TEC values on June 27, 1980, and the sharply larger TEC daytime values on September 9, 1980, are common to both locations in comparison to adjacent days. However, some of the less obvious variations (e.g., traveling ionospheric disturbances) are unique to the individual location.

On the monthly average curves the postsunset increase is averaged out, but a change of slope is noticeable in the Haifa data (Figure 3), while it is totally absent for the Athens data (Figure 4).

For comparison purposes, TEC data for November 1975 taken at Haifa using the VHF signal of the geostationary ATS 6 satellite, which was located at 35 E, are shown in Figure 5. The period of observation was near the minimum phase of the solar cycle.

The geographic subionospheric point was at 30.1°N, 35.1°E; the invariant latitude is 26.4°; the magnetic dip is 42.7°; and the L shell value is 1.25. The solar cycle variation of TEC is expressed by the near 5:1 ratio in maximum TEC values during 1980 as compared to 1975. The 1980 postsunset maximum is absent for the 1975 data; however, there are indications of morning maxima in the 1975 data.

The hourly averages of TEC at Haifa and Athens for the equinoctial, summer, and winter periods are shown in Figure 6. During the winter and the spring equinox the Haifa TEC values are always larger than the corresponding Athens values. During the fall equinox the Haifa values are larger than the Athens values at all times except the predawn period and the initial decay period after the diurnal maximum. During the summer, Athens values are larger than
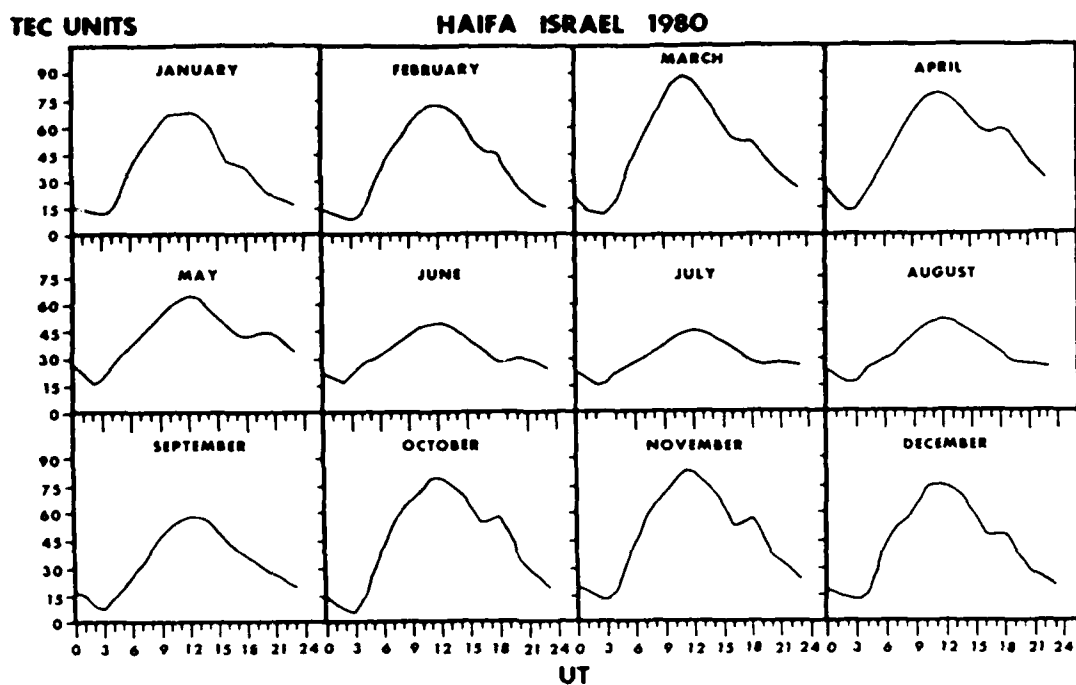
TEC UNITS   HAIFA ISRAEL 1980

Fig. 3   Monthly average variation of TEC in Haifa, Israel, for January through December 1980
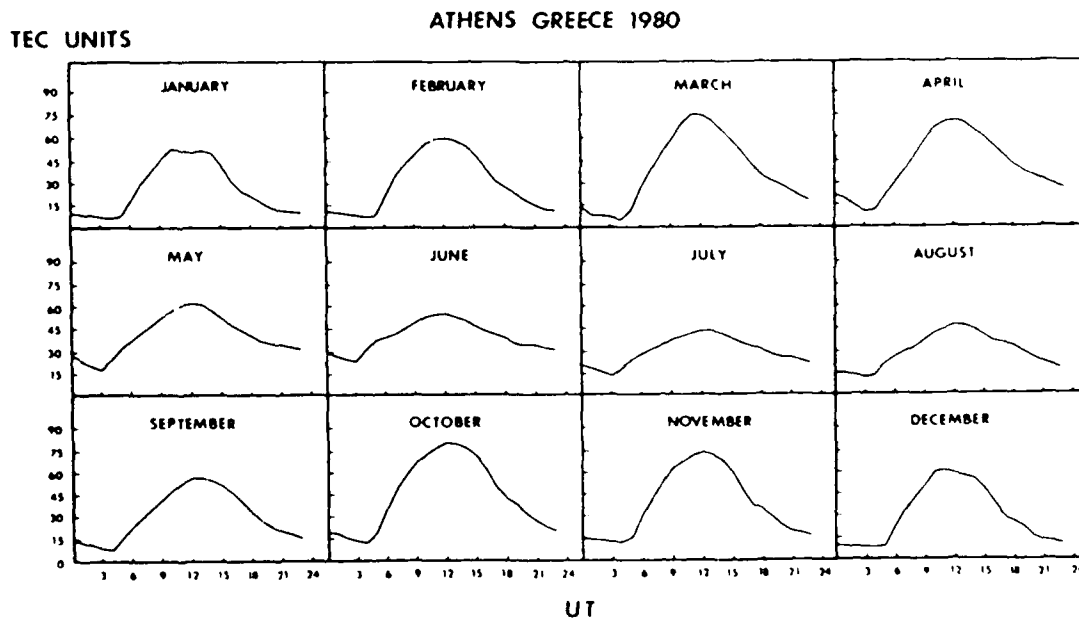
ATHENS GREECE 1980

TEC UNITS

Fig. 4.   Same as Figure 3 but for Athens, Greece

SATELLITE ATS-6 140 MHZ BEACON
NOVEMBER 1975
HAIFA, ISRAEL
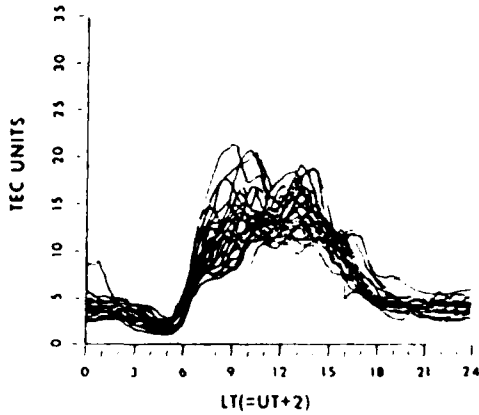
Fig 5   Same as Figure 1 but for November 1975

The day-to-day variability of TEC is clearly exhibited by the superposed diurnal curves of Figures 1 and 2. The variability is best described by the standard deviation of the daily TEC values from the average monthly values. Of more practical significance is the ratio of the standard deviation to the mean TEC values as a function of time. Such ratios are plotted for the various seasons for the Haifa and Athens locales in Figure 7. It is seen that during the daytime the ratios are reasonably constant, are independent of location and season, and rarely attain values above ~25%. During the night the ratios behave more erratically and are much higher in value. This suggests that there is an irreducible ionospheric variability which, upon normalization by the mean TEC, will be less by day than by night.

Using the smoothed hourly values of TEC from the Haifa and Athens stations, shifted to corresponding local times, correlation coefficients for the two locales were calculated for seasonally representative months as a function of universal time (Figure 8). The error bars represent 95% confidence limits, assuming a Gaussian distribution of values about the mean. The correlation coefficients exhibit a seasonally independent diurnal variation with minimum values at night and a steep increase toward maxi-

the corresponding Haifa values except during the dawn hours. While it is expected that the lower-latitude ionosphere observed from Haifa will exhibit a higher TEC than that observed from Athens, because of higher solar zenith angles, the summer data are surprising.

HOURLY AVERAGES
TOTAL ELECTRON CONTENT (TEC)

o ATHENS, GREECE
• HAIFA, ISRAEL

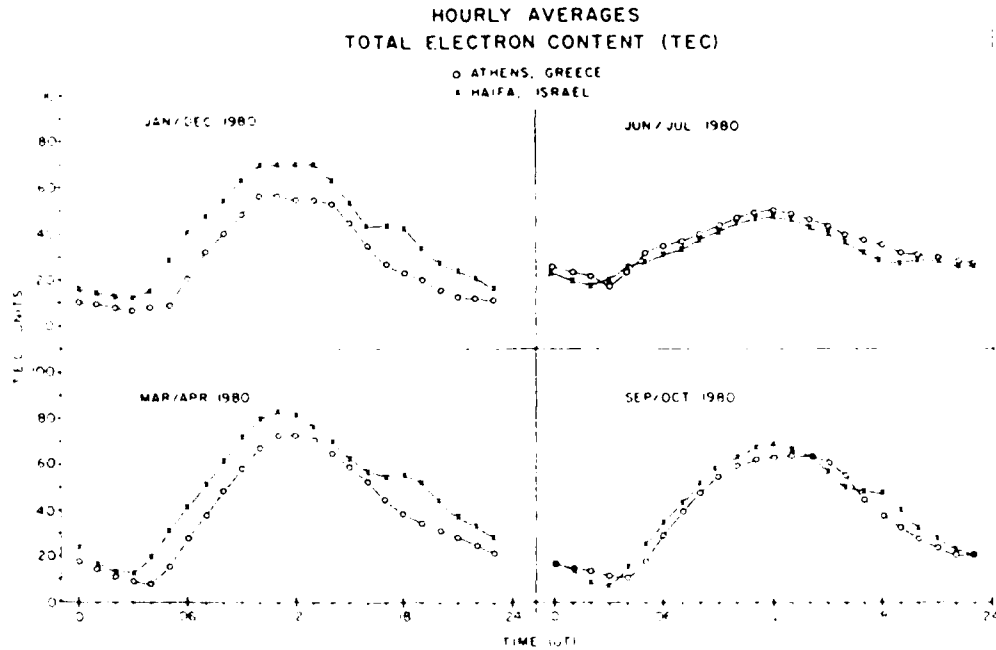Fig 6   Hourly averages of TEC at Haifa, Israel, and Athens, Greece, for the equinoctial, summer, and winter periods during 1980

DIURNAL VARIATION OF THE RATIO
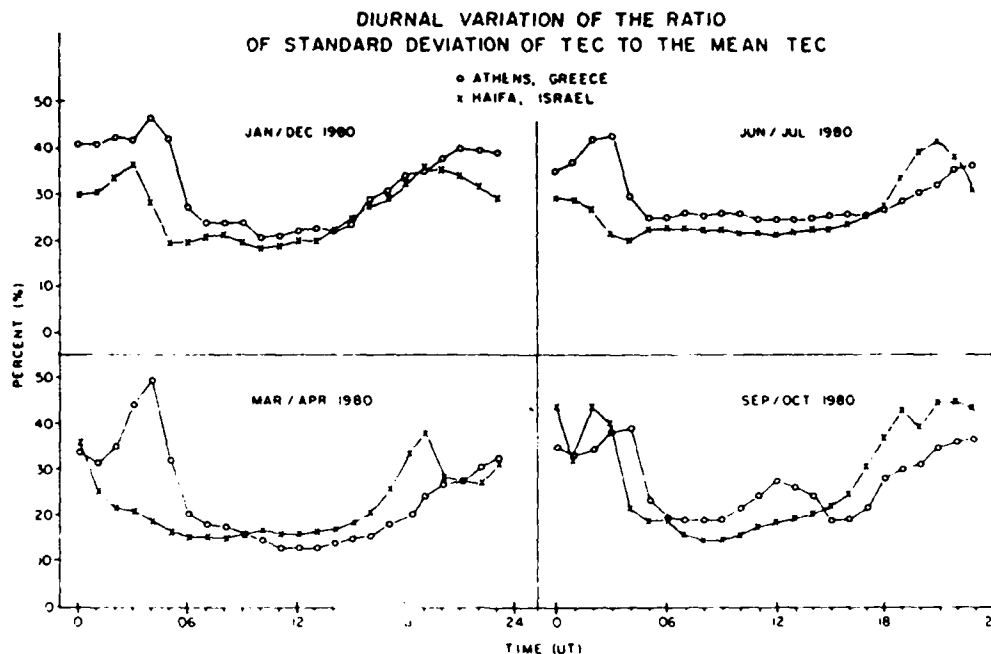OF STANDARD DEVIATION OF TEC TO THE MEAN TEC

Fig. 7. Diurnal variations of the ratio (in percent) of the monthly standard deviation of TEC to the hourly
average of TEC at Haifa, Israel, and Athens, Greece, for various seasons during 1980

mum values generally at the end of the buildup phase of TEC variation. The general trend is for the coefficient to gradually decline after reaching the maximum, although some variability is observed.

Another approach is to cross-correlate, between the two stations, the TEC values over continuous time intervals and the variability of TEC values from their monthly mean contours. By calculating the coefficient for the variabilities, rather than for the actual values of TEC, any possible influence of the different diurnal contour shapes of TEC is eliminated: The correlation is done for TEC values and variabilities during three time intervals; 0000-0400 UT, 0000-2400 UT, and 1600-2200 UT. The first time interval represents the nighttime, the second represents the full diurnal period, and the third represents the time period during which the postsunset maximum occurs in Haifa. The results are shown in Table 1.

As expected, the correlation coefficients for the actual continuous TEC values are always higher than the corresponding TEC variability coefficients. As with the smoothed hourly correlation coefficients the nighttime correlations are low in comparison to other diurnal intervals. The influence of the 24-hour

term is seen in the high correlation of the TEC values for the time interval 0000-2400. The correlation coefficients are affected significantly when the 24-hour term is removed by correlating the TEC variabilities. For the time period 1600-2200, when the postsunset maxima generally occur, the correlation coefficients for the TEC variability are always lower than the corresponding ones for the full diurnal periods, except during the month of June when the postsunset phenomenon is not prevalent.

DISCUSSION AND CONCLUSIONS

The large postsunset enhancements in TEC observed at Haifa are due to the "fountain effect" pattern of plasma motion from the equatorial regions along the magnetic lines of force. In the equatorial region, polarization fields produce large upward drifts of electrons at sunset, resulting in a rapid lifting of the F layer and massive horizontal flow of plasma along the field lines [Rishbeth, 1977; Wu, 19 '2]. A postsunset enhancement in upward E × B drift, which is a characteristic feature during solar cycle maximum periods [Anderson and Klobuchar, 1983], is pr arily responsible for the increase in TEC at

63

ATHENS VS. HAIFA
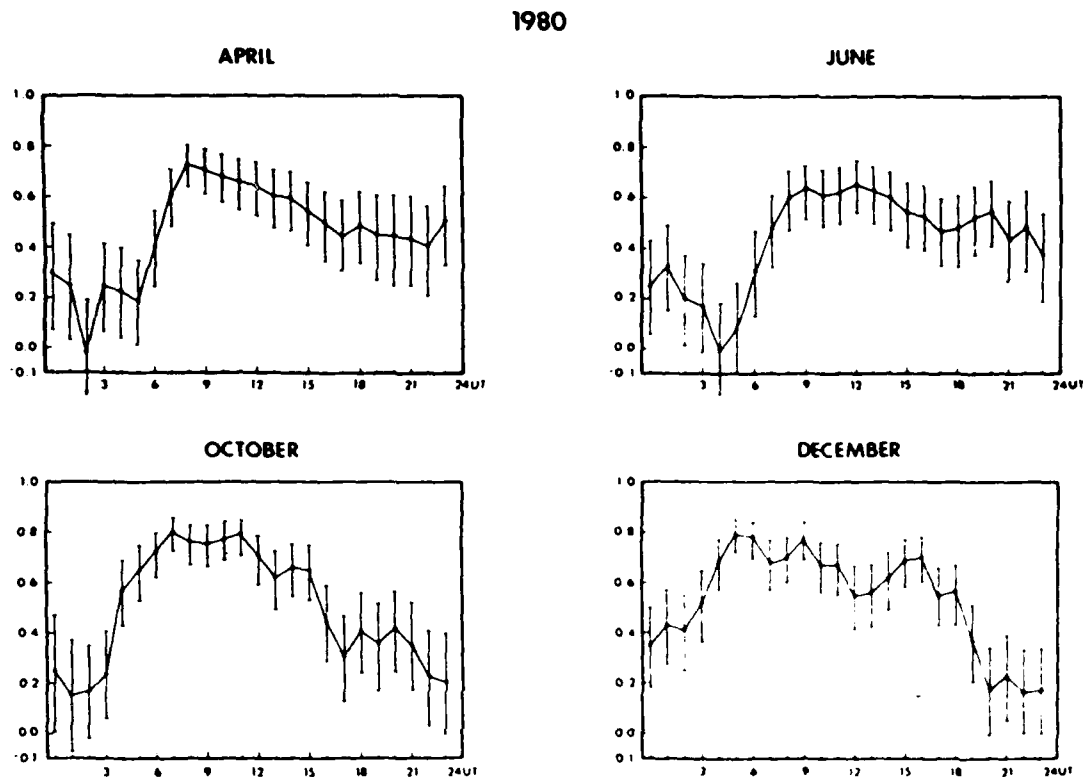## CORRELATION COEFFICIENT VS. TIME OF DAY
1980

Fig. 8. Correlation coefficients versus time of day for smoothed hourly values of TEC at Haifa, Israel, and Athens, Greece, for seasonally representative months

Haifa between about 1600 and 2000 UT. Bottomside f_oF_2 observations indicate that the "equatorial anomaly" (i.e., low values of critical frequency at the magnetic equator compared to those at latitudes approximately 15°-20° away from the magnetic equa-

TABLE 1. Correlation Coefficient of TEC Values (and Variabilities From Monthly Means) for Different Time Intervals for Seasonally Representative Months

Time Period, UT	Month (1980)			
	April	June	October	December
0000-0400	0.41	0.33	0.36	0.40
	(0.14)	(0.20)	(0.18)	(0.42)
0000-2400	0.84	0.76	0.88	0.89
	(0.49)	(0.49)	(0.51)	(0.52)
1600 2200	0.86	0.66	0.84	0.94
	(0.46)	(0.48)	(0.36)	(0.46)

tor), during sunspot maximum, may extend to 40° magnetic dip angle in the Asian sector [Rao and Malhotra, 1964] Further, the anomaly is most pronounced from about 2000 to 2200 local time in the northern latitudes Bottomside and topside soundings of the equatorial anomaly [Rush et al, 1969] along the 75°W longitude indicate that during solar maximum the maximum development of the anomaly occurs at ~2000 LT during winter and the equinoxes and at ~1700 LT in summer During years of declining solar activity the maximum development of the anomaly shifts to 1300-1500 LT

The behavior of the TEC at Haifa vis-a-vis the postsunset increase or its absence thus complements f_oF_2 data of the development of the equatorial anomaly in terms of its latitudinal extent and seasonal and solar phase development structure The absence of the postsunset ionospheric structure at

Athens, a relatively close location to Haifa, indicates that density peaks may be relatively narrow in extent with resulting strong spatial density gradients.

The ratio of the standard deviation of TEC about its monthly mean to TEC appears independent of season and of geographic location, and during daytime it is always below ~25%. This daytime ratio is similar to the ratios observed at other temperate and high latitudes [*Soicher and Gorman*, 1981].

The relatively high day-to-day variability of TEC during nighttime appears to contribute to the low correlation between the Haifa and Athens TEC at that time interval. The correlation coefficient increases steeply with time during the buildup phase of the TEC. This is indicative that production through photoionization is the dominant process and affects the TEC increases at both locations in a similar manner. The subsequent decline of the correlation coefficient is indicative of the local processes which affect the TEC structure and its variability differently at the two locales.

REFERENCES

Anderson, D. M., and J. A. Klobuchar, Pre-midnight enhancements in total electron content at Ascension Island, paper presented at International Symposium on Beacon Satellite Studies of the Earth's Environment, URSI Working Group (G 12) on Use of Beacon Satellite Transmission, New Dlehi, Feb. 7–11, 1983.

Rao, C. S. R., and P. L. Malthotra, A study of geomagnetic anomaly during IGY, *J. Atmos. Terr. Phys.*, 26(11), 1095, 1964.

Rishbeth, H., Dynamics of the equatorial F-region, *J. Atmos. Terr. Phys.*, 39, 1159, 1977.

Rush, C. M., S. V. Rush, L. R. Lyons, and S. V. Venkateswaran, Equatorial anomaly during a period of declining solar activity, *Radio Sci.*, 4(9), 829, 1969.

Soicher, H., and F. J. Gorman, Variability of total electron content at temperate and high latitudes, in *Proceedings of the COSPAR/URSI Symposium on "Scientific and Engineering Uses of Satellite Radio Beacons,"* edited by A. W. Wernik, p. 91, Polish Scientific Publishers, Warsaw, 1981.

Soicher, H., Z. Houminer, and A. Shuval, Total electron content structure in the Middle East, *Radio Sci.*, 17(6), 1623, 1982.

Wu, M. F., On the effect of the vertical drift in the equatorial F region, *Radio Sci.*, 7(12), 1079, 1972.

P. H. Doherty, Emmanuel College, Boston, MA 02115

J. A. Klobuchar, Ionospheric Physics Branch, Air Force Geophysics Laboratory, Hanscom AFB, MA 01731

H. Soicher, Center for Communications System, U.S. Army Communications-Electronics Command, Fort Monmouth, NJ 07703

ATTACHMENT 7

Multipath effects on the determination of absolute ionospheric time delay from GPS signals

G. J. Bishop and J. A. Klobuchar

Ionospheric Effects Branch, Air Force Geophysics Laboratory, Hanscom Air Force Base, Massachusetts

P. H. Doherty

Physics Research Division, Emmanuel College, Boston, Massachusetts

Signals from the Global Positioning System (GPS) satellites can be used to make measurements of absolute ionospheric group delay and relative phase advance. These ionospheric parameters have wide application in providing corrections for military systems requiring knowledge of ionospheric time delay and phase scintillation, such as satellite detection radars. Multipath effects from the local environment of the receiving antenna can cause severe contamination of ionospheric group delay measurements made with GPS pseudorandom noise receivers. Measured variations in the multipath effects in some typical clean and reflective environments are presented and shown to be consistent with signal analysis for pseudorandom noise receivers. Measured single reflector multipath is analyzed briefly and shown to correlate well with calculations. Since antennas must frequently be located in environments that are much less than ideal, data analysis procedures were developed for minimizing the impact of multipath on the group delay measurement. These include low-pass filtering, day-to-day correlation, and calibration to relative differential carrier phase advance measurements by using subsets of the absolute ionospheric group delay data. Results of these processes as applied to the test data from various multipath environments are presented.

INTRODUCTION

Signals from the Global Positioning System (GPS) satellites can be used to make measurements of absolute ionospheric group delay and relative carrier phase advance as well as amplitude at 1.2 and 1.6 GHz. These ionospheric parameters have wide applications in providing corrections for military systems requiring knowledge of ionospheric time delay and phase and amplitude scintillation, such as satellite tracking radars and space-based surveillance systems.

The Ionospheric Effects Branch of the Air Force Geophysics Laboratory (AFGL) has equipped a GPS receiver to make continuous measurements of absolute ionospheric group delay, ionospheric phase scintillation, and amplitude scintillation in high-latitude regions. This equipment has recently been operated

at Thule, Greenland, on a joint campaign in conjunction with the AFGL Airborne Ionospheric Observatory.

In the development of this equipment severe contamination of group delay measurements with multipath effects from the local environment of the receiving antenna was noted. These effects would not be critical in most navigation and geodetic applications where multipath effects can be averaged out either by the motion of the receiving system or by relatively long-time averaging. Precise measurements of ionospheric parameters, however, require these multipath effects to be drastically reduced. Ideal antenna siting environments, antennas with low gain near the horizon, and well-placed absorbing material can all contribute to reducing these effects. Many field applications, however, have less than optimal sites to locate GPS antennas, and RF absorbers may be impractical in extreme environments. Thus we investigated techniques for mitigating the effects of multipath in different environments.
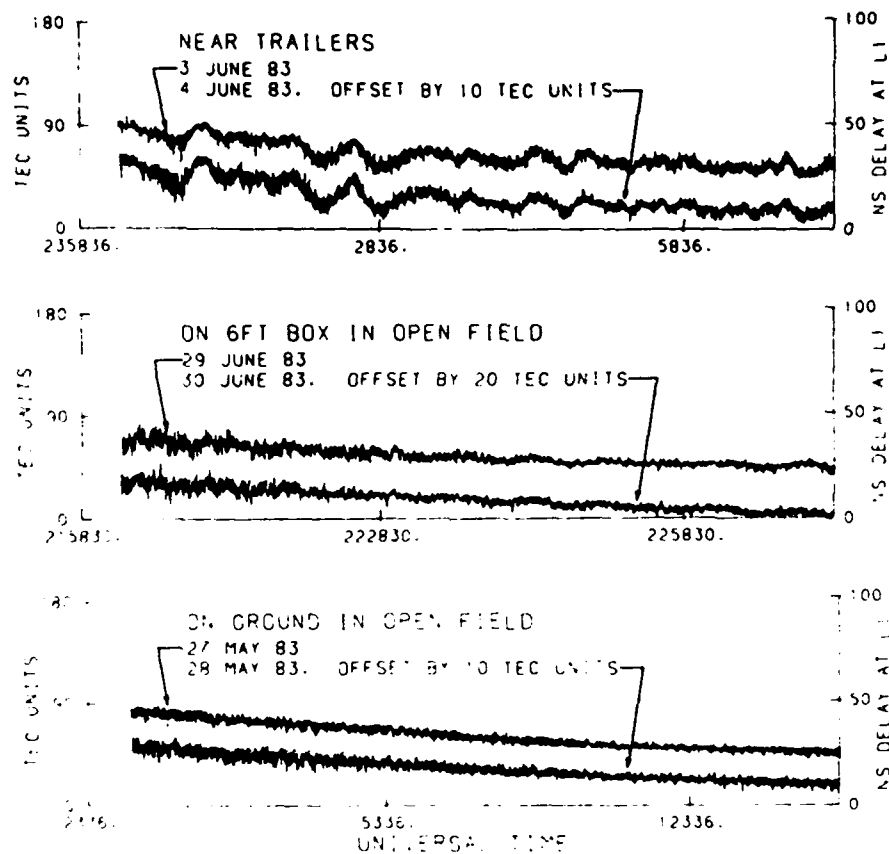
388

Fig 1   Measured variations in multipath effects on GPS signals in some typical reflective and clean environments, showing day-to-day correlation. (Each day's observation is approximately 70 min.)

MULTIPATH EFFECTS ON GPS MEASUREMENTS

Multipath-induced pseudorange (range *to satellite* measured by modulation delay) errors, delta range (time rate of change of pseudorange) errors, and signal strength fading for GPS have been analyzed and empirically tested during the concept validation phase of GPS performance testing. This work was done by *General Dynamics* [1979] for the GPS Joint Program Office. Their report indicates that: (1) multipath can cause both increases and decreases in delay; (2) theoretical maximum delay *error is 50 ns* when the reflected/direct signal ratio is 1; (3) because of the coded pulse nature of the signal, GPS precise code receivers can discriminate against multipath signals delayed by more than 150 ns; (4) typical delay errors show sinusoidal oscillations of periods 6–10 min and magnitudes of 3 ns or less (at L_1, 1.6 GHz, this is ~6 × 10^{16} cl/m² along the ray path, or 6 total electron content (TEC) units); (5) GPS multipath

errors in group delay correlate highly ($r \approx 70\%$); and (6) special antenna designs can reduce the effects of multipath.

Our initial measurements of absolute group delay were made using an antenna designed to view satellites to the horizon; this antenna has its phase centers for the two GPS frequencies (L_1 at 1.575 and L_2

TABLE 1. Characteristics of Measured Group Delay Errors Due to Multipath

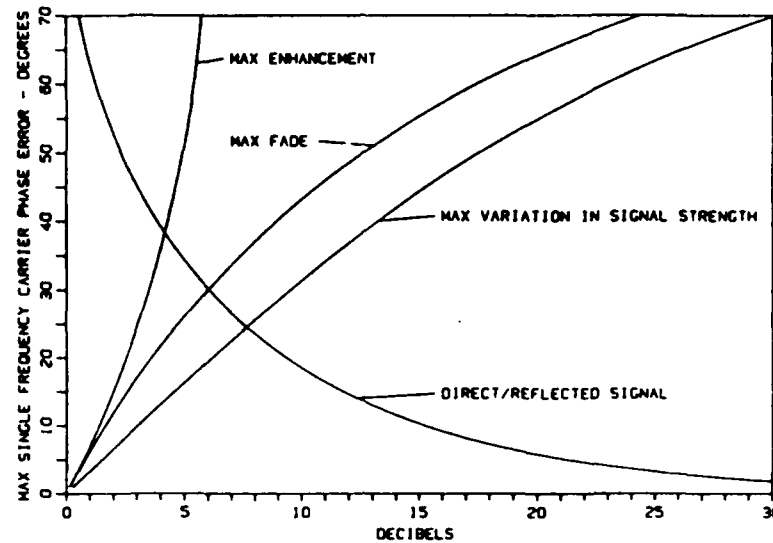| Environment	Group Delay Errors	
	Period	Amplitude
Highly reflective	1–9 min	up to 15 TEC units
Clean	3 5 min	up to 5 TEC units
Small ground Plane		
Clean	none	none
Large ground plane		

Fig. 2.   Single frequency carrier phase error and signal amplitude effects due to multipath

at 1.228 GHz) separated by about 11 cm. This antenna was located on the AFGL roof, a very non-ideal environment since there are many small antennas, vents and other reflective objects within the GPS antenna field of view. The absolute group delay measurements from this configuration showed extremely high multipath contamination as mentioned above.

To reduce the multipath, an antenna designed for geodetic measurements was used. This antenna has greatly reduced response near the horizon: -5 dB at 20° above the horizon, -10 dB at 10°, and -15 dB at 5°. The phase centers are colocated at the center of crossed dipoles above a 3-foot-square ground plane. Multipath errors were reduced by using this antenna but were still unacceptably high.

MULTIPATH MEASUREMENTS IN VARIED ENVIRONMENTS

It was decided to make absolute group delay measurements in different environments to determine how well the multipath-induced group delay errors could be eliminated by antenna siting. The GPS receiving equipment was installed in a trailer near a large flat field, and group delay measurements were made with the antenna in three different environments. (1) highly reflective: the antenna was located about 30 feet from trailers and a chain-link fence, (this environment is similar to the AFGL roof environment in terms of angular size of the reflecting

objects); (2) clean-small ground plane: the antenna was located approximately 90 feet from the nearest reflective object, and was placed atop a 6-foot high wooden box, limiting the reflective ground plane to 3 feet square; (3) clean-large ground plane: the antenna was at the same location as environment 2 but on the ground. Figure 1 shows unfiltered absolute group delay measurements made in these three environments. Each plot shows two consecutive days' measurements over approximately 1 hour of GPS SV 8's orbit. The coverage runs from approximately 20° elevation at 200° azimuth to 50° elevation at 215° azimuth.

The group delay errors due to multipath measured in these environments are clearly sinusoidal and exhibit the characteristics tabulated in Table 1.

MULTIPATH ANALYSIS

Signal strength variation and carrier phase error analysis

Consider our received signal to consist of the direct signal and one reflected signal, where

V_D directly received signal voltage;

V_R reflected signal voltage, from a single reflector, near normal incidence;

R resultant carrier signal voltage.

θ phase difference between the directly received and reflected ray;
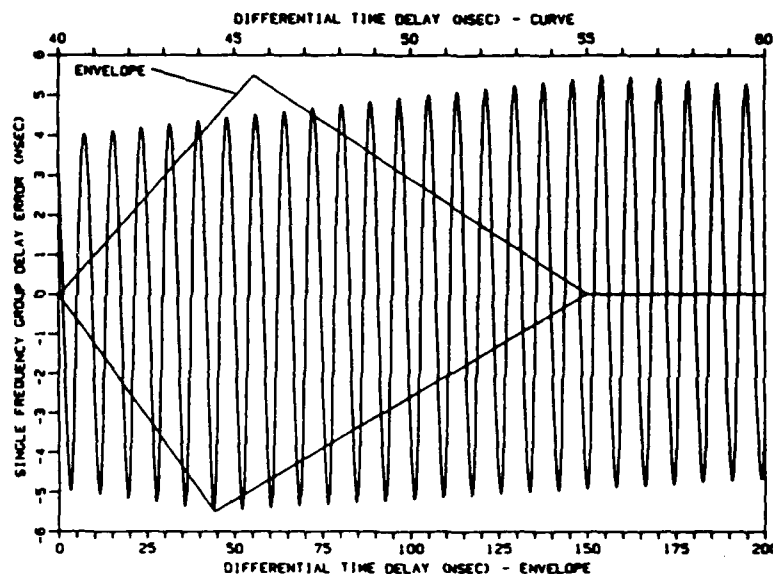
Fig. 3. GPS single frequency group delay error due to multipath versus differential time delay, for reflected-to-direct signal ratio of 0.11 at 1226 MHz. (Lower time axis for envelope, upper for sinusoid.)

x phase difference between V_D and R, or the carrier phase error due to multipath.

As the satellite motion slowly changes the geometry of the received signals, θ will vary continuously through many cycles with a a period of between 3 and 12 min for a stationary observer, *General Dynamics* [1979]. Since a typical GPS satellite pass we are considering occupies 3-5 hours, we assume V_R/V_D is constant over a few cycles of θ. It follows that the maximum carrier phase error, x_m ,occurs when

$$\theta = \cos^{-1}(-V_R/V_D) \qquad (1)$$

It follows from (1) that for a given x_m

$$V_R/V_D = \sin x_m \qquad (2)$$

max fade $= 20 \log_{10}(V_D - V_R)/V_D$

$$= 20 \log_{10}(1 - \sin x_m) \qquad (3)$$

max enhancement $\approx 20 \log_{10} (V_D + V_R)/V_D$

$$= 20 \log_{10} (1 + \sin x_m) \qquad (4)$$

The maximum fade and enhancement, V_D/V_R, and the maximum variation in signal strength (fade plus enhancement) are plotted in Figure 2. This figure is most easily read by selecting a value for V_D/V_R, in decibels, and then finding the corresponding maximum single frequency carrier phase error, x_m, from the direct/reflected signal curve. Then the corresponding values for max fade, enhancement and

signal strength variation may be read opposite this value of x_m.

The above analysis applies to a single frequency. For the differential case, assuming V_D/V_R is the same for both frequencies, x_m will be the same. However, the instantaneous value for θ and its rate of change will differ for each frequency. Thus there will occur times when one carrier has a phase error of $+x_m$, while the other carrier has a phase error of $-x_m$. Therefore the maximum differential carrier phase error for a given value of V_D/V_R will be twice the maximum single frequency carrier phase error, or 2 x_m.

Group delay error analysis

The error in group delay caused by multipath for an early/late gate pseudo noise (PN) code tracking loop of the type used in our GPS receiver is given by the root λ of the early/late gate error function [*General Dynamics*, 1979]:

$$D(\lambda) = [R(\lambda + \lambda_d) - R(\lambda - \lambda_d)] \cos(-\theta_m^*)$$
$$+ \Psi[R(\lambda + \lambda_d - \delta_m) - R(\lambda - \lambda_d + \delta_m)] \cos(\theta_m - \theta_m^*)$$
$$= 0 \qquad (5)$$

where

$$\theta_m^* = \tan^{-1}\left(\frac{\Psi R(\lambda - \delta_m) \sin \theta_m}{R(\lambda) + \Psi R(\lambda - \delta_m) \cos \theta_m}\right) \qquad (6)$$

$R(\lambda)$ is PN code cross correlation function

$R(\lambda) = 1 - (|\lambda|/T) \qquad |\lambda| \leq T \qquad T = $ PN chip time

$R(\lambda) = 0 \qquad |\lambda| > T$

and

λ group delay error;

λ_d early/late delay ($= 1/2$ PN chip $= 50$ ns);

Ψ reflected-to-direct signal voltage ratio;

θ_m multipath signal carrier phase relative to direct ray;

δ_m differential time delay between the reflected and direct ray.

As an example, group delay error is plotted versus δ_m for one specific case of $\Psi = 0.11$ in Figure 3. The envelope in this figure shows that for differential delays greater than 150 ns the receiver can discriminate against multipath, while the expanded scale curve in this figure shows the approximate sinusoidal form of the group delay error. The value of $\Psi = 0.11$ corresponds to a maximum variation in signal strength of approximately ± 2 dB, from (2), (3), and (4). The maximum single frequency group delay error of 5.5 ns shown in Figure 3 would yield a maximum error in ionospheric total electron content measurement of approximately 10×10^{16} el/m². For differential measurements, this maximum value would be doubled.

TEST WITH FLAT REFLECTOR

To verify that we were indeed observing environmental multipath a brief test was conducted using a single 60-in-wide vertical reflector installed 32 in. north of the antenna phase center along an east-west axis. The antenna was on the ground, in the "clean"

environment, in the exact spot where essentially no multipath had been observed. For a single reflector, where V_D, V_R, R and θ are defined as above, if

$f = $ carrier frequency (Hz)

and

$\tau_d(t) = $ delay of reflected signal (varies as satellite moves)

then

$$\theta = 2\pi f \tau_d(t)$$

and

$$R = [1 + 2(V_D/V_R) \cos \{2\pi f \tau_d\} + \{V_D/V_R\}^2]^{1/2} \qquad (7)$$

Figure 4 [after Greenspan et al., 1982] shows the reflection geometry, where

η_{sv} elevation angle of the space vehicle;

ϕ_{sv} azimuth of the space vehicle;

μ azimuth of vector normal to reflector, toward antenna;

$x \quad \mu - \phi_{sv}$;

m perpendicular distance from antenna to reflector.

Then the delay of the reflected signal is

$$\tau_d(t) = 2m'c \cos x \cos \eta_{sv} \qquad (8)$$

Substituting (8) into (7) and assuming $V_R/V_D = 1$ allows us to determine the values of the product $\cos x \cos \eta_{sv}$ for which R will be at a null. From the satellite orbit parameters the times of these nulls at each frequency were determined. The calculated nulls correspond closely to the observed nulls.

PROCEDURES FOR MINIMIZING MULTIPATH EFFECTS ON GROUP DELAY MEASUREMENTS

Low-pass filtering

Low-pass filtering was applied to the measurements shown in Figure 1 to determine how well the

Fig. 4. Geometry of antenna with vertical plane reflector.
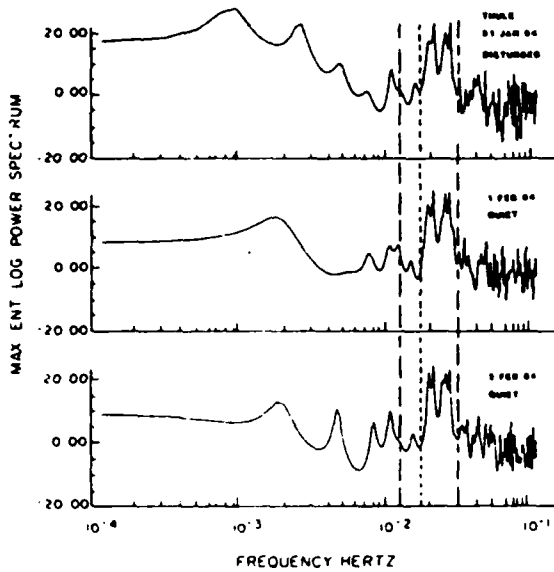
Fig 5. Group delay power spectra showing day-to-day correlation of multipath spectrum (Dotted lines bracket multipath effects, multipath is less significant in left section.)

multipath effects could be minimized. Table 2 shows the results of an approximate statistical test using a running mean.

Table 2 indicates that low-pass filtering to remove multipath may be useful in a relatively clean environment, but in a highly reflective environment even the slow changes of a quiet ionosphere would be affected over the filtering interval required.

Thus low-pass filtering to remove multipath effects appears to be useful only if a nearly ideal nonreflective environment can be obtained for the GPS antenna, or if changes in group delay occurring over periods less than 20 min are not of interest, or if it is known by independent simultaneous measurements that the ionosphere is very quiet.

Matched filtering

Since low-pass filtering would only be effective if the power spectra of multipath and ionospheric changes do not overlap, it may be possible to isolate the power spectrum of the multipath itself, for a limited data sample, and match a filter to that spectrum. To isolate the power spectrum of the multipath it is possible to use the fact that the multipath is highly
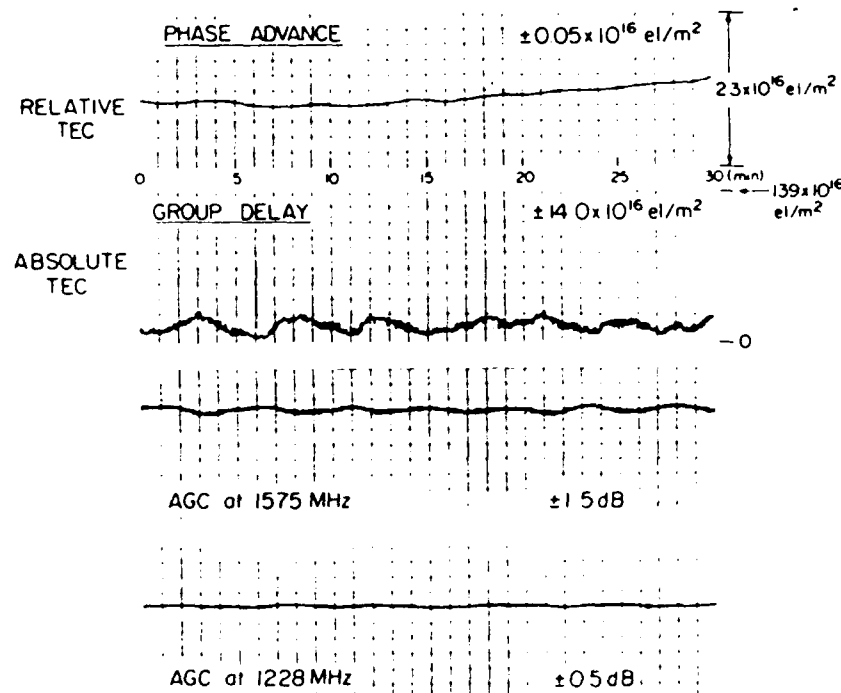
Fig 6   Multipath effects on ionospheric measurements using GPS, with receiving antenna located in a highly reflective environment and with the ionosphere quiet

71

Fig. 7   Simultaneous phase advance and group delay measurements, Thule, Greenland, Feb 4, 1984

correlated on consecutive days. If a day where a disturbed ionosphere is observed is bracketed by quiet days the multipath spectrum may be isolated. This, in fact, occurred during the recent Thule campaign where multipath of period of about 1 min was observed. Figure 5 shows the power spectra (method from *Radoski et al.* [1975]) for 1 disturbed and 2 quiet days. The multipath is around 2×10^{-2} Hz.
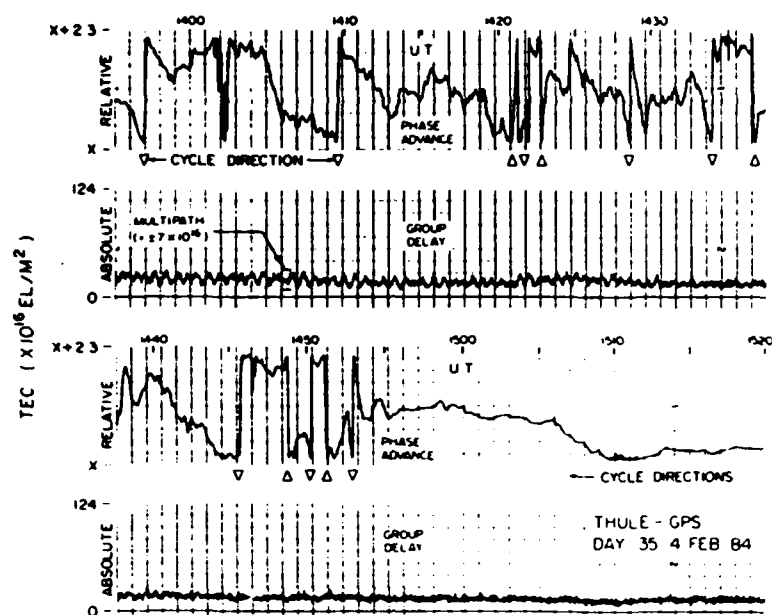
Calibration of phase advance measurements using group delay data

The group delay measurements presented here are obtained from the difference in range to the GPS satellite as derived from the relative arrival times of the clock pulses on each carrier.

Relative ionospheric delay changes can also be obtained by integrating the phase advance experienced on each carrier and subtracting the results for the two carriers to remove the effects of satellite geometric doppler shift.

Jorgensen [1978] discusses these measurements and points out that the group delay measurements may be used to obtain absolute delay values to reference the relative delay values from the carrier phase advance measurements. Thus it is only really necessary to obtain one good absolute value of delay per satellite pass to calibrate the differential carrier phase

advance channel over the entire pass. A good absolute value of group delay usually can be obtained by averaging or filtering over a sufficient length of time, generally 5-30 min, to remove the effects of the multipath. If multiple values of group delay, corrected for any multipath effects, can be obtained throughout the usual 1- to 5-hour pass of an individual GPS satellite, a "least squares" fit of the entire relative carrier phase advance data set can be made to these filtered absolute values of group delay

The analysis above indicates that the maximum carrier phase error is directly related to the ratio of the voltages of the reflected and direct signals (equation (2)). For a "worst case" V_D/V_R of 3 dB ($\phi = 0.5$), the maximum differential carrier phase error is $\approx \pm 90°$ (Figure 2), which corresponds to $\pm 0.58 \times 10^{16}$ cl/m^2 if measured at 1228 MHz. This "worst case" is 2 orders of magnitude smaller than typical differential group delay errors due to multipath. For example, for a maximum variation in single frequency signal strength of 2 dB due to multipath, the maximum differential carrier phase error is only $\pm 14°$ (Figure 2), or less than $\pm 0.09 \times 10^{16}$ el/m^2. The carrier phase fluctuations due to receiver noise with the typical nearly omnidirectional GPS receiving antenna and a 16 Hz receiving bandwidth are only slightly less than this. Thus reasonable multipath levels are barely detectable in the phase
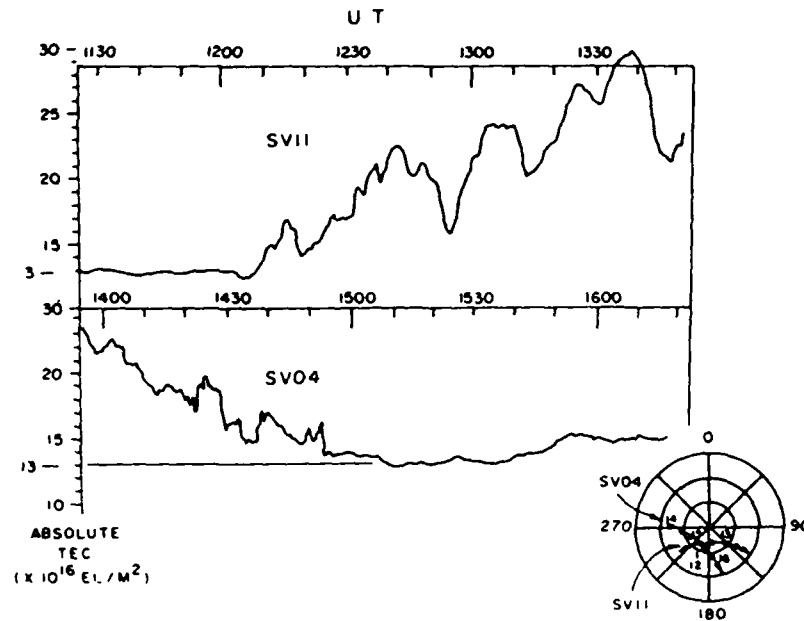
Fig. 8. Absolute ionospheric slant electron content derived from unfolded and referenced phase advance measurements, Thule, Greenland, Feb 4, 1984. (Local azimuth/el for satellites plotted at lower right, center = 90° elevation, outer circle = 0 elevation.)

advance records. On the other hand, this same 2-dB maximum variation in signal strength, corresponding to $\Psi = 0.11$, would yield a maximum differential group delay error of ± 5.5 ns or $\pm 31 \times 10^{16}$ el/m^2 as in Figure 3. This example corresponds well with the measurements presented in Figure 6, which shows multipath effects observed with the antenna located on the AFGL roof, where there are many vents and other sources of reflections.

As an illustration of the use of the phase advance measurements, Figure 7 shows about eighty minutes of simultaneous group delay and phase advance data from Thule. The first half of the group delay data shows multipath with amplitude of 7 TEC units and period approximately one minute. The latter half of the group delay data shows little or no multipath as the satellite rose to higher elevation angles. The phase advance data reveals a very disturbed iono-sphere, no multipath, and a general downward trend in TEC from 1355 to 1455 UT, followed by a 10-min period where the ionosphere is very quiet, between 1510 and 1520 UT. A very good value of absolute TEC may be obtained by averaging 3-5 min of group delay data during the 1510-1520 UT interval, where there is no discernable multipath. This good

absolute TEC value may then be used to reference the steady, quiet relative TEC level observed simulta-neously on the phase advance channel. The lower plot on Figure 8 shows the resulting referenced and unfolded phase advance data.

The same procedure applied to the preceding satel-lite pass resulted in the upper plot on Figure 8. It is noteworthy that this figure shows a 3-hour highly disturbed period, bordered by very quiet periods having nearly the same steady state absolute slant TEC. (Both passes had maximum elevation angles of about 75°.)

Thus a continuous measure of absolute iono-spheric delay can be determined, free from most multipath effects, if accurate measurements of abso-lute delay can be obtained from group delay measurements using low pass or matched filters. These points of absolute delay can then be used to reference continuous relative delay measurements ob-tained using the phase advance technique.

It is also possible to calibrate a relative iono-spheric group delay measurement made by carrier phase advance by performing a least squares fit to a 1-2 hour sample of unfiltered absolute ionospheric group delay measurements. This should work well,

since the multipath on the group delay measurement is nearly sinusoidal (Figure 3) and would average out over the data sample.

CONCLUSIONS

Multipath effects on absolute group delay measurements can be very serious to stationary users who require high precision. These effects, however, can be significantly reduced by a combination of antenna design and siting, data processing, day-to-day correlation, and fitting of data to simultaneous "phase advance" measurements.

REFERENCES

General Dynamics, Electronics Division, Final user field test report for the NAVSTAR global positioning system phase I, major field test objective no. 17: Environmental effects, multipath rejection. *Rep. GPS-GD-025-C-US-7008,* sect. II, pp. 1-7, San Diego, Calif., March 28, 1979.

Greenspan, R. L., A. Y. Ng, J. M. Przyjemski, and J. D. Veale, Accuracy of relative positioning by interferometry with reconstructed carrier GPS: Experimental results, paper presented at Third International Symposium on Satellite Doppler Positioning, Def. Mapping Agency and Natl. Ocean Surv., Las Cruces, N. M., February 1982.

Jorgensen, P. S., Ionospheric measurements from NAVSTAR satellites, *Rep. SAMSO-TR-79-29,* pp. 30-48, Aerospace Corp., El Segundo, Calif., December 1978.

Radoski, H. R., P. F. Fougere, and E. J. Zawalick, A comparison of power spectral estimates and applications of the maximum entropy method, *J. Geophys. Res., 80,* 610-625, 1975

G. J. Bishop and J. A. Klobuchar, Ionospheric Effects Branch, Air Force Geophysics Laboratory, Hanscom Air Force Base, MA 01731.

P. H. Doherty, Physics Research Division, Emmanuel College, 400 The Fenway, Boston, MA 02115

ATTACHMENT 8

Scintillations Associated With Bottomside Sinusoidal Irregularities in the Equatorial F Region

Santimay Basu[1] and Sunanda Basu

Emmanuel College, Boston, Massachusetts

C. E. Valladares[2]

University of Texas at Dallas, Richardson

A. DasGupta[3] and H. E. Whitney

Air Force Geophysics Laboratory, Hanscom Air Force Base, Massachusetts

A new category of equatorial F region plasma irregularities characterized by nearly sinusoidal waveforms in the ion number density N, observed by the Atmosphere Explorer satellites has recently been discussed by Valladares et al. (1983) and Cragin et al. (1985). We present multisatellite scintillation observations made at Huancayo, Peru, and spaced-receiver drift measurements made at Ancon, Peru, associated with such irregularities observed by AE-E on a few nights in December 1979. Utilizing ray paths to various geostationary satellites, it is found that the irregularities grow and decay almost simultaneously in long-lived patches extending at least 1000 km in the E-W direction. The scintillations continue for a period of almost 6 hours, at a level that varies from moderate to fairly intense ($S_4 = 0.1$–0.8 at 250 MHz), and these S_4 fluctuations are quite well correlated, even over a distance of 1000 km. The irregularities constituting the large patch are found to drift eastward at a velocity of approximately 140 m/s. This and other such events are accompanied by the frequency spread signatures on Huancayo ionograms, as previously reported. The unique feature of the Fourier spectra associated with such bottomside sinusoidal (BSS) irregularities is the presence of Fresnel oscillations, which allow a determination of the velocity of the diffraction pattern perpendicular to the direction of the ray from the satellite to the ground station. The velocity so determined agrees well with the results of simultaneously performed spaced-receiver drift measurements. The presence of Fresnel oscillations indicates that the BSS irregularities occur in a relatively thin layer. However, while the scintillation data indicate a high-frequency roll-off with a spectral index of the order of -3 to -4, the in situ data tend to indicate that the index is of the order of -5 to -6. Modeling studies are necessary to resolve this difference.

INTRODUCTION

A new category of equatorial F region plasma irregularities having properties which are quite different from those associated with plasma bubbles [McClure et al., 1977] has recently been discussed by Valladares et al. [1983] and Cragin et al. [1985]. Using primarily the low orbital inclination (19.76°) Atmosphere Explorer E (AE-E) data, they determined that this type of irregularity, which is characterized by quasi-sinusoidal fluctuations in the ion number density N, can exist in long-lived patches extending up to 7000 km or more in the E-W direction, that they are a bottomside phenomenon, and that they are able to retain their sinusoidal nature sometimes for a period of at least 300 min. The high-resolution retarding potential analyzer (RPA) showed that the central wavelength of these quasi-sinusoids varied from 300 m to 3 km and that their peak-to-peak

irregularity amplitude $\Delta N_s/N$, could be as large as several tens of percent. A relevant question is, how do these irregularities affect scintillations?

A morphological study of VHF scintillations and associated total electron content (TEC) depletions made at Arequipa, Peru, by DasGupta et al. [1983] had already pointed out certain characteristics of the scintillation pattern that were consistent with the bottomside sinusoidal (BSS) irregularity behavior. For instance, they found that during the December solstice, a period of maximum BSS occurrence according to Valladares et al. [1983], TEC depletions associated with bubble-type scintillations were at a minimum and continuous scintillation patches of a duration of 5–6 hours were generally observed. This is in sharp contrast to numerous patches of much shorter duration seen in conjunction with TEC depletions during the equinoxes, when BSS occurrence was found by Valladares et al. [1983] to be a minimum. The object of this paper is to present the first coordinated study of BSS irregularities and their signature on scintillation spectra observed near Huancayo, Peru, on December 8 and 11, 1979. Observations made by multiple geostationary satellites in the VHF-UHF range whose subionospheric (400 km) intersections span 1000 km in the E-W direction will be presented to elucidate the nature of these BSS irregularities and their effect on transionospheric propagation. Further spaced receiver measurements made
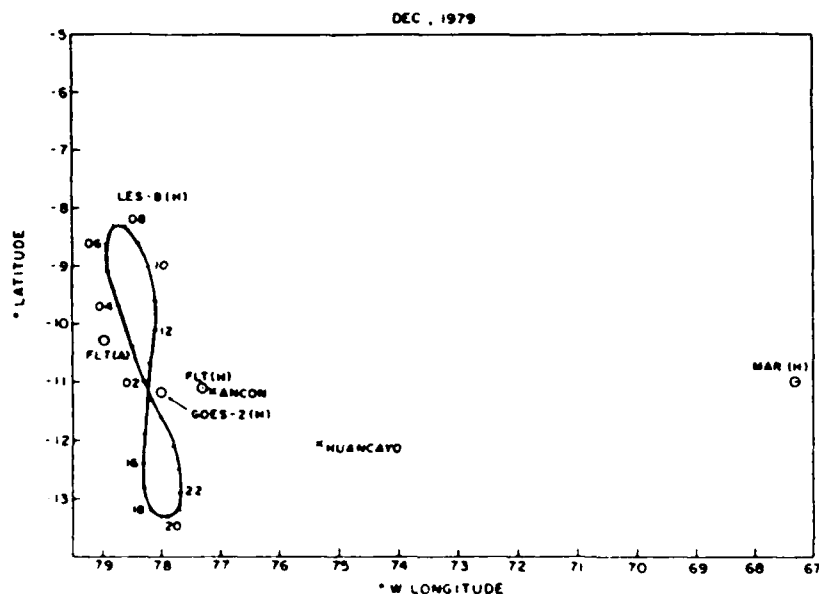
DEC , 1979

Fig 1   Geometry of scintillation observations during the occurrence of bottomside sinusoidal irregularities (BSS) indicating the ground stations at Ancon (A) and Huancayo (H) and the intersections of the propagation paths to various geostationary satellites with the ionospheric height of 350 km The intersection points are labeled with the names of the appropriate satellite. Fleetsat (FLT), GOES 2. LES 8, and Marisat (MAR), followed by the station name

at Ancon, Peru, on December 9, 1979, will also be presented to determine the drift of these irregularities in the E-W direction While the anticorrelation of the vertical drift with the N waveforms in BSS irregularities was discussed by *Valladares et al* [1983] and *Cragin et al* [1985], our spaced-receiver drift measurements will provide the first estimates of the zonal motion of these irregularities

RESULTS

Magnetic tape recordings of scintillation data were made at Huancayo and Ancon in December 1979 in support of a ground based and aircraft, polar and equatorial, airglow and scintillation campaign conducted primarily around Thule, Greenland [*Weber and Buchau*, 1981] and Ascension Island [*Weber et al* 1982, 1983, *Basu et al* 1983] While single antenna measurements were being made at Huancayo using four geostationary (or near geostationary) satellites, namely, starting from the westernmost location LES 8 at 249 MHz, GOES 2 at 137 MHz Fleetsat 1 at 244 MHz and Marisat 1 at 257 and 1541 MHz observations using three spaced antennas were being made at Ancon using a single satellite, namely Fleetsat 1 The intersections with the lower F region at 350 km altitude of the ray paths from these satellites to the two ground stations are shown in Figure 1 We will discuss the BSS and scintillation data from Huancayo for December 8 and 11 1979, and the spaced receiver measurements from Ancon for December 9 1979 Our task has been made simpler by *Valladares et al* [1983] who in their comprehensive paper have shown the low resolution ion number density data from the ion drift meter for two orbits 22653 and 22654 (their Figures 3d and 3e) obtained during the night of December 8 and the corresponding Huancayo ionograms (their Figures 16a and 16b) the high resolution density and vertical velocity data from orbit 22653 (their Figure 13) and various derived parameters related to the spectral characteristics of these sinusoids over

large portions of both these orbits in their Figures 14 and 15. We will have reason to discuss most of these diagrams in association with our scintillation data and their spectral analysis to be presented below.

To give an overview of the scintillation activity associated with BSS on a typical night, we present in Figure 2 the scintillations observed on December 8, 1979 (LT date is December 7–8), using LES 8, Fleetsat 1, and Marisat 1, the latter being observed at two frequencies simultaneously. We note that the first discrete structure of the evening, of approximately 1-hour duration at all the intersection points, is probably associated with bubble-type scintillations. Range spread was observed at Huancayo from 1930 to 2200 LT (0030 to 0300 UT) The only gigahertz scintillation event of the night, associated with >22-dB scintillation at 257 MHz, occurred during this period but was generated at a point that was 8° east of Huancayo (cf Figure 1), out of the field of view of the Huancayo ionosonde

The scintillations we associate with BSS start somewhat earlier than 0400 UT and continue without a break for more than 6 hours The GOES 2 satellite, transmitting at 137 MHz with its intersection point very close to that of LES 8, shows completely saturated scintillation throughout this period, which is not shown A study of the temporal behavior of the scintillations shows that the irregularities seem to be generated simultaneously over a very large region with E-W dimensions of at least 1000 km Within this large irregularity patch the individual irregularities drift from W to E, as we shall show with the spaced receiver measurements from Ancon The irregularities also seem to be quenched near-simultaneously These characteristics are very different from bubble type scintillations observed earlier at Huancayo with their limited durations and staggered onsets on different ray paths [*Basu et al*, 1978, 1980] *Valladares et al* [1983] have shown the BSS signature on the low-resolution ion density plots in their Figures 3d and 3e in the

DECEMBER 8, 1979

HUANCAYO, PERU

arrows labeled S in the figure show for each satellite the central time of the 6-min period for which the spectral analysis is presented.

The top, center, and bottom panels of Figure 3 show 6-min samples of scintillation data obtained at Huancayo from LES 8, Fleetsat, and Marisat, respectively, between 0328 and 0334 UT, and their corresponding spectra. The scintillation data, acquired on FM analog tapes, were digitized at 36 Hz and then decimated to 18 Hz. The spectra of the 6-min samples were obtained via a fast Fourier transform (FFT) algorithm. The spectral features displayed at frequencies above 5 Hz were introduced by the tape recorder at Huancayo and are not of ionospheric origin. Above approximately 0.7–1 Hz the power spectral density (PSD) is near the noise level and is nearly independent of frequency. Between 0.1 and 0.7 Hz the spectra decay from their maxima toward the noise level in approximately a linear fashion on the log-log scale shown, indicating a power law variation f^{p_2} of PSD with frequency. We use p_2 to signify the spectral index of scintillations in order to distinguish it from the one-dimensional in situ irregularity spectral index p_1, to be used later. The power law indices p_2 are determined from the
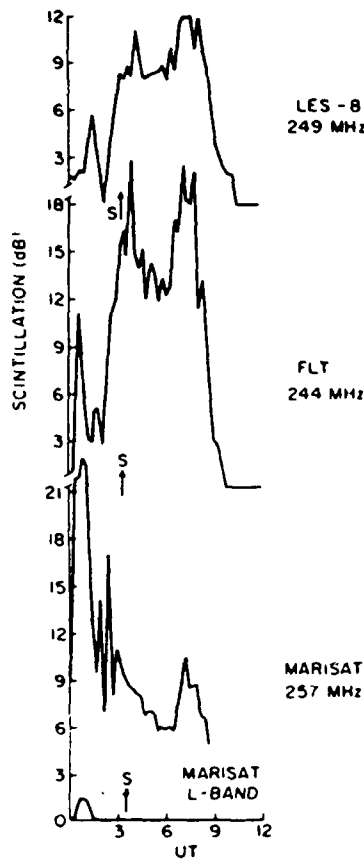
HUANCAYO
DEC. 8, 1979

Fig. 2 Temporal variation of scintillations observed at Huancayo on links with three geostationary satellites on December 8 1979 during the occurrence of BSS irregularities. The arrows labeled S indicate for each satellite the central time of the period for which spectral analysis is performed.

Huancayo longitude sector during this time period, and the corresponding Huancayo ionograms for 2245 LT (December 8) and 0010 LT (December 8) (their Figures 16a and 16b) show this altitude type frequency spread. As a matter of fact frequency spread was observed in Huancayo beginning at 2000 LT shortly after high scintillation activity. An earlier study showed that frequency spread is related to scintillations in the high VHF band. However during periods when the ambient density is large it appears to be related to also found in Figure occurs on the elevation angle near midnight

data segments of scintillations associated and their spectra. The S index of scintilla indices of the best fit straight line between the diagram

Fig. 4. The bottom panel shows the fluctuations of ion density (solid curve) from the RPA during a 3-s interval starting at 0449:30 UT on December 11, 1979, and the pitch or vertical drift (curve with solid circles) from the ion drift meter. The top panel shows the FFT (crosses) and maximum entropy method (solid line) spectrum of ion density fluctuations. The percent irregularity amplitude (sigma), the background ion density (NI) and the power law index (slope) of the roll-off portion of the spectrum are indicated on the diagram. The satellite altitude was 440 km.

slope of the best fitting straight line in the frequency range 0.1–0.7 Hz and are indicated on the spectral plots.

The data shown in Figure 3 and all others obtained on this evening have a systematic modulation superimposed on the linear roll-off portion of the spectra. For the data of Figure 3 the minima are observed at f_1, $2^{1/2}f_1$, $3^{1/2}f_1$, etc., where f_1 = 0.125 Hz for LES 8, 0.157 Hz for Fleetsat, and 0.089 Hz for Mansat. Such ordered modulation, known as Fresnel oscillation, is expected in the Fourier spectrum based on thin screen weak scattering theory when the diffraction pattern is elongated, when it has a component of motion normal to the direction of elongation, and when the spatial spectrum of electron density fluctuations is sufficiently smooth [Singleton, 1974]. Further, it has been shown that $f_1 = V_\perp/(\lambda z)^{1/2}$, where λ is the wavelength of scintillation measurement, z is the range of the observer to the irregularity layer, and $V_\perp$ is the irregularity velocity normal to the propagation path. An important point to note here is that in the equatorial F region the geometry needed for Fresnel modulations always prevails, namely, the irregularities are elongated in the N-S direction and the resulting anisotropic pattern drifts in the E-W direction because of "superrotation" [Woodman 1972]. These Fresnel oscillations are observed only occasionally in equatorial scintillation data, and when they are observed [Basu and Whitney, 1983; Basu et al., 1983], they usually are not seen as clearly as they are seen in the present data, nor are they usually seen continuously for a period of many hours. This indicates that we are dealing with a much

thinner layer of irregularities in the present (BSS) case. We have mentioned earlier that the frequencies of Fresnel maxima and minima depend on the range of the observer to the irregularity layer. Therefore for an extended layer the maxima and minima of Fresnel oscillations on the ground due to the lowest and highest levels of the layer may be sufficiently shifted with respect to one another to be to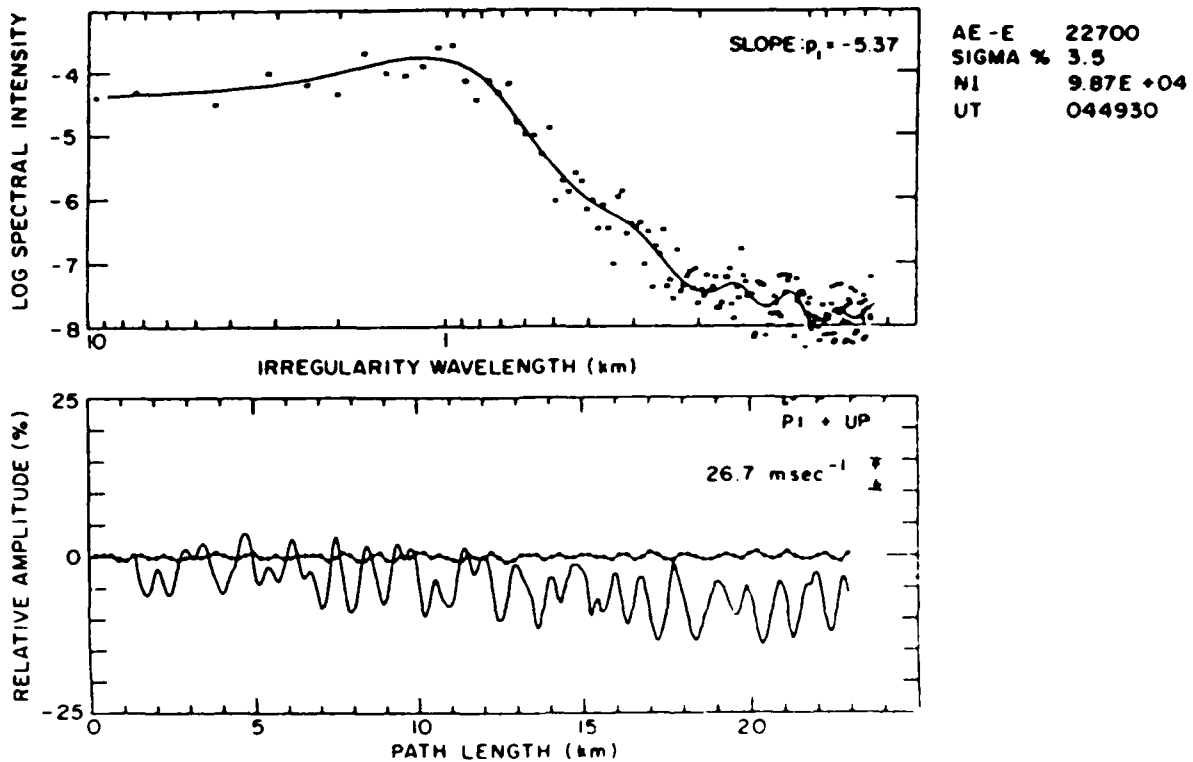tally smeared. From our knowledge of the resolution of two discrete sources, we estimate that for the propagation geometry appropriate to the observations of the Fleetsat satellite complete smearing of Fresnel oscillations will occur if the irregularity layer thickness exceeds 100 km around an average layer height of 450 km. Thus the present scintillation measurements indicate that BSS irregularities during their entire lifetime exist in relatively thin layers, while irregularities within plasma bubbles, even in their late phase, usually exist in much thicker layers.

A typical 3-s sample of high resolution in situ data obtained from AE-E orbit 22700 on December 11, 1979 during its passage through BSS irregularities near the Huancayo longitude sector is shown in the bottom panel of Figure 4. The variations of the relative amplitude of ion density $\Delta N/N$ (solid curve) and the pitch or vertical plasma drift (curve with solid circles) are illustrated in the diagram. The spectrum of the relative ion density fluctuations after detrending is shown in the top panel. The rms irregularity amplitude of the sample is 3.5% and the background density is 9.9×10^{10} m^{-3}. The relevant spectral analysis technique
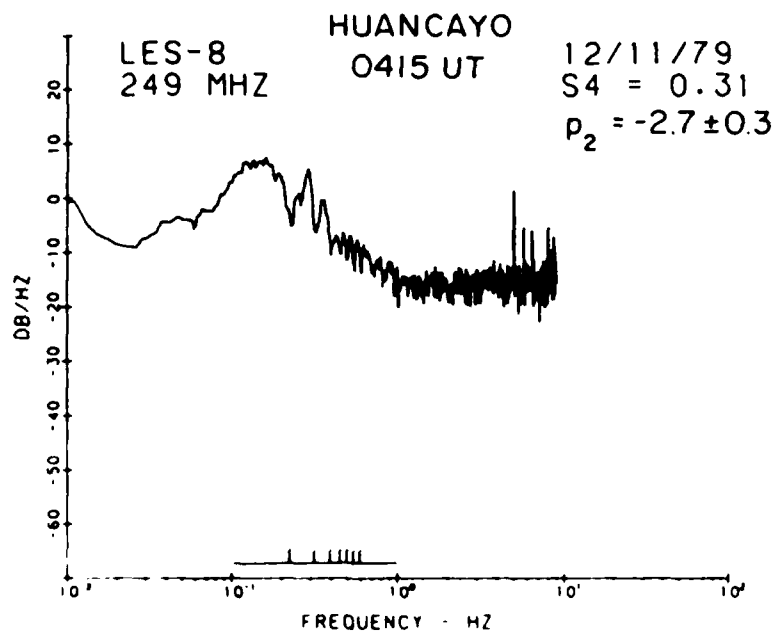
Fig 5   The spectrum of LES 8 scintillations observed at Huancayo on December 11, 1979, in the presence of BSS irregularities of the type shown in Figure 4. The power law index (p_2) of the roll-off portion of the spectrum is indicated The scale above the frquency axis indicates the frequencies of the first seven Fresnel minima

has been described in many recent publications [*Basu et al*, 1980, 1983; *Valladares et al*, 1983]. From the bottom panel we note that the irregularity waveform looks for the most part quite smooth and sinusoidal, as was also the case with many samples shown by *Valladares et al* [1983]

The one-dimensional spectrum shown in the top panel can be approximated over the scale length range of 800–100 m by a smooth power law variation of PSD with scale length having a one-dimensional power spectral index $p_1 = -5.37$ The spectrum obtained with the FFT algorithm (crosses in the top panel of Figure 4) agrees well with that obtained by using the maximum entropy method (solid curve) There is a noticeable spectral enhancement near 1 km scale size and a fall in PSD at scale lengths longer than 1 km

The fall off in PSD at the long scale lengths is probably the most significant difference between BSS spectra and that obtained within bubbles [cf *Basu et al*, 1983, Figure 4d] Figure 5 shows the spectrum of scintillations observed on 249-MHz transmissions from LES 8 satellite received at Huancayo in fairly close time correspondence with the in situ measurements discussed above The spectrum indicates a power law variation $f^{-2.7}$ of PSD with frequency at frequencies greater than 0.1 Hz But the power spectrum of scintillations arising from BSS irregularities having a large power law index or having a Gaussian form is also expected to be Gaussian [*Cronyn*, 1970. *Singleton*, 1974] This discrepancy may be explained if we assume that the characteristic scale of the Gaussian spectrum of BSS irregularities varies with altitude The integrated electron density deviation may then have a power law form with a small power law index even though the spectrum at a given altitude conforms to a Gaussian form The second noticeable feature of the scintillation spectrum is the existence of distinct Fresnel modulations In the spectrum of Figure 5, at least seven Fresnel minima at frequencies f_1, $2^{1/2}f_1$, $3^{1/2}f_1$, etc where f_1

= 0.22 Hz, are discernible, as indicated by the scale above the frequency axis

Since BSS irregularities were detected by the AE-E satellite at an altitude of 400 km, the slant range z of the irregularity layer for LES 8 satellite observations can be computed as 588 km Since $f_1 = V_\perp/(\lambda z)^{1/2}$, the irregularity drift speed u normal to the propagation path can be derived as $V_\perp = 185$ m/s The presence of distinct Fresnel minima in the scintillation spectrum up to the fifth order indicates that the bulk of scintillations arise from a rather concentrated layer not exceeding 50 km On the other hand, in order to obtain the shallow spectral index of the scintillation spectrum, an altitude distribution of irregularities with varying characteristic scales is required

The horizontal motion of the individual irregularities within the large BSS patch can be determined from spaced-receiver scintillation measurements, as was done earlier for bubble associated irregularities by *Basu and Whitney* [1983] Figure 6 shows an approximately 90-min data segment obtained at Ancon from Fleetsat on December 8-9, 1979, when measurements were made using three receiving systems spaced in the E-W direction by separations of 122 m between the west and central stations and 244 m between the central and east stations An almost uniform apparent drift [*Wernik et al*, 1983] of 140 m s⁻¹ from W to E was seen at both separations (compare top panel) The cross correlation coefficients on the 244-m separated channels were uniformly high, exceeding 0.6 (compare second panel) The two bottom panels show the S_4 index and the spectral index of 1 min scintillation samples When S_4 0.2, the spectral index is 3 Thus BSS irregularities seem to participate in the general nighttime zonal motion of F region irregularities and the spectral index of scintillations caused by these irregularities is, in general shallower than that indicated by in situ measurements
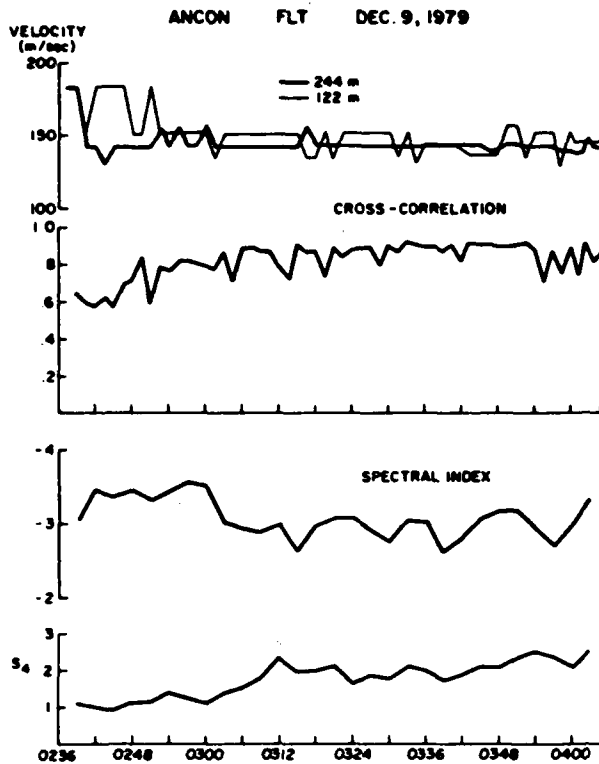
ANCON   FLT   DEC. 9, 1979

VELOCITY
(m/sec)

— 244 m
— 122 m

CROSS-CORRELATION

SPECTRAL INDEX

S_4

0236   0248   0300   0312   0324   0336   0348   0400

Fig. 6. The temporal variation of the S_4 index of scintillation, the power law index of scintillation spectrum, the cross-correlation coefficient of spaced-receiver scintillation data, and the apparent zonal drift observed at Ancon on December 9, 1979, during the occurrence of BSS irregularities.

DISCUSSION

The characteristic features of scintillations associated with BSS are the near-simultaneous onset and decay of scintillations at widely spaced (in longitude) ray paths to geostationary satellites, and the occurrence of continuous moderate to fairly intense 250-MHz scintillations (S_4 values from 0.1 to 0.8) for a period of 5–6 hours. It is also found that frequency spread is observed at such times on Huancayo ionograms. Further, TEC and scintillation measurements made at the nearby station of Arequipa, Peru, show that such long-lived scintillation events with wide spatial coverage are not accompanied by any TEC depletions [DasGupta et al., 1983]. Thus all the above findings, which are distinct from bubble-related events, clearly distinguish this class of scintillation.

As mentioned earlier, a further distinguishing feature is that Fresnel oscillations are typically present in the frequency spectrum of amplitude scintillation associated with BSS. This provides a tool for determining the drift velocity of irregularities in a direction perpendicular to the ray path, even when spaced-receiver measurements are not available. For instance, the drift velocity $V_\perp$, given by $V_\perp/(\lambda z)^{1/2} = f_1$, corresponding to $f_1 = 0.125$ Hz in the top panel of Figure 3 for LES 8 (wavelength λ = 1.2 m) measurements from Huancayo is 112 m s^{-1} when we consider a slant range of 668 km, corresponding to an irregularity layer height of 450 km and an ionospheric zenith angle of 45.5°. Considering the propagation geometry and assuming no vertical velocity, the derived V_{EW} = 160 m s^{-1}. At the same time we found f_1 =

0.157 for Fleetsat measurements, corresponding to $V_\perp$ = 126 m s^{-1}. The slant range in this case was 524 km, and the ionospheric zenith angle was 27.8°. The derived V_{EW} = 142 m s^{-1}, which agrees well with that obtained from LES 8 observations. Unfortunately, this technique does not give very reliable results when the ionospheric zenith angles are very large, such as those for our measurements with Marisat at a zenith angle of 62°. In discussing Figure 5 we had earlier shown that the drift speed on December 11, 1979, was somewhat higher, being of the order of 180 m s^{-1}. However, the zonal drift speed at F region heights shows considerable day-to-day variation and such values are quite common [Basu et al., 1986].

On the next day we have similar multisatellite amplitude scintillation data from Huancayo plus spaced-receiver measurements from Ancon. On this date the first Fresnel minimum frequency was f_1 = 0.145 Hz (spectrum not shown), which corresponds to $V_\perp$ = 116 m s^{-1}. Considering the geometry of observations, the derived V_{EW} = 131 m s^{-1}. The actual spaced-receiver measurements, on the other hand, shown in Figure 6, yield a value of 140 m s^{-1}, in very good agreement with that derived on the basis of the Fresnel minima.

The presence of Fresnel modulations in the scintillation spectrum requires the major scintillation effect to be caused by a concentrated layer of irregularities. On the other hand, the apparent discrepancy between the Gaussian form of BSS irregularities measured in situ and the small (−2 to −3) power law index of the associated scintillation spectrum can be explained if the irregularities are distributed over an altitude interval having a variation of the characteristic scale size with altitude. Modeling of the temporal structure of scintillations caused by BSS irregularities, as was done by Franke and Liu [1983] for bubble-type irregularities, is necessary to derive correct estimates of the irregularity layer thickness and the appropriate variation of the characteristic scale size. Such efforts may also resolve whether the persistent absence of gigahertz scintillations in the case of BSS irregularities is due to their Gaussian power spectrum having low PSD at short spatial wavelengths or a generally reduced level of integrated electron density deviation caused by the small irregularity layer thickness.

REFERENCES

Basu, S., and H. E. Whitney, The temporal structure of intensity scintillations near the magnetic equator. Radio Sci., 18, 263, 1983.

Basu, S., Su. Basu, J. Aarons, J. P. McClure, and M. D. Cousins, On the coexistence of kilometer- and meter-scale irregularities in the nighttime equatorial F region, J. Geophys. Res., 83, 4219, 1978.

Basu, S., J. P. McClure, Su. Basu, W. B. Hanson, and J. Aarons, Coordinated study of equatorial scintillation and in situ and radar observations of nighttime F region irregularities, J. Geophys. Res., 85, 5119, 1980.

Basu, S., Su. Basu, J. LaBelle, E. Kudeki, B. G. Fejer, M. C. Kelley, H. E. Whitney, and A. Bushby, Gigahertz scintillations and spaced receiver drift measurements during Project Condor

equatorial F region rocket campaign in Peru, *J. Geophys. Res.*, in press, 1986.

Basu. Su.. S. Basu. J. P. McClure. W. B. Hanson, and H. E. Whitney, High-resolution topside in situ data of electron densities and VHF/GHz scintillations in the equatorial region, *J. Geophys. Res.*, *88*, 403, 1983.

Cragin, B. L.. C. E. Valladares. W. B. Hanson, and J. P. McClure, Bottomside sinusoidal irregularities in the equatorial F region, 2. Cross correlations and spectral analysis, *J. Geophys. Res.*, *90*, 1721, 1985.

Cronyn, W. M., The analysis of radio scattering and space probe observations of small-scale structure in the interplanetary medium, *Astrophys. J.*, *161*, 755, 1970.

DasGupta, A.. S. Basu, J. Aarons, J. A. Klobuchar, Su. Basu, and A. Bushby, VHF amplitude scintillations and associated electron content depletions as observed at Arequipa, Peru, *J. Atmos. Terr. Phys.*, *45*, 15, 1983.

Franke. S. J.. and C. H. Liu, Observations and modeling of multifrequency VHF and GHz scintillations in the equatorial region, *J. Geophys. Res.*, *88*, 7075, 1983.

McClure, J. P.. W. B. Hanson, and J. H. Hoffman, Plasma bubbles and irregularities in the equatorial ionosphere, *J. Geophys. Res.*, *82*, 2650, 1977.

Rastogi. R. G.. and J. Aarons, Nighttime ionospheric radio scintillations and vertical drifts at the magnetic equator, *J. Atmos. Terr. Phys.*, *42*, 583, 1980.

Singleton, D. G.. Power spectra of ionospheric scintillations, *J. Atmos. Terr. Phys.*, *36*, 113, 1974.

Valladares, C. E.. W. B. Hanson, J. P. McClure, and B. L. Cragin,

Bottomside sinusoidal irregularities in the equatorial F region, *J. Geophys. Res.*, *88*, 8025, 1983.

Weber, E. J.. and J. Buchau, Polar cap F layer auroras, *Geophys. Res. Lett.*, *8*, 125, 1981.

Weber. E. J.. H. C. Brinton, J. Buchau, and J. G. Moore, Coordinated airborne and satellite measurements of equatorial plasma depletions, *J. Geophys. Res.*, *87*, 503, 1982.

Weber, E. J.. J. Aarons, and A. L. Johnson, Conjugate studies of an isolated equatorial irregularity region, *J. Geophys. Res.*, *88*, 3175, 1983.

Wernik, A. W.. C. H. Liu, and K. C. Yeh, Modeling of spaced receiver scintillation measurements, *Radio Sci.*, *18*, 743, 1983.

Whitney, H. E., Notes on the relationship of scintillation index to probability distributions and their uses for system design, *Rep. AFCRL-TR-74-0004*, Air Force Cambridge Res. Lab., Bedford, Mass., 1974, AD778092.

Woodman. R. F., East-west ionospheric drifts at the magnetic equator, *Space Res.*, *12*, 969, 1972.

S. Basu and H. E. Whitney, Air Force Geophysics Laboratory, Hanscom Air Force Base, MA 01731.

Su. Basu, Emmanuel College, Boston, MA 02115.

A. DasGupta, Institute of Radio Physics and Electronics, University of Calcutta, India.

C. E. Valladares, Radio Physics Laboratories, SRI International, Menlo Park, CA 94025.

The Condor Equatorial Spread F Campaign:
Overview and Results of the Large-Scale Measurements

M. C. Kelley,[1] J. LaBelle,[1] E. Kudeki,[1,2] B. G. Fejer,[1] Sa. Basu,[3,4] Su. Basu,[3] K. D. Baker,[5] C. Hanuise,[6]
P. Argo,[7] R. F. Woodman,[8] W. E. Swartz,[1] D. T. Farley,[1] and J. W. Meriwether, Jr.[9]

During the Condor campaign a number of instruments were set up in Peru to support the rocket experiments. In this series of papers we report on the results of the experiments designed to study the equatorial F region. In this overview paper we summarize the main results as well as report upon the macroscopic developments of spread F as evidenced by data from backscatter radars, from scintillation observations, and from digital ionosonde measurements. In this latter regard, we argue here that at least two factors other than the classical gravitational Rayleigh-Taylor plasma instability process must operate to yield the longest-scale horizontal organization of spread F structures. The horizontal scale typical of plume separation distances can be explained by invoking the effect of a shear in the plasma flow, although detailed comparison with theory seems to require shear frequencies a bit higher than observations indicate. On the other hand, the largest-scale organization or modulation of the scattering layer cannot be explained by the shear theory and must be due to local time variations in the ionospheric drift or to gravity wave induced vertical motions. Using simultaneous rocket and radar data, we were also able to confirm the oft quoted hypothesis that rapid overhead height variations in the scattering region over Jicamarca are primarily spatial structures advecting overhead. The detailed rocket-radar comparison verified several other earlier results and speculations, particularly those made in the PLUMEX experiments. In particular, companion papers discuss and extend some of the PLUMEX results to include the role of anomalous diffusion (LaBelle et al., this issue) in the theory of equatorial spread F and to shed light upon the shallow spectral form often observed in the intermediate-scale regime (LaBelle and Kelley, this issue).

1. Introduction

Equatorial F region irregularities, also known as equatorial spread F or ESF, have been studied extensively over the last few decades with a variety of experimental techniques including radars, scintillations, radio sounders, in situ rocket and satellite detectors, and a number of theoretical methods. Recent reviews of the topic include those by *Fejer and Kelley* [1980], *Ossakow* [1981], *Kelley and McClure* [1981], *Kelley* [1985], and *Basu and Basu* [1985].

As a part of project Condor a variety of instruments were clustered together near the magnetic equator to perform coordinated measurements of the same spread F events simultaneously. The idea behind the "cluster technique" is to learn more from a set of simultaneous measurements than can be learned from the individual experiments operated independently. The instruments used, along with their locations and operating institutions, are listed in Table 1. The locations are

also indicated on the map in Figure 1. Two Terrier-Malemute rockets instrumented with electric field, plasma density, and energetic particle detectors were launched from the Punta Lobos Rocket Range (1 in Figure 1) in the approximately southward and southwestward trajectories indicated in Figure 1. The Jicamarca Radio Observatory (JRO), located to the north of the rocket range (2), provided continuous monitoring of 3-meter (3-m) F region irregularities with backscatter power and interferometric drift velocity measurements at an operation frequency of 50 MHz. At Ancon (3) a 14-MHz HF radar was operated to monitor the evolution of 10-m density irregularities. Scintillations and spaced receiver drift measurements were also conducted at the same location using several satellite transmissions. Analog and digital ionosonde measurements were conducted at the Huancayo station (4) (where VHF and UHF scintillation measurements were also performed), while Fabry-Perot measurements of neutral winds were made at Arequipa (just south of the region shown in Figure 1). The rocket project was a joint undertaking by the National Aeronautics and Space Administration of the United States and the Comisson Nacional de Investigacion y Desarrollo Aerospacial (CONIDA) of Peru, and the JRO operations were a joint effort by the Instituto Geofisico del Peru and the National Science Foundation of the United States. A number of other results from Condor dealing with the equatorial electrojet, the critical velocity effect, middle atmospheric electrodynamic, etc., are published elsewhere.

The equatorial spread F aspects of the Condor project form part of a series of similar projects, which utilized simultaneous rocket and radar probing of the disturbed equatorial F region ionosphere. The series began on 1972 in India [*Balsley et al.*, 1972] and was followed by campaigns in Brazil [*Kelley et al.*, 1976], Peru [*Morse et al.*, 1977], Kwajalein [*Szuszczewicz et al.*, 1980], and India (S. Prakash, personal communication, 1983). During this same interval, great theoretical advances have occurred, particularly with respect to computer simula-

[1] School of Electrical Engineering, Cornell University, Ithaca, New York

[2] Now at Department of Electrical Engineering, University of Illinois, Urbana

[3] Emmanuel College, Boston, Massachusetts

[4] Now at Air Force Geophysics Laboratory, Hanscom Air Force Base, Massachusetts.

[5] Center for Atmospheric and Space Sciences, Utah State University, Logan

[6] Laboratoire de Sondages Electromagnétiques de l'Environnement Terrestre, University of Toulon, France

[7] Los Alamos National Laboratory, Los Alamos, New Mexico

[8] Instituto Geofisico del Peru, Lima

[9] Space Physics Research Laboratory, University of Michigan, Ann Arbor

82

TABLE 1. Instrumentation Used During Project Condor, With the Locations and Operating Institutions

Instrumentation	Location	Institution(s)
Two Terrier-Malemute rocket-borne payloads	Punta Lobos Rocket Range	NASA, CONIDA, Cornell University, Utah State University, University of Illinois
50-MHz radar	Jicamarca	Instituto Geofisico del Peru, Cornell University National Science Foundation
14-MHz radar	Ancon	University of Toulon
VHF and UHF scintillation VHF spaced receiver system	Ancon	Air Force Geophysical Laboratory
Digital ionosonde	Huancayo	Los Alamos National Laboratory
Fabry-Perot interferometer	Arequipa	University of Michigan
Ionogram records and magnetometer	Huancayo	Instituto Geofisico del Peru

tion of ESF. The rocket experiments mentioned above solidi-fied the importance of the generalized Rayleigh-Taylor insta-bility as the basic theoretical construct about which to under-stand equatorial spread F. In addition, the results of the latter campaign, which has often been referred to as the PLUMEX experiments (Plume Experiments; actually PLUMEX I and PLUMEX II since there were two rockets launched), brought to light some important new aspects of the ESF problem which were not included in the computer simulations For example. Kelley et al [1982a] and Kelley [1982] interpreted the electric field and density fluctuation spectra in the transi-tional wavelength (≤200 m) range as due to a drift wave mode This important result was supported by a similar detec-tor on the same rocket [Singh and Szuszczewicz, 1984] but not, prior to Condor, in an independent geophysical event Similarly, the PLUMEX data indicated that a density fluctu-ation spectral form may exist in the intermediate wavelength range which is quite different from that predicted by simula-tions [Rino et al. 1981. Kelley et al. 1982b] Part of the purpose of the Condor ESF experiments was to verify and understand these important results and their implication for ESF theory As we shall see, this was accomplished, and new insights were obtained concerning the crucial role played by anomalous diffusion in determining the nonlinear saturation of ESF [LaBelle et al. this issue] and concerning the possible origins of the surprising shallow spectral form [LaBelle and Kelley, this issue]

The detailed results of the Condor coordinated F region experiments are reported in the series of papers published in this issue In this paper we present an overview of the experi-mental results and in addition report on some new aspects of the large-scale organization of plasma during ESF which are based primarily upon the radar backscatter maps made during the course of the rocket launch operation We also summarize some of the main conclusions of the set of experiments

2 DATA PRESENTATION

2.1 Backscatter Maps and Scintillation Measurements on Nights Without Rocket Launches

Real-time measurements at the Jicamarca Radio Observa-tory of backscattered power from 3-m F region irregularities

played a crucial role in the rocket launch decisions of the Condor spread F campaign. In such measurements the re-ceived backscattered power is proportional to the square of the amplitude of the field-aligned density irregularities which have wave vectors in the direction of the radar line of sight. The Jicamarca radar beam is pointed almost vertically, about 3° north of the on-axis position, to achieve perpendicularity to the geomagnetic field at F region altitudes [see Woodman, 1970]. Power maps similar in essence to those published else-where in the literature [e.g., Woodman and LaHoz, 1976] were generated in real time to monitor the spread F activity level during the campaign. When rocket launch decisions were taken, the radar operation was switched to the more versatile radar interferometer mode capable of measuring the power spectra of the radar echoes as well as the east-west drift veloci-ty of the scattering centers [Kudeki et al., 1981] In this section we present Jicamarca data obtained on nights with no rocket launches The interferometer mode was not used on these nights, and the data presentation is limited to the power maps shown in Figures 2a-2c

The upper panel in each figure is the radar map, while the lower panel is a plot of the scintillation index (SI) expressed in decibel excursions [Whitney et al., 1969] at a frequency of 1.694 gigahertz (GHz) The latter data were obtained at Ancon using the GOES 5 satellite transmissions with an ionospheric intersection point at 300 km altitude only 30 km west of the Jicamarca beam This distance is equivalent to only 3-5 min of time difference between the corresponding structures caus-ing scintillation and radar backscatter when the eastward ionospheric drift is taken into account The relationship be-tween SI and the commonly used S_4 index as obtained by Whitney [1974] is given in the Figure 2a caption At such high frequencies the scintillations conform to weak scatter theories,
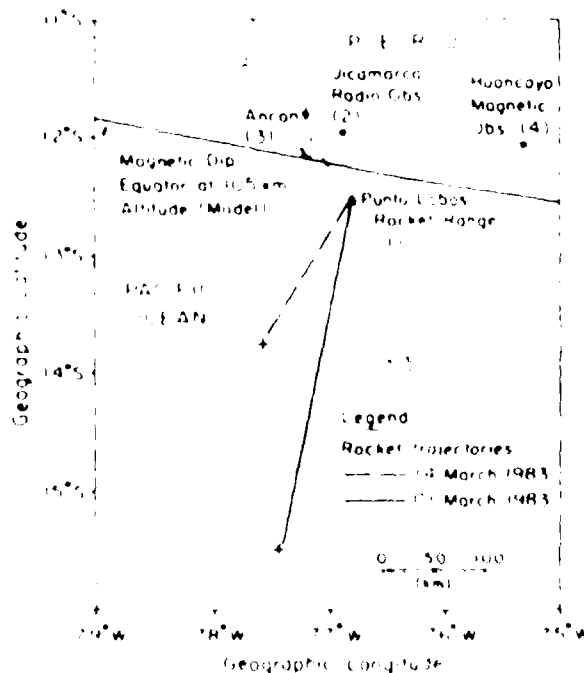
Fig 1 Map of the coast of Peru, showing the trajectories of the two spread F rockets as well as the locations of various ground based instrumentation
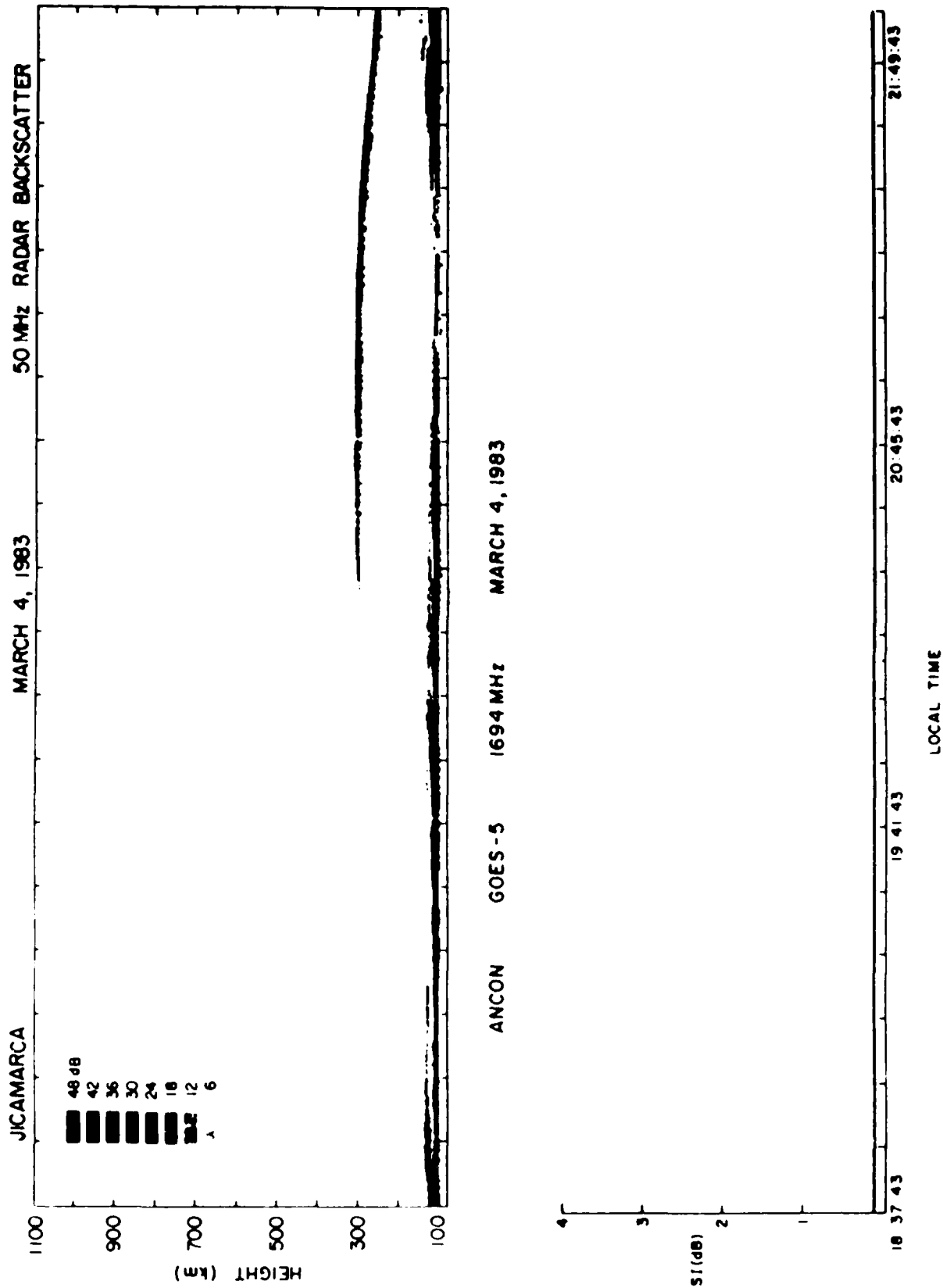
Fig. 2a. The top panel displays the backscatter power at 50 MHz observed at Jicamarca on the night of March 4, 1983, as a function of time and altitude. The bottom panel is a plot of the SI index of the 1694-MHz signal observed at Ancon. The SI index is the peak-to-peak signal fluctuation amplitude in decibels [Whitney et al., 1969]. Some discrete relationships between SI and S_4 are 1 dB = 0.075, 3 dB = 0.17, 6 dB = 0.3, and 10 dB = 0.45.
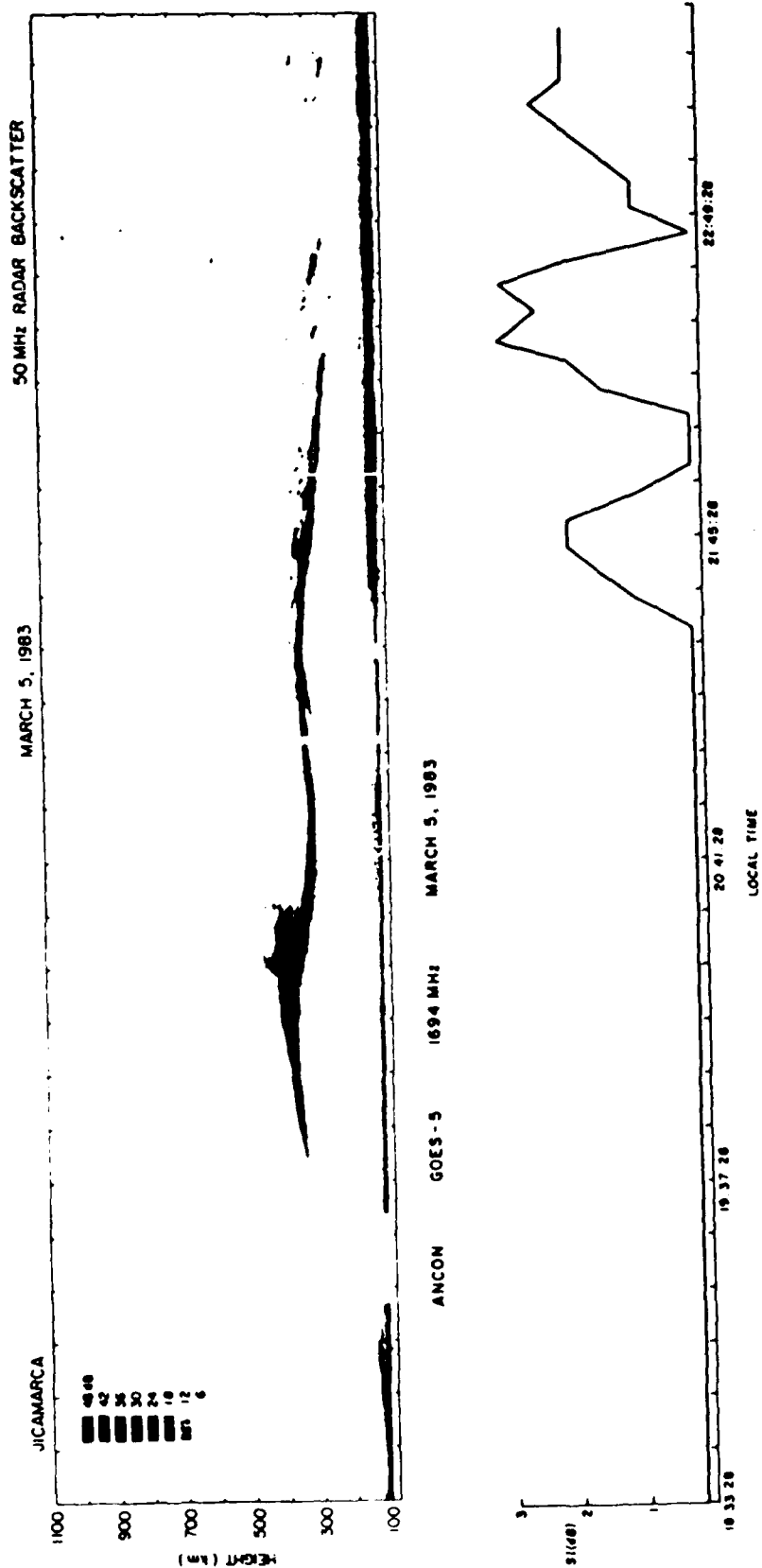
Fig. 2b   Same as Figure 2a, but for the night of March 5, 1983.
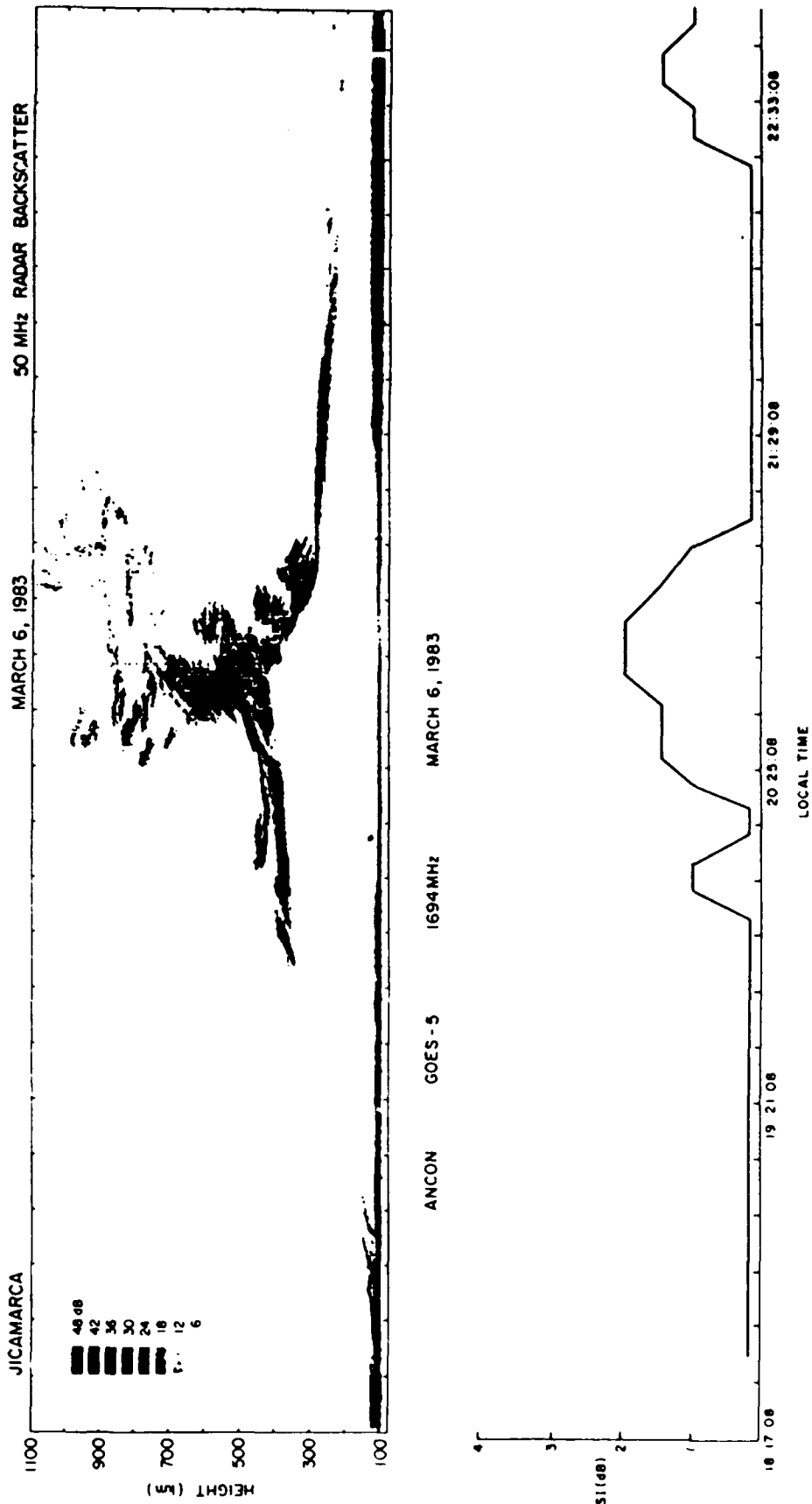
Fig. 2c. Same as Figure 2a, but for the night of March 6, 1983.
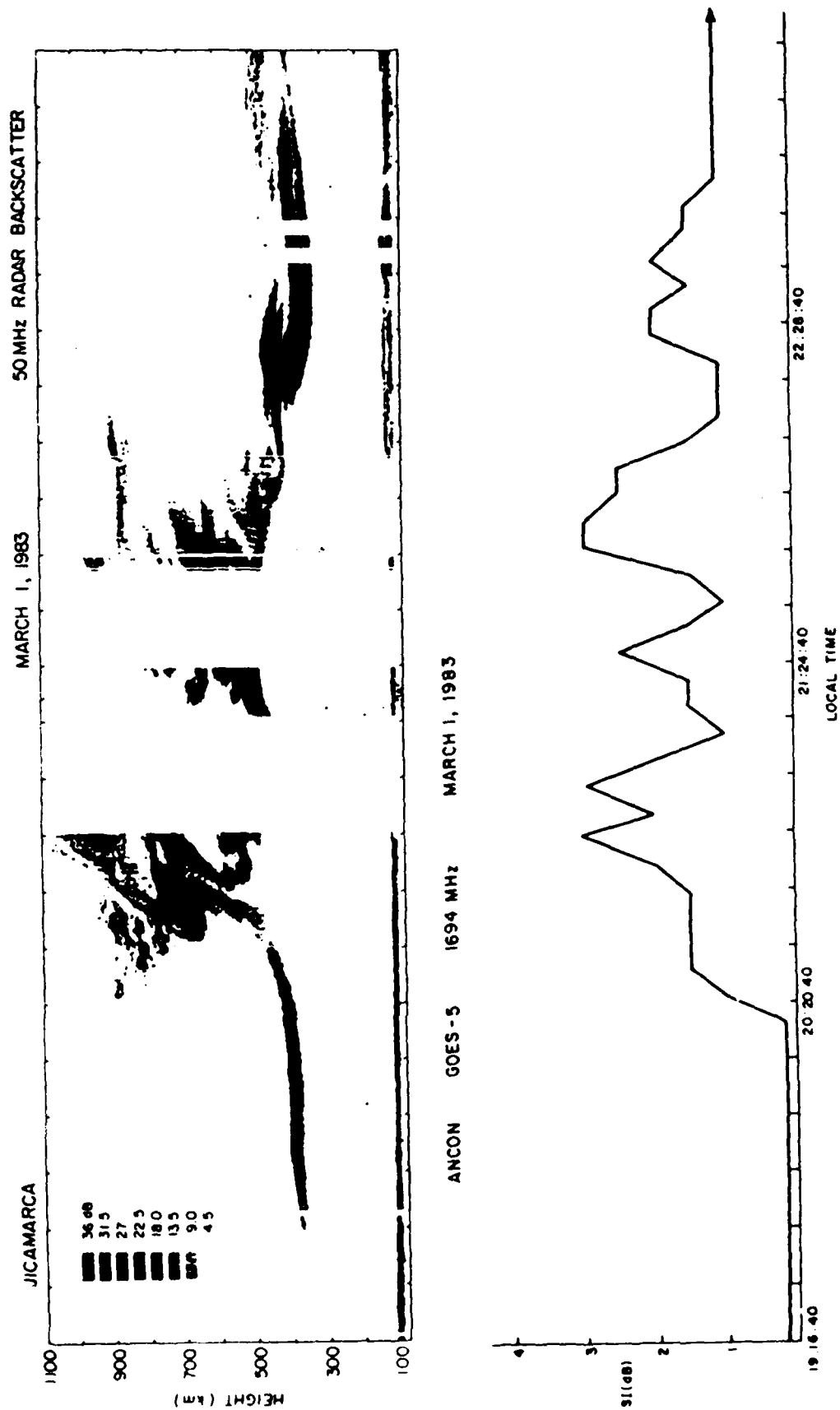
Fig. 3a. The top panel displays the Jicamarca 50-MHz backscatter power map recorder the night of March 1, 1983. The mottled portion around 2150 LT indicates the time period when the radar was operated in the interferometer mode, and the data gaps near 2104 LT and 2134 LT result from software tests which were conducted before the rocket launch. The bottom panel shows the scintillation index at 1694 MHz observed at Ancon during the same time period.

87

Jicamarca Radio Observatory
March 1, 1983
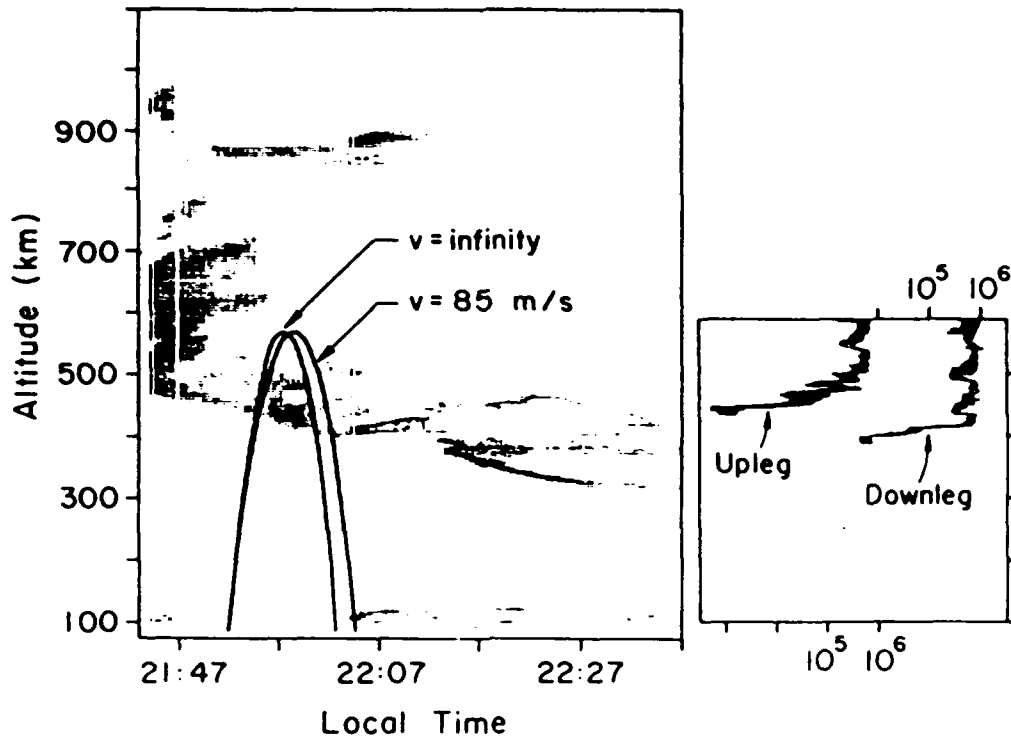
Fig. 3b. Expanded version of the Jicamarca radar power map with the rocket trajectory superposed. The inset at right illustrates the relative electron density profile obtained from a rocket-borne Langmuir probe. The densities listed assume a constant relationship between collected current and density equal to the value found near apogee on the second flight.

and a linear relationship holds between the S_4 index and the irregularity strength or electron density deviation (ΔN). At 1.7 GHz, scintillations are caused by irregularities in the range 35–350 m in dimension. We should therefore not expect a one-to-one relationship between 50-MHz backscatter, which is caused by 3-m irregularities, and the 1.7-GHz forward scatter.

In viewing the Jicamarca power maps it is important to remember that they provide vertical images or slices of the instantaneous overhead scattering structures which are then plotted as a function of time. A rigid scattering pattern drifting overhead with a constant velocity would be faithfully reproduced in these plots, and in this case the map can be considered as a view of the ionosphere looking southward. As pointed out by *Woodman and LaHoz* [1976], however, the technique is much like the slit cameras used in racing events which distort an image if it changes in time as it drifts by. In the description we try to remind the reader of this by using the words "apparent" to describe the motion of the scattering layer. Power maps display the echo power received by the Jicamarca radar, as functions of time and altitude, using a logarithmic gray scale coding. For each day a power level of 0 dB on these maps roughly corresponds to 3% of the estimated sky noise. There was no attempt made to maintain a uniform output power from day to day, but the scales differ by only ±6 dB.

The power maps of Figure 2 are representative of common types of spread F events observed at Jicamarca. In these plots the tick marks indicate 10.67 min (six ticks corresponding to

64 min). Throughout the discussion below, reference will be made to the local time at the 75° meridian—the time indicated in the plots. On March 4, 1983, a thin (10 km) scattering layer developed at about 2020 LT (Figure 2a). The position of the scattering layer was moving upward at an apparent velocity of about 2.5 m/s but never attained a height greater than 300 km. At "apogee" the layer broadened very slightly to a thickness of about 15 km. As the scattering layer descended, its thickness decreased. The structured echoing region near 100 km is due to 3-m irregularities excited by the equatorial electrojet instabilities. Notice that there are three gaps in the electrojet echoes at 2105, 2133, and 2141 LT when the F layer is hovering near its highest point. Furthermore, close inspection shows that the E layer scattering heights shift in altitude across the gaps as predicted by the linear electrojet theory when the zonal electric field changes sign [*Fejer et al.*, 1975]. This feature is fairly common, and the interpretation is that the E layer instabilities cease temporarily when the zonal electric field component passes through zero. Thus, even though the upward "motion" of the scattering layer is not a definitive measure of the actual vertical drift, the data are internally consistent with a pure bottomside F layer instability commencing while the F layer is rising and continuing virtually unchanged when the vertical drift reverses. The temporal behavior of the scattering height is also consistent with the well-established time dependence of the vertical drift velocity which creates a corresponding local time dependence of the ionospheric height. As the earth rotates under this local time de-

pendent feature, the ionosphere will seem to rise and then fall to a vertically looking radar. No detectable level of scintillation occurred at 1.7 GHz.

The March 5 night, illustrated in Figure 2b, was considerably more active than the previous example. The echoing layer started its development at an altitude higher than that on March 4. Just at and after "apogee" the layer broadened considerably, but no extended plumes developed, and the layer height decreased very quickly. The layer height then started to increase again, reaching 330 km before starting its final decrease for this evening. Notice that three distinct scattering patches developed in the second descending phase of the ionospheric oscillation and that the height oscillations were nearly sinusoidal in form. The characteristic gap in E region structure discussed above occurred only in conjunction with the second apogee, although the 100-km scattering layer became slightly more narrow in conjunction with the first apparent flow reversal. (When gaps occur in both the E and F region traces, they are due to a data loss.) The variations in altitude displayed on this night are much more rapid than those expected from the local time dependent zonal electric field effect described above. A number of weak 3-m scattering patches remained for a long time, including one between 500 and 600 km. The scintillation behavior on this night was very unusual; we return to this point after discussing the March 6 event.

On March 6 (Figure 2c) a spectacular plume event occurred over Jicamarca. The layered echoes commenced at 350 km altitude, considerably higher than on March 4. By 2010 LT the scattering layer was extended in altitude and displayed a bifurcated form. The height of the scattering layer increased abruptly at about 2025 LT, and shortly thereafter, a large plume event commenced which extended at times to more than 1000 km altitude. It is important to note that the highest-altitude scatterers were detected even before the plume feature was seen overhead between 400 and 600 km, and that three distinct miniplumes developed as the scattering layer descended. In this classic example of Murphy's law, a power failure occurred at the rocket range between 2025 and 2100 LT, precluding any rocket launch on this night.

At first glance, the scintillation data seem well correlated with the radar observations. A burst of strong gigahertz scintillation accompanied the bifurcation at 2010. This was followed by a long-lived event commencing at 2017 and lasting throughout the major plume event. The VHF scintillation index remained saturated during this event. At 2222 the scintillation level again rose dramatically, however, this time accompanied only by very weak patches of 3-m backscatter. One of these patches was centered at 360 km, even though the bottomside of the F layer was barely higher than 200 km at that time. The scintillation is nearly as strong as that associated with the plume itself and is more typical of previously published postmidnight events [Basu et al., 1978]. Clearly the ~300-m structures are still very large in amplitude even though the 3-m waves have virtually disappeared.

Returning to the scintillation data on March 5, we note that the scintillation index reached values well above those associated with the major plume event on March 6 but were associated with only faint traces of 3-m backscatter. These patchy traces of 3-m backscatter were extended in altitude. Thus the pattern of scintillation data observed on March 5 resembles that observed late in the evening on March 6. It is possible that the first backscatter structure of the March 5 evening, characterized by an absence of scintillations, may have evolved directly over Jicamarca and drifted eastward so that it

was not intercepted by the propagation path to the satellite. Similar events were discussed by Aarons et al [1980]

2.2. Data Obtained on March 1-2, 1983

The backscatter power and scintillation data obtained on the evening of March 1-2, 1983, are presented in Figure 3a This was the first night during which all the necessary radar analysis and display programs were functional, and some last minute testing led to the data gaps in the plot. The rectangular mottled area centered at about 2155 corresponds to the period when the radar was operated in the interferometer mode. In this mode the whole antenna array is used for transmission, but the backscattered signal is received independently by both the east and west quarters of the array, whose phase centers are separated by about 203 m. The phase difference between the simultaneous samples from these two quarters is related to the angular position of any localized scattering centers inside the common scattering volume. The east-west drift velocity of these localized scatterers is derived from the temporal changes of the measured positions [see Kudeki et al., 1981, Fejer et al., 1985]. Since vast amounts of raw data must be recorded for off-line processing, a smaller altitude range was sampled in the interferometer mode than in the power map modes before and after.

The figure shows an initial plume event centered at 2040 which followed a rapid apparent rise of the scattering layer and was preceded by high-altitude scatterers by some 10 min Although the data gap creates some ambiguity, it appears that the layer descended and then began to rise once again at about 2120 LT, creating the second plume event into which the rocket was fired. The lower trace shows the results of simultaneous L band (1694 MHz) scintillation measurements performed at Ancon. Using the eastward F region drift speed measured by two independent methods (described below) for this night, the separation distance between these two measurements corresponds to only 3-5 min of local time difference The data gaps are somewhat of a problem, but there again seems to be a good correlation between the SI index and the 3-m backscatter power. In particular, the thickness of the 3-m scattering patch and the magnitude of SI seem to be very well correlated. The backscatter map displays several "miniplumes" which extend like fingers pointing toward later local times (or pointing westward, if the features of these maps are considered frozen in the eastward drifting plasma). These features are similar to the secondary plumes detected with the Altair radar

Figure 3b is an expanded version of the power map in Figure 3a and includes the rocket trajectory, which is plotted in two ways. The "V = infinity" parabola is plotted as though the radar and rocket observations were simultaneous in local time as well as in universal time. However, since the rocket traveled magnetically west of the radar while the ionosphere was drifting eastward, the rocket data at a certain time should be compared with the radar data a short time later, the exact time delay depending on the time it takes the ionospheric plasma to drift from the rocket's location to the longitude of Jicamarca [Morse et al., 1977]. The second parabola includes the F region ionospheric drift of about 85 m/s as measured by the interferometer techniques during the shaded time period Since the rocket trajectory also had a significant component magnetically southward, such a comparison relies upon the field-aligned nature of large-scale F region structures Tsunoda [1981] has used the steerable incoherent scatter Altair radar to show that large-scale (≈50 km) features indeed do map along the magnetic field lines for large distances Airglow data
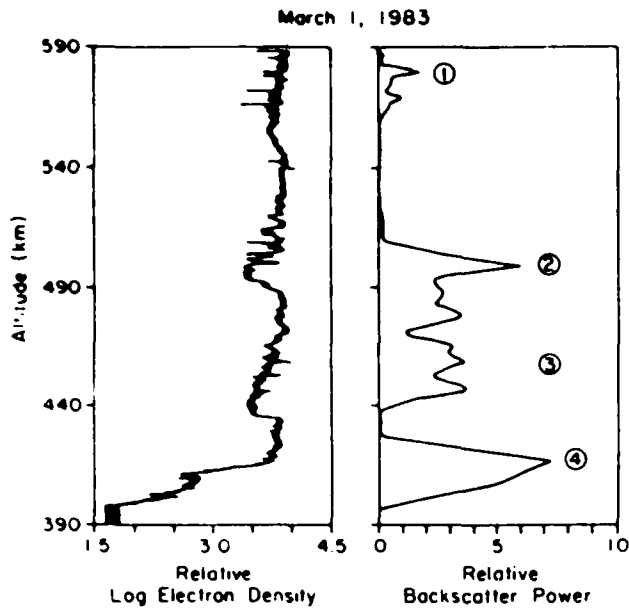
March 1, 1983

Fig. 4. Comparison between the relative electron density profile obtained from the rocket-borne probe and the relative backscatter power measured with the Jicamarca radar, which is sensitive to 3-m irregularities.

at conjugate off-equatorial latitudes also show this mapping quite clearly [*Mendillo and Tyler*, 1983].

The right-hand panel of Figure 3b displays electron current profiles detected by a fixed-bias Langmuir probe which are approximately proportional to the electron density. During the upleg of the rocket flight the steep upward gradient in plasma density and the associated irregularities observed at the bottomside of the F region coincide extremely well with the band of 3-m turbulence observed by the radar and first encountered by the rocket at 445 km altitude. On the downleg the lower edge as observed by the rocket-borne probe was nealy 40 km lower in altitude than on the upleg. This is in good agreement with the radar observations, which show that the layer height was decreasing over Jicamarca during this time. The small discrepancy between the downleg rocket data and the radar data can be explained quantitatively by the change in altitude of the field line which maps from the rocket's position to the latitude of Jicamarca. These data show conclusively that the bottom side of the F layer was higher over Jicamarca than at the rocket when it passed through the bottomside on the downleg. This implies that (1) a strong westward gradient in plasma density must exist and (2) for rapid height variations such as these the interpretation of the Jicamarca map in terms of a quasi-rigid motion of the scattering regions is valid at least for the bottomside.

In the topside the in situ probe detected several large regions of depleted electron density, along with associated smaller-scale irregularities. The amplitude of the depletions is about 50%, and their vertical size is in the range of 20–50 km. On the downleg, depletions of nearly identical properties were detected. On both downleg and upleg these depletions correspond one-to-one with the westward tilted miniplumes seen on the radar power map. Figure 4 illustrates more clearly this correlation between the depletions encountered by the rocket and the miniplumes in the radar backscatter power map. Only the downleg Langmuir probe data are plotted, and the altitude of the radar backscatter power has been adjusted in order to make a comparison more accurate, since the rocket moves magnetically south, intersecting field lines which map to higher altitudes at the equator above Jicamarca, as noted above. In Figure 4 an excellent correlation is observed between the radar backscatter power and those regions of upward directed density gradients detected by the rocket, as well as with the intermediate-scale fluctuations apparent to the eye in the rocket data.

Zonal plasma drift data are plotted in Figure 5 for both this day and the March 14–15 event discussed below. These velocity profiles were obtained using the Jicamarca radar interferometer procedure described by *Kudeki et al.* [1981]. Interferometer observations were made for about 15 min on each night, corresponding to the shaded regions in Figures 3a and
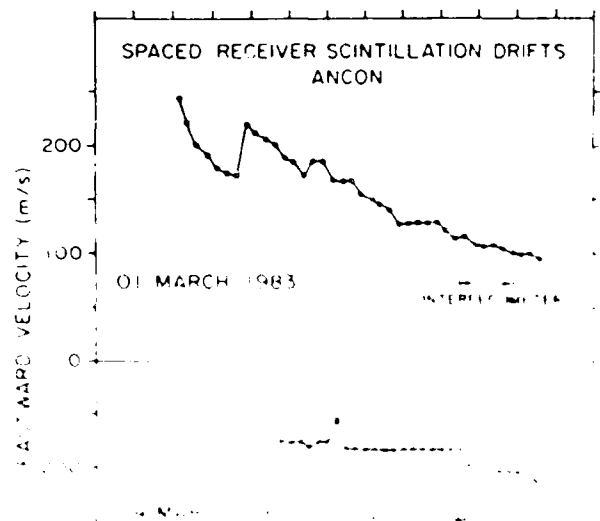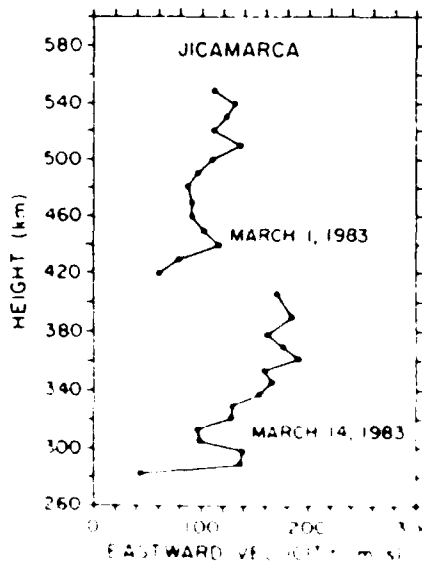

Fig. 5. F region zonal plasma drifts measured with the interferometer technique. Each curve represents the average during the periods indicated in Figures 3a and 3b.
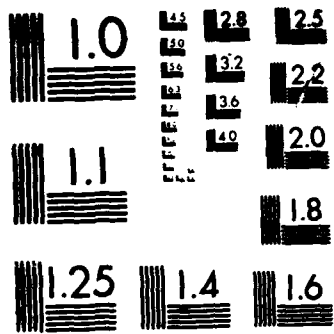
MICROCOPY RESOLUTION TEST CHART
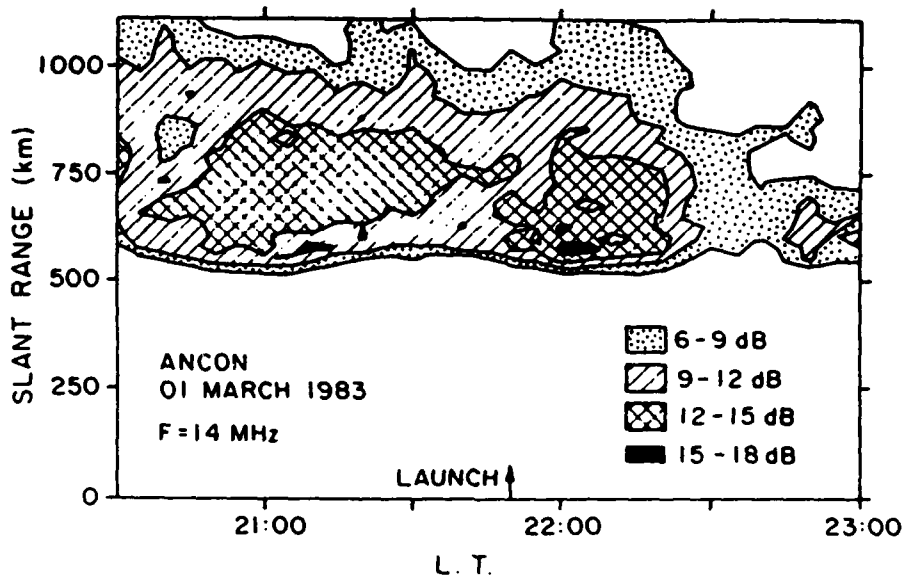
NATIONAL BUREAU OF STANDARDS 1963-A

Fig. 7.   Radar backscatter power measured with the 14-MHz radar at Ancon.

8a, but velocity measurements are only possible during periods and at heights where discrete scatterers are present. As a result, velocity estimates could not be made over the entire scattering region; velocities are plotted in Figure 5 only at altitudes for which discrete scatterers were present during at least 2 min of the 15-min interval, and in each case, the average value of drift velocity over the 15-min interval is plotted. The observed velocities are variable in time and height. On the night of March 1, 1983, the velocity in the region of the strongest echoes was about 90 m/s. A vertical shear in the zonal flow with mean value of 6×10^{-4} s^{-1} is indicated since the flow increases from about 60 m/s at 420 km to over 120 m/s at 520 km.

Drift measurements were also made using the spaced receiver scintillation technique which is sensitive to subkilometer irregularities. These measurements were made at 244 MHz with a short (123 m) and a long (246 m) baseline [Basu and Whitney, 1983]. The temporal variations of the apparent velocities during March 1 and March 14 are shown in Figure 6. The spaced receiver scintillation drifts are in fairly good agreement with the interferometer drifts on March 1 but are somewhat larger than the corresponding Jicamarca measurements made on March 14.

We turn now to HF backscatter measurements made at Ancon. A range-time-intensity plot of the echoes received at 14 MHz, corresponding to a backscatter wavelength of 10 m, is presented in Figure 7. In this experiment the antenna was directed upward, but because of the wide beam, echoes were obtained from angles ±30° from vertical. It seems that the strongest HF scatter originates from the bottomside spread F at a slant range of about 550 km. This scatter corresponds to the strong echoes received at Jicamarca at around the same altitude. However, note that the shortest range at which 14-MHz echoes were received is somewhat longer than the lowest-altitude 3-m echoes observed by Jicamarca; this is probably an indication of the relative sensitivity of the two radars. The extension of the 14-MHz echoes to over 1000 km in range is due to oblique returns. Representative spectra at a fixed range (500 km) (not shown) are very narrow and display sequences of Doppler shifts which changed from negative to positive over the 1-hour period 2145-2245 LT. Because of the

antenna beam width, this variation is most probably due to the horizontal motion of scatterers across the beam (the radar measures the radial line-of-sight velocity). If the scatterers which produce these spectra originate approximately from the same altitude as the strongest backscatter observed by Jicamarca, then the variation of the Doppler spectra as a function of time indicates an average drift velocity of about 100 m/s. This value agrees well with the interferometer and spaced receiver drift measurements. No digital ionosonde data were available on this night.

2.3.   Data Obtained on March 14-15, 1983

Composite data presentations for the night of March 14-15 are given in Figures 8a and 8b. In this case, the electron density profile displayed in the inset of Figure 8b was obtained from two different rocket-borne instruments. An RF probe determined the absolute electron density by locking onto the local upper hybrid frequency in the plasma when the plasma density exceeded about 10^5 cm^{-3} [Baker et al., 1969, 1985]. At lower densities the data profile was extended using the relative density measurement from the fixed-bias Langmuir probe, normalized to match the value of absolute density measured by the RF probe at 350 km.

The morphology of the March 14 event in many ways resembles the March 1 data set. The major difference is the altitude of the event. For example, the bottomside and F peak heights were more than 100 km lower on March 14-15. Once again, the steep upward gradient in plasma density and the associated irregularities observed at the bottomside of the F region coincide with the band of 3-m turbulence observed by the radar and encountered by the rocket between 290 and 340 km. A density depletion just below the F peak corresponds to the patch of 3-m irregularities at 360 km altitude. The scintillation index SI correlates well with the thickness of the backscatter region, although it commenced earlier than did the VHF scatter.

In the topside the in situ probe detected a distinct region of depleted electron density above 410 km altitude on the upleg. A nearly identical feature was observed on the downleg at a higher altitude. However, turning to the backscatter power

91

JICAMARCA   MARCH 14, 1983   50 MHz RADAR BACKSCATTER

ANCON   GOES-5   1694 MHz   MARCH 14, 1983
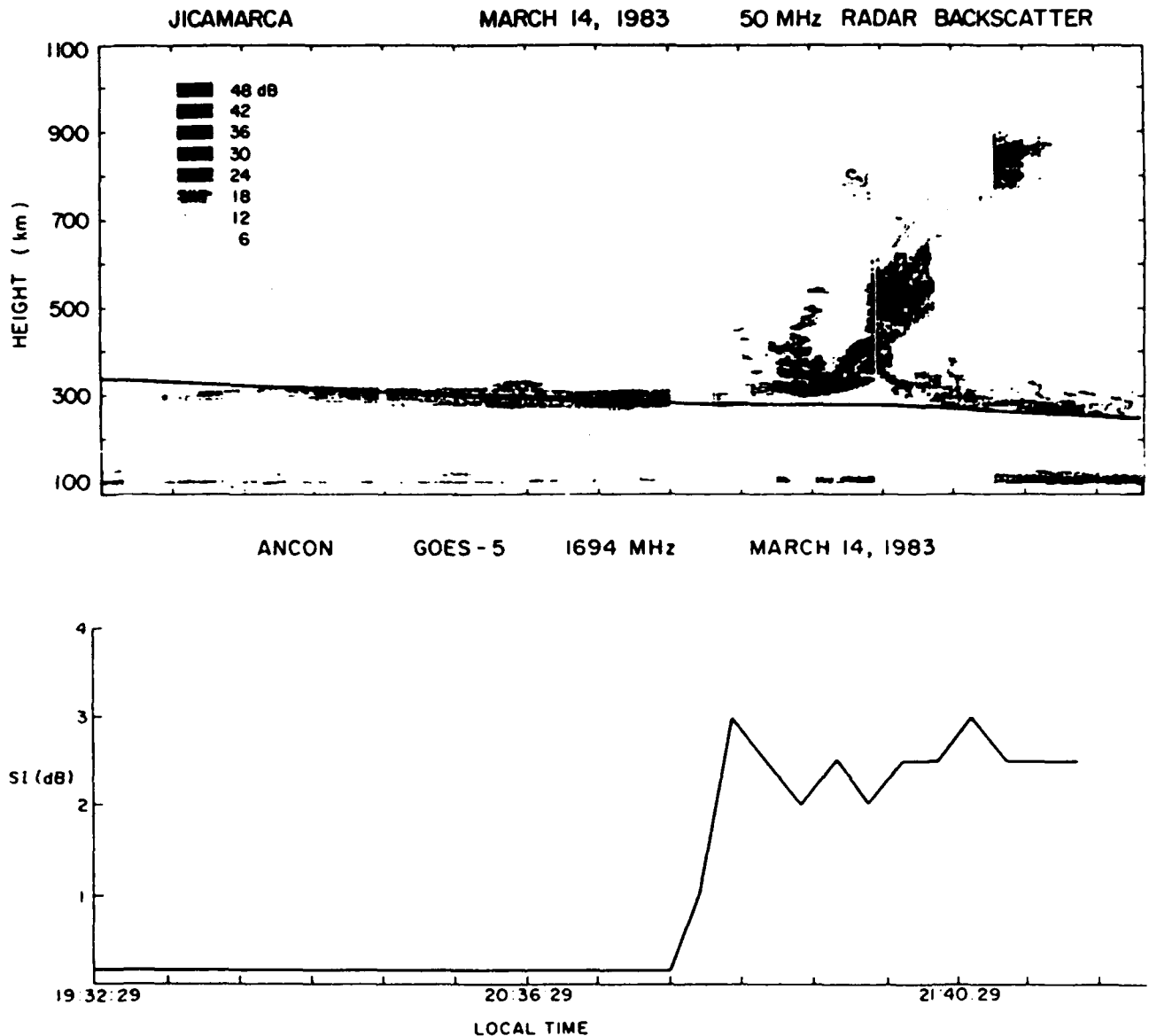
Fig. 8a.   The top panel displays the Jicamarca 50-MHz backscatter power map recorded the night of March 14, 1983. The solid line indicates the altitude h_{min} as measured from the ionosonde at Huancayo. The bottom panel shows the scintillation index at 1694 MHz observed at Ancon during the same time period.

map, within the range of sensitivity of the Jicamarca radar, no 3-m irregularities are seen during the portions of the rocket trajectory described above; that is, the "bubble" observed by the rocket during both upleg and downleg apparently was invisible to the radar by the time it was overhead. However, at an earlier local time (2133 LT), Jicama.ca did detect a westward tilted miniplume which, if extended, would intercept the rocket trajectory at about the right places. Furthermore, if we identify the upleg depletion with its downleg twin, observed 5 min later in local time and 40 km higher in altitude, there is a remarkable similarity to the March 1 data.

Interferometer drift data for this night were presented earlier in Figure 5 (upper trace). The observed drift again exhibits a strong vertical shear (8×10^{-4} s^{-1}), increasing from near 100 m/s to about 180 m/s over a 100-km height range. The comparison in Figure 6 shows that on both nights (March 1 and March 14), spaced-receiver drifts are higher than those measured by the interferometer. This seems to be a general

feature of the spaced receiver technique. In addition, the interferometer drift measurements indicate that the zonal plasma drift velocity can change significantly with height and time. The spaced-receiver drifts, on the other hand, yield information on the region with the largest electron density fluctuations. This intercomparison is discussed in more detail in a companion paper [Basu et al., this issue].

Figure 9 shows two spectra of the intermediate-scale density irregularities measured by the Utah State absolute density probe. The upper panel corresponds to turbulence in the topside well above the F peak, while the lower panel corresponds to the intense turbulence just above the peak in F region density. Comparison of the two spectra reveals a remarkable feature in the lower-altitude March 14 spectrum: the intermediate range of wavelengths is characterized by two distinct subranges, with a break in the spectrum near 1 km. The portion of the spectrum consisting of wavelengths smaller than about 1 km displays a k^{-n} form with spectral index $n \geq 2.5$,

92

Jicamarca Radio Observatory
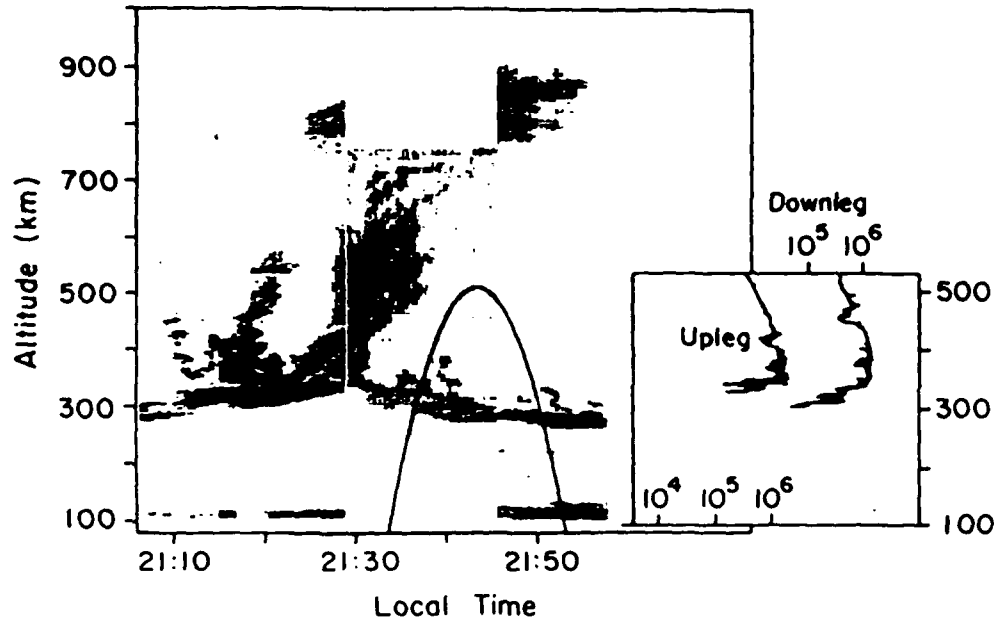## March 14, 1983

Fig. 8b. Expanded version of the Jicamarca radar power map with the rocket trajectory superposed. The inset at right shows the electron density profile obtained from the plasma frequency probe and extended using the Langmuir probe.

while for wavelengths longer than about 1 km the spectrum exhibits a smaller spectral index. This feature has been observed previously in in situ rocket spectra [Rino et al., 1981], and there is some evidence for such a variation in the spectral index of satellite-measured spectra [Livingston et al., 1981; Basu et al., 1983]. The generation of enhanced turbulence near and above the kilometer scale in spread F and in scintillation spectra is examined in detail in a companion paper [LaBelle and Kelley, this issue]. This height region corresponds to one which had very broad VHF spectral signatures (wide Doppler spectra), which also suggests a very turbulent medium.

Data from the digital ionosonde located at Huancayo are included in Figure 8a, in which the altitude of the bottom of the F layer (h_{min}) over Huancayo has been superposed upon the Jicamarca backscatter map. Early in the evening the F layer is higher at Huancayo, with the roles reversing around 2030 LT. This is also the time when the 3-m scattering layer over JRO stalls in its slow upward drift. Notice that the brief increase in the irregularity layer thickness and the gap in E region irregularities occur at the same time as the reversal. The apparent drift observed by Jicamarca is consistent with a typical vertical drift morphology [Fejer et al., 1979], in which the plasma moves upward at all local times before 2030 (on this night) and downward after this time. The ionospheric tilt associated with this morphology would have the Huancayo layer above the Jicamarca layer before 2030 and vice versa afterward, as observed. However, the apparent tilt is much more pronounced than the small longitude difference would imply, as discussed in detail in a companion paper [Argo and Kelley, this issue]. The abrupt uplift after 2100 is nearly simultaneous at both sites, suggesting that the associated eastward electric field extended over both Huancayo and Jicamarca.

3. DISCUSSION OF THE LARGE-SCALE RESULTS

3.1. Implications for the Large-Scale Development of Equatorial Spread F

Interpretation of the Jicamarca radar backscatter map often uses the assumption that the relatively thin echoing regions correspond to the structured bottomside of the layer [e.g., Kelley et al., 1981]. This important hypothesis is upheld in great detail by the combined rocket and radar data obtained during the upleg of both Condor rocket flights, as well as during the equatorial ionosphere (Equion) experiment [Morse et al., 1977]. For example, the echoing layer is more than 100 km higher on March 14, as are the bottomside gradient and the F peak deduced from the rocket data.

Using this relatively firm assumption, we note immediately that widespread equatorial spread F develops only when the layer is high. For example, in Figure 2a the height of the echoing layer never exceeds 300 km and never exceeds 10 km in vertical extent. The layer seems to be rising when echoes first appear, and the backscatter signal continues virtually unchanged as the layer reverses, dying out as the echo height slowly comes down again. Conversely, the initial position of the structured F layer is highest on March 1, the night with the most sustained 3-m backscatter activity. This requirement has been noted previously [e.g., Farley et al., 1970]. Plume development is also well correlated with layer height. Kelley et al. [1981] noted a distinct tendency for plumes to form either at layer "apogee" or when it seems to be descending. This is also upheld in detail by the present data set. The major plumes on March 1, 6, and 14 are all of the apogee type. Even in the relatively quiet 3-m backscatter observed on the evening
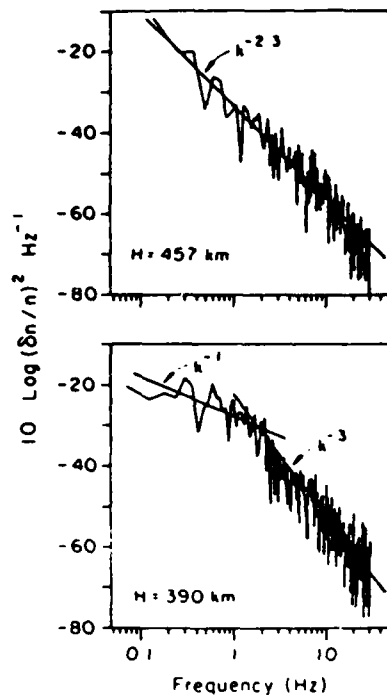
93

Fig. 9. Two examples of the spectrum of density fluctuations detected by the second Condor spread F rocket (March 14, 1983). The top panel corresponds to an altitude of 457 km, and the bottom panel corresponds to an altitude of 390 km.

of March 5, a plume seemed to almost develop at 2010 LT when the layer reached its peak altitude. A very similar "near-plume" feature was seen at 2030 LT on March 14. This result is very strong evidence for the importance of the gravitational term in the generalized Rayleigh-Taylor (GRT) instability [Kelley et al., 1981] as the major controlling influence on equatorial spread F, since the growth rate is inversely proportional to the ion-neutral collision frequency $(v_{i,n})$. Using a local value for $v_{i,n}$, the growth rate due to a purely gravitationally driven process is given as a function of height approximately by the expression

$$\gamma_g \simeq 0.09 \exp [(h - 300)/50] \quad \min^{-1}$$

in which we have assumed a vertical gradient scale length of 20 km and a neutral scale height of 50 km. This implies that the e-folding time for irregularity growth decreases from 11 to 4 min between 300 and 350 km. Of course, a feature as extensive as a plume cannot grow from thermal noise in a few e-folding times, so seed structure must be present at much larger scales than 3 m in the bottomside region as it drifts upward. Indeed, the rocket data reported by Kelley et al. [1976] and Costa and Kelley [1978] showed well-developed bottomside 1- to 4-km structures $(\delta n/n \approx 30\%)$ in just such conditions, e.g., F peak at 300 km, slow 10-m/s uplift determined by barium cloud drifts, and weak 3-m structures which seemed to erupt into a plume a few minutes later.

The other terms in the GRT process, which involve electric fields and neutral winds as sources of free energy, do not depend upon the collision frequency and hence are not altitude dependent. These terms are not negligible, and the present data set confirms and extends several conclusions of Kelley et al. [1981] in this regard. First, we note the tendency for two types of ionospheric uplift. On March 5 (Figure 2c),

three gentle wavelike undulations of the F layer are apparent. This is to be constrasted with the sharp uplifts at 2145 LT on March 1 (Figure 3a), at 2050 LT on March 6, and at 2128 LT on March 14. The first and third of these three examples followed a cycle of gentle wavelike undulations with the plume and associated rapid uplift seeming to feed upon the more gentle uplift. We first discuss the origin and effects of "gentle" undulations, returning to the other class in section 3.2.

Although data gaps confuse the issue somewhat, the March 1 data (Figure 3a) display as many as four wavelike oscillations, two of which are punctuated by apogee plumes. The apparent descending phase of such oscillations is often characterized by the development of several isolated plumes. It takes some imagination to see this on March 1, but on March 6 (Figure 2b), three such "postapogee" plumes occur. Even on the relatively quiet night of March 5 (Figure 2c) the second undulation has three separate regions in which the scattering layer broadens briefly, which are centered at 2145, 2154, and 2203 LT. In the spectacular event studied by Kelley et al. [1981], also, two plumes developed on the "descending phase" of both of two extreme oscillations (≥ 300 km amplitude) recorded on March 21, 1979. Both of these major undulations had large apogee plumes.

The rocket data show definitely that ionospheric tilts can be significant and that the hypothesized tilt suggested by Kelley et al. [1981] is indeed the correct one when the scattering layer seems to rapidly descend over Jicamarca. The ionospheric orientation during such an event is such that the plasma density gradient has a westward component. The typical zonal wind direction for this local time sector is eastward [Sipler and Biondi et al., 1978; Meriwether et al., this issue]. Since the magnitude of the zonal wind component u must be larger than the eastward plasma drift velocity it generates by the F region dynamo effect, the vertical electric field in the neutral frame, $E_z' = E_z + uB$, must be upward. This further implies that $\mathbf{E}' \times \mathbf{B}$ has a component parallel to the westward zonal plasma density gradient mentioned above. This is a linearly unstable condition. The horizontal density gradient scale length can be estimated from the rocket data to be 14 km. For $E'/B \approx 100$ m/s this yields an exponential growth time of 2.3 min, which is very fast.

There are presently two competing theoretical explanations for the organization of equatorial spread F at the largest scales, gravity wave seeding, and velocity shear instabilities. By large scale we mean $\lambda \gg L$, the vertical density gradient scale length. Kelley et al. [1981] argued that the quasi-sinusoidal undulations were due to gravity wave seeding as described by Klostermeyer [1978]. Once seeded, such structures may then be amplified preferentially by a plasma instability process. In the other view, large-scale undulations are driven directly by a velocity shear instability. The advantage of the latter process over a Rayleigh-Taylor instability is that the growth rate peaks at $\lambda \geq L$ for the velocity shear instability whereas the opposite inequality holds for the Rayleigh-Taylor mode.

To investigate this further, we first study the spacing between multiple plumes such as those detected on March 6, 1983, while the scattering layer height is decreasing over Jicamarca. The usual assumption is that the spacing can be estimated by using a mean eastward plasma velocity $V_E = 150$ m/s and then converting the time Δt between events in terms of a distance L via $L = V_E \Delta t$. To test this methodology, we can use the scanning Altair radar on Kwajalein, for which
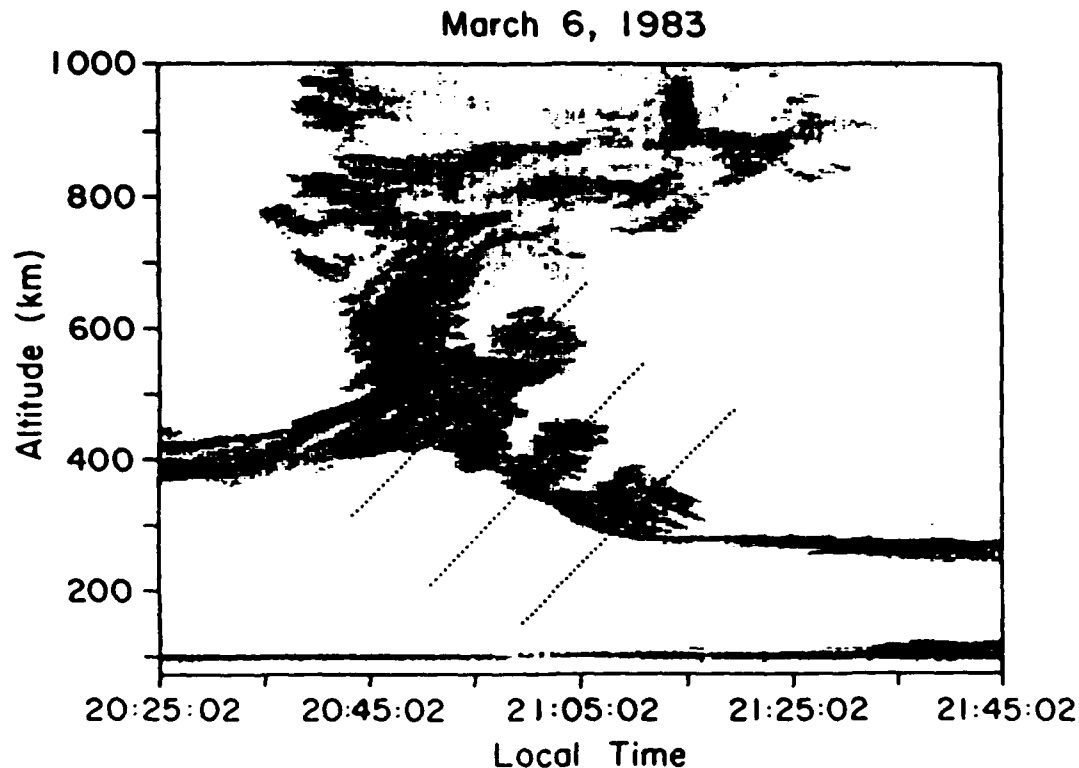
94

March 6, 1983

Fig. 10. The Jicamarca backscatter power map from the night of March 6, 1983, showing three prominent plume structures which erupt from the bottomside spread F as the scattering layer decends. Superposed are the relative positions of three similar structures observed using a scanning radar [Tsunoda, 1983].

there is not an ambiguous relationship between time and space, and compare the separation of multiple plumes measured there to the separations deduced from the Jicamarca data. To make this comparison, we have taken a scanning radar plot from Figure 2b of Tsunoda [1983], reversed it east-west, and plotted the position of his three multiple plumes over the March 6 event in Figure 10. As noted above, we assumed an eastward drift of 150 m/s to convert time to space in the Jacamarca plot. Notice that under this assumption the spacing of the Altair plumes is nearly identical to that registered by the Jicamarca radar.

We now use this method to investigate what seems to be a characteristic spacing between such plumes. From the March 1, 5, and 6 data we have determined four sets of spacings in time and converted them to spatial units (assuming a 150-m/s eastward velocity). Four more plume spacings were estimated from the data published by Kelley et al. [1981], and two more actual spacings determined from the work by Tsunoda [1983] discussed in the previous paragraph. The spacings d range from 91 to 206 km with a mean value of 150 km. In terms of the normalized wave number $k = 2\pi L/d$, where L is the zero-order bottomside density gradient taken to be 20 km, these spacings correspond to the range $k = 0.6$–1.38 with an average of $k = 0.84$.

Guzdar et al. [1982] and Satyanarayana et al. [1984] have studied the generalized Rayleigh-Taylor process, including the effect on the growth rate of a vertical shear in the eastward plasma drift velocity. Although such a shear lowers the growth rate, it also moves the most unstable waves from a normalized $k \simeq 10$ to values in the range 0.5–2, which is much more consistent with the spacings reported here. We thus might con-

clude that the shear is important in determining the outer horizontal scale of equatorial spread F. However, using the theory of Satyanarayana et al. [1984] and assuming that the wavelength of the maximum linear growth rate corresponds to the observed spacings, the range of k found above corresponds to plasma shears (dV_x/dx) in the range 2.6×10^{-2} to 6×10^{-3} s^{-1}. These shears are about 10 times the values indicated by Figure 5, as well as by other radar-based shear measurements [Kudeki et al., 1981; Tsunoda et al., 1981].

One possible way out of this dilemma is to conjecture that the shear is higher in a localized region within the plasma gradient than indicated by the radar data, say 100 m/s over a 10-km bottomside height range. Neutral wind shears of this magnitude have been reported [Bhavsar et al., 1965]. Another possibility is that the dominant horizontal wave number in the fully developed process is smaller than the wave number of maximum growth. This might imply an inverse cascade of energy to larger scales in this two-dimensionally turbulent medium. A less exotic explanation is that although the growth rate is lower at small k, the initial amplitude was higher and the longer-wavelength waves saturated earlier.

In summary, the present analysis supports the notion that velocity shear plays a role in determining the plume spacings which occur in the range $k \approx 1$. However, it should be noted that to reach this conclusion, very high shears must be invoked. To push the shear explanation to even longer wavelengths, and hence to explain the "gentle undulations" of the F layer, does not seem at all realistic. We thus fall back upon the conclusions of Kelley et al. [1981] as well as Röttger [1973], Klostermeyer [1978], and many others, that gravity waves and their associated electric fields must organize the plasma at

95

scales of ≥ 200 km. This area is also discussed in some detail in the companion paper by *Argo and Kelley* [this issue].

3.2. *Wedges or Bubbles?*

It was originally conjectured that the plasma depletions associated with equatorial spread F may either pinch off, forming bubbles of low-density plasma, or be wedges linked to the bottomside by a region of low density [*Woodman and LaHoz*, 1976]. The radar structure linking the plume head to the bottomside, in the pinch model, was then due to a turbulent wake [*Woodman and LaHoz*, 1976; *Kelley and Ott*, 1978]. Recent experimental evidence [*Mendillo and Tyler*, 1983; *Tsunoda et al.*, 1982], theoretical calculations based on satellite data [*Hanson and Bamgboye*, 1984], and computer simulations by *Zalesak et al.* [1982] support the wedge concept.

Returning to Figure 3b comparison of the highest-altitude depletions on the two rocket profile shows that the downleg depletion was encountered well above the corresponding upleg event. This seems to imply that the depletion was located at a higher altitude west of Jicamarca. The radar data confirm this hypothesis. In Figure 3b an arrow points out a "miniplume" of 3-m echoes which intersects the parabola labeled $V = 85$ m/s at the same height as the uppermost depletion in the rocket plasma density profile. Although this echoing region was decaying in power with time over Jicamarca, the patch can also be seen to intersect the rocket parabola during its downleg at the height of the uppermost depletion in the rocket profile.

It would be remarkable indeed if a rocket penetrated two pinched-off bubbles along its trajectory, even allowing for magnetic field alignment (a cylindrical bubble). However, a fully developed wedge, tilted toward the west and also field aligned, would be quite easy to penetrate on upleg and downleg. Since both of the Condor rockets penetrated such structures during both upleg and downleg, and because a nearly identical double penetration was observed during the PLUMEX I flight, the rocket data seem to support the wedge model.

We return now to the common cusplike feature associated with many of the JRO plumes. The straightforward explanation is that they correspond to wedges with strong scatter along the walls. The low backscatter levels in the cavity of these caps may be due to the low plasma density in this region, which has been drawn up from low altitudes, rather than a low turbulence level. (Radars respond to $\Delta n^2(k)$, not $[\Delta n(k)/n]^2$.) The uplift in such a cusp is far too rapid to be generated by a pure gravity wave induced electric field since such a field can be no greater than wB where w is the vertical neutral wind in the gravity wave and B the magnetic field. This has been pointed out previously [*Kelley et al.* 1981] and is discussed by *Argo and Kelley* [this issue]. The implication is that the generalized Rayleigh-Taylor process must be invoked to locally amplify the electric field associated with the seed structure. In reference to the previous discussion, the scale size for this amplification seems to be $k \leq 1$, implying that velocity shear is an important factor.

4. SUMMARY OF THE CONDOR EQUATORIAL SPREAD F RESULTS

The key results are summarized in order of their presentation in the present series of papers beginning with the present paper.

Paper 1 (this paper). The combined rocket-radar data

have been used to show that during rapid decreases of the scattering layer height over Jicamarca, the ionosphere is tilted such that the region to the west is lower than the adjacent region to the east. Such a configuration is shown to have a very high growth rate due to a wind-driven $E \times B$ instability ($\gamma \approx 3$ min^{-1}). These results verify previous conjectures concerning the tendency for multiple plumes to form in such a configuration. The case is further made that a characteristic separation distance exists between such plumes, which have a normalized $k = k/2\pi L \approx 1$, where L is the zero-order vertical gradient scale length. This separation is consistent with a generalized Rayleigh-Taylor (or $E \times B$) instability which includes velocity shear. The magnitude of the required shear is larger than existing observations suggest, but higher localized shears may exist. The gentle undulations which have scales 5–6 times larger almost certainly must correspond to gravity wave induced effects. Further evidence that plumes are due to wedge-like features is also presented.

Paper 2 [LaBelle and Kelley, this issue]. Further evidence is presented to show that shallow spectral indices may at times characterize the spectral development in the intermediate-scale regime. In this context we define shallow to be a power law index of the form k^{-n} where n is less than 2. One reason that this result is important is that, to date, no computer simulation has yet yielded a spectral index shallower than k^{-2}. Until this experimental result is reproduced, one must question what aspect of the physics has been left out of the simulations. Several sources for the spectral form are investigated in paper 2. The nonlinear turbulence theory of *Sudan and Keskinen* [1984] predicts a $k^{-5/3}$ law which LaBelle and Kelley show quantitatively fits the data reasonably well, provided that a large anomalous diffusion coefficient is used (see also paper 3). The authors speculate that the turbulent cascade and $k^{-5/3}$ law applies when the exchange of energy between large and small eddies, which is measured by the nonlinear growth rate Γ, exceeds the energy input measured by the linear growth rate γ. The observed spectral forms even shallower than $k^{-5/3}$ are not explained by this argument. In addition to the comparison with nonlinear theory, LaBelle and Kelley point out two other processes which might elevate the relative power in the range near the 1-km scale and hence result in a shallower spectral slope at lower k. One such mechanism is an injection process due to wall turbulence driven by steep horizontal gradients. They show an example of wall turbulence which has a peak in $[\delta n(k)/n]^2$ near 1 km. The other process is similar but appeals to a lowering of the growth rate at k values above and below the 1-km scale by F region shorting of electric fields. Near 1 km the formation of images maintains the growth rate at a relatively high value.

Paper 3 [LaBelle et al., this issue]. The result based on PLUMEX data [*Kelley et al.*, 1982a; *Singh and Szuszczewicz*, 1984] that density fluctuation spectra display a very steep power law (k^{-5}) for wavelengths less than 100 m was verified in both Condor flights. The fact that the $E^2(k)$ spectrum measured simultaneously varies as k^{-3} was also verified and, taken together, strongly verifies the conjecture [*Kelley*, 1982] that drift waves, or at least some similar process involving finite $k_{||}$, play an essential role in the evolution of equatorial spread F. Building upon this verification, LaBelle et al. show quantitatively that anomalous diffusion should occur because of the observed drift wave turbulence. The diffusion coefficient calculated fits the values needed to explain the balance of growth versus decay in the saturated turbulence spectra ob-

served in the Condor experiments. Typical values of the anomalous diffusion coefficient are in the range 200–500 m^2/s, which is 2 orders of magnitude higher than the collisional value. It is of interest to note that the same calculations applied to bottomside spread F and to low-altitude barium cloud power spectra reveal that the collisional diffusion coefficient is adequate to explain the results in such conditions. The implication is that an altitude (collision frequency?) threshold exists for onset of the anomalous diffusion effect. Curiously, the critical scale for onset of the steep spectral form becomes larger as the turbulence strength increases. This is opposite to what happens in neutral gas turbulence and may be related to the fact that the diffusion coefficient in a plasma process is k dependent.

Paper 4 [Basu et al., this issue]. Radar backscatter at 50 MHz, rocket, and VHF/GHz scintillation measurements of spread F irregularities at the magnetic equator in Peru were made during the Project Condor campaign in March 1983. It was found that the radar backscatter with extended plumes occurs, in association with the maximum values of 1.7-GHz scintillations. This established that the height-integrated electron density deviation of 200-m scale irregularities causing 1.7-GHz scintillations maximizes in extended 3-m plume structures. The magnitude of 1.7-GHz scintillations recorded at high elevation angles (~76°) near the magnetic equator did not exceed a value of $S_4 = 0.2$ (4 dB) in contrast to the near-saturated 1.5-GHz scintillations routinely observed at Ascension Island near the crests of the equatorial anomaly of F_2 ionization. The observed scintillation magnitudes at 1.7 GHz have, however, been found to be compatible with the ambient F region and the irregularity parameters measured by the rockets. The spectral index n of scintillations was found to be shallow ($n \sim 3$) on March 1, 1983, when the F region was high, while the index was steep ($n \sim 5$) on March 14, 1983, when the F region was at a lower altitude. Curiously, the F region rocket measured nearly identical one-dimensional spectral indices of intermediate-scale irregularities on both evenings, which was compatible only with the shallower spectral index of the scintillations. The irregularity drift velocities measured by the spaced receiver scintillation measurements were in general agreement with the radar interferometer results except that the spaced-receiver drifts were 20% higher. The zonal drift was observed to be about 100 m/s when the F region was high and about 200 m/s when the F region was low. This result may be a consequence of the fact that the F region dynamo field at higher altitude above the magnetic equator becomes coupled with the off-equatorial locations through the earth's magnetic field and that the zonal neutral wind decreases with increasing latitude.

Paper 5 [Argo and Kelley, this issue]. As part of Project Condor a digital ionosonde was established at Huancayo, Peru. Five days of data were obtained, one simultaneous with Jicamarca VHF observations and a rocket flight. The direction-finding capability of the system coupled with the VHF data has given clearer insight into operation of the ionosonde system and its equatorial spread F in general. A modified phenomenology is developed which uses the radar's ability to do echo location. The onset of irregularities is seen to occur in the east and to move westward, while inside this large-scale structure the plasma is found to drift eastward. A very curious difference has been identified between spread F observations with the HF radar and with the VHF radar at Jicamarca. At VHF, spread F onset often occurs when the

ionosphere is rising, whereas in all five examples presented here, the digital ionosonde detected onset when the apparent ionosphere motion was downward. The effect could be instrumental but may be related to the considerable orographic differences in the two sites. Isolated scattering patches are observed and tentatively identified as detached or "fossil" plumes. Additional evidence is presented that acoustic gravity waves play an important role in equatorial spread F.

Paper 6 [Meriwether et al., this issue]. Nighttime measurements of equatorial thermospheric wind dynamics at Arequipa, Peru, were made with an automated field-widened Fabry-Perot interferometer between April 1983 and August 1983. Data have been reduced for 62 nights. Significant seasonal variations in both zonal and meridional components of the thermospheric neutral wind vector were observed near the equinox. Between 2000 and 2300 LT the zonal wind component is eastward with an amplitude between 100 and 150 m/s that gradually ebbs to zero by dawn. The meridional component is generally small throughout the night. In the winter months (May–August) and at the winter solstice the zonal wind persists eastward throughout the night with speeds between 50 and 150 m/s. The meridional component is directed poleward (southward) toward the winter hemisphere with a speed of 50–75 m/s that decays to zero by midnight. Comparison with the predictions of the National Center for Atmospheric Research thermospheric general circulation model (TGCM) for equinoctial and solstice conditions shows good agreement. We conclude that the observed seasonal changes are caused by the changing nature of the solar forcing functions. The Arequipa results indicate that the day-to-day variability in the winter thermospheric winds is less than that found for the summer equatorial observations obtained at Kwajalein.

REFERENCES

Aarons, J., J. P. Mullen, H. E. Whitney, and E. M. E. MacKenzie, The dynamics of equatorial irregularity patch formation, motion, and decay, J. Geophys. Res., 85, 139, 1980.

Argo, P. E., and M. C. Kelley, Digital ionosonde observations during equatorial spread F, J. Geophys. Res., this issue.

Baker, K. D., E. F. Pound, and J. C. Ulwick, Digital plasma frequency probe for fine scale ionospheric measurements, in Small Rocket Instrumentation Techniques, edited by K. Maeda, p. 49, North Holland, Amsterdam, 1969.

Baker, K. D., J. LaBelle, R. F. Pfaff, L. C. Howlett, N. B. Rao, J. C. Ulwick, and M. C. Kelley, Absolute electron density measurements in the equatorial ionosphere, J. Atmos. Terr. Phys., 47, 781, 1985.

Balsley, B. B., G. Haerendel, and R. A. Greenwald, Equatorial spread F: Recent observations and a new interpretation, J. Geophys. Res., 77, 5625, 1972.

Basu, S., and H. E. Whitney, The temporal structure of intensity scintillations over the magnetic equator, Radio Sci., 18, 263, 1983.

Basu, S., Su. Basu, J. Aarons, J. P. McClure, and M. D. Cousins, On the coexistence of kilometer and meter scale irregularities in the nighttime equatorial F region, J. Geophys. Res., 83, 4219, 1978.

Basu, S., Su. Basu, J. LaBelle, E. Kudeki, B. G. Fejer, M. C. Kelley, H. F. Whitney, and A. Bushby, Gigahertz scintillations and spaced

receiver drift measurements during Project Condor equatorial F region rocket campaign in Peru, J. Geophys. Res., this issue.

Basu, Su., and S. Basu, Equatorial scintillations: Progress since ISEA-6, J. Atmos. Terr. Phys., 47, 753, 1985.

Basu, Su., S. Basu, J. P. McClure, W. B. Hanson, and H. E. Whitney, High-resolution topside in situ data of electron densities and VHF/GHz scintillation in the equatorial region, J. Geophys. Res., 88, 403, 1983.

Bhavsar, P. D., K. Ramanvjaro, and K. G. Verenekar, Study of the neutral upper atmosphere winds near the equator, Space Res., V, 986, 1965.

Costa, E., and M. C. Kelley, On the role of steepened structures and drift waves in equatorial spread F, J. Geophys. Res., 83, 4359, 1978.

Farley, D. T., B. B. Balsley, R. F. Woodman, and J. P. McClure, Equatorial spread F: Implications of VHF radar observations, J. Geophys. Res., 75, 7199, 1970.

Fejer, B. G., and M. C. Kelley, Ionospheric irregularities, Rev. Geophys., 18, 401, 1980.

Fejer, B. G., D. T. Farley, B. B. Balsley, and R. F. Woodman, Vertical structure of the VHF backscattering region in the equatorial electrojet and the gradient drift instability, J. Geophys. Res., 80, 1313, 1975.

Fejer, B. G., D. T. Farley, R. F. Woodman, and C. Calderon, Dependence of equatorial F region vertical drifts on season and solar cycle, J. Geophys. Res., 84, 5792, 1979.

Fejer, B. G., E. Kudeki, and D. T. Farley, Equatorial F region zonal plasma drifts, J. Geophys. Res., 90, 12,249, 1985.

Guzdar, P. N., P. Satyanarayana, J. D. Huba, and S. L. Ossakow, Influence of velocity shear on the Rayleigh-Taylor instability, Geophys. Res. Lett., 9, 547, 1982.

Hanson, W. B., and D. K. Bamgboye, The measured motions inside equatorial plasma bubbles, J. Geophys. Res., 89, 8997, 1984.

Kelley, M. C., Nonlinear saturation spectra of electric fields and density fluctuations in drift wave turbulence, Phys. Fluids, 25, 1002, 1982.

Kelley, M. C., Equatorial spread F: Recent results and outstanding problems, J. Atmos. Terr. Phys., 47, 745, 1985.

Kelley, M. C., and J. P. McClure, Equatorial spread-F: A review of recent experimental results, J. Atmos. Terr. Phys., 43, 427, 1981.

Kelley, M. C., and E. Ott, Two-dimensional turbulence in equatorial spread F, J. Geophys. Res., 83, 4369, 1978.

Kelley, M. C., G. Haerendel, H. Kappler, A. Valenzuela, B. B. Balsley, D. A. Carter, W. L. Ecklund, C. W. Carlson, B. Hausler, and R. Torbert, Evidence for a Rayleigh-Taylor type instability and upwelling of depleted density regions during equatorial spread F, Geophys. Res. Lett., 3, 448, 1976

Kelley, M. C., M. F. Larsen, C. LaHoz, and J. P. McClure, Gravity wave initiation of equatorial spread F: A case study, J. Geophys Res., 86, 9087, 1981.

Kelley, M. C., R. Pfaff, K. D. Baker, J. C. Ulwick, R. C. Livingston, C. L. Rino, and R. T. Tsunoda, Simultaneous rocket probe and radar measurements of equatorial spread F: Transitional and short-wavelength results, J. Geophys. Res., 87(A3), 1575, 1982a.

Kelley, M. C., R. C. Livingston, C. L. Rino, and R. T. Tsunoda, The vertical wave number spectrum of topside equatorial spread F: Estimates of backscatter levels and implications for a unified theory, J. Geophys. Res., 87, 5217, 1982b.

Klostermeyer, J., Nonlinear investigation of the spatial resonance effect in the nighttime equatorial F region, J. Geophys. Res., 83, 3753, 1978.

Kudeki, E., B. G. Fejer, D. T. Farley, and H. M. Ierkic, Interferometer studies of equatorial F region irregularities and drifts, Geophys. Res. Lett., 8, 377, 1981.

LaBelle, J., and M. C. Kelley, The generation of kilometer scale irregularities in equatorial spread F, J. Geophys. Res., this issue

LaBelle, J., M. C. Kelley, and C. E. Seyler, An analysis of the role of drift waves in equatorial spread F, J. Geophys. Res., this issue

Livingston, R. C., C. L. Rino, J. P. McClure, and W. B. Hanson, Spectral characteristics of medium-scale equatorial F region irregularities, J. Geophys. Res., 86, 2421, 1981

Mendillo, M., and A. Tyler, Geometry of depleted plasma regions in the equatorial ionosphere, J. Geophys. Res., 88, 5778, 1983

Meriwether, J. W., Jr., J. W. Moody, M. A. Biondi, and R. G. Roble, Optical interferometric measurements of nighttime equatorial thermospheric winds at Arequipa, Peru, J. Geophys Res. this issue

Morse, F. A., B. C. Edgar, H. C. Koons, C. J. Rice, W. J. Heikkila, J. H. Hoffman, B. A. Tinsley, J. D. Winningham, A. B. Christensen, R. F. Woodman, J. Pomalaza, and R. N. Teixeira, Equion, an equatorial ionospheric irregularity experiment, J. Geophys Res., 82, 578, 1977.

Ossakow, S. L., Spread F theories—A review, J. Atmos Terr. Phys., 43, 437, 1981.

Rino, C. L., R. T. Tsunoda, J. Petriceks, R. C. Livingston, M. C. Kelley, and K. D. Baker, Simultaneous rocket-borne beacon and in situ measurements of equatorial spread F: Intermediate wavelength results, J. Geophys. Res., 86, 2411, 1981.

Röttger, J., Wave like structures of large scale equatorial spread F irregularities, J. Atmos. Terr. Phys., 35, 1195, 1973.

Satyanarayana, P., P. N. Guzdar, J. D. Huba, and S. L. Ossakow, Rayleigh-Taylor instability in the presence of a stratified shear layer, J. Geophys. Res., 89, 2945, 1984.

Singh, M., and E. P. Szuszczewicz, Composite equatorial spread F wave number spectra from medium to short wavelengths, J. Geophys. Res., 89, 2313, 1984.

Sipler, D. P., and M. A. Biondi, Equatorial F region neutral winds from nightglow OI 630.0 nm Doppler shifts, Geophys. Res. Lett., 5, 373, 1978.

Sudan, R. N., and M. J. Keskinen, Unified theory of the power spectrum of intermediate wavelength ionospheric electron density fluctuations, J. Geophys. Res., 89, 9840, 1984.

Szuszczewicz, E. P., R. T. Tsunoda, R. Narcisi, and J. C. Holmes, Coincident radar and rocket observations of equatorial spread-F, Geophys Res Lett., 7, 537, 1980.

Tsunoda, R. T., Time evolution and dynamics of equatorial backscatter plumes, 1, Growth phase, J. Geophys. Res., 86, 139, 1981.

Tsunoda, R. T., On the generation and growth of equatorial backscatter plumes, 2, Structuring of the west walls of upwellings, J. Geophys. Res., 88, 4869, 1983

Tsunoda, R. T., R. C. Livingston, and C. L. Rino, Evidence of a velocity shear in bulk plasma motion associated with the post-sunset rise of the equatorial F-layer, Geophys. Res. Lett., 8, 807, 1981

Tsunoda, R. T., R. C. Livingston, J. P. McClure, and W. B. Hanson, Equatorial plasma bubbles: Vertically elongated wedges from the bottomside F layer, J. Geophys. Res., 87, 9171, 1982

Whitney, H. E., Notes on the relationship of scintillation index to probability distributions and then uses for system design, Rep D. A. Carter, W. L. Ecklund, AFCRL-TR-74-0004, Air Force Cambridge Res Lab., Bedford, Mass., 1974, AD778092.

Whitney, H. E., J. Aarons, and C. Malik, A proposed index for measuring ionospheric scintillations, Planet. Space Sci., 17, 1069, 1969

Woodman, R. F., Vertical drift velocities and east-west electric fields at the magnetic equator, J. Geophys Res., 75, 6249, 1970

Woodman, R. F., and C. LaHoz, Radar observations of F region equatorial irregularities, J. Geophys. Res., 81, 5447, 1976

Zalesak, S. T., S. L. Ossakow, and P. K. Chaturvedi, Nonlinear equatorial spread F: The effect of neutral winds and background Pedersen conductivity, J. Geophys Res., 87, 151, 1982

P. Argo, Atmospheric Sciences Group, Earth and Space Sciences Division, Los Alamos National Laboratory, Los Alamos, NM 87545

K. D. Baker, CASS, Utah State University, Logan, UT 84332

Santimay Basu, Air Force Geophysics Laboratory, Hanscom Air Force Base, MA 01731

Sunanda Basu, Emmanuel College, Boston, MA 02115

D. T. Farley, B. G. Fejer, M. C. Kelley, J. LaBelle, and W. E. Swartz, School of Electrical Engineering, Cornell University, Ithaca, NY 14853

C. Hanuise, LSEET, CNRS, University of Toulon, 639 Boulevard des Armaris, 83100 Toulon, France

E. Kudeki, Department of Electrical Engineering, University of Illinois, Urbana, IL 61801

J. W. Meriwether, Jr., Space Physics Research Laboratory, University of Michigan, Ann Arbor, MI 48109

R. F. Woodman, Instituto Geofisico del Peru, Apartado 3747, Lima 100, Peru

Gigahertz Scintillations and Spaced Receiver Drift Measurements During Project Condor Equatorial F Region Rocket Campaign in Peru

Santimay Basu,[1,2] Sunanda Basu,[1] J. LaBelle,[3] E. Kudeki,[3,4] B. G. Fejer,[3]
M. C. Kelley,[3] H. E. Whitney,[5] and A. Bushby[6]

Radar backscatter at 50 MHz, rocket, and VHF/GHz scintillation measurements of spread F irregularities at the magnetic equator in Peru were made during the Project Condor campaign in March 1983. The paper discusses the coordinated set of observations on two evenings, March 1 and March 14, 1983, when the altitude of the F region peak differed by more than 150 km. The full complement of equatorial spread F phenomena, namely, the occurrence of 3-m plume structures and VHF/GHz scintillations, were recorded on both these evenings. It was found that the radar backscatter with extended plumes occurs in association with maximum 1.7-GHz scintillations. This established that the height-integrated rms electron density deviation of ~200-m scale irregularities causing 1.7-GHz scintillations maximizes in extended 3-m plume structures. The magnitude of 1.7-GHz scintillations recorded at high elevation angles (~76°) near the magnetic equator did not exceed a value of $S_4 = 0.2$ (4 dB) in contrast to the near saturated 1.5-GHz scintillations routinely observed at Ascension Island near the crests of the equatorial anomaly of F_2 ionization. The observed scintillation magnitudes at 1.7 GHz have, however, been found to be compatible with the ambient F region and the irregularity parameters measured by the rocket. The spectral index n of scintillations has been found to be relatively less steep ($n \sim -3$) on March 1, 1983, when the F region was high, and the index is steep ($n \sim -5$) on March 14, 1983, when the F region was at a lower altitude. The F region rocket, however, measured nearly identical one-dimensional spectral indices of intermediate-scale irregularities on both evenings, compatible with the less steep spectral index of scintillations. The irregularity drift velocities measured by the spaced receiver scintillation measurements were in general agreement with the radar interferometer results except that the spaced receiver drifts were 20% higher. The zonal drift was observed to be ~100 m/s on the night of March 1 and ~200 m/s on the night of March 14. This result may be a consequence of the day-to-day variability of the measured zonal neutral winds and field line integrated Pedersen conductivities.

1. Introduction

During February–March 1983 the Project Condor equatorial spread F campaign was launched in Peru, which allowed the clustering of a variety of experimental techniques for the measurement of different spread F parameters [*Kelley et al.*, this issue]. At this time, VHF/UHF scintillation measurements were conducted not only at the permanent Huancayo site where routine scintillation observations are made but at the Ancon Observatory as well. The latter site allowed high elevation angle scintillation measurements at 1694 MHz to be performed virtually through the same magnetic meridian over which radar backscatter power maps at 50 MHz were acquired by the Jicamarca Observatory. In addition, VHF scintillation measurements by spaced receivers were conducted at both Huancayo and Ancon to measure the drift speed of the ionospheric irregularities. The VHF scintillation measurements from Ancon provided an ionospheric intersection about 200 km to the west of the planned rocket trajectory and the radar backscatter measurements. Since the evening spread F irregularities drift eastward, the irregularity patches

generated in the west caused VHF scintillations first before arriving at the ionospheric location probed by the radar and rocket. Since this delay is about 15 min, the occurrence of VHF scintillations could be used to make short-term predictions for radar and rocket measurements.

The objectives of these coordinated UHF (1694 MHz) scintillation, rocket, and radar observations were to compare the form of the irregularity spectrum predicted by the UHF scintillation measurements in the scale length range of about 500–50 m with the vertical wave number spectrum measured in situ by the rocket, to determine the consistency of the measured UHF scintillation magnitudes with those derived from the model computations based on the irregularity parameters measured by the rocket probes, and to investigate the evolution of decameter (~500–50 m) scale irregularities causing scintillations and 3-m irregularities responsible for the 50-MHz radar backscatter [*Morse et al.*, 1977; *Basu et al.*, 1978, 1980; *Rino et al.*, 1981; *Franke and Liu*, 1983; *Basu and Basu*, 1985]. In addition, the spaced receiver scintillation measurements at 244 MHz were performed in coordination with the radar interferometer measurements at Jicamarca. This provided a unique opportunity to compare the zonal drift of large-scale irregularities (~1.5 km to 150 m) causing scintillations with the drift of localized scatterers of 3 m wavelength. The comparison was made with the knowledge that the radar interferometer measured the drift at a variety of altitudes where localized 3-m scatterers were obtained and the drift measured by the scintillation technique referred to the altitude range around the peak of the F region which yielded the maximum integrated rms electron density deviation of kilometer scale irregularities.

The plan of the paper is to present the observational material in section 2 followed by the coordinated scintillation, radar, and rocket measurements of spread F for the nights of March

[1] Emmanuel College, Boston, Massachusetts
[2] Now at Air Force Geophysics Laboratory, Hanscom Air Force Base, Massachusetts
[3] Cornell University, Ithaca, New York
[4] Now at Department of Electrical Engineering, University of Illinois, Urbana
[5] Air Force Geophysics Laboratory, Hanscom Air Force Base, Massachusetts
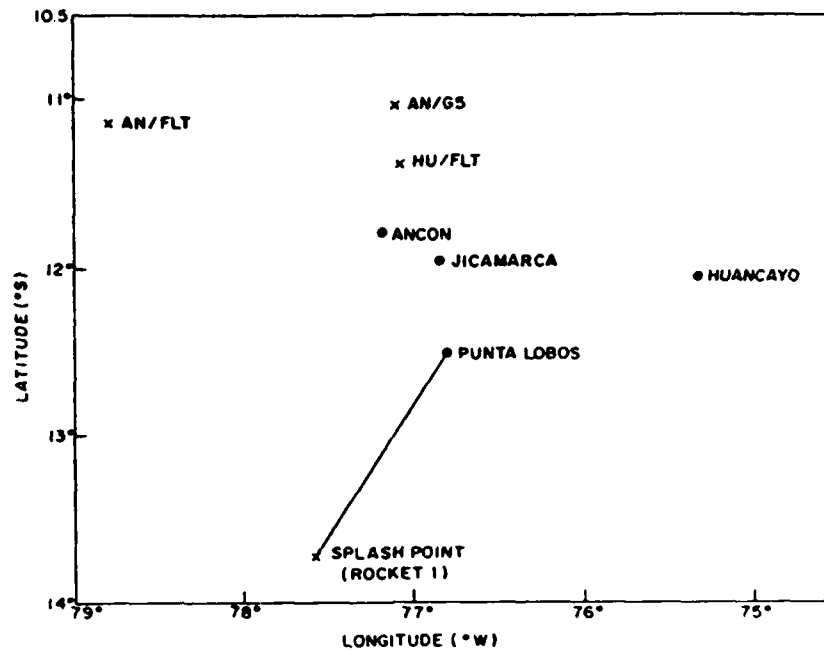[6] Instituto Geofisico del Peru, Lima

Fig. 1. Locations of 50-MHz backscatter radar at Jicamarca, Peru, the rocket range at Punta Lobos, and the scintillation observing stations at Ancon (AN) and Huancayo (HU). The 350-km ionospheric intersections of the propagation paths from the two ground stations (AN, HU) to the various geostationary satellites are indicated. The satellites Fleetsatcom and GOES 5 are abbreviated as FLT and G5, respectively. The projected flight path of the F region rocket launched on March 2, 1983 (UT date), is also shown.

1, 1983, and March 14, 1983, in section 3. These results are discussed in section 4. The implications of the spatial spectrum of electron density irregularities measured by the rocket and the irregularity drift on the temporal structure of scintillations are pointed out.

2. OBSERVATIONS

Figure 1 shows the geometry of radar, rocket, and scintillation measurements. At Jicamarca (latitude: 11.95°S; longitude: 76.86°W; magnetic dip: 0.3°S) the 50-MHz radar was operated in the total power mode to obtain the two-dimensional power maps of 3-m irregularities [Woodman and LaHoz, 1976] and also operated in the interferometer mode [Kudeki et al., 1981] to determine the zonal plasma drift of discrete 3-m scatterers. The diagram shows the rocket range at Punta Lobos and the projected path of the F region rocket which was launched on March 1, 1983. Scintillation measurements were performed at two ground stations, Ancon (AN) and Huancayo (HU). At Ancon the 1694-MHz transmissions from the geostationary satellite GOES 5 were received, the intersection of the propagation path with the 350-km altitude being indicated by the location marked AN/G5. The Fleetsatcom (FLT) transmissions at 244 MHz were received at Ancon by three spaced receivers on a baseline oriented in the magnetic east-west direction. The intersection point of this propagation path with the 350-km altitude occupied the westernmost position indicated by AN/FLT. The same Fleetsatcom satellite was also received at Huancayo on a spaced receiver system, the subionospheric point being showr .1U/FLT.

In addition, the ground station at Huancayo recorded 1541-MHz signals from the Marisat satellite. In contrast to the high elevation angle observations of GOES 5 at Ancon, the Marisat satellite was viewed from Huancayo due east at a low elevation angle of 20°, providing the subionospheric point at a latitude of 12°S and longitude of 67.5°E. Thus scintillation

observations with the Fleetsatcom satellite at Ancon and Marisat satellite at Huancayo provided a longitude coverage of nearly 12° along the magnetic equator. Since the nighttime drift of the irregularities is predominantly zonal at the magnetic equator, the wide longitude coverage of scintillation was advantageous in following the evolution of the irregularities.

Two F region rockets were launched as part of Project Condor [Kelley et al., this issue]. The first rocket was launched into spread F irregularities on March 1, 1983, at 2151 LT. On this night the F region altitude was high, the base of the F region, $h_{min}F$, being located at 430 km. The second rocket was launched during spread F conditions on March 14, 1983, at 2133 LT. On this night, however, the F region altitude was low, $h_{min}F$ being only 300 km. As we shall show presently, background parameters characterizing the F region of the ionosphere were very different on the two nights.

3. RESULTS

Event of March 1, 1983

Figure 2 illustrates the onset of spread F with spaced receiver scintillation data obtained at Ancon from the Fleetsatcom satellite at 244 MHz. As shown in Figure 1, the subionospheric position for this observation (AN/FLT) occupied the westernmost location. The three panels in Figure 2 starting from the top represent the receiver in the east (E), center (C), and west (W) over a baseline oriented in the magnetic east-west direction. The receiver separation for the top two panels was 244 m, and for the bottom two panels the separation was 123 m. It may be noted that the scintillations on all three channels started with the execution of a slow deep fade. This is similar to the diffraction pattern caused by a sharp phase changing boundary [Basu and DasGupta, 1969; Davies and Whitehead, 1977], so that the slow deep fade possibly signifies an encounter of the ray path with the eastern edge of a bubble.

100

0059   0100   0101 UT

FLT(E)

FLT(C)
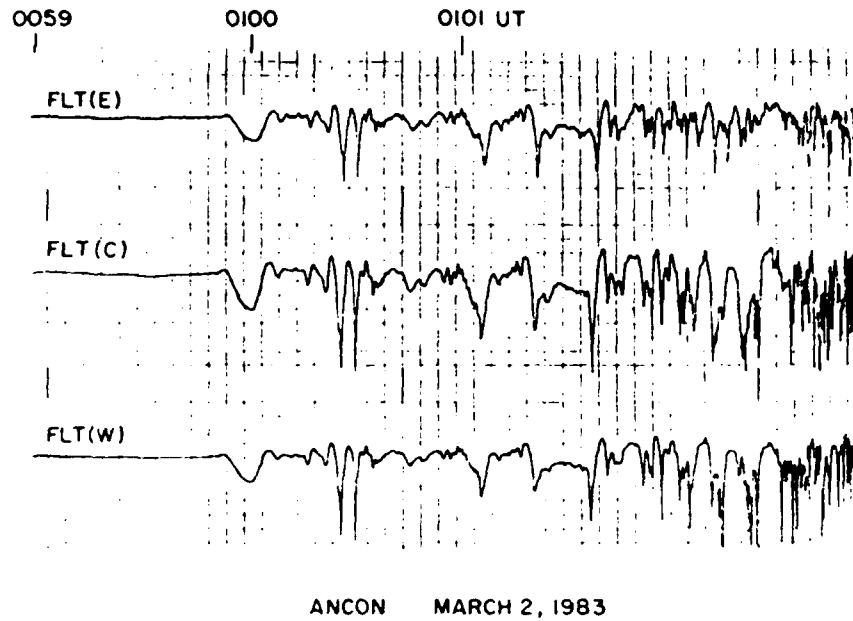
FLT(W)

ANCON   MARCH 2, 1983

Fig. 2. Onset of scintillation on the 244-MHz signal from the Fleetsatcom satellite as recorded by the three spaced receivers at Ancon on March 2, 1983 (UT date). The three panels from the top to bottom show data recorded by the eastern, central, and western receiving systems.

After about 2 min the characteristic equatorial scintillations with deep and fast fadings are obtained. The deepest fades at 244 MHz exceeded the 30-dB dynamic range of the receivers.

The top panel of Figure 3 shows the 50-MHz radar backscatter power map acquired at Jicamarca on this evening, and the bottom panel shows the temporal variation of the magnitude of scintillations at 1694 MHz recorded at Ancon by the use of transmissions from the geostationary satellite GOES 5. The scintillation magnitude is expressed in terms of the S_4 index, which is defined as the normalized second central moment of intensity. From the top panel it may be noted that a thin layer of bottomside backscatter formed shortly after 1940 LT (75°W time) at an altitude of about 375 km. The altitude of this thin backscattering layer increases to about 500 km in 1 hour, when the plume development took place. It may be noted that the Jicamarca radar first detected the portion of the tilted plume in the topside at an altitude of about 900 km, and later the low-altitude portion of the plume was detected. Two data gaps existed around 2100 and 2130 LT; yet it is possible to construct from the trends a reduction of F region altitude at about 2100 LT and subsequent increase of altitude during the detection of the second plume around 2130 LT.

The rectangular mottled area on the radar map centered at 2155 LT indicates that during this period the radar was operated in the interferometer mode. In contrast to the total power mode, the radar during its operation in the interferometer mode received the backscattered signal independently in the east and west quarters of the antenna array. By locating the angular position of a scattering center and by noting the temporal variation of its position, the east-west drift velocities of the 3-m scattering centers were determined [Kudeki et al., 1981; Kelley et al., this issue; Fejer et al., 1985].

In the bottom panel the temporal variation of the S_4 index of scintillation at 1694 MHz is shown. This measurement explored the ionospheric location AN/G5 shown in Figure 1 as being located about 35 km to the west of the meridian which was probed by the Jicamarca radar. As we shall show later,

the irregularity drift velocity at the onset time was about 100 m/s in the eastward direction. As such, the spatial separation between the magnetic meridians passing through the ionospheric points explored by the radar and GOES 5 scintillation observations corresponded to a delay of about 5 min. Thus in comparing the radar and scintillation data sets the bottom panel needs to be shifted to the right by about 5 min. Overall, it may be noted that two scintillation structures before and after 2100 LT are correlated with the two plumes centered at 2045 and 2145 LT. It is unfortunate that a data gap exists at the time the second plume may have attained its maximum extent. The correlation between the plume and the scintillation structures indicates that the rms electron density deviation of irregularities in the scale length range of 500-50 m integrated through the ionosphere becomes maximum where the plumes become most extended in altitude. These irregularities control, in a sensitive manner, the magnitude of 1694-MHz scintillations.

On March 1, 1983, the F region rocket was launched at 0251 UT and measured a maximum electron density of 10^{12} m^{-3}, irregularity amplitude of 10%, and one-dimensional spectral index of -2.5 in the scale length range of 1 km to 100 m [LaBelle and Kelley, this issue]. The extent of the plumes and the nature of the electron density profile recorded by the rocket indicated that an irregularity layer thickness of 200 km is not an overestimate. Furthermore, the irregularities near the magnetic equator in the scale length range of a few hundred meters may be assumed to be rodlike with an axial ratio of at least 5:1. By using the geometry of 1694-MHz scintillation observations and the F region parameters actually measured by the rocket, as outlined above, a scintillation index of S_4 = 0.07 at 1694 MHz is estimated in the framework of weak-scatter theory [Rino, 1979]. From the bottom panel of Figure 2 it may be noted that an S_4 index of 0.12 was actually measured at the time of the rocket flight. Since a background $S_4 \approx 0.02$ is inherent in the measurement because of receiver noise temperature and there exists an uncertainty in the assumed value of the irregularity layer thickness, we consider
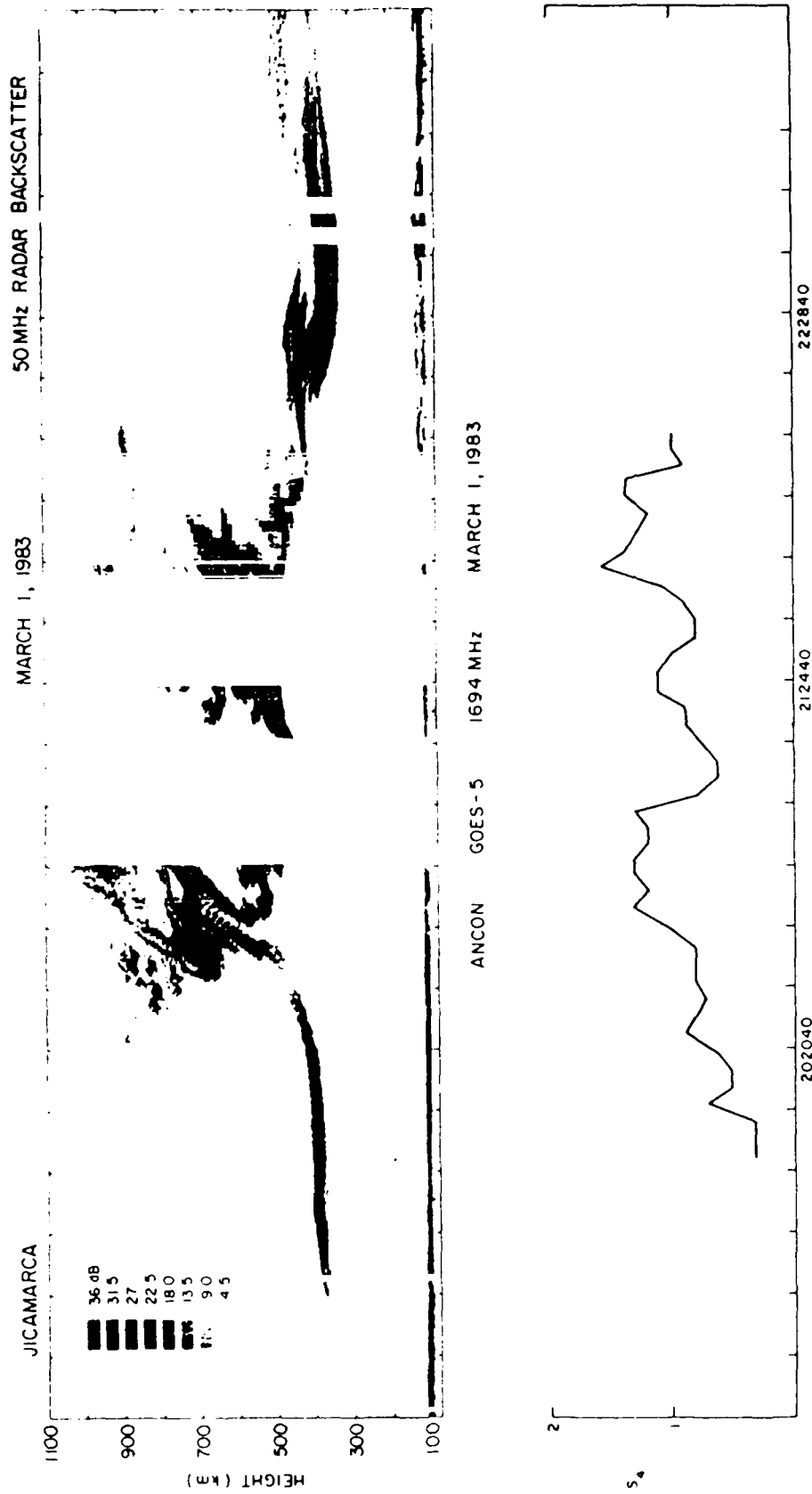
101

Fig. 3. (Top) Temporal variation of the range and intensity of 50-MHz radar backscatter observed at Jicamarca. (Bottom) Variation of the amplitude scintillation index (S_4) of 1694-MHz signals from the geostationary satellite GOES 5 recorded at Ancon.
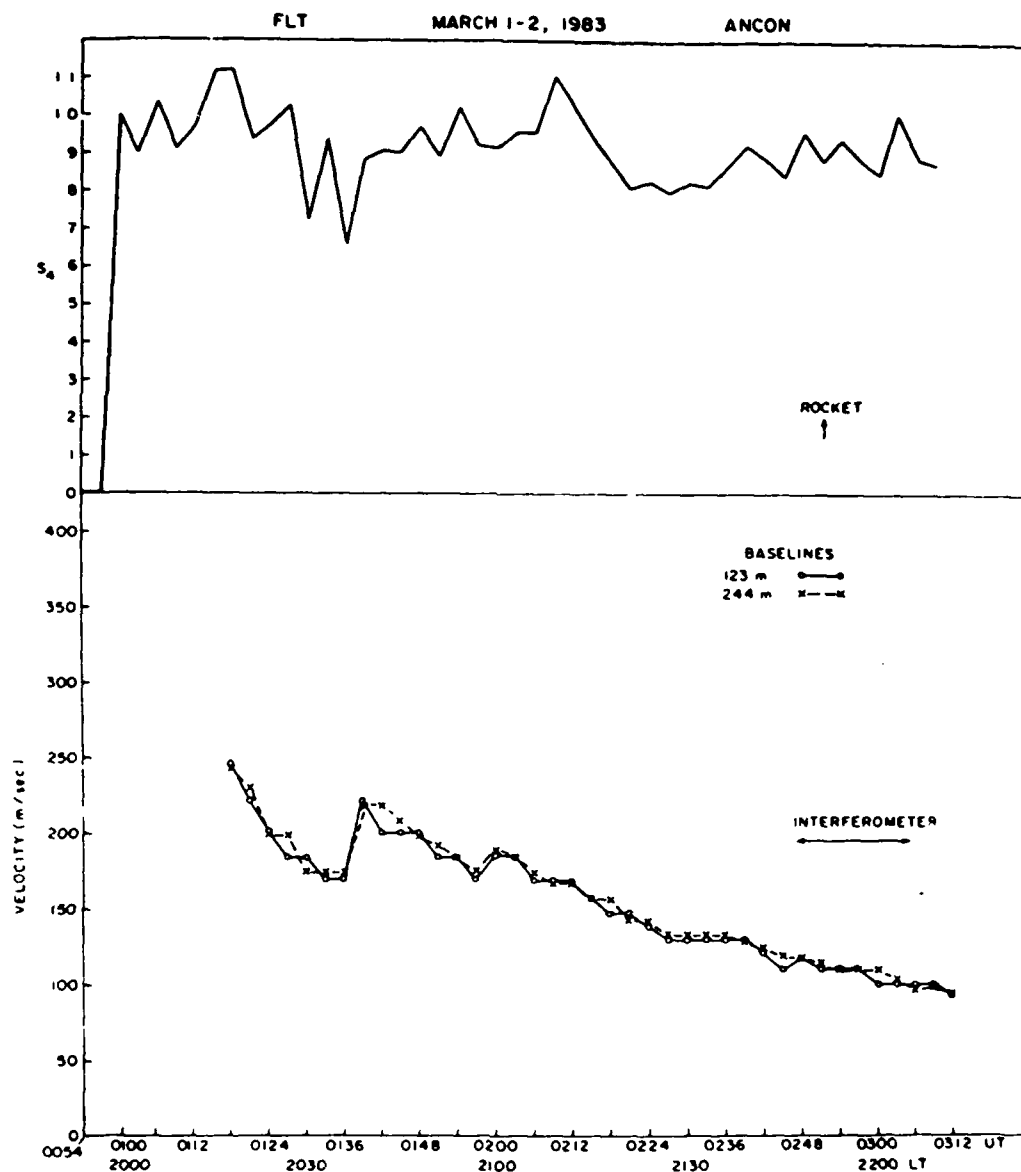
Fig. 4. (Top) Temporal variation of the amplitude scintillation index of 244-MHz signals from the Fleetsatcom geostationary satellite recorded at Ancon between 0100 and 0312 UT on March 2, 1983. (Bottom) Apparent zonal drift of irregularities derived from the spaced receiver recordings made at Ancon. The drifts obtained from both the short (123 m) and the long (244 m) baselines are indicated in the bottom panel.

that the observed and the estimated values of scintillation are in reasonably good agreement.

The weak-scatter computations in the previous paragraph indicate that the observed maximum levels of $S_4 \approx 0.1$ at 1.7 GHz can arise from an irregularity layer of 200 km thickness with rms electron density deviation, $\langle(\Delta N)^2\rangle^{1/2}$, of 2×10^{10} m^{-3}, at an outer scale of 1 km having a one-dimensional spectral index of -2.5. If we assume that the irregularities are of a turbulent type and are described by dual power law regimes having a one-dimensional power law index of -2.5 between 1 km and 100 m followed by a much steeper index of -5 [Kelley et al., 1982] between 100 and 3 m, it is possible to investigate if the observed backscattered power level at 50 MHz is compatible with GHZ scintillation magnitudes. First, it is found that the level of rms electron density deviation $\langle(\Delta N)^2\rangle^{1/2} = 2 \times 10^{10}$ m^{-3} required by the scintillation observations translates to $\langle(\Delta N)^2\rangle^{1/2} = 10^9$ m^{-3} at scale lengths

≤ 100 m. On the other hand, following Woodman and Basu [1978], it can be shown that the observed maximum back-scattered power level of 27 dB requires a rms electron density deviation of 4.5×10^{10} m^{-3} at scale lengths ≤ 100 m when an ambient ionization density of 10^{12} m^{-3} is assumed and the irregularities are considered to be cylindrically symmetric, infinitely elongated along the magnetic field, and having a steep one-dimensional spectral index of k^{-5}. Thus there is a factor of ~ 50 discrepancy between scintillation and backscatter observations in regard to the value of rms electron density deviation at scales ≤ 100 m where the spectral break is assumed to occur. However, this discrepancy is not really significant when one considers the range of errors possible in the determination of spectral indices of rocket or scintillation measurements which may be as large as ± 0.5. Thus this calculation shows that the existence of a k^{-5} regime in the one-dimensional electron density irregularity spectrum brings the backscatter

103

data more or less in agreement with the scintillation observations, in contrast to the case of a uniform k^{-2} spectrum as investigated by Woodman and Basu [1978]. However, it is impossible to derive from this calculation whether there exists another break in the spectrum near the irregularity wavelength of 3 m due to the excitation of microinstabilities. These high-frequency drift waves have been proposed to explain the 1-m, 36-cm, and 11-cm irregularities observed by Tsunoda [1980]. It is possible that these short-scale irregularities do not always exist, requiring, as they do for their excitation, regions with highly depleted electron densities. The rocket observations show that during these events the depletions were not deep enough to linearly excite the microinstabilities [Kelley et al., this issue].

Figure 4 shows the results of spaced receiver scintillation observations performed at Ancon by the use of 244-MHz transmissions from the Fleetsatcom geostationary satellite. This observation was made by three independent receiving systems with their antennas placed in the magnetic east-west direction. Since the F region irregularities are highly elongated in the magnetic N-S direction, a baseline along the magnetic E-W direction is sufficient to derive drift parameters. In this experiment the longest baseline between the two extreme antennas was 367 m, while the third antenna was asymmetrically placed between the two antennas at a distance of 123 m from the westernmost antenna.

The apparent velocity in the magnetic E-W direction, defined as the ratio of the E-W distance between the spaced receivers to the time lag at which the cross correlation is maximum, was derived every 3 min from the digitized data set [Basu and Whitney, 1983; Wernik et al., 1983]. The bottom panel of Figure 4 shows the time variation of the apparent velocity derived for the antenna pair occupying the central and the western positions with a baseline of 123 m as well as for the antenna pair in the east and the center with a baseline of 244 m. The top panel, showing the variation of S_4 index of 244-MHz scintillation, indicates that strong scattering prevailed for most of the evening. The time of the rocket flight and the period during which the radar interferometer measurements were performed are indicated on the diagram. The apparent eastward velocity was determined only when the cross-correlation coefficient exceeded 0.5. A gradual decrease of the zonal irregularity velocity from 200 to 75 m/s occurred over the first 1.5 hours of the evening. Briggs et al. [1950] viewed the correlation analysis of spaced receiver drift data from a statistical standpoint and showed that the apparent velocity v', defined earlier, is related to the mean velocity v obtained from the intersection of autocorrelation and cross correlation by the relation $v' = v + v_c^2/v$ where v_c is the characteristic velocity.

Wernik et al. [1983] used weak-scatter theory and made model computations to indicate that the characteristic velocity v_c is related to physical parameters such as velocity fluctuations or velocity gradient across the ray path through the irregular medium. Even though the present observations conform to strong scattering, we follow their method of computations and find that the characteristic velocity $v_c \approx 28$ m/s at 0250 UT when the rocket was launched and the radar interferometer measurements were performed. On this basis the mean drift speed is obtained as $v = 107$ m/s for an apparent velocity $v' = 114$ m/s. Thus at 0250 UT the mean drift speed is lower than the apparent velocity by about 7%. However, shortly after the onset of scintillations at 0130 UT, an apparent veloc-

ity of 210 m/s was found to correspond to a mean drift speed of 186 m/s due to a larger value of characteristic velocity $v_c = 67$ m/s. The larger characteristic velocity signifies that earlier in the evening the velocity fluctuations across the ray path were larger.

It should be noted that the drift speed shown in Figure 4 can be identified with the zonal irregularity drift only in the absence of any vertical drift. In the presence of a vertically upward component v_y of the drift, the measured drift v is related to the zonal drift v_z by the relation $v = v_z - v_y \tan\theta \sin\phi$ where θ is the zenith angle and ϕ is the azimuth angle of the wave vector from the magnetic plane. From the geometry of the present observations, $\theta = 29°$ and $\phi = 66°$, and therefore $v_z = v - 0.50v_y$. This relation indicates the possible contamination of zonal drift values in the presence of vertical drift.

At the time of the radar interferometer observations the spaced receiver measurements yielded a value of the apparent drift speed as $v' = 114$ m/s, true drift speed $v = 107$ m/s, and characteristic velocity $v_c = 28$ m/s. Considering the radar interferometer measurements of zonal drift speed at altitudes ranging between 510 and 540 km corresponding to maximum ionization density, an average drift speed of 114 m/s with rms fluctuation of 22 m/s is obtained. This is in surprisingly good agreement with the true drift speed of 107 m/s obtained from spaced receiver measurements. However, a disagreement between the two sets of results is noted when the interferometer results pertaining to the bottomside or the topside are used in the comparison. This is because scintillation measurements are weighted heavily by the levels with high ionization density while the zonal drift has a considerable variation with altitude.

In Figure 5 the apparent eastward drift speed for the rest of the measurement period of March 1, 1983, is shown. In view of a reduction of the drift speed, the cross-correlation analysis is performed over a 6-min stationary sample instead of 3 min as in Figure 4. At about 2330 LT the drift speed is only 10 m/s when extremely slow fading rates of signals are encountered. From the top panel of Figure 5 it may be noted that the depth of fluctuations is quite deep, providing S_4 varying between 0.6 and 1.0. Such deep signal fadings with a long period of the order of a minute or longer degrade modern transionospheric communication systems at VHF. Figure 6 shows the nature of such deep and slow signal fadings recorded by the three spaced receivers. Since the zonal drift speed in the equatorial F region attains very low values in the postmidnight time frame for an extended period before reversing from the eastward to the westward direction, the degradation of communication systems can routinely occur at this time. On most occasions the equatorial irregularities decay after midnight, so that the problem is not quite as severe. On magnetically disturbed nights, however, irregularities may be freshly generated in the postmidnight period [Rastogi and Woodman, 1978], so that these do not decay even around the sunrise period [Aarons and DasGupta, 1984]. On such occasions, prolonged periods of slow and deep fadings may be encountered which may pose problems for transionospheric communication systems.

In Figure 7 we show two 3-min samples of weak 1.7-GHz scintillations recorded at the time of the rocket flight. The analog data acquired in the field were digitized at 36 Hz, and the spectra obtained with the fast Fourier transform (FFT) technique are shown in the figure. Each spectrum indicates that maximum power spectral density is obtained at a fre-
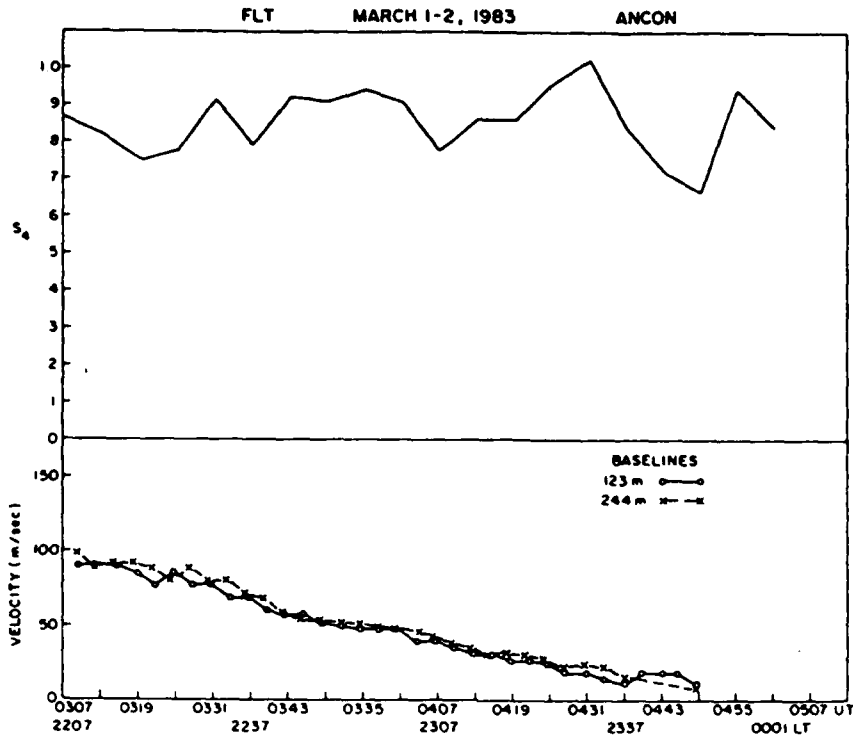
Fig. 5. Same as Figure 4 for the period 0307–0507 UT.

quency of $f_m = 0.2$ Hz. The frequency of the Fresnel maximum is $f_m = u/(2\lambda z)^{1/2}$ where u is the irregularity drift speed orthogonal to the ray path, λ the wavelength of observations, and z the slant range to the irregularity layer. Substituting $\lambda = 0.18$ m and $z = 550 \times 10^3$ m, we find that $u = 90$ m/s. In view of the fact that 1.7-GHz scintillation measurements were performed at an elevation angle of 76° and azimuth of only 8°, the direction of u is virtually along the E-W direction. We therefore find a close correspondence between u and the zonal drift speed obtained from spaced receiver drift data shown in Figure 5.

The linear roll-off portions of the spectra shown in Figure 7 indicating a linear variation of the logarithm of power spectral density (PSD) with the logarithm of fluctuation frequency f imply a power law variation of PSD with f of the form f^n. The roll-off portions of either spectra shown in Figure 7 can be best fitted to a power law form f^n with $n = -2.9$ over the frequency range 0.4–1 Hz, which can be translated to a spatial scale length range of 250–100 m by the use of the measured zonal drift speed of ∼100 m/s at this time. In general, the temporal spectrum of scintillations is a result of both the spatial spectrum of the irregularities and the distribution function of irregularity velocity [Lotova, 1981]. If, however, the velocity distribution is assumed to be very narrow in comparison to the spatial spectrum of electron density fluctuations, the spectral index n of scintillations can be related to the rocket-measured one-dimensional spectral index p_1 of electron density fluctuations as $n = -(1 - p_1)$ [Cronyn, 1970]. The rocket measurements indicated $p_1 = -2.5$ in the scale length range of 1 km to 100 m [LaBelle and Kelley, this issue] around an
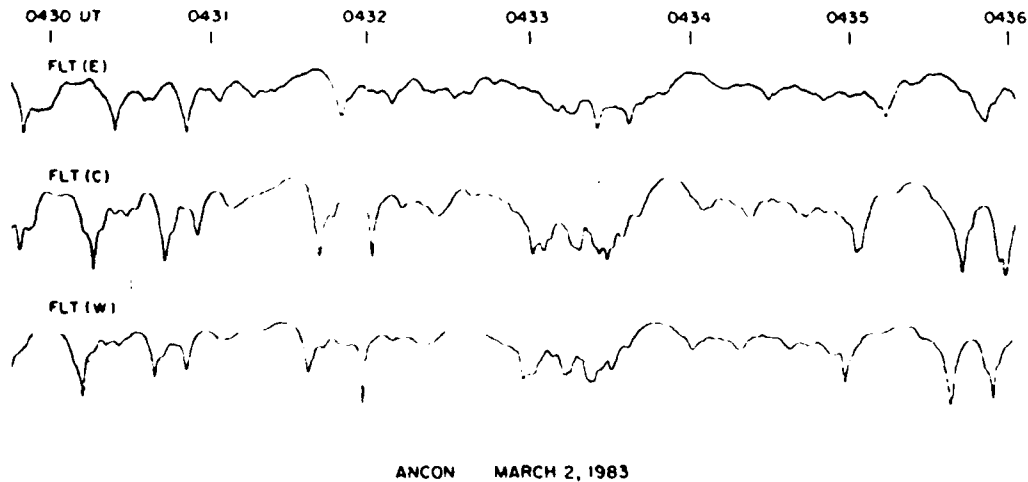

ANCON   MARCH 2, 1983

Fig. 6. Same as Figure 2 for the period 0430–0436 UT, illustrating the slow fadings of 244-MHz scintillation.

ANCON, PERU   GOES 5   1694 MHz
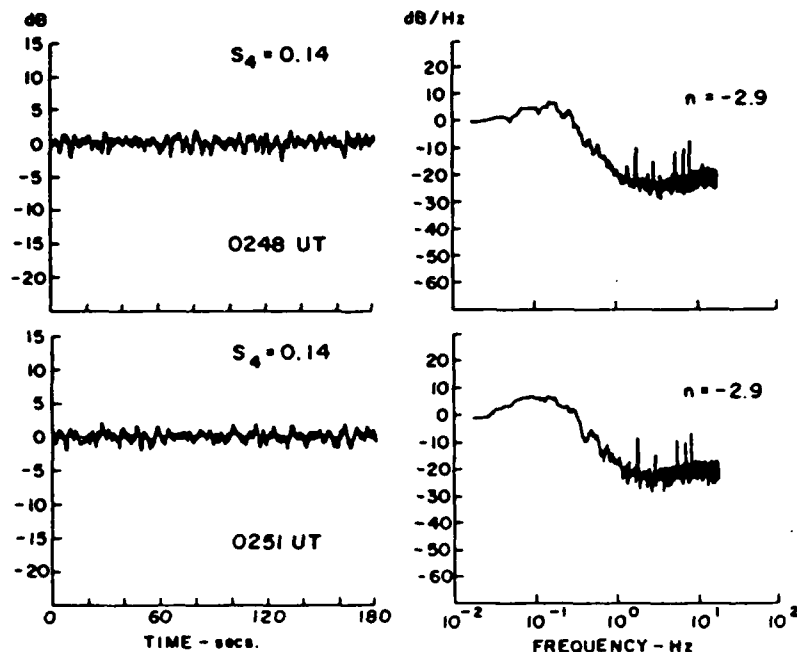MARCH 2, 1983

Fig. 7. Two 3-min samples of 1694-MHz scintillation recorded at Ancon during the rocket flight on March 2, 1983 (UT date), and their FFT spectra. The spectral index n of the roll-off portions of the spectra between 0.4 and 1 Hz is indicated.

altitude of 500 km corresponding to the level of ionization density, whereas scintillation measurements yielded $n = -2.9$ between 0.4 and 1 Hz corresponding to the scale length range of 250-100 m. These two measurements within 20% of one another are considered to be quite compatible.

On the same evening, 1.54-GHz scintillation measurements were performed from the Huancayo station by the use of transmissions from the Marisat satellite. Two data samples and their spectra corresponding to Figure 7 are shown in Figure 8. It is interesting to point out the consistency between a range of parameters that can be deduced from the intensity scintillation spectra. First, it may be noted that in Figure 8 the maximum PSD is obtained at a frequency of $f_m \approx 0.1$ Hz, which is a factor of 2 lower than that obtained from Ancon for GOES 5 observations. The Marisat satellite observations from Huancayo are performed at an elevation angle of 22° at an azimuth corresponding to virtually the eastward direction. For the same 500-km altitude of maximum ionization density, assumed in the discussion of Figure 7, the slant range of the Huancayo site to the irregularity layer at the low elevation angle of measurement becomes $z = 1123$ km. Hence the spatial scale corresponding to the Fresnel maximum may be deduced as $\Lambda = (2\lambda z)^{1/2} = 661$ m. Since the frequency of Fresnel maximum indicated by the spectra if $f_m \approx 0.1$ Hz, the irregularity drift velocity orthogonal to the propagation path is deduced as $u = f_m \Lambda = 66$ m/s. Considering the ionospheric zenith angle of 59°, the equivalent zonal drift is 132 m/s as compared to the true drift of 107 m/s derived from the spaced receivers. Thus this value is within 20% of that deduced from the spaced receivers. In general, however, this technique is not very accurate for large zenith angles such as in the present case.

Finally, the roll-off portions of Marisat scintillation spectra in the frequency range 0.1-0.7 Hz corresponding to the scale length range 650-100 m are found to be best fitted by a power law form of f^n with $n = -3.2$. This result agrees with 1.7-GHz measurements at Ancon described earlier and is also consistent with the rocket measurements of the one-dimensional spectral index of electron density irregularities [LaBelle and Kelley, this issue].

Event of March 15, 1983

The second F region rocket was launched at 2133 LT on March 14, 1983. The radar and scintillation measurements were performed throughout the evening as was done on March 1, 1983, and discussed in the previous paragraphs. In this section we shall concern ourselves with comparing the observational material obtained on the second night rather than discussing the second night's measurements as an independent data set.

The behavior of the F region on the evening of March 14 was very different from that of March 1. The F layer was much lower on March 14, the virtual height of the bottomside F region being only 300 km as compared to 430 km on March 1. Just before the onset of spread F the altitude of the F region maximum was around 360 km on March 14 as compared to 520 km on March 1. The critical frequencies were comparable on the two evenings, being 11.5 MHz on March 1 and 10 MHz on March 14. As we shall show presently, the magnitude of 1.7-GHz scintillation on March 14 was slightly higher, but the zonal drift speed measured by the spaced receivers was nearly a factor of 2 higher on this evening as compared to March 1, and the spectral index of GHz scintillations was considerably steeper on the second night.
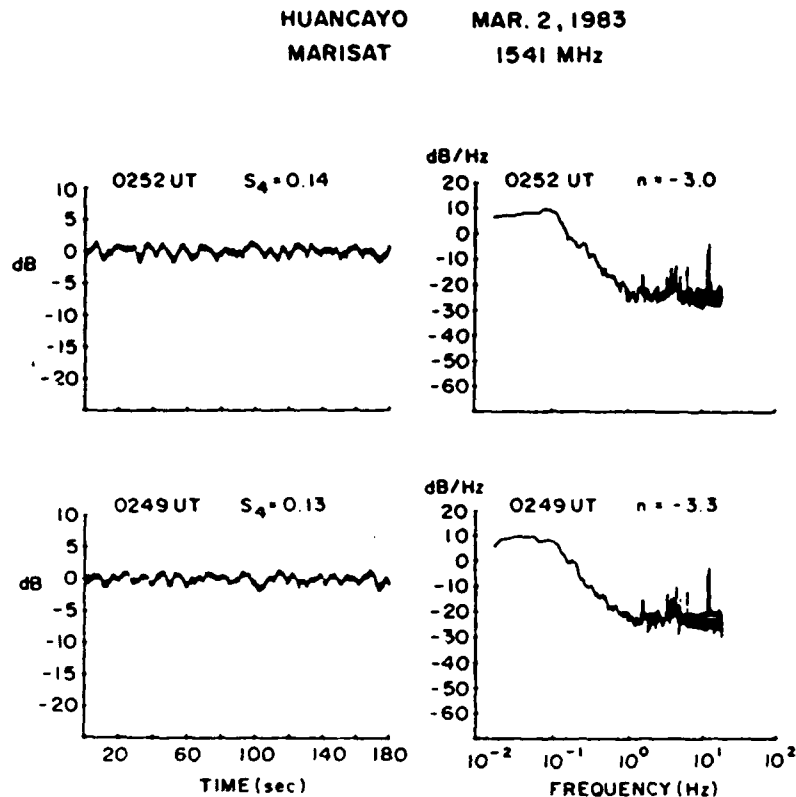
HUANCAYO   MAR. 2, 1983

MARISAT   1541 MHz

Fig. 8. Two 3-min samples of 1541-MHz scintillation of Marisat satellite signals recorded at Huancayo on March 2, 1983 (UT date), and their FFT spectra. Values of the spectral index n of the roll-off portions of the spectra between 0.1 and 0.7 Hz are indicated.

Figure 9 compares the radar backscatter and 1.7-GHz scintillation measurements on March 14 in a form similar to that of Figure 3. The maximum backscattered power level at 50 MHz and the S_4 index of 1.7-GHz scintillations are found to be slightly higher than on March 1. Since the irregularity drift speed was a factor of 2 higher on March 14 as compared to March 1, a study of the correspondence of radar and GHz scintillation requires only a time shift of +3 min for the scintillation data relative to the backscatter map. The first two scintillation structures (marked I and II on Figure 9) are found to correspond to the first two plume structures, whereas the equally strong third scintillation structure (marked III) does not have a developed plume at the altitude of the F region maximum. The existence of a thin backscatter layer in the bottomside and the top portion of a westward tilted plume structure at altitudes above 800 km are the only signatures of 3-m irregularities in association with the third scintillation structure. Since at these altitudes the ambient ionization density is very low, we conclude that the irregularities with scale lengths ~ 100 m causing GHz scintillations have no associated 3-m irregularities of consequence because of either the erosion of 3-m irregularities generated earlier in the evening [Basu et al., 1980] or a lack of generation of meter scale irregularities in the absence of steep density gradients [Rino et al., 1981].

However, the scintillation and rocket measurements were compatible. For example, if we assume the irregularity distribution parameters to be similar to those of March 1 and the spectral index of scintillation to be steeper ($n = -4.5$, as will be shown later) in keeping with the observations, the weak-scatter computations indicate that a rms electron density deviation of 2.7×10^{10} m^{-3} for irregularities in the scale length

range 1 km to 100 m is necessary to produce $S_4 \approx 0.17$ at the time of the rocket flight. The rocket measurements indicated that at the level of maximum ionization density of 1.26×10^{12} m^{-3} the irregularity amplitude $\langle (\Delta N/N)^2 \rangle^{1/2}$ was 1.7% in the scale length range 1 km to 100 m, providing a rms electron density deviation of 2.1×10^{10} m^{-3}. This is in good agreement with the predictions of weak-scatter computations given above.

Figure 10 shows the variation of the apparent eastward motion of the irregularities derived from the spaced receiver scintillation measurements. Comparing Figures 10 and 4, it may be noted that the eastward drift on March 14 is a factor of 2 higher than that measured on March 1. Further, the drift remains elevated without showing any decrease with local time. At the time of the rocket flight, when the interferometer measurements were performed, we obtained the values of the apparent, characteristic, and true velocities as 218, 43, and 210 m/s, respectively. This showed that not only was the zonal drift higher on March 14 but the velocity fluctuations were larger as well, being about 20% of the average value. The radar interferometer measurements recorded an average zonal drift of about 170 m/s in the height range 350–380 km with a velocity fluctuation of about 20% about the average. Thus both the interferometer and the spaced receiver scintillation measurements recorded much higher zonal drift on March 14 when the second F region rocket was flown. It should, however, be noted that the spaced receiver drifts were 20% higher than the radar interferometer measurements. The marked day-to-day variability of zonal drift is rather interesting, particularly when we observe 75–100% higher drift speeds with the F region at a lower altitude.
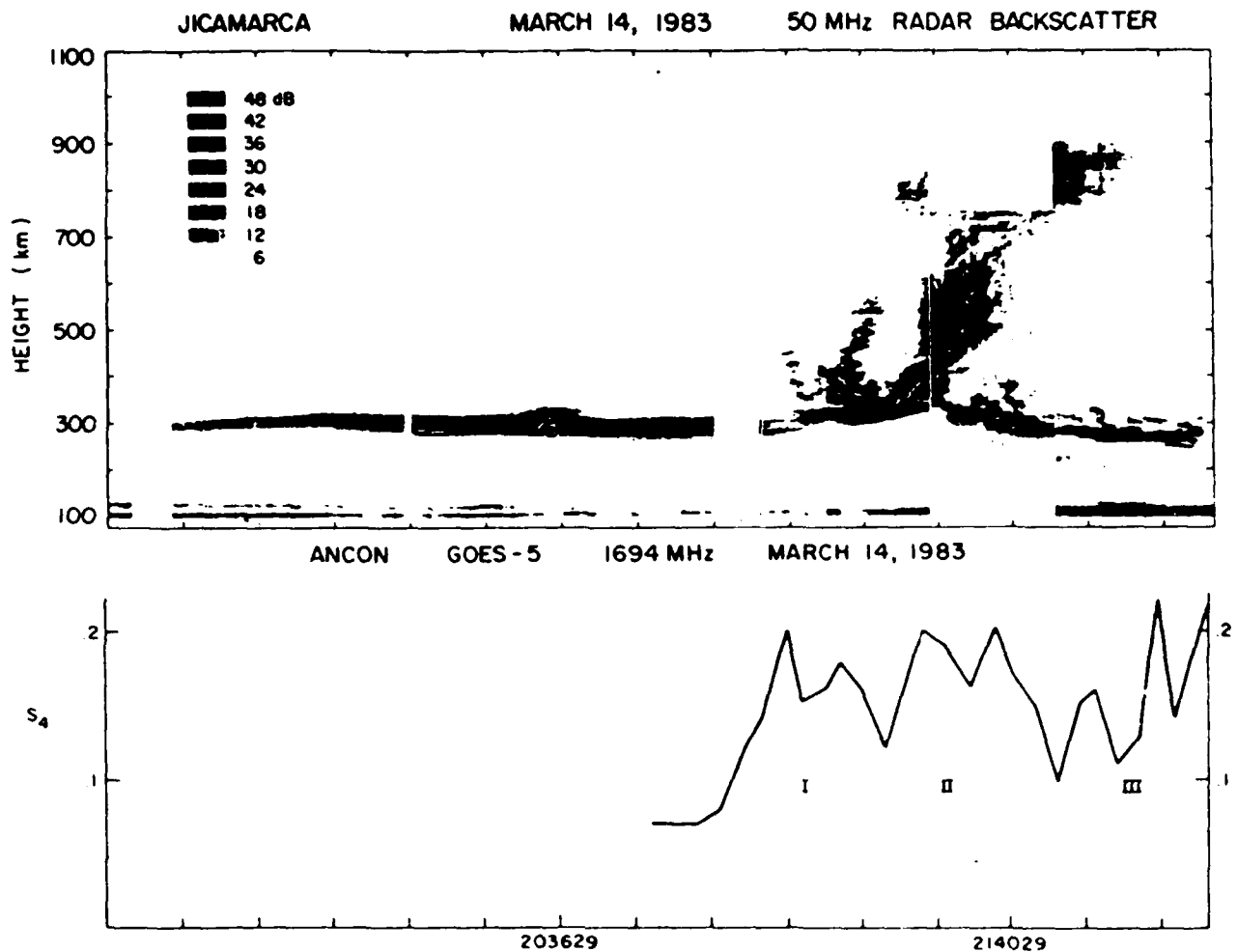
Fig. 9. Same as Figure 3 for March 15, 1983 (UT date)

Figure 11 shows two 3-min samples of 1.7-GHz scintillations and their spectra obtained during the rocket flight of March 14, 1985. In view of the lower altitude of the F region maximum the slant range of AN/G5 measurements to the irregularity layer is obtained as 400 km. Since the roll-off of the spectra occurs at a frequency of about $f_m = 0.50$ Hz, the irregularity drift velocity orthogonal to the propagation path is obtained as 190 m/s. This corresponds closely to the zonal drift speed obtained from the spaced receiver measurements at this time. A quick comparison with the spectra of March 1 shown in Figure 7 indicates a high-frequency displacement of the spectral peak in Figure 11 due to the increased irregularity drift. The roll-off portions of the present spectra computed over 0.6–1.5 Hz, corresponding to scale lengths in the range of 330–130 m, are shown to follow a power law form expressed as f^n with $n = -5$. As discussed in connection with the March 1 event, the observed spectral index of the scintillation index implies a one-dimensional irregularity spectral index of -4. The rocket in situ probes, however, detected an irregularity spectral index of -2.5 in the range 1 km to 100 m. From the Huancayo station, 1.5-GHz scintillation observations were performed on this evening. These spectra also indicated steep slopes, $n = -5$, similar to those observed at the Ancon station. Since the scintillation spectrum is steeper than that predicted from the irregularity spectrum, it is not possible to explain the observed discrepancy in terms of a spatial distribution of irregularity drifts [Blums and Lotota, 1981]. It is not clear if through any possible uncertainty in the determination of spatial scales in the rocket spectrum, the scintillation spectrum is reflecting the steeper irregularity spectrum characteristic of short-scale drift wave structures [Kelley et al., 1982; LaBelle et al., this issue]. Another possible reason for the discrepancy could be the anisotropy of the wave number spectrum in the vertical and horizontal directions observed in the simulation studies of the collisional Rayleigh-Taylor instability by Seyler and Zargahm [1985]. If this is indeed the case, the horizontal scintillation spectrum will not necessarily map the vertical rocket spectrum. In closing we note that GHz scintillation spectra from both stations, Huancayo and Ancon, recording two independent satellites yielded steep spectral indices in the range of -4 to -5 throughout the evening.

4. CONCLUSIONS

The coordinated radar, rocket, and scintillation measurements performed during Project Condor allowed an intercomparison of complementary data sets on equatorial F region irregularities in the wide scale length range of 3 m to a few kilometers. In fact, this data set presents for the first time the simultaneous radar backscatter and GHz scintillation observations virtually over the magnetic equator. In addition, the simultaneous radar interferometer and spaced receiver scintil-
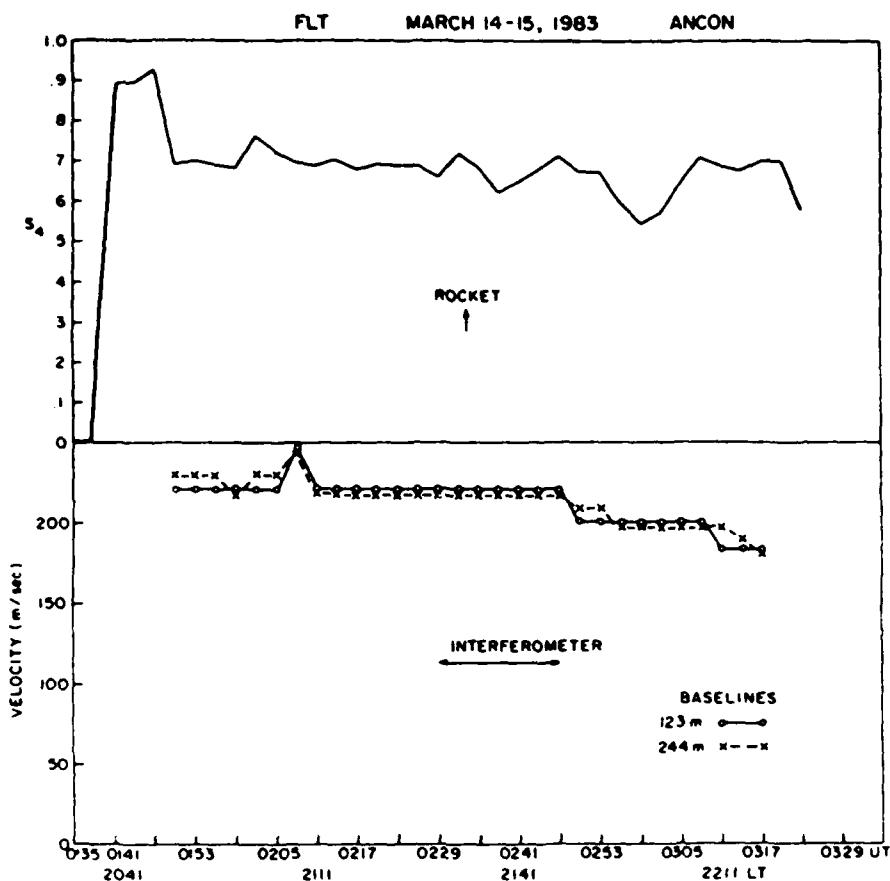
Fig. 10. Same as Figure 4 for March 15, 1983 (UT date)

lation measurements allowed an opportunity to track the zonal motion of the scattering centers causing the 3-m backscatter and the motion of kilometer scale irregularities giving rise to VHF scintillations. The full complement of equatorial irregularity phenomena was observed on the two nights (March 1 and March 14, 1983) with a very conspicuous difference in the altitude of the F region offering significantly different levels of coupling between the neutrals and the ionized components.

On both evenings, very good agreement between the GHz scintillation structures and the extended 3-m plume structures was noted. This result indicates that the height-integrated electron density deviation of 200-m scale irregularities becomes maximum when the 3-m backscattered power becomes most intense and the backscatter structures are most extended [Basu et al., 1978; Tsunoda, 1981]. This is because the ionospheric regions with high plasma density near the F region peak causing intense scintillations lie adjacent to the depletions associated with the 3-m backscatter plumes [Rino et al., 1981]. While this agreement is routinely observed in the early phase, the March 14 result indicated that a late phase GHz scintillation structure may not be accompanied by any conspicuous plume structure near the F region peak possibly as a result of the erosion of sharp density gradients.

It should be noted that in spite of the presence of intense and extended plume structures at 3 m, the associated 1.7-GHz scintillation was observed to be very weak in comparison with the saturated GHz scintillations reported from Ascension Island near the crest of the equatorial anomaly [Basu et al., 1983]. The modeling results of Anderson and Klobuchar

[1983] indicate that the meridional transport in the postsunset period favors the off-equatorial locations at African longitudes in providing an environment of extremely high electron content. When irregularities develop to a few percent amplitude in such an environment, saturated GHz scintillations may be obtained. It should be noted that at the magnetic equator even with the F region critical frequencies in the range 10–12 MHz as measured by the rocket, the 1.7-GHz scintillations did not exceed S_4 of 0.2 (4-dB fluctuations) for overhead propagation paths.

The spectral index of GHz scintillations was shown to be compatible on one night with the one-dimensional irregularity spectral index as measured by the rocket, whereas on the other night the spectral index of scintillations was far too steep in comparison to the irregularity spectral index in the intermediate scale. The scintillation measurements reflected instead the steep short-wavelength irregularities. This discrepancy occurred in the evening of March 14 when the irregularity drift speed was high, of the order of 200 m/s with about 20% fluctuation. In view of this result it may be useful to perform experiments providing both the velocity and density turbulence spectra.

The coordinated irregularity drift measurements by the radar interferometer and spaced receiver scintillation measurements indicated that the spaced receiver drifts are about 10–20% higher on both nights. It is not clear at this moment why the zonal drift speed of scattering centers of 3-m wavelength measured by the radar interferometer should be systematically lower than the drift of 1-km irregularities. On the other hand, both techniques recorded a twofold increase of

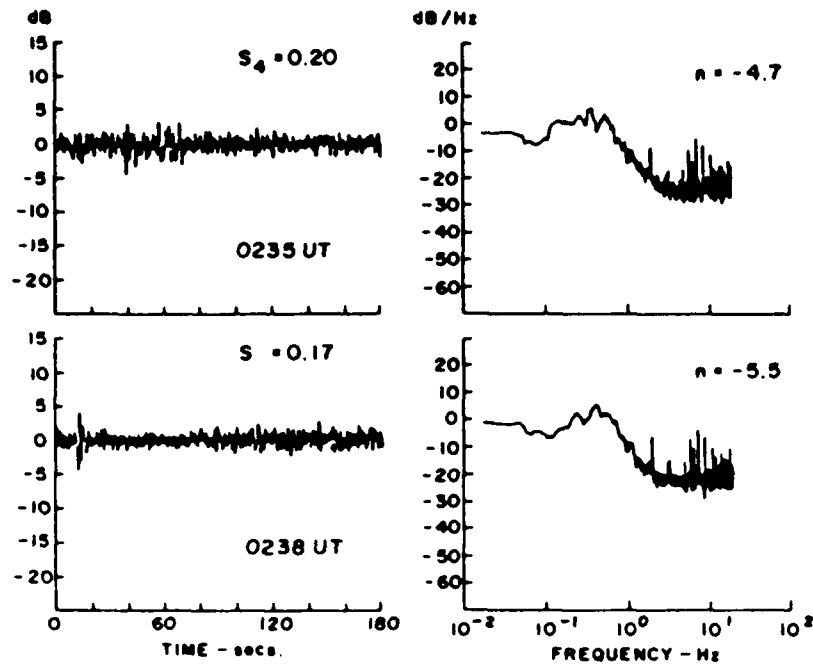ANCON, PERU   GOES 5   1694 MHz

MARCH 15, 1983

Fig. 11. Same as Figure 7 for March 15, 1983. The spectral index n has been computed over the frequency interval 0.6-1.5 Hz.

zonal drift speed between March 1 and March 14, 1983. It should be mentioned that the spaced receiver drift analysis during strong scintillations which represent the present situation is yet to be modeled theoretically. It is unfortunate that although neutral wind measurements were performed during this period at Arequipa, Peru, by *Meriwether et al.* [this issue], no measurements could be made on these two nights. However, these Fabry-Perot interferometer measurements show large day-to-day variability in the zonal wind speeds. Coordinated Fabry-Perot, spaced receiver scintillation, and radar interferometer observations are being planned in Peru to make simultaneous measurements of neutral wind and drifts of small- and large-scale irregularities. This will allow us to explore the relationship between the neutral wind, F region plasma motion, and field line integrated Pedersen conductivities near the magnetic equator. It should also be interesting to study the effect of the transequatorial component of neutral wind on the day-to-day variability of spread F generation recently proposed by *Maruyama and Matuura* [1984].

REFERENCES

Aarons, J., and A. DasGupta, Equatorial scintillations during the major storm of April 1981, *Radio Sci.*, *19*, 731-739, 1984.

Anderson, D. N., and J. A. Klobuchar, Modeling the total electron content observations above Ascension Island, *J. Geophys. Res.*, *88*, 8020-8024, 1983.

Basu, S., and A. DasGupta, Scintillations of satellite signals by ionospheric irregularities with sharp boundary, *J. Geophys. Res.*, *74*, 1294-1300, 1969.

Basu, S., and H. E. Whitney, The temporal structure of intensity scintillations near the magnetic equator, *Radio Sci.*, *18*, 263-271, 1983.

Basu, S., Su. Basu, J. Aarons, J. P. McClure, and M. D. Cousins, On the coexistence of kilometer and meter scale irregularities in the nighttime equatorial F region, *J. Geophys. Res.*, *83*, 4219-4226, 1978.

Basu, S., J. P. McClure, Su. Basu, W. B. Hanson, and J. Aarons, Coordinated study of equatorial scintillations and in situ and radar observations of nighttime F region irregularities, *J. Geophys. Res.*, *85*, 5119-5130, 1980.

Basu, Su., and S. Basu, Equatorial scintillations—Advances since ISEA-6, *J. Atmos. Terr. Phys.*, *47*, 753-768, 1985.

Basu, Su., S. Basu, J. P. McClure, W. B. Hanson, and H. E. Whitney, High-resolution topside in situ data of electron densities and VHF/GHz scintillations in the equatorial region, *J. Geophys. Res.*, *88*, 403-415, 1983.

Blums, D. F., and N. A. Lotova, Analysis of the temporal spectra of scintillation with allowance for solar-wind velocity distribution, *Geomagn. Aeron.*, Engl. Transl., *21*, 149-152, 1981.

Briggs, B. H., G. J. Phillips, and D. H. Shinn, The analysis of observations on spaced receivers of the fading radio signals, *Proc. Phys. Soc. London*, *63*, 106-121, 1950.

Cronyn, W. M., The analysis of radio scattering and space probe observations of small-scale structure in the interplanetary medium, *Astrophys. J.*, *161*, 755-763, 1970.

Davies, K., and J. D. Whitehead, A lens in the ionosphere, *J. Atmos. Terr. Phys.*, *39*, 383-387, 1977.

Fejer, B. G., E. Kudeki, and D. T. Farley, Equatorial F region zonal plasma drifts, *J. Geophys. Res.*, *90*, 12,249, 1985.

Franke, S. J., and C. H. Liu, Observations and modeling of multifrequency VHF and GHz scintillations in the equatorial region, *J. Geophys. Res.*, *88*, 7075-7085, 1983.

Kelley, M. C., R. Pfaff, K. D. Baker, J. C. Ulwick, R. Livingston, C. Rino, and R. Tsunoda, Simultaneous rocket probe and radar

110

measurements of equatorial spread F: Transitional and short wave-length results, *J. Geophys. Res.*, *87*, 1575–1588, 1982.

Kelley, M. C., J. LaBelle, E. Kudeki, B. G. Fejer, S. Basu, Su. Basu, K. D. Baker, C. Hanuise, P. Argo, R. F. Woodman, W. E. Swartz, D. T. Farley, and J. W. Meriwether, Jr., The Condor equatorial spread F campaign: Overview and results of the large-scale measurements, *J. Geophys. Res.*, this issue.

Kudeki, E., B. G. Fejer, D. T. Farley, and H. M. Ierkic, Interferometer studies of equatorial F-region irregularities and drifts, *Geophys. Res. Lett.*, *8*, 377–380, 1981.

LaBelle, J., and M. C. Kelley, The generation of kilometer scale irregularities in equatorial spread F, *J. Geophys. Res.*, this issue.

LaBelle, J., M. C. Kelley, and C. E. Seyler, An analysis of the role of drift waves in equatorial spread F, *J. Geophys. Res.*, this issue.

Lotova, N. A., Temporal scintillation spectra with allowance for the solar wind velocity distribution: Theory, *Geomagn. Aeron.*, Engl. Transl., *21*, 447–449, 1981.

Maruyama, T., and N. Matuura, Longitudinal variability of annual changes in activity of equatorial spread F and plasma bubbles, *J. Geophys. Res.*, *89*, 10,903–10,912, 1984.

Meriwether, J. W., Jr., J. W. Moody, M. A. Biondi, and R. G. Roble, Optical interferometric measurements of nighttime equatorial thermospheric winds at Arequipa, Peru, *J. Geophys. Res.*, this issue.

Morse, F. A., B. C. Edgar, H. C. Koons, C. J. Rice, W. J. Heikkila, J. H. Hoffman, B. A. Tinsley, J. D. Winningham, A. B. Christensen, R. F. Woodman, J. Pomalaza, and N. R. Teixeira, Equion, an equatorial ionospheric irregularity experiment, *J. Geophys. Res.*, *82*, 578–592, 1977.

Rastogi, R. G., and R. F. Woodman, Spread-F in equatorial ionograms associated with reversal of horizontal F-region electric field, *Ann. Geophys.*, *34*, 31–36, 1978.

Rino, C. L., A power law phase screen model for ionospheric scintillation, 1. Weak scatter, *Radio Sci.*, *14*, 1135–1145, 1979.

Rino, C. L., R. T. Tsunoda, J. Petriceks, R. C. Livingston, M. C. Kelley, and K. D. Baker, Simultaneous rocket-borne beacon and in situ measurements of equatorial spread F: Intermediate wavelength results, *J. Geophys. Res.*, *86*, 2411–2420, 1981.

Seyler, C., and S. Zargahm, Forced Rayleigh-Taylor and gradient drift turbulence (abstract), *Eos Trans. AGU*, *66*, 327, 1985.

Tsunoda, R. T., Magnetic field aligned characteristics of plasma bubbles in the nighttime equatorial ionosphere, *J. Atmos. Terr. Phys.*, *42*, 743–752, 1980.

Tsunoda, R. T., Time evolution and dynamics of equatorial backscatter plumes, 1, Growth phase, *J. Geophys. Res.*, *86*, 139–149, 1981.

Wernik, A. W., C. H. Liu, and K. C. Yeh, Modeling of spaced-receiver scintillation measurements, *Radio Sci.*, *18*, 743–764, 1983.

Woodman, R. F., and Su. Basu, Comparison between in-situ spectral measurements of F-region irregularities and backscatter observations at 3 m wavelength, *Geophys. Res. Lett.*, *5*, 869–872, 1978.

Woodman, R. F., and C. LaHoz, Radar observations of F region equatorial irregularities, *J. Geophys. Res.*, *81*, 5447–5466, 1976.

Santimay Basu and H. E. Whitney, Air Force Geophysics Laboratory, Hanscom Air Force Base, MA 01731.

Sunanda Basu, Emmanuel College, Boston, MA 02115.

A. Bushby, Instituto Geofisico del Peru, Lima 100, Peru.

B. G. Fejer, M. C. Kelley, and J. LaBelle, School of Electrical Engineering, Cornell University, Ithaca, NY 14853.

E. Kudeki, Department of Electrical Engineering, University of Illinois, Urbana, IL 61801

END

9-87

DTIC